APPLIED COMPUTATIONAL ELECTROMAGNETICS SOCIETY JOURNAL

March 2017
Vol. 32 No. 3
ISSN 1054-4887

The ACES Journal is abstracted in INSPEC, in Engineering Index, DTIC, Science Citation Index Expanded, the Research Alert, and to Current Contents/Engineering, Computing & Technology.

The illustrations on the front cover have been obtained from the research groups at the Department of Electrical Engineering, The University of Mississippi.

EMERITUS EDITORIAL ASSISTANTS

MARCH 2017 REVIEWERS

THE APPLIED COMPUTATIONAL ELECTROMAGNETICS SOCIETY

JOURNAL

Vol. 32 No. 3 March 2017

TABLE OF CONTENTS

Bandwidth Optimization of a Wideband Co-Co Antenna Array on a Thin Flexible Dielectric using HFSS®

Joseph D. Majkowski

Harris Communication Systems
Rochester NY, 14610, United States
Jmajkows@harris.com

Abstract ─ This paper presents several novel techniques for designing a compact Co-Co antenna array for optimal performance over a broad frequency range of one and half octaves. The antenna was modeled and tested on 6 mil Polyimide composite, a thin, flexible, substrate, in order to meet size requirements. A slotting technique was used to increase both the impedance and gain bandwidth of the antenna. The final design produced an omnidirectional antenna with peak gain greater than 1 dBi and S(1,1) less than -8 dB over a frequency range of 2.8*F1. In order to make a manufacture-able antenna, the microstrip transmission line width was increased for co-axial feeding of the antenna with a second slotting technique.

Index Terms ─ Co-Co antenna, flexible, slotting, transmission line.

I. INTRODUCTION

Wide bandwidth antennas with omnidirectional performance at the horizon (azimuth plane) have grown in demand greatly over the last few years. This demand comes as military radios grow in both their capabilities and usable frequency range. The end user no longer picks up the radio just to make simple voice communication, but may also be utilizing the radio as a way to communicate mission plans, send pictures or video, or even act as a node in a network. These new capabilities offer many advantages but require much higher frequency ranges than traditional voice communications. Thus, to prevent adding another antenna to the soldiers burden, as well as to seamlessly switch between these capabilities, a single, wideband, antenna solution is needed.

The typical antenna of choice in military communication is a vertical monopole or dipole antenna with half wavelength resonant structure and broadband matching [1], [2]. However, the peak theoretical gain, 2.15 dBi, which one can achieve with a dipole or monopole may not be enough to achieve the high speed or even distance required with some of the higher frequency data waveforms. Thus we look to the coaxial, collinear (Co-Co) antenna [3], [4] to enhance the gain. It is seen that the gain and omnidirectional nature of the Co-Co antenna is very good; however, the bandwidth is very narrow. Thus, in order to improve bandwidth and functionality of the Co-Co antenna, various techniques such as altering element gap [5], moving feed location [6], tilting the elements [7], and varying element shapes [8] have been tried. While these techniques succeed, they only manage to achieve 10% to 15% increases in BW [5-7]. Other omnidirectional dipole printed antenna designs have been proposed in recent years [9], [10]. However, while these designs produce omnidirectional patterns, high gain and can increase bandwidth, they are also incredibly large and do not fit the required footprint for this antenna. In order to shrink overall size, techniques such as slots [11], [12] and utilizing a 3-D structure [12] have been utilized in more recent works.

In this paper, a novel 2 element wideband collinear dipole array with slots is designed, fabricated, and measured. The slotting technique helps to induce 2 modes of operation in the antenna and enhance both the gain and impedance bandwidth of the antenna. This technique keeps the current and voltage in phase for both a dipole excitation at low frequency and a Co-Co excitation for enhanced gains at the upper frequencies. Details of the proposed antenna are described and experimental results are presented along with the numerical results.

II. CO-CO ANTENNA BACKGROUND

The Co-linear, Co-polar (Co-Co) antenna array has been being used for decades due to its ease of manufacturing, high gain, and omnidirectional pattern.

The Co-Co antenna can be thought of as a set of $\ell/2$ co-axial transmission lines. The outer conductor and the inner conductor will alternate every $\ell/2$ in order to setup discontinuities. Voltage maximums will occur at these discontinuities between elements which encourages the antenna to radiate at these points. Thus, the more discontinuities the higher the antenna gain, however more elements produce a diminishing return

Submitted On: July 25, 2016
Accepted On: February 4, 2017

and comes at the cost of bandwidth.

Co-Co antennas can also be built with flat transmission line with one shorting pin at each end of the antenna. A second variation can also be built utilizing just one shorting pin farthest from the feed point. The shorting pins are utilized in the design to allow for the currents to be setup in-phase as seen in Fig. 1. Once the currents are in phase it allows for the antenna to have an omnidirectional radiation characteristic. The shorting pin closest to driving point of the antenna is primarily utilized as a balun to help reduce surface currents at the feed point, allowing more energy to make it to the antenna. However, the use of this shorting pin location comes at the cost of making the antenna much harder to match from a broadband impedance standpoint.

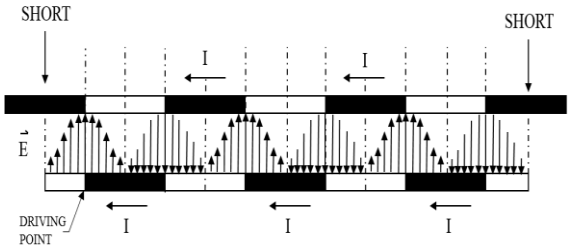

Fig. 1. Side view of the Co-Co antenna current and voltage distributions [8].

The shape of the elements can also be varied in order to achieve optimal performance. The tried element shapes have varied from circular, elliptical, rectangular and hybrids of any three of these shapes. It was found that by tapering the elements to form either circular or elliptical element shapes helps reduce side lobes levels. An image of these various techniques on 7 element Co-Co antennas can be seen below in Fig. 2. Image of the proposed antenna design are seen in Fig. 3. The slots on the top, bottom, and middle section are all controlled and defined in the same manner.

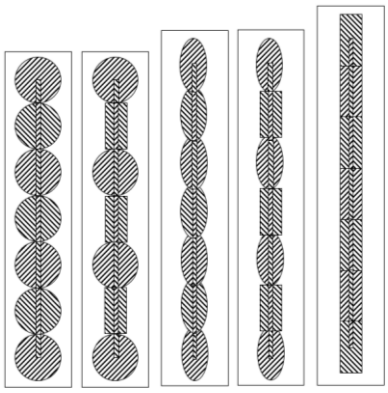

Fig. 2. Image of various element shapes and techniques of a 7 element design [8].

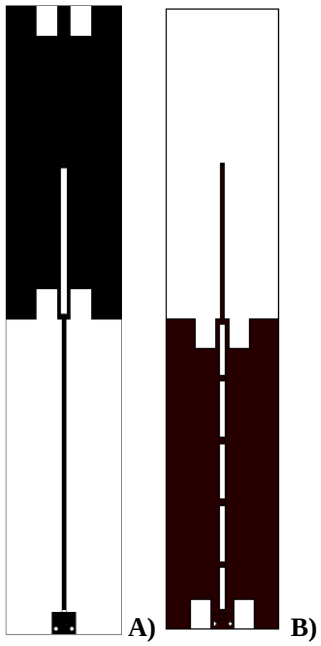

Fig. 3. Image of proposed antenna: (A) front view and (B) rear view.

III. SLOTTING TECHNIQUE

Given the advantages of the Co-Co antenna, it still did not have the bandwidth required. Thus, slots were added to increase the bandwidth.

Due to the nature of the Co-Co antenna array, the antenna elements need to be approximately $\ell/2$ in length, where ℓ is the center frequency's electrical length, in order to produce a maximum electric field at the reversal of ground plane and trace [13]. Due to required size of the antenna, the element lengths were chosen to be $\ell/2$ for a frequency slightly below $1.4*F_1$. However, it was seen that the S(1,1) of the antenna was only good for a bandwidth of approximately $1.8*F_1$ as seen in Fig. 3. This in turn caused the antenna to be a poor radiator at the higher frequencies ($2.8*F_1$). Four rectangular slots were cut into each element, two on the bottom and two on the top, in order to produce electrically shorter elements that extended the bandwidth. The slots were tuned using HFSS® parametric sweeps [14] to find the optimum length, width, and separation of the slots. The effect of the slots in both S(1,1) and electric field can be seen in Figs. 4 and 5. The S(1,1) improves significantly in the 1.7*F1-2.8*F1 range with the addition of the slots. The electric field shows that the antenna also radiates much more efficiently at 2.8*F1 with the addition of the slots.

The parametric sweeps of the slot parameters can be seen in Fig. 6. Slot length, (H-length), is swept 1 mm to 13 mm in the diagram. It is seen that as the length of the slot reached the 5 mm to 9 mm range that resonance circles start to form in the impedance and quickly

disappear in the swept frequency range above and below these lengths. In B, width of the slot, (H-width) is swept 1 mm to 6 mm. As this parameter increases, the impedance spirals clockwise and mimics the change presented by increasing a series inductor. Finally as the slot separation, (Hs), is swept from 2 to 8 mm, it is seen to have the effect of a decreasing parallel inductor. The closer the slots the better the impedance is and the farther apart the quicker the impedance begins to unravel.

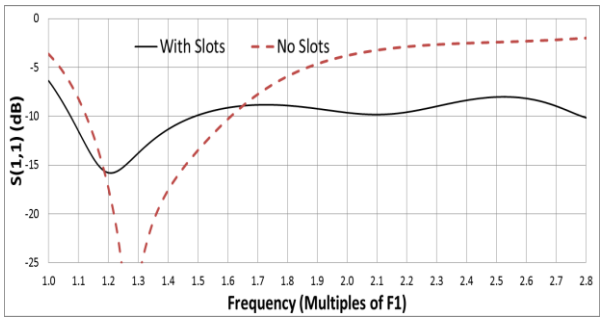

Fig. 4. S(1,1) in dB comparison of the slotted and non slotted antenna.

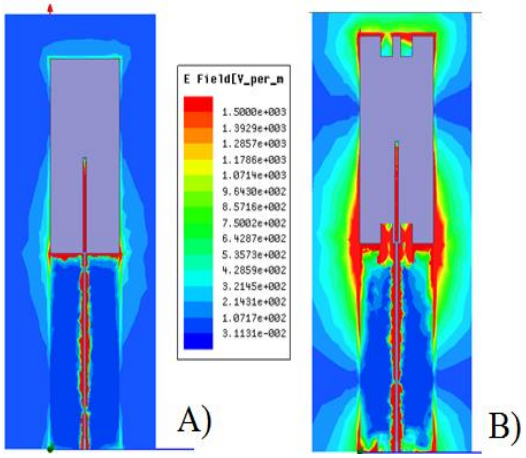

Fig. 5. Colored contour electric field plot (V/M) on a plane that bisects the PCB between the elements at 2.8*F_1. (A) No slots and (B) with slots.

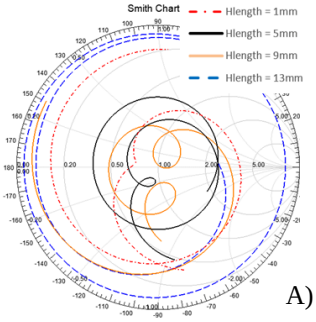

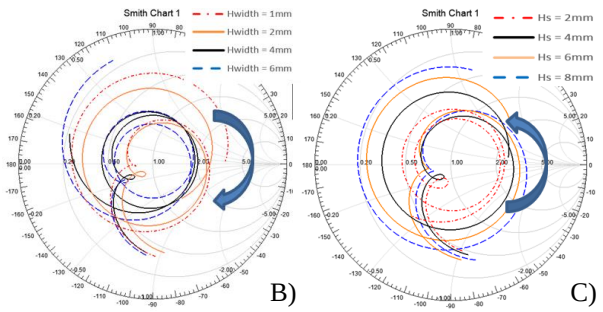

Fig. 6. Impedance of parametric sweep of: (A) H-length (length of slot), (B) H-width (width of slot), and (C) Hs (slot separation).

IV. MODES OF OPERATION

The antenna has two differing modes of operation. A "dipole" mode of operation, which occurs over the lowest frequencies (1-1.4)*F_1 and a "Co-Co" mode of operation that occurs over the rest of the frequency band (1.4-2.8)*F_1.

The "dipole" mode of operation performs as the name implies. The antenna begins to radiate, much like a dipole, at the element ends. This is due to the currents reaching a maximum at the junction between the two elements as seen in Fig. 7. The voltage thus reaches maximums at the end of the two elements which allows for the antenna to radiate as seen in Fig. 7. Here the performance is slightly lower than that of the "CoCo" mode as you are not able to radiate effectively at the junction between elements. The typical gain performance in this region of operation is 0-2 dBi at the horizon.

The "CoCo" mode of operation is when the antenna truly acts as an array. Currents are setup in this mode such that they reach maximums in the middle of each element which produces voltage maximums at the elements ends as well as the junction between the two elements. This can be seen in Fig. 8. Typical performance in this mode is more desirable as it surpasses the dipole mode with 1-4 dBi of gain at the horizon.

While it is certainly desirable to maintain the "CoCo" mode of radiation over the entire bandwidth it was simply not achievable. Both modes must be used to obtain and maximize bandwidth. The antenna was however able to be designed such that the crossover between the two modes caused no negative effects on the performance of the antenna. Thus, the antenna was able to cover the entire bandwidth with a slight 1 dB ripple in performance over some of the lower frequencies. The antenna is able to maintain an omnidirectional pattern throughout the transition between modes without introducing any side lobes to the pattern.

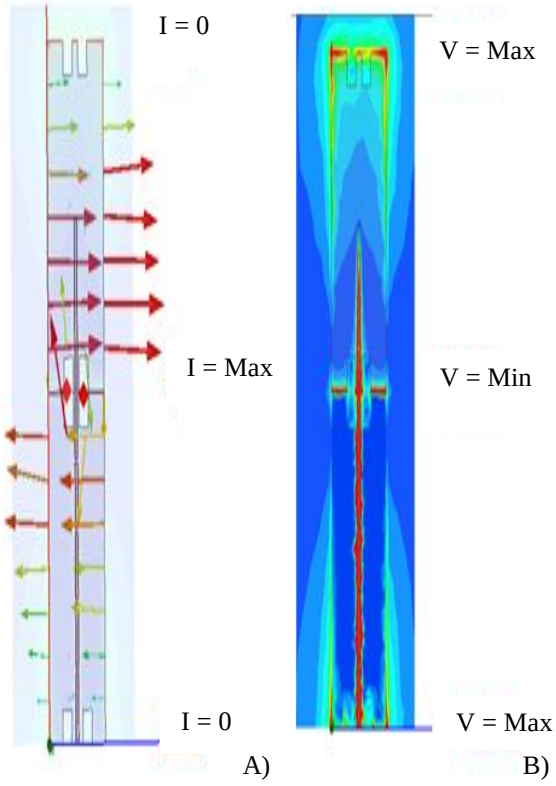

Fig. 7. HFSS simulation of the "dipole" mode of operation for: (A) current vectors at F_1 and (B) colored contour plot of electric field at F_1.

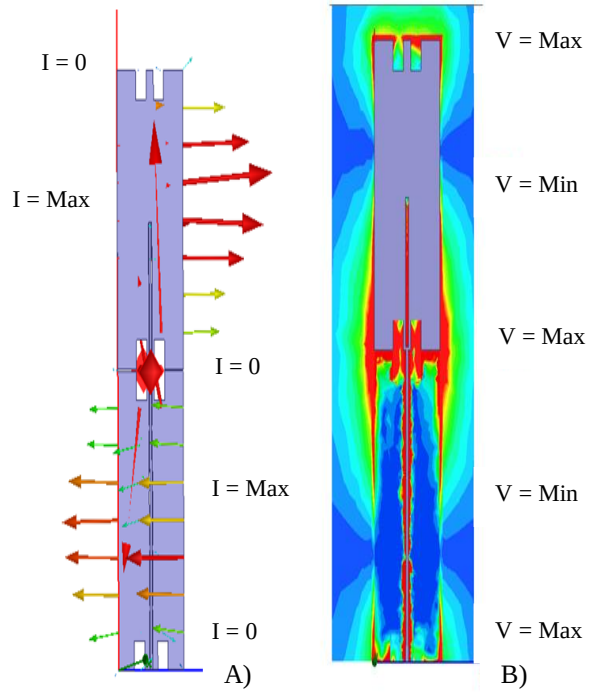

Fig. 8 HFSS simulation of the "CoCo" mode of operation for: (A) current vectors at $2*F_1$, and (B) colored contour plot of electric field between elements at $2*F_1$.

V. TRANSMISSION LINE ON A THIN SUBSTRATE

The transmission line width for a 50 ohm line on 6 mil polyimide is roughly 0.1 mm. This transmission line size is too thin and challenging to manufacture consistently. Also, due to the thin size of the transmission line there is concern from a manufacturing standpoint about the stability of the PCB when it is conformed to the inside of the radome. Thus, rectangular slots were cut in the ground plane, behind the transmission line to eliminate the overlap electric fields and leave only the fringe electric fields on the transmission line as seen in Fig. 9 [13]. The slots reduce the capacitance between the transmission line and the ground plane and allow flexibility to the designer in terms of the final width of the transmission line. That being said, the transmission line was designed to approximately 7 times its original width in order to allow for the board to be more consistently manufactured.

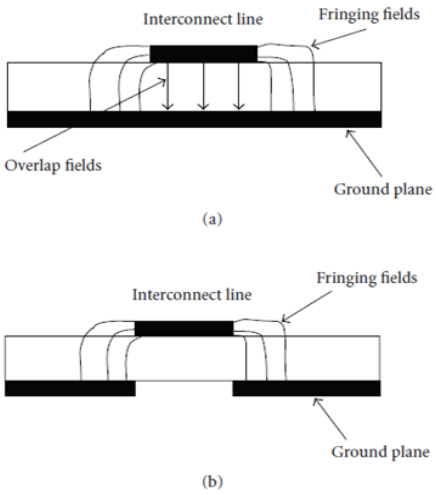

Fig. 9. Microstrip cross section for: (A) normal microstrip transmission line, and (B) slotted microstrip transmission line [13].

Shorting bars were also placed in the slot to connect both sides of the ground. The PCB image in Fig. 3 (B), rear view, shows the bottom element with this grid like setup of shorting bars. The bars were placed on the element to prevent voltage differential from giving rise to another mode forming on the antenna. The shorting bars were optimized in quantity, separation, location, and thickness. This was done with HFSS through parametric sweeps and genetic algorithms in order to arrive at their optimal performance.

VI. BENDING EFFECTS

In order to meet the required bandwidth, the PCB needed to be wider than the desired ¾ inch radome tube. In order to combat this problem the PCB was

designed on a flexible substrate to allow it to be curved and placed within the radome. Thus, the board was able to maintain the wider elements characteristics and still fit the mechanical envelope. The first step was designing the antenna on a flat PCB which drastically decreased the simulation time relative to a curved surface simulation. Thus, the runtime of optimizations and parametric sweeps was reduced and we were able to get the desired performance on a flat PCB much quicker.

The curved antenna can be simulated in HFSS with three approaches: use cylindrical geometry, use flat "sheet" geometry and wrap around a cylinder, then one can leave it as a sheet or "thicken" the sheet to better simulate the real world. Using cylindrical geometry, shapes can be cut out of a cylinder until the final antenna shape is realized. HFSS provides a simpler technique using "sheets", where one can create the geometry utilizing sheets [14]. Once the antenna geometry is created in two dimensions, it can be wrapped around a "non-model" cylinder. These "sheets" can be simulated by making the sheet a perfect E conductor with no thickness. This method will decrease run time at the cost of accuracy, but allows for many parametric runs to converge on the ideal solution. Once the design is optimized, one can "thicken" the "sheet" and assign it a metal material. The results shown are for a thickened sheet case.

It was noted that, as the PCB was transitioned from a flat to cylindrical shape inside a radome, that the impedance of the antenna took on more capacitance. The pattern at the horizon was also reduced slightly once the PCB was simulated in the cylindrical form. The maximum to minimum azmuthal pattern performance at $2*F_1$ was measured at approximately 4 dBi and increased as the frequency increased. Thus, the minimum specification for omnidirectionality was not met with its current dimensions.

It was found during simulations that the farther it wrapped around the radome, the worse the front-to-back ratio in the azmuthal pattern became. Thus, the element width needed to be decreased to a point that allowed for a good front to back ratio while maintaining the wide bandwidth and gain performance of the antenna. The antenna was then re-optimized with an element width that would provide good omnidirectional performance. The parameters that were re-optimized included the slots in terms of length, width, and separation, as well as the separation between the two elements. The antenna was thus successfully re-tuned to have good omnidirectional performance, within the radome, as seen in Fig. 10, while maintaining a good S(1,1) over the bandwidth.

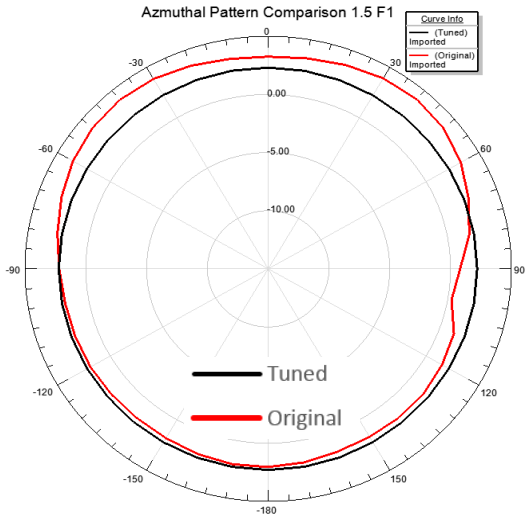

Fig. 10. Azmuthal pattern at $1.5*F_1$ of the antenna within the radome in its pre and post optimization form.

VII. DC BLOCK

The final antenna was then fabricated and placed within the radome. The antenna inside a clear radome is seen in Fig. 11, it shows the antenna does not conform to the inside of the radome. Rather, the rigidity of the PCB material keeps the board forming a slightly tighter C shape (view from top), than modeled. This discrepancy in bend radius of the board would explain difference in the model and proto-type performance.

The final designed antenna can be seen in Fig. 12. The board contains a break in the microstrip transmission line near the feed to incorporate a DC blocking capacitor. The capacitor was selected to be of a large enough value that it had absolutely no effect on the final antenna impedance. The location of the capacitor did however make a difference in the performance of the antenna. If placed too far up the transmission line the capacitor would shift the elevation of the pattern, reducing performance of the antenna at $\theta = 90°$ (horizon). Thus, on the first run of PCBS, a study was performed to determine the optimal location of the capacitor on the transmission line. This was done simply by removing the transmission line at various heights and soldering the capacitor in and comparing. It was found that the optimum location was as close as possible to the base of the board. However, the co-axial feeding forced the capacitor to be moved up slightly to allow for soldering of the co-axial line as well as some mechanical stability. A small, thin, flat portion of FR-4 was also added to the back of the board to provide mechanical stability to the capacitor as the PCB is bent and placed in the radome.

Fig. 11. Fabricated antenna board inside a clear tube.

Fig. 12. Image of both the front and back of the final fabricated PCB.

VIII. RESULTS

The S(1,1) of the antenna can be seen in Fig. 13. Overall the performance of the antenna matches closely with the simulation and the discrepancies can be chalked up to the antenna location in the radome and the excess bending the antenna is under. However, the -6 dB specification is met over the entire desired bandwidth. This specification is the maximum S(1,1) the radio can see before it is forced to cut-back power.

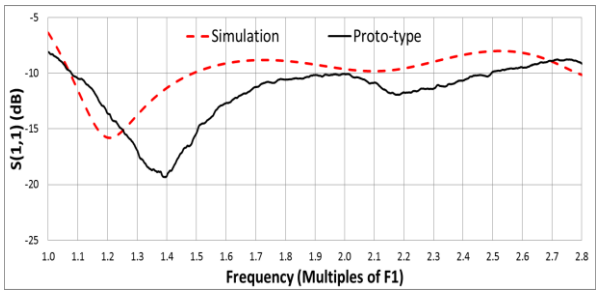

Fig. 13. S(1,1) in dB comparisons of the simulation and the fabricated antenna.

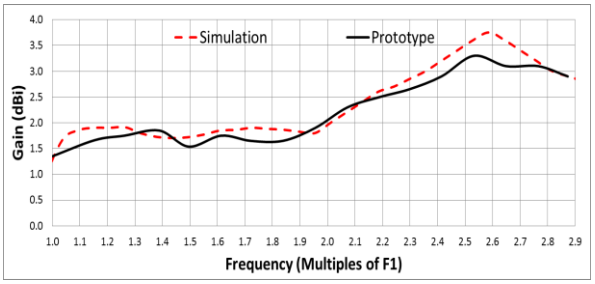

Fig. 14. Maximum gain comparisons at $\theta = 90$ of the simulation and the fabricated antenna.

The maximum gain of the antenna at $\theta = 90°$ is seen in Fig. 14. Overall, the two are very close in agreement. The elevation patterns of the antenna shown in Fig. 15 agree with the simulation and vary only slightly. It is seen that at F1 the pattern lobes down slightly while as we reach the end of the bandwidth of 2.8*F1 the pattern starts to lobe up slightly. However, despite the small discrepancies between the simulations and measurements, the patterns meet specification and show good performance at the horizon with no side lobes.

The antenna pattern was measured in the azimuthal plane at $\theta = 90°$ across the frequency band. This was done in order to verify the omnidirectional nature of the antenna. As seen in Fig. 16, the antenna ended up having a much higher maximum to minimum delta gain than the simulation. This was expected as the final shape of the antenna inside the radome varied slightly from the simulation. However, due to the nature of the original design, the fabricated antenna was still able to maintain a delta <3 dB over the frequency band.

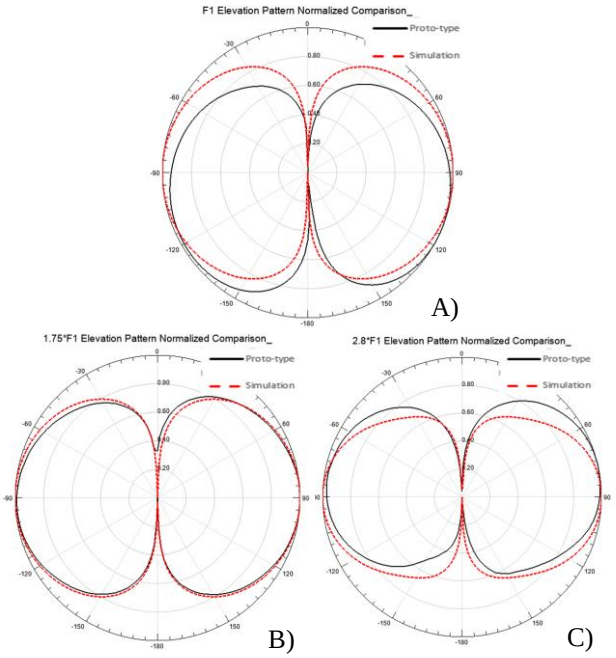

Fig. 15. Elevation pattern comparisons at: (A) F_1, (B) $1.75*F_1$, and (C) $2.8*F_1$.

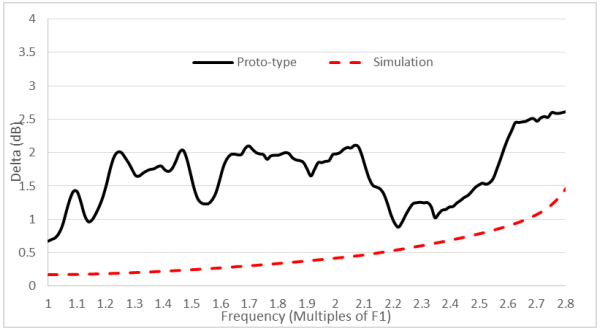

Fig. 16. Maximum to minimum delta gain comparison of azmuthal pattern at Θ=90.

IX. CONCLUSION

A very thin antenna was able to be designed and fabricated for performance over a very large bandwidth. Multiple modes of operation were required in order to meet the 1.5 octave bandwidth without a matching network. A slotting technique was able to be utilized to push the bandwidth limits of the "Co-Co" antenna further. A differing slotting technique was able to be utilized on a microstrip transmission line, on a thin dielectric, to increase the width of the transmission line of the antenna. This allowed for ease of manufacturing and for more consistency between antennas. The C-shape of the antenna produced undesirable capacitive loading as well as larger front-to-back ratios on the azmuthal patterns. The antenna needed to be re-optimized for its new shape. Overall, the measurements matched the simulations very well despite the differences between the simulation and the measurement configurations. All antenna specifications were able to be met over the 1.5 octave bandwidth.

It is also seen from the results that as the antenna is placed inside the radome the final shape will alter performance slightly. However, modeling these physical attributes of the system add to the simulation complexity and henceforth time. As computing and simulation tools become faster and more efficient these attributes of the system can also be simulated without adding cost to the design process. This will allow for the simulation and final product to be incredibly similar in their performance. Overall, despite these differences the antenna varied a small amount and still fell within the desired specifications.

ACKNOWLEDGEMENTS

The author would like to acknowledge Malcolm Packer of Harris Communications for his help in editing this paper and his constant guidance and support.

REFERENCES

[1] C. Sairam, et al., "Design and development of broadband blade monopole antenna," *2008 International Conference on Recent Advances in Microwave Theory and Applications*, 2008.

[2] Z. Zhang, et al., "Dual-band WLAN dipole antenna using an internal matching circuit," *IEEE Transactions on Antennas and Propagation*, vol. 53, no. 5, pp. 1813-1818, 2005.

[3] H. Wheeler, "A vertical antenna made of transposed sections of coaxial cable," *IRE International Convention Record*, vol. 4, pt. 1, pp. 160-164, 1956.

[4] T. J. Judasz and B. B. Balsley, "Improved theoretical and experimental models for the coaxial colinear antenna," *IEEE Transactions on Antennas and Propagation*, vol. 37, no. 3, pp. 289-296, 1989.

[5] L. Wang, et al., "A wideband omnidirectional planar microstrip antenna for WLAN applications," *2011 IEEE Electrical Design of Advanced Packaging and Systems Symposium (EDAPS)*, 2011.

[6] R. Bancroft and B. Bateman, "An omnidirectional planar microstrip antenna," *IEEE Transactions on Antennas and Propagation*, vol. 52, no. 11, pp. 3151-3153, 2004.

[7] Y. Zhou, et al., "A technique for improving bandwidth of COCO antenna array," *2008 4th International Conference on Wireless Communications, Networking and Mobile Computing*, 2008.

[8] R. Bancroft, *Microstrip and Printed Antenna Design*. 2nd ed, Raleigh, NC: SciTech, Print, 2009.

[9] K.-L. Wong, et al., "Omnidirectional planar dipole array antenna," *IEEE Transactions on Antennas and Propagation*, vol. 52, no. 2, pp. 624-628, 2004.

[10] Y. Yu, et al., "A wideband omnidirectional antenna array with low gain variation," *IEEE Antennas and Wireless Propagation Letters*, vol. 15, pp. 386-389, 2016.

[11] Y. Li, et al., "Design of penta-band omni-directional slot antenna with slender columnar structure," *IEEE Transactions on Antennas and Propagation*, vol. 62, no. 2, pp. 594-601, 2014.

[12] K. Wei, et al., "A triband shunt-fed omni-directional planar dipole array," *IEEE Antennas and Wireless Propagation Letters*, vol. 9, pp. 850-853, 2010.

[13] R. Sharma, et al., "Characteristic impedance of a microstrip-like interconnect line in presence of ground plane aperture," *International Journal of Microwave Science and Technology*, vol. 2007, ID 41951, 5 pages, 2007.

[14] ANSYS HFSS, 3D Full-wave Electromagnetic Field Simulation by Ansoft.

Joseph Daniel Majkowski received his B.S. and M.S. degrees in Electrical Engineering from the Rochester Institute of Technology in 2012.

He joined Harris Communications in 2012 where he began as a Systems Engineer. In 2013 he changed roles within the company to an RF and Antenna Design Engineer position.

Printed UWB Pacman-Shaped Antenna with Two Frequency Rejection Bands

Shaimaa' Naser and Nihad Dib

Department of Electrical Engineering
Jordan University of Science and Technology, P. O. Box 3030, Irbid 22110, Jordan
naser.shaimaa@yahoo.com, nihad@just.edu.jo

Abstract ─ In this paper, the design and analysis of microstrip-fed low-profile, compact ultra-wideband (UWB) monopole antenna with two band-notches characteristics is carried out. The antenna is mounted on a low-cost FR-4 substrate with dimensions of 25×38×1.6 mm^3, and relative permittivity of 4.4. The original shape of the patch is circular with radius of 11.5 mm, and then a sector is removed from the patch (making it a *Pacman*-shaped antenna) to improve the impedance bandwidth. The proposed antenna provides an impedance bandwidth between 2.9-15 GHz with better than 10 dB return loss and has nearly an omni-directional radiation pattern. Additionally, the antenna can reject the interference from WiMAX (3.5 GHz center frequency) and WLAN (5.5 GHz center frequency).

Index Terms ─ Monopole antennas, notch filters, ultra wideband antennas.

I. INTRODUCTION

Nowadays, Ultra-wideband (UWB) technology is widely used due to its capability of transmitting high data rates through the large bandwidth it utilizes. UWB technology is suited for systems that use short range communications and high data rates. Such systems include: radar applications, sensor data collection, precision locating, wireless sensor networks, ad-hoc networks and tracking applications. Federal communications commission (FCC) has adopted the band 3.1-10.6 GHz for the UWB signal and power spectral density emission limit for UWB transmitters of −41.3 dBm/MHz [1].

One of the most important parts of an UWB system is the antenna. The design of UWB antennas must ensure high radiation efficiency, low cost, and small size. There are many types of UWB antennas in the literature, but, recently, most researchers have been focusing on the design of printed monopole antennas since they have broad bandwidth, low cost, and low profile. Since the adoption of the FCC, many studies have been made on the design and performance of UWB antennas [2-8].

UWB signals can introduce interference with common wireless technologies such as WiMAX (3.5 GHz) and WLAN (5.5 GHz). So, another key design issue is to reject the interference from such technologies. Different methods have been used for designing the notch filters such as inserting slots either on the patch, the ground, or on the feeding line [9-17]. This method is very simple and does not add any overhead on the antenna structure but, using this method, it is difficult to achieve narrow band-stop region. Another method includes inserting parasitic elements that provide current flowing in opposite directions at the notch frequency [18]. Although this method increases the size of the antenna, it can achieve very narrow band stop regions.

The rest of the paper is organized as follows: Section II describes the design procedure of the proposed antenna and the optimum design parameters. Section III describes the antenna characteristics. Section IV presents a parametric study of several design parameters that affect the antenna performance. Finally, Section V concludes and summarizes the study.

II. ANTENNA DESIGN

Figure 1 illustrates the geometry of the proposed *Pacman*-shaped printed microstrip-fed UWB antenna. The antenna is mounted on a compact size FR-4 substrate of dimensions 25 mm× 38 mm, dielectric constant 4.4, loss tangent of 0.02, and thickness of 1.6 mm. The original patch has circular shape since it has the largest bandwidth among the other regular shapes and has good radiation characteristics [19]. The radius was approximated to be λ/4 at the lower frequency edge of the UWB range as follows [20]:

$$R = \frac{c}{4 f_l \sqrt{\varepsilon_r}}, \quad (1)$$

where R is the patch radius, f_l is the lower frequency edge (i.e., 3.1 GHz), c is the free-space speed of light, and ε_r is the substrate dielectric constant. The feeding line has a length of 12 mm and a width of 3 mm to achieve a characteristic impedance of 50 Ω. From simulation, it has been found that the distance p ($p = L_{feeding} - W_{gnd}$) between the feeding point and the ground plane has an effect on the performance of the antenna. Its value was chosen to be 0.2 mm. A partial ground plane is used with a notch cut near the feeding line to improve the impedance bandwidth. The notch

Submitted On: July 24, 2016
Accepted On: January 28, 2017

dimensions were varied to have good return loss; the optimum values chosen are W_1 = 0.8 mm and L_1 = 5 mm. Then, a sector was removed from the circular patch (making it a *Pacman*-shaped antenna) to improve the impedance bandwidth, and its angle was optimized to be 80° to have a good return loss and large bandwidth. Finally, a U-shaped slot and a straight slot were etched in the patch to reject the interference from WiMAX and WLAN, respectively. The total lengths of the slots were approximated to be λ/2 at the notched frequencies [12-14]:

$$L_{notch} = \frac{c}{2 f_{notch}\sqrt{\varepsilon_{eff}}}, \quad (2)$$

where f_{notch} is the center frequency of the notched band, and $\varepsilon_{eff} = \frac{\varepsilon_r+1}{2}$.

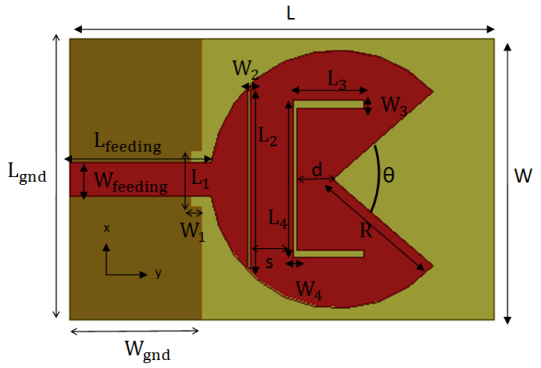

Fig. 1. The layout of the proposed *Pacman*-shaped antenna.

To model and optimize the proposed antenna, HFSS simulator was used. A radiation box placed at a distance of $\lambda/4$ from the substrate was used to measure the far field parameters. The solution frequency was set to 3.1 GHz which is the lowest frequency edge, with maximum delta S = 0.01 and number of passes of 12. After several simulations and performing a parametric study (described in Section IV), the optimum parameters of the proposed UWB antenna are chosen as follows:
L = 38 mm, W = L_{gnd} = 25 mm, $L_{feeding}$ = 12 mm, $W_{feeding}$ = 3 mm, W_{gnd} = 11.8 mm, R = 11.5 mm, W_1 = 0.8 mm, L_1 = 5 mm, W_2 = 0.2 mm, L_2 = 15.8 mm, W_3 = 0.7 mm, L_3 = 6mm, W_4 = 0.3 mm, L_4 = 14 mm, θ = 80°, S = 3.8 mm, and d = 3.1 mm.
The optimum design parameters were used to build a prototype of the proposed antenna which is shown in Fig. 2.

Measurements were performed in the laboratory environment using an Agilent Vector Network Analyzer (VNA). Figure 3 shows the simulated and measured voltage standing wave ratio (VSWR) of the proposed antenna. It can be observed that measurement agrees well with simulation except in the range 11-13 GHz which could be due to experimental tolerances, fabrication tolerances, and the effect of the connector. The antenna works in the UWB range with the VSWR being less than 2 in the frequency band 2.9-15 GHz except around the notched frequencies. As desired, the antenna has filter characteristics around 3.5 GHz (the center frequency of WiMAX) and 5.5 GHz (the center frequency of WLAN). A small shift in the measured notched frequencies can be noticed because the simulation environment is different from the real environment, and the fact that the substrate relative permittivity decreases as the frequency increases [21]. Similar shifts in the notched frequencies were seen in other papers for the same causes [10], [11], [16].

Fig. 2. Picture of the fabricated *Pacman*-shaped UWB antenna.

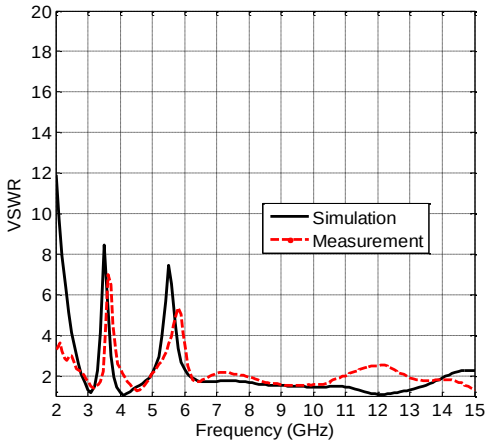

Fig. 3. The simulated and measured VSWR of the antenna.

III. ANTENNA PARAMETERS

This section elaborates more on the proposed antenna parameters. Since UWB antennas involve transmission of large bandwidths, time domain parameters are as important as the frequency domain parameters because they determine how much the antenna disperses the received signal. Different frequency domain parameters and the group delay for the proposed antenna will be discussed in this section.

A. Antenna gain

Usually, when one talks about the antenna gain, he/she refers to the realized peak gain which takes into account the mismatch losses. The simulated gain of the

antenna is illustrated in Fig. 4. The gain increases in the whole antenna bandwidth from 2 dB to nearly 8 dB, while it drops to -5.4 dB at 3.5 GHz (the center frequency of WiMAX) and to -2.9 dB at 5.5 GHz (the center frequency of WLAN).

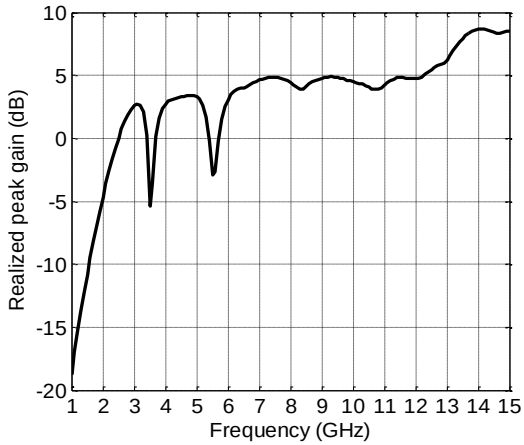

Fig. 4. The realized peak gain of the antenna

B. Radiation pattern

UWB printed monopole antennas are known to have omni-directional pattern similar to the linear monopole antenna in which the E-plane has the figure-8 shaped pattern, and the H-plane is non-directional. Moreover, an antenna can have two polarizations, one is in the intended direction (co-polarization), and the other is orthogonal on it (cross-polarization) [22]. One should try to minimize the cross-polarization to reduce polarization mismatch. Figure 5 illustrates the E-plane (yz-plane) and H-plane (xz-plane) co-polarization and cross-polarization patterns of the antenna at 4, 6, and 9 GHz.

It is clear that the antenna has the figure-8 shape in the E-plane with very small cross-polarization component, but as the frequency increases, the radiation pattern becomes distorted and the cross-polarization component increases. On the other hand, the antenna is non-directional (having an O-shaped pattern) in the H-plane with cross-polarization component lower than the co-polarization one.

C. Current distribution

The last frequency domain parameter to consider is the current distribution. Figure 6 illustrates the current distribution at 3.5, 5.5, 9, and 12 GHz. It can be observed that the current is mainly concentrated at the edges of the circular patch and the feeding line, but, this does not happen at 3.5 GHz where the current is mainly concentrated at the U-shaped slot (WiMAX slot) and 5.5 GHz where the current is mainly concentrated at the WLAN straight slot. This indicates that the notches have a short circuit effect to prevent interference from WLAN and WiMAX.

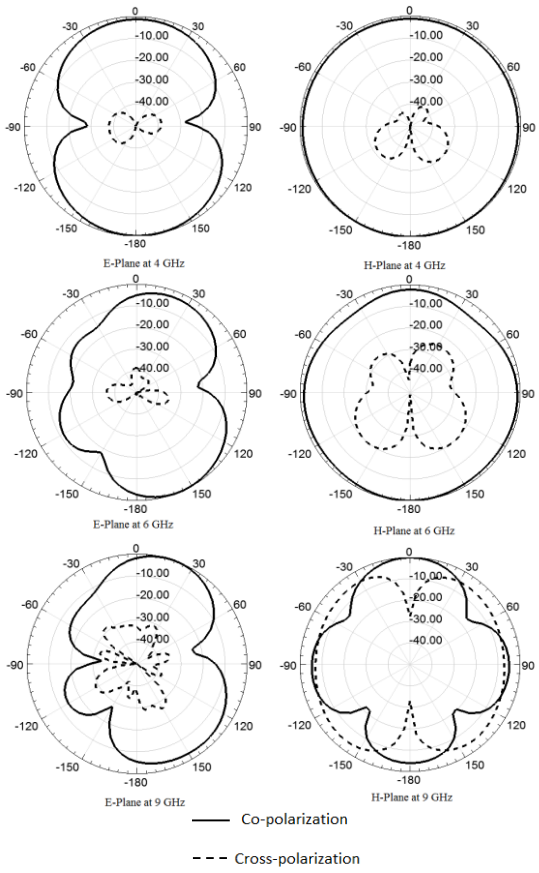

Fig. 5. The normalized E-plane and H-plane co-polarization and cross-polarization patterns (in dB) at 4, 6, and 9 GHz.

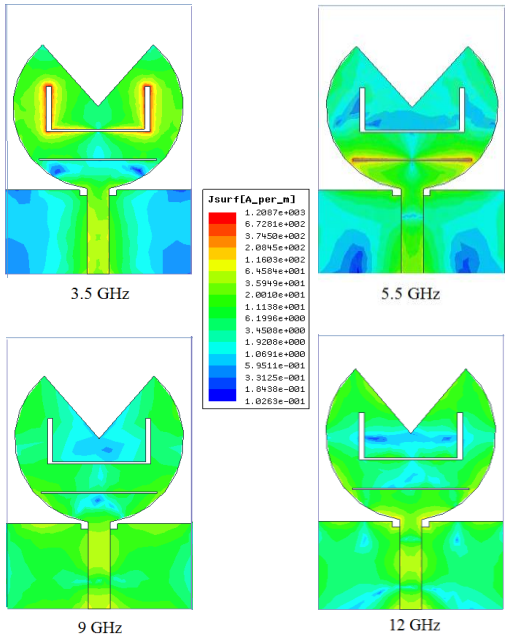

Fig. 6. The current distrbution at 3.5, 5.5, 9, and 12 GHz.

D. Group delay

Group delay has an important role in the dispersion characteristics of the antenna. A comparison between the simulated group delay (using S_{11} and S_{21}) and the measured one (computed using the measured S_{11}) is illustrated in Fig. 7. To compute the group delay from the phase of S_{21}, two similar proposed antennas were placed face-to-face a distance of 30 cm. The group delay is almost constant over the whole band except at the notched frequencies. In fact, using S_{21} to compute the group delay gives more realistic results. Since the measured group delay is almost constant, little distortion is introduced by the antenna.

Table 1 lists a comparison between the proposed antenna and six other ones that have recently appeared in literature. It can be seen that the proposed design has a comparable size compared to others, with a larger peak gain. Moreover, the low and high frequency edges compete with the ones cited in the table.

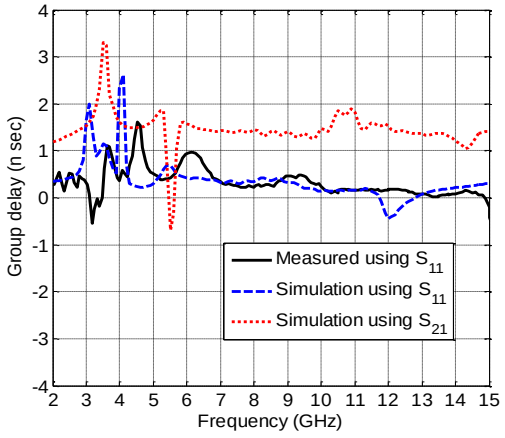

Fig. 7. The simulated and measured group delay of the proposed antenna.

Table 1: Comparison between the proposed design and previous designs

Ref.	Dimension	Peak Gain (dB)	f_l (GHz)	f_H (GHz)
[8]	12 mm × 18 mm	6	2.8	11.6
[17]	42 mm × 40 mm	4.4	2.44	11.9
[9]	25 mm × 20 mm	3	2.63	13.02
[2]	29 mm × 20.5 mm	6	3	10.72
[23]	41 mm × 34 mm	4.85	3.26	19.1
[24]	63.25 mm × 51 mm	-	3.1	15
Proposed	38 mm × 25 mm	8	2.9	15

IV. PARAMETRIC STUDY

A parametric study of the proposed antenna was performed to control the antenna and the notch filters operations. The first parameter to consider is the effect of the angle of the sector on the antenna return loss (without the existence of the filtering slots) which is illustrated in Fig. 8. It is clear that the angle of the sector highly affects the return loss. As the angle is varied, the return loss and the input impedance change. So, a value that achieves a good return loss, good input impedance, and wide bandwidth was chosen to be 80°.

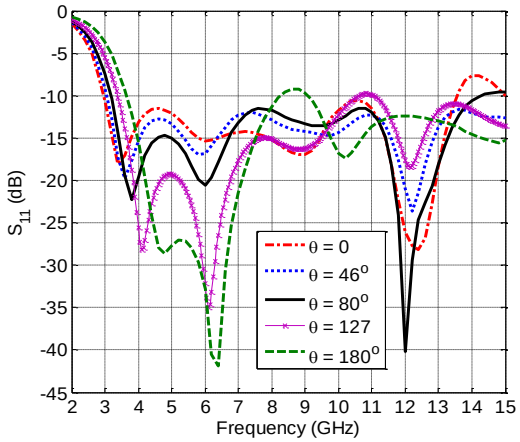

Fig. 8. The effect of varying the angle of the sector with R = 11.5 mm, p = 0.2 mm, and W_1 = 0.8 mm.

Then, the effect of the slots dimensions on the notched frequencies is studied. The notches lengths were initially computed to be λ/2 at the notch frequencies, and then their widths, lengths, and positions (S and d) were optimized. Figures 9, 10, and 11 show the effect of varying the widths of the notches W_2, W_3, and W_4, respectively, while keeping the radius, the gap *p*, the ground plane notch dimensions, and the sector angle fixed to the optimum values. From Fig. 9, it can be seen that changing W_2 has no effect on the center frequency of the WiMAX, while it changes the center frequency of the WLAN. Its value was set to 0.2 mm to have the center frequency at 5.5 GHz and notch characteristic from 5 to 6 GHz. In Figs. 10 and 11, the WLAN center frequency somewhat varies with W_3 and W_4, but the major variation is in the WiMAX center frequency. Their values were chosen as 0.7 mm and 0.3 mm, respectively, to have the center frequency at 3.5 GHz.

The notches lengths also have effects on the notches operation. In Fig. 12, the effect of varying the length of the WLAN notch filter is illustrated. As expected, as the length changes, the center frequency of the WLAN changes too, while the center frequency of WiMAX is fixed. The value was chosen to be 15.8 mm. Figures 13 and 14 illustrate the effect of varying the lengths L_3 and L_4 (the total length of the WiMAX notch). The values of L_3 and L_4 mainly affect the center frequency of the WiMAX, while the center frequency of the WLAN is slightly affected. The optimum values were chosen 6 mm and 14 mm, respectively, where the sum of L_3 and L_4 is the same as the total length of the WiMAX notch computed using Equation (2).

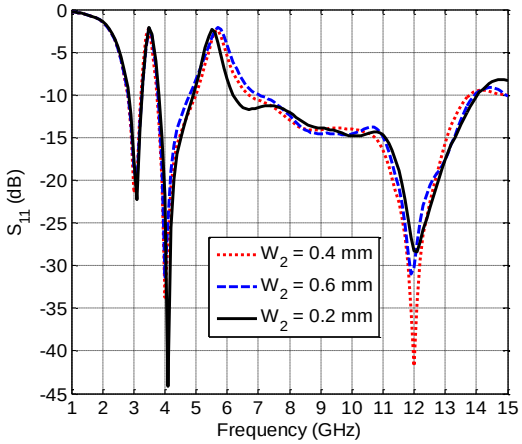

Fig. 9. The effect of varying the value of W_2 with W_3 = 0.7 mm, W_4 = 0.3 mm, and optimum notches lengths.

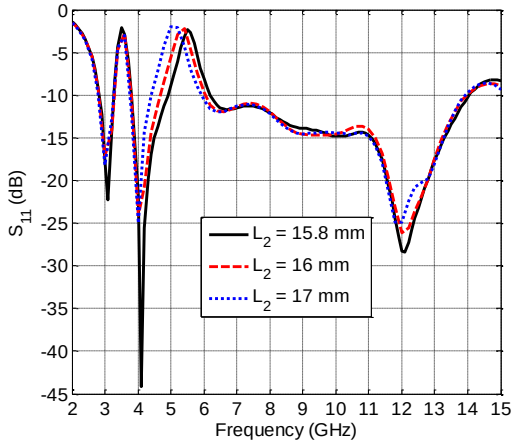

Fig. 12. The effect of varying the value of L_2 with L_3 = 6 mm, L_4 = 14 mm and optimum notches widths.

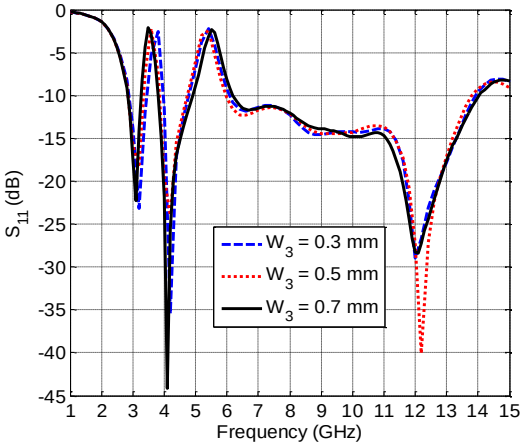

Fig. 10. The effect of varying the value of W_3 with W_2 = 0.2 mm, W_4 = 0.3 mm and optimum notches lengths.

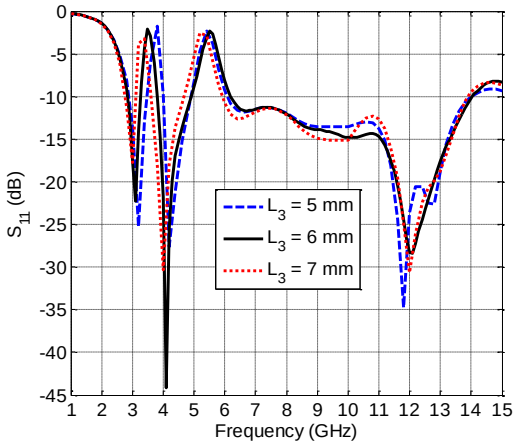

Fig. 13. The effect of varying the value of L_3 with L_2 = 15.8 mm, L_4 = 14 mm and optimum notches widths.

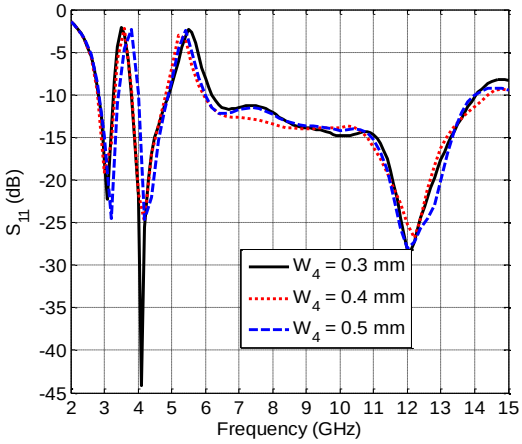

Fig. 11. The effect of varying the value of W_4 with W_2 = 0.2 mm, W_3 = 0.7 mm and optimum notches lengths.

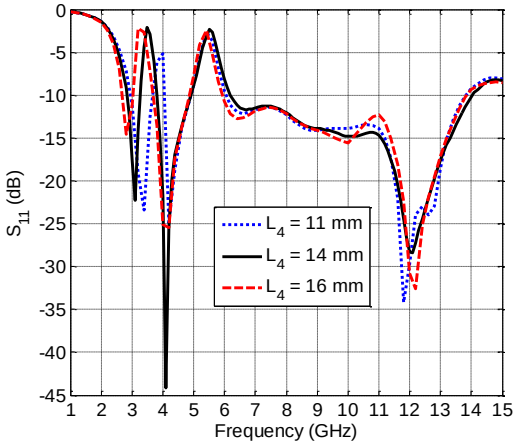

Fig. 14. The effect of varying the value of L_4 with L_2 = 15.8 mm, L_3 = 6 mm and optimum notches widths.

V. CONCLUSIONS

In this paper, a simple printed monopole UWB antenna with two band-notched frequencies was designed and analyzed. Simulations showed that the antenna works well in the UWB range with better than 10 dB return loss. Experimental results were very close to the simulation ones. Frequency domain and time domain characteristics were investigated. The antenna exhibits an omni-directional radiation pattern with high peak gain except at the notched frequencies. Also, the group delay of the antenna was almost constant such that the distortion caused by the antenna is very small except at the notched frequencies. The advantages of the proposed antenna are: cheap, simple and compact for small portable devices. Additionally, the proposed antenna has stable radiation characteristics and can reject interference from existing wireless systems working in the same band of frequencies.

REFERENCES

[1] Federal Communications Commission, First Report and Order, Revision of Part 15 of Commission's Rule Regarding UWB Transmission System FCC 02-48, Washington, DC, USA, 2002.

[2] R. Azim and M. T. Islam, "Ultra-wideband planar antenna with notched bands at 3.5/5.5 GHz," *ACES Journal*, vol. 31, no. 4, pp. 388-395, April 2016.

[3] S. Ojaroudi, Y. Ojaroudi, N. Ghadimi, and N. Ojaroudi, "UWB monopole antenna with dual band-stop performance using G-shaped SRR and SIR structures at feed line," *ACES Journal*, vol. 29, no. 10, pp. 807-812, October 2014.

[4] R. V. R. Krishna, R. Kumar, and N. Kushwaha, "An UWB dual polarized microstrip fed L-shape slot antenna," *International Journal of Microwave and Wireless Technologies*. Available on: CJO2015. doi:10.1017/S1759078715000124

[5] J. Zolghadr, Y. Cai, and N. Ojaroudi, "UWB slot antenna with band-notched property with time domain modeling based on genetic algorithm optimization," *ACES Journal*, vol. 31, no.8, pp. 926-932, August 2016.

[6] A. A. Omar, "Design of ultra-wideband coplanar waveguide-fed Koch-fractal triangular antenna," *International Journal of RF and Microwave Computer-Aided Engineering*, vol. 23, pp. 200-207, 2013.

[7] A. Nemati and B. A. Ganji, "UWB monopole antenna with switchable band-notch characteristic using a novel MEMS afloat," *ACES Journal*, vol. 30, no. 12, pp. 1306-1312, December 2015.

[8] J. Mazloum and N. Ojaroudi, "Utilization of protruded strip resonators to design a compact UWB antenna with WiMAX and WLAN notch bands," *ACES Journal*, vol. 31, no. 2, pp. 204-209, February 2016.

[9] M. Devi, A. K. Gautam, and B. K. Kanaujia, "A compact ultra wideband antenna with triple band-notch characteristics," *International Journal of Microwave and Wireless Technologies*. Available on: CJO2015.doi: 10.1017/S1759078715000409

[10] S. Trinh-Van and Ch. Dao-Ngoc, "Dual band-notched UWB antenna based on electromagnetic band gap structures," *REV Journal on Electronics and Communications*, vol. 1, no. 2, pp. 130-136, April-June 2011.

[11] H. J. Lak, C. Ghobadi, and J. Nourinia, "A novel ultra-wideband monopole antenna with band-stop characteristic," *Wireless Engineering and Technology*, vol. 2, pp. 235-239, 2011.

[12] Y.-S. Li, X.-D. Yang, Q. Yang, and C.-Y. Liu, "Compact coplanar waveguide fed ultra wideband antenna with a notch band characteristic," *International Journal of Electronics and Communications*, vol. 65, no. 11, pp. 961-966, 2011.

[13] J. Zang and X. Wang, "A compact C-shaped printed UWB antenna with band-notched characteristic," *Progress In Electromagnetics Research Letters*, vol. 43, pp. 15-23, 2013.

[14] M. Ojaroudi, G. Ghanbari, N. Ojaroudi, and C. Ghobadi, "Small square monopole antenna for UWB applications with variable frequency band-notch function," *IEEE Antennas and Wireless Propagation Letters*, vol. 8, pp. 1061-1064, 2009.

[15] P. Lotfi, S. Soltani, and M. Azarmanesh, "Triple band-notched UWB CPW and microstrip line fed monopole antenna using broken ∩-shaped slot," *International Journal of Electronics and Communications*, vol. 67, pp. 734-741, 2013.

[16] Z. Yu, G. Wang, J. Liang, and X. Gao, "A semicircular band-notch ultra wideband printed antenna based on CSRR," *Microwave and Optical Technology Letters*, vol. 52, no. 10, pp. 2387-2390, October 2010.

[17] I. Messaoudene, T. A. Denidni, and A. Benghalia, "A hybrid integrated ultra-wideband/dual-band antenna with high isolation," *International Journal of Microwave and Wireless Technologies.* Available on: CJO2015.doi:10.1017/S1759078715000033

[18] M. Yazdi and N. Komjani, "A compact band-notched UWB planar monopole antenna with parasitic elements," *Progress In Electromagnetics Research Letters*, vol. 24, pp. 129-138, 2011.

[19] J. Liang, Ch. Chiau, X. Chen, and C.-G. Parini, "Study of a printed circular disc monopole antenna for UWB systems," *IEEE Transactions on Antennas and Propagations*, vol. 53, no. 11, pp. 3500-3504, November 2005.

[20] T. Wu, H. Bai, P. Li, and X. Shi, "A simple planar monopole UWB slot antenna with dual independently and reconfigurable band-notched characteristics," *International Journal of RF and Microwave Computer-Aided Engineering*, vol. 24, pp. 706-

712, November 2014.
[21] S. Mumby and J. Yuan, "Dielectric properties of FR-4 laminates as a function of thickness and the electrical frequency of the measurement," *Journal of Electronic Materials*, vol. 18, iss. 2, pp. 287-292, March 1989.
[22] C. Balanis, *Antenna Theory: Analysis and Design*, 3rd edition, Wiley Interscience, 2005.
[23] S. Singhal and A. Singh, "Crescent-shaped dipole antenna for ultra-wideband applications," *Microwave and Optical Technology Letters*, vol. 57, iss. 8, pp. 1773-1782, August 2015.
[24] K. Sawant and C. R. Kumar, "CPW fed hexagonal microstrip fractal antenna for UWB wireless communications," *International Journal of Electronics and Communications*, vol. 69, pp. 31-38, 2015.

Shaimaa' A. Naser obtained her B.Sc. in Communications and Electronics Engineering from Jordan University of Science and Technology (JUST), Jordan in 2013. In the same year, she joined the Master program in the Electrical Engineering Department at JUST majoring in Wireless Communications. She obtained her M.Sc. degree in 2015. Her main research interests are in the analysis and design of antennas.

Nihad I. Dib obtained his B.Sc. and M.Sc. in Electrical Engineering from Kuwait University in 1985 and 1987, respectively. He obtained his Ph.D. in EE (major in Electromagnetics) in 1992 from University of Michigan, Ann Arbor. Then, he worked as an Assistant Research Scientist in the Radiation Laboratory at the same school. In Sep. 1995, he joined the EE Department at Jordan University of Science and Technology (JUST) as an Assistant Professor and became a Full Professor in Aug. 2006. His research interests are in computational electromagnetics, antennas and modeling of planar microwave circuits.

Small-Size Tapered Slot Antenna (TSA) Design for use in 5G Phased Array Applications

Naser Ojaroudi Parchin, Ming Shen, and Gert Frølund Pedersen

Antennas, Propagation, and Radio Networking (APNet) Section
Department of Electronic Systems, Faculty of Engineering and Science
Aalborg University, DK-9220, Aalborg, Denmark
naser@es.aau.dk, mish@es.aau.dk, gfp@es.aau.dk

Abstract ─ The design and development of a compact tapered slot antenna (TSA) for the fifth generation (5G) phased array communications is described in this manuscript. The proposed low-profile TSA element is designed on a *Rogers RT 5880* (ε=2.2 and δ=0.0009) dielectric to work in the frequency range from 21 to 23 GHz. The configuration of the employed TSA antenna elements is composed of a slot-line flare from a small gap to a large opening, matching to free space's wave impedance. Eight TSA elements with well-defined end-fire radiation patterns have been used on the top portion of a mobile-phone PCB to form a 1×8 linear phased array. The TSA elements are fed by hockey-stick baluns. In addition, the radiation performance and SAR characteristics of the phased array 5G antenna in the vicinity of user's hand & head have been investigated in this study. The results show that the proposed design provides good characteristics in terms of S-parameters, antenna gain, efficiency, SAR, and beam steering, which fit the need of 5G cellular communications.

Index Terms ─ 5G wireless networks, cellular communications, planar phased array, TSA.

I. INTRODUCTION

The fifth generation (5G) networks are expected to use the higher frequency bandwidths due to the growing need for wider bandwidths and higher data rates [1-2]. Compared with the cellular networks used today (operating at the frequencies less than 4 GHz), 5G mobile networks will use broader mm-Wave frequency bandwidths [3]. 22 GHz, 28 GHz, and 38 GHz are some of the candidate bands for 5G wireless communications [4-5]. Different from the conventional antennas (patch and slot antennas) in order to cover the required coverage-space of 5G communications, the end-fire antennas, such as horn waveguide antenna, Yagi antenna and linear tapered slot antenna (LTSA) are more suitable. Among them, the TSA is a promising candidate for reasons such as easy fabrication and easy integration [6-7]. Our work presents the study on the design of a 22 GHz phased array tapered slot antenna for the future 5G cellular communication applications.

Tapered slot antenna (TSA) has received considerable amount of research effort owing to their attractive futures such as high gain and relatively wide bandwidth compared with other designs such as typical patch antennas. They can provide excellent directional propagation at the higher frequencies and could be used for radar, detecting and phased array applications [8-9]. The TSA array with compact size and high-gain characteristics is also among one of the most promising candidates meeting the requirements of 5G systems, and hence, could be used to form multiple antenna systems for 5G systems [10].

The designed TSA element is operating from 21 to 23 GHz and has compact-size, sufficient-gain, high-efficiency, high-fidelity, and good end-fire radiation pattern. The designed antenna element has a good potential to be used in linear and planar phased array applications. Eight elements of the TSAs have been used to form a linear phased array in the edge region (top-side) of a 5G mobile phone PCB. Another set of the linear phased array could be used on the bottom portion of the PCB. The designed 5G phased array mobile-phone antenna provides good features in terms of fundamental radiation properties. Furthermore, 64-elements of the antennas are employed to form a planar phased array with high-gain property. More than 20 dB gain, and -0.5 dB (90%) total efficiency have been obtained when its beam is tilted to 0^o elevation. The results show that the designed TSA arrays (linear & planar) satisfy general requirements for use in 5G platforms.

II. SINGLE ELEMENT TSA

The configuration of the single element TSA is shown in Fig. 1. As illustrated, it contains a slot-line flare from a small gap to a large opening, matching to free space's wave with hockey-stick balun feed technique. The strip-line/slot-line transition is specified by W_f (strip-line width) and W_2 (slot-line width). The

Submitted On: July 6, 2016
Accepted On: September 25, 2016

exponential taper profile is defined by the opening rate and two points P_1 (z_1, y_1) and P_2 (z_2, y_2):

$$y = c_1 e^{Rz} + c_2, \quad (1)$$

where $c_1 = \frac{y_2 - y_1}{e^{Rz_2} - e^{Rz_1}}$ and $c_2 = \frac{y_1 e^{Rz_2} - y_2 e^{Rz_1}}{e^{Rz_2} - e^{Rz_1}}$.

The taper length L is z_2-z_1 and the aperture height H is $2(y_2$-$y_1)+W_f$. In the case where x approaches zero, the exponential taper results in a so-called linearly tapered slot antenna (LTSA) for which the taper slope is constant and given by $s_0 = (y_2$-$y_1)/(z_2$-$z_1)$. For the exponential taper defined by (1), the taper slope changes continuously from s_1 to s_2, where s_1 and s_2 are the taper slope at $z=z_1$ and at $z=z_2$, respectively, and $s_1 < s < s_2$ for $x>0$. The taper flare angle has been defined by $\alpha = tan^{-1}s$. In theory, the maximum opening width [11] is:

$$\lambda_g = \frac{c}{f_{\min}\sqrt{\varepsilon_r}}, \quad (2)$$

where C is speed of light, f_{min} is frequency minimum, and ε_r is dielectric constant of the substrate.

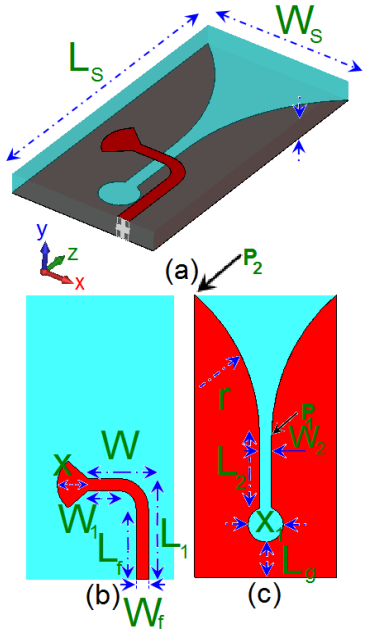

Fig. 1. Proposed TSA configuration: (a) side view, (b) top layer, and (c) bottom layer.

The equivalent circuit for the TSA is shown in Fig. 2. The total impedance Z_{RP} at the reference plane T on the strip-line can be expressed as a series connection of the strip-line stub reactance JX_{STB} and the antenna impedance Z_A [12]. Based on Fig. 2, $Z_{input}(s)$ and $\Gamma_z(s)$ of the TSA can be calculated as:

$$Z_{input}(s) = L_1 S + R \| L_2 \| \frac{1}{C_1 S},$$

which is equal to:

$$Z_{input}(s) = S\left\{\frac{(R_1 L_2 + R_1 L_1) + L_1 L_2 S + R_1 L_1 L_2 C S^2}{R_1 + L_2 S + R_1 L_2 C S_2}\right\}, \quad (3)$$

$$\Gamma_z(s) = \frac{Z_{input}(s)}{Z_{input}(s) + 2Z_0}. \quad (4)$$

The antenna has a compact size of $W_S \times L_S$. The design parameters of the antenna and the proposed array are specified in Table 1. The simulated S_{11} characteristic of the designed TSA is illustrated in Fig. 3. It can be seen that the proposed TSA antenna covers the frequency band from 21 to 23 GHz (2 GHz bandwidth for S_{11} less than -10) and has a reflection coefficient of -30 dB at the resonance frequency (22 GHz).

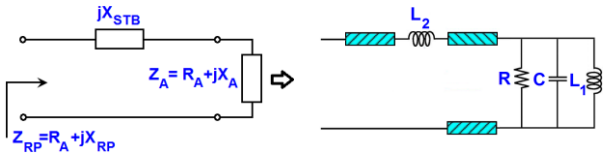

Fig. 2. Equivalent circuit for the TSA.

Table 1: Dimension of the antenna parameters

Parameter	W_X	L_X	W_S	L_S=L_a	W_a	h
Value (mm)	48	42.8	6	12	48	0.8
Parameter	L_g	W	L	W_1	L_1	r
Value (mm)	1.5	2.25	4	1.1	4.25	8
Parameter	W_2	L_2	W_f	L_f	X	X_1
Value (mm)	0.5	3	0.5	3	1.25	1.5

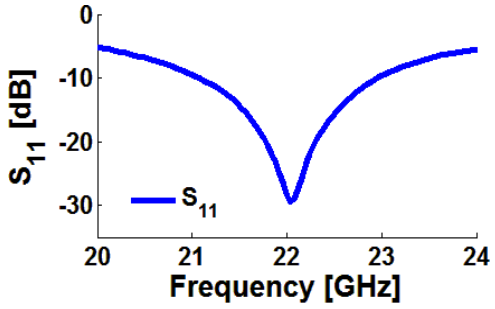

Fig. 3. S_{11} characteristic of the LTSA.

The frequency response (S_{11}) of the designed TSA can be controlled by changing the values of critical parameters such as the width of the hockey-stick balun. Figure 4 depicts the S_{11} characteristics of the antenna for different values of W_1. As illustrated, when the value of W_1 increases from 2.05 to 2.45 mm, the resonance of the antenna response increases from 22.05 to 22.6 GHz. The efficiency characteristics of the antenna over the operation band is described in Fig. 5 (a). In theory, the radiation and total efficienies are related according as:

$$e_0 = e_r e_{cd}. \quad (5)$$

In addition, the 3D radiation pattern of the antenna at 22 GHz is illustrated in Fig. 5 (b). The antenna gain can be calculated using the total efficiency and the directivity as follows:

$$G_0\,(dB) = 10\log(e_0 D_0), \tag{6}$$

where e_0 is the total antenna efficiency, er is reflection (mismatch) efficiency=(1-|Γ|2), e_{cd} is antenna radiation efficiency and D_0 is the antenna directivity [13]. As can be seen, the antenna has a desirable end-fire radiation property with 4.45 dB gain (IEEE gain×missmatch). Based on the obtained results, the antenna has high efficiency function at the different frequency of the operation band (especially at the resonance frequency= 22 GHz).

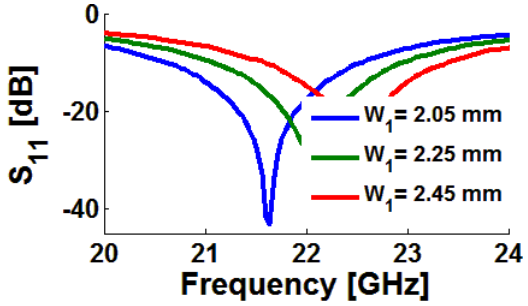

Fig. 4. S_{11} curves for different values of W_1.

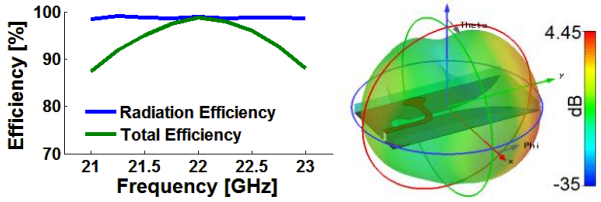

(a) (b)

Fig. 5. Simulated (a) efficiencies and (b) radiation pattern of the designed TSA.

In the analysis on the microstrip antennas, the transfer function is transformed to time domain by performing the inverse Fourier transform. The fourth derivative of a Gaussian function is selected as the transmitted pulse. Therefore the output waveform at the receiving antenna terminal can be expressed by convoluting the input signal and the transfer function. The shape of the transmitted signal in free space is shown in Fig. 6.

The input and received waveforms for the face-to-face and side-by-side orientations of the antenna are shown in Fig. 7. It can be seen that the shape of the pulse is preserved in all the cases. There is slight distortion on received pulses but it was expected. Using the reference and received signals, it becomes possible to quantify the level of similarity between signals.

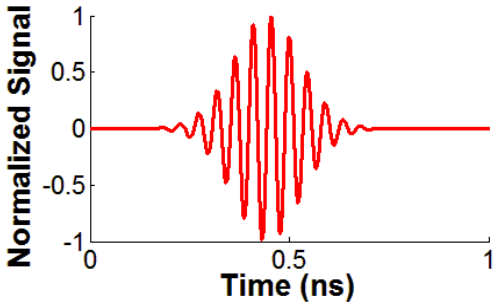

Fig. 6. Transmitted signal in free space.

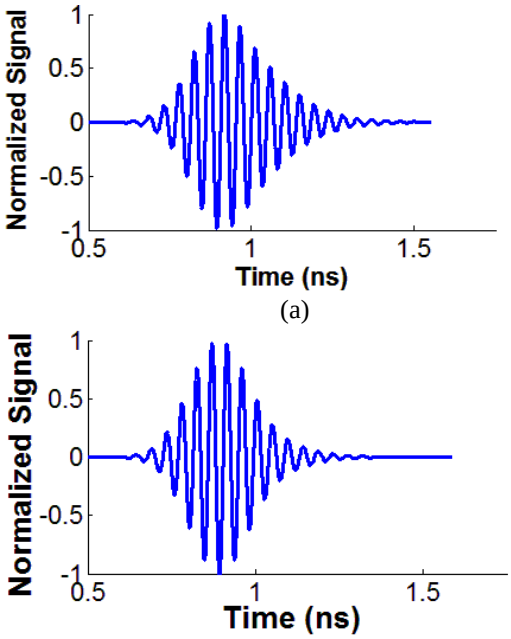

Fig. 7. Received pulses (a) side by side and (b) face to face.

In telecommunication systems, the correlation between the transmitted (T_X) and received (R_X) signals is evaluated using the fidelity factor (7):

$$F = Max_{\tau}\left|\frac{\int_{-\infty}^{+\infty} s(t)r(t-\tau)}{\sqrt{\int_{-\infty}^{+\infty} s(t)^2\,dt.\int_{-\infty}^{+\infty} r(t)^2\,dt}}\right|, \tag{7}$$

where $s(t)$ and $r(t)$ are the T_X and R_X signals, respectively. For impulse radio in UWB communications, it is necessary to have a high degree of correlation between the TX and RX signals to avoid losing the modulated information. However for most of other telecommunication systems, the fidelity parameter is not that relevant. In order to evaluate the pulse transmission characteristics of the proposed antenna, two configurations (side-by-side and face-to-face

orientations) were chosen. The transmitting and receiving antennas were placed in a distance of d=100 mm. As shown in Fig. 7, although the received pulses in each of two orientations are broadened, a relatively good similarity exists between the R_X and T_X pulses. Using (7), the fidelity factor for the face-to-face and side-by-side configurations were obtained equal to 0.93 and 0.97, respectively. The obtained values of the fidelity factor show that the antenna imposes negligible effects on the transmitted pulses. The pulse transmission results are obtained using CST [14].

III. THE TSA LINEAR PHASED ARRAY

The proposed phased array antenna is designed using eight elements of TSAs. Figure 8 illustrates the configuration of the linear phased array. The array has a compact size of $W_a \times L_a$=48×12 mm^2. The antenna element are arranged with a distance of $d=W_S$.

Figure 9 shows the S parameters (S_{21} to S_{81}) of the array. As shown, the array has a good performance in the frequency range of 21 to 23 GHz. The highest mutual-coupling characteristic (S_{21}) between the TSA elements is less than -12 dB at the center frequency of the operation band (22 GHz).

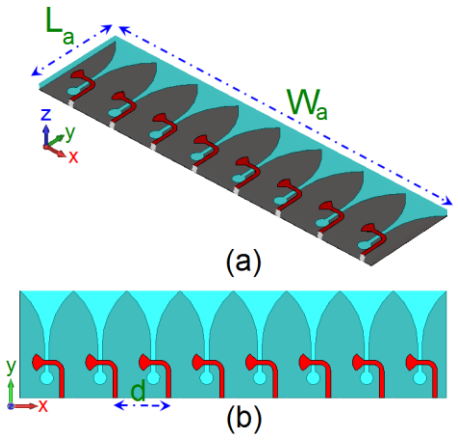

Fig. 8. Geometry of the linear array: (a) side view and (b) top view.

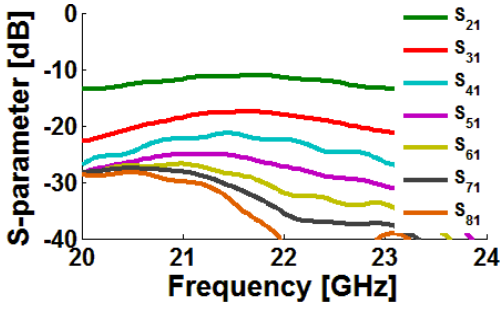

Fig. 9. S parameters of the array shown in Fig. 8.

In array designing, the adjacent element spacing must be chosen carefully due to its effect on the radiation performance of the array [15-16]. Figure 10 shows the configurations of the proposed array with different distance (d) between the elements. Simulated mutual coupling characteristics of the middle elements of the array for different values of d are illustrated in Fig. 11. As seen, in order to obtain a low mutual coupling characteristic for the antenna array, the distance between antenna elements must be near λ/2. When the distance between antenna elements increases from 7 to 5 mm, the mutual coupling characteristic of the array decreases from -9 to -16 dB. In addition, the radiation performance of the array for different values of d has been investigated.

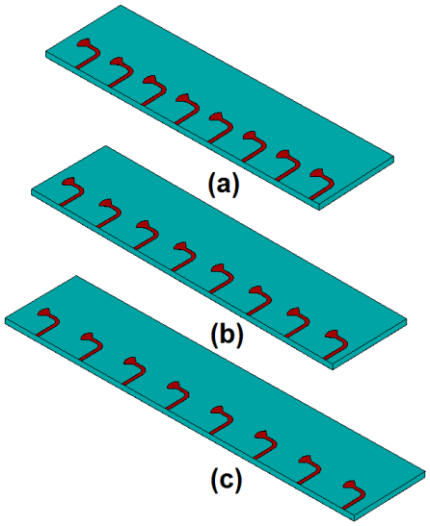

Fig. 10. Side views of the array for: (a) d=5 mm, (b) d=6 mm, and (c) d=7 mm.

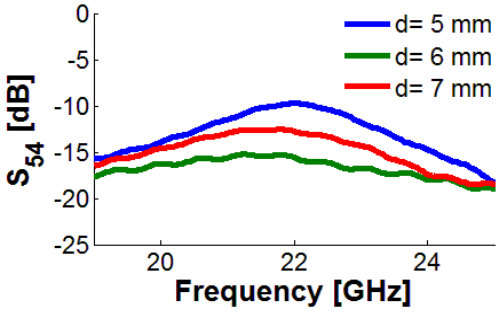

Fig. 11. Simulated S_{21} characteristics of the antenna for different values of d.

Figure 12 shows the main radiation beams of the array at 0° of scanning for different values of d. It can be seen for d=6 mm, the array has good efficiency, sufficienct gain level and compact size which is suitable

for cellular phased array applications. As illustrated, the array has 11.2, 12.2, and 12.7 dB gains with -0.54, -0.67, and -0.84 values of total efficiency for d=5 mm, d=6 mm, and d=7 mm, respectively. Based on the obtained results, in order to have high-gain, high-efficiency beams of antenna array with wide scanning function (0 to 75 degree), the distance between elements (*d*) must be calculated near λ/2 of the operation frequency (d=6 mm).

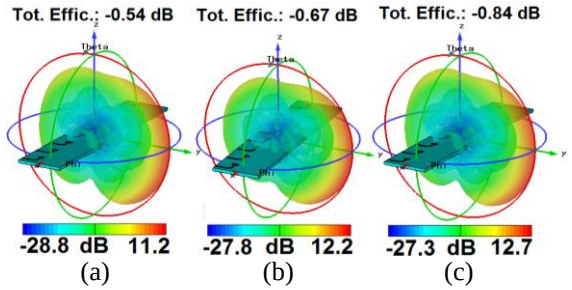

Fig. 12. 3D beams (at 0°) of the array for different values of *d*: (a) d=5 mm, (b) d=6 mm, and (c) d=7 mm.

Figure 13 (a) illustrates a system architecture in which the proposed linear phased array antenna can be used for 5G applications. For operations using time division duplex, the feed network can be implemented using low loss phase shifters (such as *HMC933LP4E* [17]) for beam steering). One of the important issues to achieve a functional array antenna is the feed network.

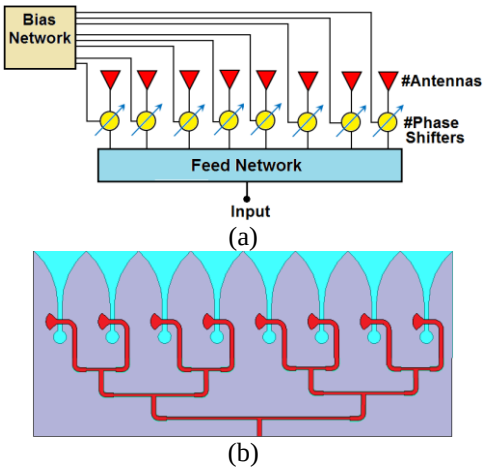

Fig. 13. (a) Phased array architecture for the proposed design, and (b) typical 1:8 feed network.

In the proposed design, a 1×8 uniform linear array antennas could be used and each radiating element with equal magnitude must be excited. There are various techniques of feed network design for this purpose: parallel [Fig. 13 (b)], series, and etc. The power dividers (such as Wilkinson) divide the power to equally 1:N and also unequally by changing the input and output [9]. It should be noted the usage of the feed network could has influence on the antenna parameters in terms of directivity, mutual coupling, gain and etc. Additionally, the mutual coupling in combination with the feed network causes notable changes in the excitation currents. So, the losses of the antenna performance in the vicinity of feeding network and active elements should be considered.

IV. APPLICATION OF THE LINEAR ARRAY FOR 5G HANDHELD DEVICES

Figure 14 depicts the configuration of the 5G mobile-phone antenna. It consists of eight 22-GHz TSA elements used to form a linear phased array in the edge region (top-side) on a mobile phone PCB. Another set of the designed array could be used in two sets of phased arrays in the top and bottom portion of the mobile phone PCB [18].

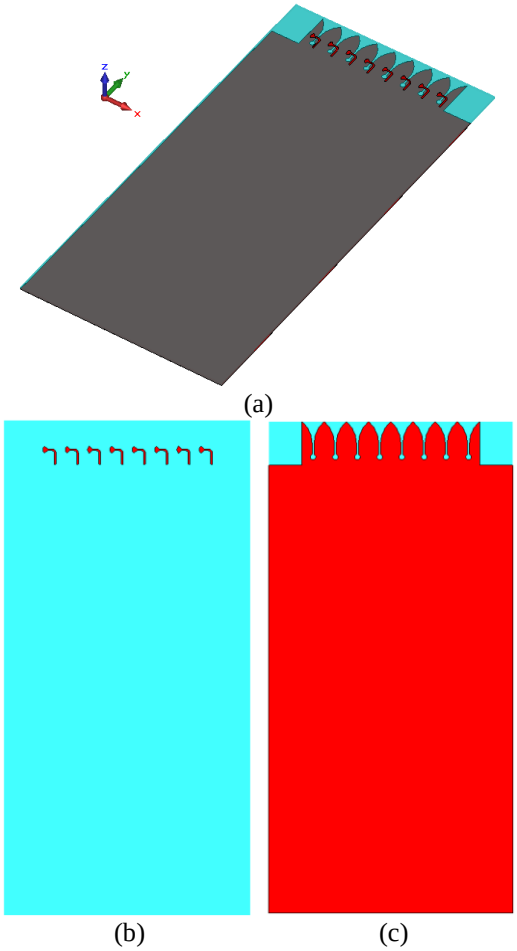

Fig. 14. Phased array 5G antenna configuration: (a) side view, (b) top layer, and (c) bottom layer (GND).

The simulated S-parameters (S_{11} to S_{81}) of the designed 5G mobile-phone antenna are shown in Fig. 15. The antenna operates at the central frequency of 22 GHz (2 GHz bandwidth). It can be seen that the highest mutual-coupling characteristic between the elements is less than -12 dB which is sufficient for typical phased array applications.

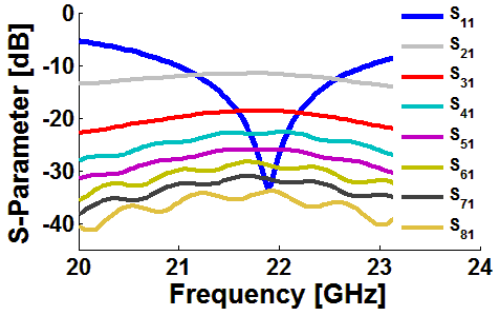

Fig. 15. Simulated S-parameters of the proposed 5G mobile-phone antenna.

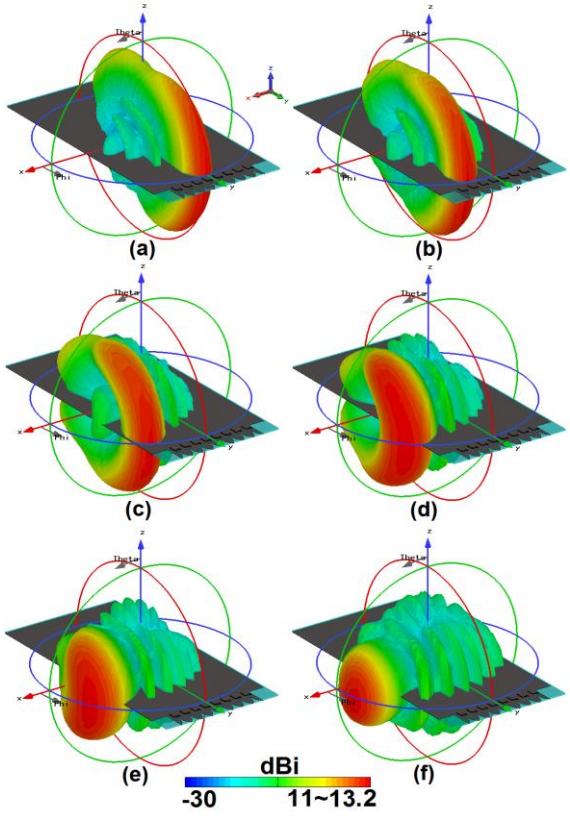

Fig. 16. 3D Radiation beams with directivity values at: (a) 0°, (b) 15°, (c) 30°, (d) 45°, (e) 60°, and (f) 75°.

The beam steering characteristic of the antenna with directivity values at different scanning angles (0° to 75°) are shown in Fig. 16. The analysis and performance of the antenna beams are obtained by using CST Microwave Studio®. The shape and direction of the array beams are determined by relative phases amplitudes applied to each radiating element as below:

$$\psi = 2\pi (d/\lambda) \sin\theta, \quad (8)$$

where d is the distance between the radiation elements and θ is the angle of incidence.

As seen, the proposed antenna has a sufficient beam-steering function in the scanning range of 0 to 75 degree. It should be noted that for plus-minus (±) scanning angles, the beam-steering characteristic of the antenna are almost the same. Figure 17 (a) illustrates the simulated realized gains of the proposed 5G mobile-phone antenna at different angles. From the beam steering characteristic, it can be observed that the antenna has sufficient gains at different scanning angles. For the scanning range of 0 to 75 degree, the antenna gains are almost constant and more than 10 dB.

Figure 17 (b) describes the fundamental radiation properties of the antenna beams for the scanning range of 0 to 70 degree. As seen, in the scanning angle of 0-60 degree, the antenna has more than -0.1 dB -0.5 dB radiation and total efficiencies, respectively. It is noted that the antenna has high efficiencies for different scanning angles. Furthermore, when the scanning angle of the radiation beam is ≤+60°, the proposed antenna has more than 11 dBi directivity.

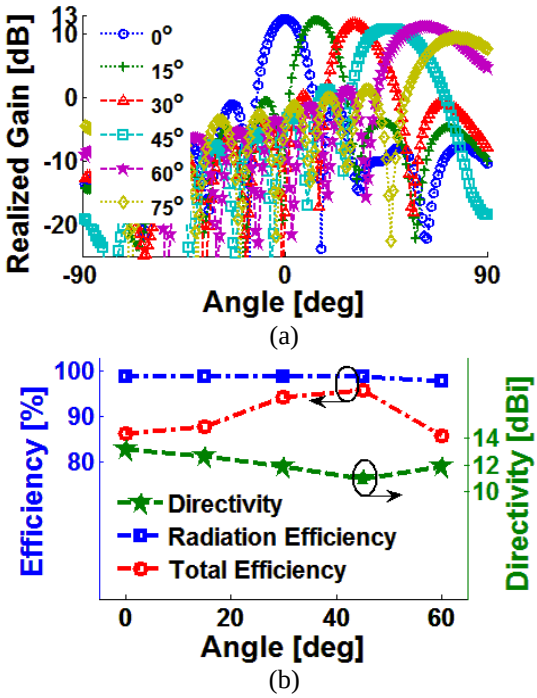

Fig. 17. (a) Realized gains and (b) radiation properties of the antenna at different scanning angles.

The radiation performances of the proposed 5G mobile-phone antenna with different lengths of the PCB ground-plane have been investigated in Fig. 18. As illustrated, the size of PCB ground plane does not have significant impact on the radiation properties of the antenna in terms of gain and total efficiency.

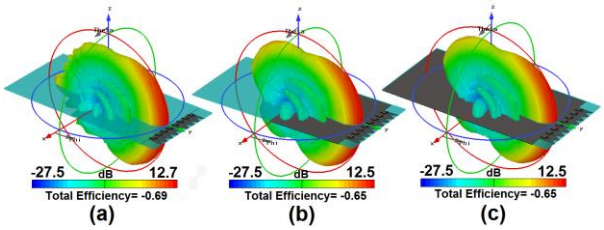

Fig. 18. Radiation characteristics of the 5G mobile-phone antenna (at 0°) for different length of the ground plane: (a) full, (b) half, and (c) without PCB-GND.

The handsets for mobile communication systems are practically operated in the vicinity of a human body. Especially, the user's hand is one of the parts that touch the mobile handsets most frequently [19-20]. In general, the user's hand has a negative impact on the antenna performance in terms of efficiency, gain, impedance-matching etc. Changing its position can increase/ decrease the amount of the losses. The impact of user-hand on the performance of the proposed phased array TSA has been studied and Fig. 19 illustrates different placement of the antenna in the presence of the user's hand.

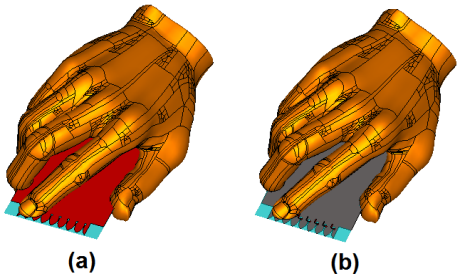

Fig. 19. Different placement of the antenna in the vicinity of user's hand: (a) bottom and (b) top positions.

Table 2 summarizes the effect of user's hand on the properties of the proposed phased array TSA. The total losses of antenna parameters in terms of realized gain, radiation efficiency, and total efficiency are about 3 dB, 15%, and 25%, respectively.

Table 2: Total losses of the antenna parameters

Antenna Parameters	Position (a)	Position (b)
Radiation efficiency	10~25%	10~20%
Total efficiency	20~35%	15~35%
Realized gain	0.5~2.5 dB	1~2 dB

Figure 20 shows the 3D radiation beams of the antenna patterns in the vicinity of user's hand for different scanning angles at different positions. As illustrated, the antenna has a good beam steering function with acceptable gain levels at different scanning angles.

In addition, the S_{nn} characteristics of the designed 5G mobile-phone antenna in the presence of the user's hand is illustrated in Fig. 21. As can be observed, the antenna has good impedance matching with less than 0.4 GHz frequency-shifting in the operation band of the designed array in free space.

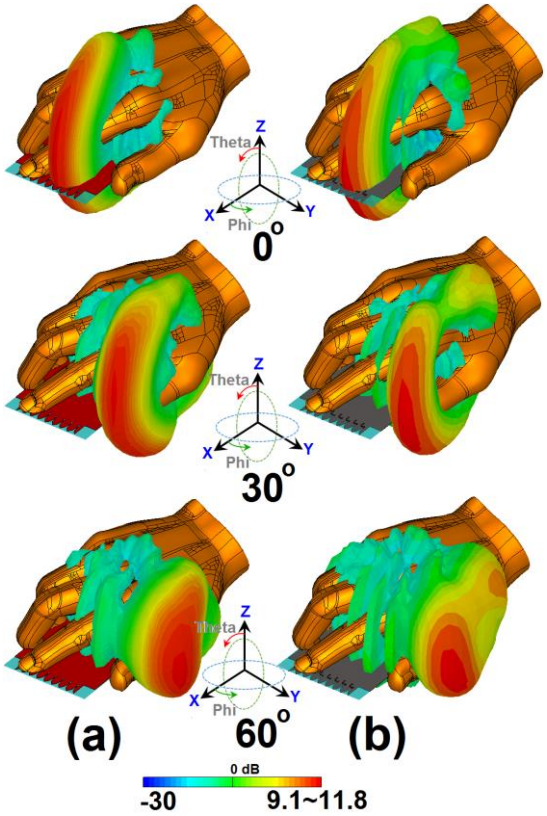

Fig. 20. Radiation beams at different scanning angles for: (a) bottom position and (b) top position.

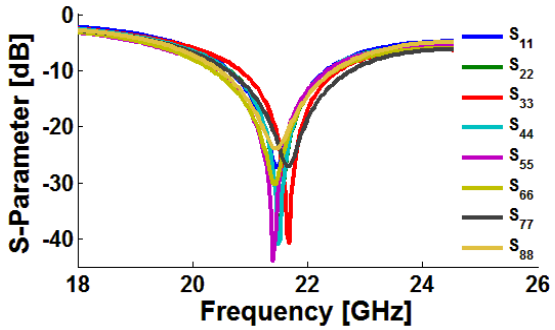

Fig. 21. Snn characteristics of the antenna in the presence of the user-hand (S11 to S88).

The proposed antenna's specification absorption rate (SAR) is studied in Fig. 22. SAR is the measurement of the energy has absorbed by the human body during transmit the radio frequency electromagnetic field. The human body absorbed the energy that's mean we will lose some energy the second problem that's mean will affect the human body badly [21-24]. The SAR is described by the following equation:

$$SAR = \int \frac{\sigma(r)|E(r)|^2}{\rho(r)} dr. \quad (9)$$

As illustrated in Fig. 22, the antenna has sufficient SAR values. It should be noted the distance between 5G antenna PCB and human-hand in z-axis is less than 10 mm. As can be seen, due to close distance of the designed phased array with the head in top location, there is a difference between the SAR values of the top and bottom locations which it was predictable.

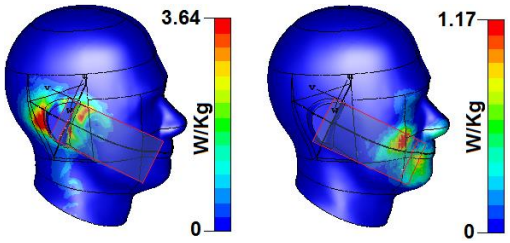

(a) (b)

Fig. 22. Analysis specific absorption rates of the proposed 5G antenna at 22 GHz: (a) top location and (b) bottom location.

Figure 23 depicts the 3D-directional radiation beams of the proposed 5G phased array antenna in the presence of the human-hand (top location) at different scanning angles. As seen, the antenna has good beam-steering characteristics with good gain values at different angles.

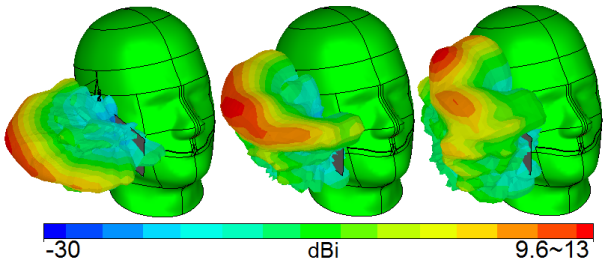

Fig. 23. Radiation beams of the 5G antenna at different angle in the presence of the human-head.

V. PLANAR PHASED ARRAY TSA DESIGN FOR 5G CHANNEL MEASUREMENTS

Figure 24 displays the 3D view of the planar phased array TSA. 64-elements of 22 GHz TSAs with hockey-stick balun Feeds have been used to form the proposed planar array design. On the other hand, the proposed planar array have been designed using eight rows of the proposed linear phased array described in Section III. The designed planar phased array antenna has a compact size of $W_X \times L_X$.

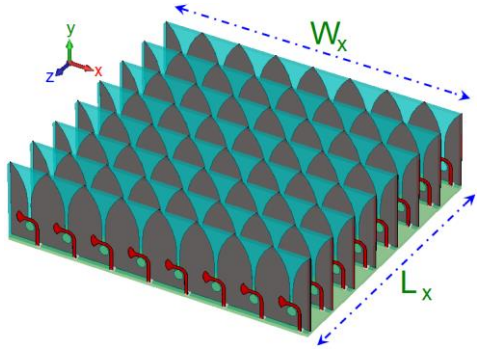

Fig. 24. 3D view of the designed 8×8 planar phased array TSA.

The proposed planar phased array antenna is operating in the same operation band of the single element TSA (frequency range from 21 to 23 GHz). It has compact-size, high-gain, sufficient-efficiency and beam-steering properties. The designed planar array could be used for 5G base station or channel measurement applications [25].

The 3D directional radiation beams of the proposed antenna with directivity values at different angles are shown in Fig. 25. It can be seen that the antenna has a good beam steering characteristic with high-level realized gains. The planar phased array design has more than 21 dB realized gain when its beam is tilted to 0 degree.

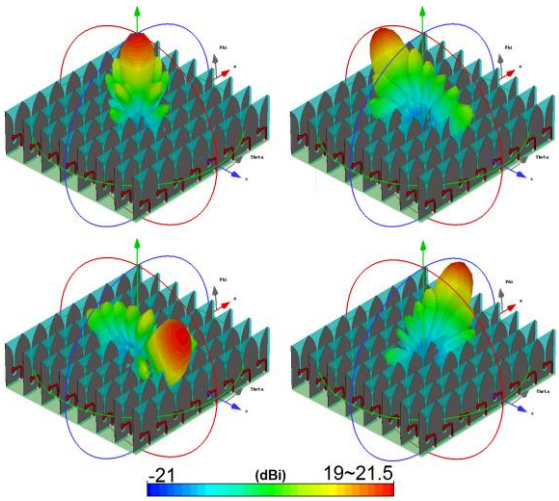

Fig. 25. 3D beams of the proposed phased array at different angles.

VI. CONCLUSION

Low-profile TSA arrays for 5G channel measurement applications are designed and investigated in this study. The antenna elements are designed to work at 22 GHz which is one of the candidate bands for the future communication systems and have a 2 GHz bandwidth. Eight TSA elements formed a linear phased array in the top portion of the mobile-phone PCB. For the deigned 5G mobile-phone antenna, fundamental radiation properties and also user's hand and head impact are studied. The designed array features high-gain/high-efficiency, compact-size good and beam-steering characteristic. In addition, using 8×8 elements of the single element 22 GHz TSA, a planar phased array with high-gain property is designed and its characteristics are investigated. Based on the obtained result, the TSA element, its linear and planar arrays are promising for 5G applications.

REFERENCES

[1] A. Osseiran, et al., "Scenarios for 5G mobile and wireless communications: The vision of the METIS project," *IEEE Commun. Mag*., vol. 52, pp. 26-35, 2014.

[2] T. S. Rappaport, et al., "Millimeter wave mobile communications for 5G cellular: It will work!," *IEEE Access*, vol. 1, pp. 335-349, 2013.

[3] P. Gupta, "Evolvement of mobile generations: 1G to 5G," *International Journal for Technological Research in Engineering*, vol. 1, pp. 152-157, 2013.

[4] W. Roh, et al., "Millimeter-wave beamforming as an enabling technology for 5G cellular communications: Theoretical feasibility and prototype results," *IEEE Commun. Mag.*, vol. 52, pp. 106-113, 2014.

[5] N. Ojaroudiparchin, M. Shen, and G. F. Pedersen, "A compact design of planar array antenna with fractal elements for future generation applications," *Applied Computational Electromagnetics Society (ACES) Journal*, vol. 31, pp. 789-796, 2016.

[6] K. S. Yngvesson, T. L. Korzeniowski, Y. S. Kim, E. L. Kollberg, and J. F. Johansson, "The tapered slot antema—A new integrated element for MM wave applications," *IEEE Trans. Microw. Theory Tech*., vol. 37, pp. 365-374, 1989.

[7] A. Kedar and K. S. Beenamole, "Widebeam tapered slot antenna for wide angle scanning phased array antenna," *Progress in Electromagnetics Research*, vo1. 27, pp. 235-251, 2011.

[8] L. S. Locke, J. Bornemann, and S. Claude, "Substrate integrated waveguide-fed tapered slot antenna with smooth performance characteristics over an ultra-wide bandwidth," *Applied Computational Electromagnetics Society (ACES) Journal*, vol. 28, pp. 454-462, 2013.

[9] S. A. Elechi and B. A. Lail, "Design of a high directivity dual tapered slotline antenna," *27th Annual Review of Progress in Applied Computational Electromagnetics*, pp. 839-842, Williamsburg, Virginia, USA, 2011.

[10] W. Hong, K. Baek, Y. Lee, and Y. G. Kim, "Design and analysis of a low-profile 28 GHz beam steering antenna solution for future 5G cellular applications," *IEEE International Microwave Symposium*, Tampa Bay, Florida, June 1-6, 2014.

[11] N. Amitay, V. Galindo, and C. P. Wu, *Theory and Analysis of Phased Array Antennas*. Wiley Interscience, 1972.

[12] W. O. Coburnand and A. I. Zaghloul, "Numerical analysis of stacked tapered slot antennas," *28th Annual Review of Progress in Applied Computational Electromagnetics*, pp. 112-117, Columbus, Ohio, April 10-14, 2012.

[13] J. R. Jamesn and P. S. Hall, *Handbook of Microstrip Antennas*. Peter Peregrinus Ltd., London, 1989.

[14] *CST Microwave Studio.* ver. 2014, CST, Framingham, MA, USA, 2014.

[15] R. C. Hansen, *Phased Array Antennas*, John Wiley & Sons, Inc., New York, 2009.

[16] A. Farahbakhsh, G. Moradi, and S. Mohanna, "Reduction of mutual coupling in microstrip array antenna using polygonal defected ground structure," *Applied Computational Electromagnetics Society (ACES) Journal*, vol. 26, pp. 334-339, 2011.

[17] HMC933LP4E, "*Analog Phase Shifter*," Hittite Microwave Company.

[18] W. Hong, et al., "mmWave phased-array with hemispheric coverage for5th generation cellular handsets," EuCAP, pp. 714-716, 2014.

[19] N. Ojaroudiparchin, M. Shen, and G. F. Pedersen, "Design of Vivaldi antenna array with end-fire beam steering function for 5G mobile terminals," *Telecommunications Forum* (*TELFOR 2015)*, Serbia, November 2015.

[20] K. Zhao, Z. Ting, and S. He, "Human exposure to mmwave phased array antennas in mobile terminalfor 5G mobile system," *IEEE Vehicular Technology Conference (VTC Spring)*, Glasgow, pp. 1-2, 2015.

[21] J. Moustafa, N. J. McEwan, R. A. Abd-Alhameed, and P. S. Excell, "Low SAR phased antenna array for mobile handsets," *Applied Computational Electromagnetics Society (ACES) Journal*, vol. 21, pp. 196-205, 2006.

[22] I. B. Bonev, O. Franek, and G. F. Pedersen, "Impact of the hand on the specific absorption rate in the head," *Applied Computational Electromagnetics Society (ACES) Journal*, vol. 29, pp. 470-

477, 2014.
[23] M. R. I. Faruque, M. T. Islam, and N. Misran, "Evaluation of EM absorption in human head with metamaterial attachment," *Applied Computational Electromagnetics Society (ACES) Journal*, pp. 1097-1107, vol. 25, 2010.
[24] M. Fallah, A. A. Heydari, A. R. Mallahzadeh, and F. H. Kashani, "Design and SAR reduction of the vest antenna using metamaterial for broadband applications," *Applied Computational Electromagnetics Society (ACES) Journal*, vol. 26, pp. 141-155, 2011.
[25] N. Ojaroudiparchin, M. Shen, and G. F. Pedersen, "8×8 planar phased array antenna with high efficiency and insensitivity properties for 5G mobile base stations," *EuCAP 2016*, Switzerland, 2016.

Naser Ojaroudi Parchin was born on 1986 in Iran. He received M.Sc. degree in Telecommunication Engineering from Shahid Rajaee University (SRTTU), Tehran, Iran in 2013. His research interests include multi-band/UWB antennas, MIMO antennas, Fabry resonators, Fractal antennas, mm-Wave phased array 5G antennas, band-stop/band-pass microwave filters, and reconfigurable structure.

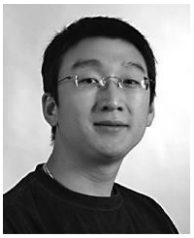

Ming Shen received the Master and Ph.D. degrees in Electrical Engineering from the University of Chinese Academy of Sciences, China in 2005, and from Aalborg University, Denmark in 2010, respectively. Since 2007, he has been with the Department of Electronic Systems, Aalborg University, where he is currently an Assistant Professor. He is the author of more than 30 technical papers and book chapters. His current research interests include: energy harvesting and battery-less low power circuits and systems, 5G mm-Wave circuits and antennas, remote patient monitoring, and wireless power transfer technologies.

Gert Frølund Pedersen received the B.Sc. E. E. degree, with honor, in Electrical Engineering from College of Technology in Dublin, Ireland in 1991, and the M.Sc. E. E. degree and Ph.D. from Aalborg University in 1993 and 2003. He has been with Aalborg University since 1993 where he is a Full Professor heading the Antenna, Propagation and Networking LAB with 36 researchers. Further he is also the Head of the doctoral school on wireless communication with some 100 Ph.D. students enrolled. His research has focused on radio communication for mobile terminals especially small Antennas, Diversity systems, Propagation and Biological effects and he has published more than 175 peer-reviewed papers and holds 28 patents. He has also worked as Consultant for developments of more than 100 antennas for mobile terminals including the first internal antenna for mobile phones in 1994 with lowest SAR, first internal triple-band antenna in1998 with low SAR and high TRP and TIS, and lately various multi antenna systems rated as the most efficient on the market. He has worked most of the time with joint university and industry projects and have received more than 12 M$ in direct research funding. Latest he is the project leader of the SAFE project with a total budget of 8 M$ investigating tunable front end including tunable antennas for the future multiband mobile phones. He has been one of the pioneers in establishing Over-The-Air (OTA) measurement systems. The measurement technique is now well established for mobile terminals with single antennas and he was chairing the various COST groups (swg2.2 of COST 259, 273, 2100 and now ICT1004) with liaison to 3GPP for over-the air test of MIMO terminals.

An Interdigital FSS based Dual Channel UWB-MIMO Antenna Array for System-in-Package Applications

M. Bilal [1], K. Khalil [1], R. Saleem [1], F. A. Tahir [2], and M. F. Shafique [3]

[1] Department of Telecommunication Engineering
University of Engineering and Technology, Taxila, 47050, Pakistan

[2] School of Electrical Engineering & Computer Science (SEECS)
National University of Sciences and Technology (NUST), H-12 Campus, Islamabad, 44000, Pakistan

[3] Center for Advanced Studies in Telecom (CAST)
COMSATS Institute of Information Technology (CIIT), Park Road, Chak Shahzad, Islamabad, 45550, Pakistan

Abstract ─ In this paper, a miniaturized, dual channel Multiple Input Multiple Output (MIMO) antenna array is presented for Ultra Wideband applications. The array configuration is well suited for 3-D system-in-package applications. MIMO antennas are reported in two different configurations, i.e., back-to-back and orthogonal/corner. The array is designed on an FR-4 substrate of thickness 1 mm and compact dimensions of 40 mm × 35 mm. An Interdigital FSS based decoupling structure is analyzed and deployed to reduce mutual coupling between array ports. Simulated and measured results show that an isolation better than 20 dB is achieved over most of the band. More importantly, other performance criteria such as envelope correlation coefficient, total active reflection coefficient, channel capacity loss and gain also indicate that the proposed array is a potential candidate for UWB-MIMO applications.

Index Terms ─ Frequency Selective Surfaces (FSS), microstrip antennas, Multiple-Input Multiple-Output (MIMO), mutual coupling, Ultra Wideband (UWB) antennas.

I. INTRODUCTION

Any radio system that has a bandwidth more than 25 percent of its central frequency or a bandwidth larger than 500 MHz may be referred to as an Ultra Wideband (UWB) system. U.S. Federal Communications Commission (FCC) has allocated a bandwidth of 7.5 GHz, ranging from 3.1-10.6 GHz, for the UWB applications [1]. In general, UWB antennas are employed due to compact size and ease of integration in compact devices. In MIMO arrays, multiple antennas are deployed at both transmitter and receiver sides. MIMO antennas are important for increasing channel capacity and link reliability [2]. As compact antenna arrays are needed in modern smart miniaturized gadgets, MIMO elements have to be placed in close proximity to one another. However, mutual coupling increases when MIMO antenna elements are placed close to each other. For MIMO arrays, mutual coupling is undesirable as it distorts the radiation patterns of individual antenna elements and decreases overall diversity gain of the MIMO array. In general, to obtain full advantages of a MIMO array, mutual coupling has to be suppressed effectively. Various techniques have been proposed in the existing literature to achieve isolation among antenna ports in a MIMO array. These techniques include but are not limited to Defected Ground Structure (DGS) [3-4], neutralization technique [5], Electronic Band Gap (EBG) structures [6], Frequency Selective Surfaces (FSS) [10] and parasitic elements [7]. These decoupling techniques are reported for planar antennas.

MIMO designs can be broadly characterized as planar [8] and non-planar arrangements [9-10]. In planar arrangements, multiple antennas are placed in a single plane. Generally, for planar arrangements, ground plane is shared by the MIMO elements. Planar MIMO configurations may be suitable when there is no limitation on horizontal size. Non-planar MIMO configurations are well-suited when there are constraints on placing antennas horizontally. More importantly, non-planar arrangements are well suited for around-corner mounting or 3-D system-in-package applications [1]. However, it may not be possible to provide a shared ground plane to corner-mounted or 3-D MIMO antenna arrangements, especially when multiple configurations are required.

As shown in Fig. 1, in this work, a dual port/channel, UWB-MIMO antenna is reported for orthogonal and back-to-back configurations. The antennas are fabricated on 40 mm × 35 mm FR-4 substrate. A 20 mm thick polystyrene block with relative permittivity of 2.6 and dielectric loss tangent, $tan\delta$ of 3×10^{-4} supports the antennas for both configurations.

Submitted On: March 22, 2015
Accepted On: January 28, 2017

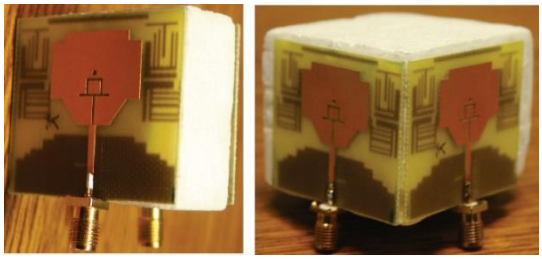

(a) (b)

Fig. 1. Fabricated MIMO configurations: (a) back-to-back, and (b) orthogonal.

Rest of this paper is organized as follows: Section II details the antenna element and MIMO array configurations. In Section III, simulated and measured performance parameters are discussed, and finally Section IV concludes the paper.

II. DESIGN LAYOUT

The simulated design layout is shown in Figs. 2 (a) and 2 (b). The design has radiating element on one side of the substrate while ground plane and decoupling structure are placed on flip side of the substrate. A T-shaped slot is etched at center of radiating element for enhanced impedance match on higher frequencies. The radiating element is beveled near the feed for an overall impedance match. Moreover, the proposed MIMO design has a defected ground structure (DGS) for improved impedance match and isolation characteristics, especially at higher frequencies. The isolation structure is a grid-like Interdigital FSS, formed by an arrangement of strips.

The proposed antenna geometry is shown in Fig. 2 (a). The antenna is fabricated on an FR-4 substrate with thickness of 1 mm and compact dimensions of 40 mm × 35 mm. The design is matched to a 50-Ω feed line with a length of 14 mm and width 2 mm. The radiating element employs beveling and slot etching for bandwidth enhancement. Moreover, chamfering small squares in top of radiating patch gives impedance match on middle frequency band.

The decoupling structure along with defected ground plane is shown in Fig. 2 (b). The ground plane has an L-type slot etched in the top edge for enhanced impedance match and improved isolation among antenna ports, especially on higher band frequencies. The stepped profile of ground plane helps improve the overall impedance match.

A pair of Interdigital FSSs are placed as decoupling structures above the ground plane, on either side of the radiation element. This Interdigital FSS is an arrangement of horizontal and vertical strips. In the existing literature, different metamaterial and FSS based structures are reported [1, 8, 10] as decoupling structures. This Interdigital FSS arrangement prevents propagation of surface waves, which otherwise cause coupling in both antennas. In the proposed design, position, thickness and gaps of Interdigital FSSs are optimized for better isolation and impedance match characteristics.

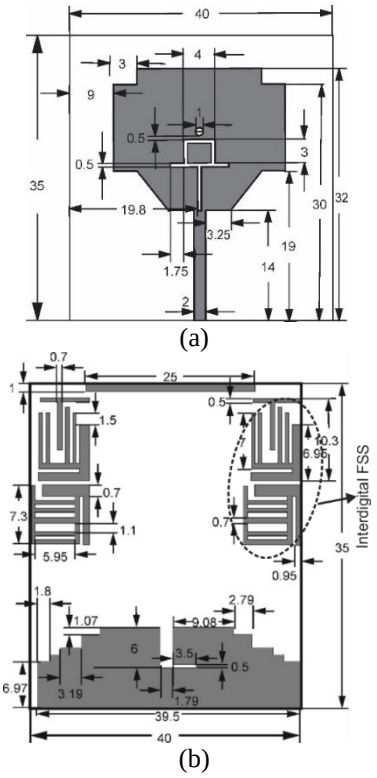

Fig. 2. UWB-MIMO array - all dimensions are in mm: (a) front view and (b) back view.

III. SIMULATED AND MEASURED PERFORMANCE CRITERIA

A. Return loss

To investigate return loss performance, the proposed MIMO antenna is simulated in the proposed dual configurations, both with and without the decoupling structure. The return loss of single antenna element and the proposed MIMO system in both configurations are presented in Fig. 3. As illustrated in Fig. 3, this MIMO antenna system exhibits good impedance match, with and without the decoupling structure in both configurations.

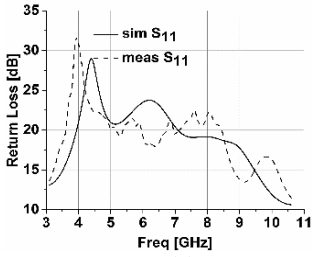

(a)

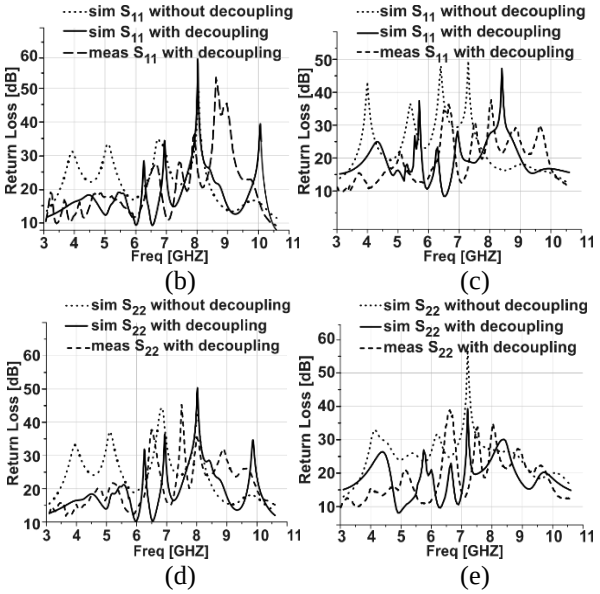

Fig. 3. Return loss: (a) single antenna element, (b), (d) back-to-back, and (d), (e) orthogonal.

B. Isolation characteristics

Interdigital FSS are etched on rear side of each antenna element to not only suppress the undesired coupling but also improve the impedance match. The analysis and optimization of these structures is performed by using a full-wave Finite Element Method (FEM) based electromagnetic solver (Ansys HFSS®). To analyze and optimize transmission loss of the proposed FSS structures, FEM based wave guide excitation method is employed as shown in Fig. 4 (a). A pair of perfect E and perfect H boundaries are assigned to confine analysis to area that contains FSS. Moreover, two wave ports are modelled at distances of $\lambda/4$ from the surface to evaluate the transmittance in the confined region [10]. The proposed FSSs are optimized to achieve overall transmission loss over UWB band, in particular, at higher frequencies as shown in Fig. 4 (b). The simulated and measured results are shown in Fig. 4 (c) and Fig. 4 (d) for both configurations. In general, the decoupling is more than 20 dB over most of the frequency band. In particular, the decoupling is more than 30 dB over higher band frequencies.

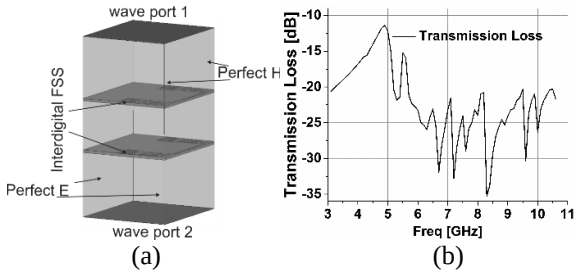

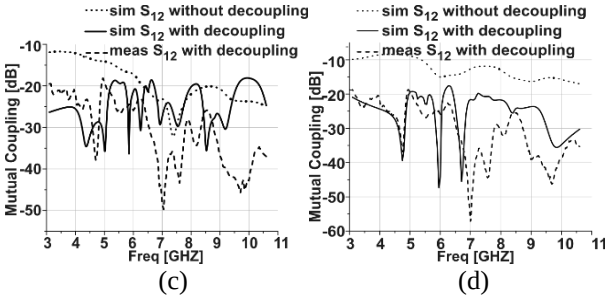

Fig. 4. Transmission loss and isolation: (a) FSS simulation setup, (b) transmission loss, (c) back-to-back, and (d) orthogonal.

C. Induced current suppression

Surface current density plots are shown in Fig. 5. In obtaining the surface current density plot, one antenna is excited and the other is matched terminated. When the proposed MIMO design is simulated without the decoupling structure, undesired surface currents are induced on antenna feedline and radiating element causing significant mutual coupling. However, these surface currents are suppressed effectively by employing the Interdigital FSS

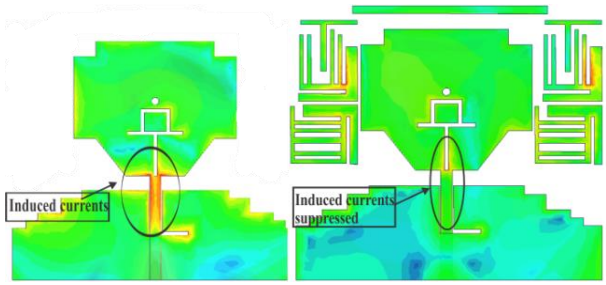

Fig. 5. Surface current distribution at 5 GHz.

D. MIMO performance criteria

TARC (Total Active Reflection Coefficient), ECC (Envelope Correlation Coefficient), CCL (Channel Capacity Loss) and overall gain of the proposed MIMO system are computed to analyze the diversity performance of the proposed design. For acceptable MIMO performance, it is desirable to have TARC < 0 dB, ECC < -3 dB and CCL < 0.5 bits/sec/Hz. The proposed design exhibits TARC < -8 dB, ECC < -40 dB and CCL < 0.45 in both configurations as shown in Fig. 6 [1, 10]. Moreover, both the configurations achieve at least 3 dB gain enhancement in most of the UWB band. However, the Interdigital FSS slightly reduces the gain in the middle frequency band. This loss may be attributed to transmission loss.

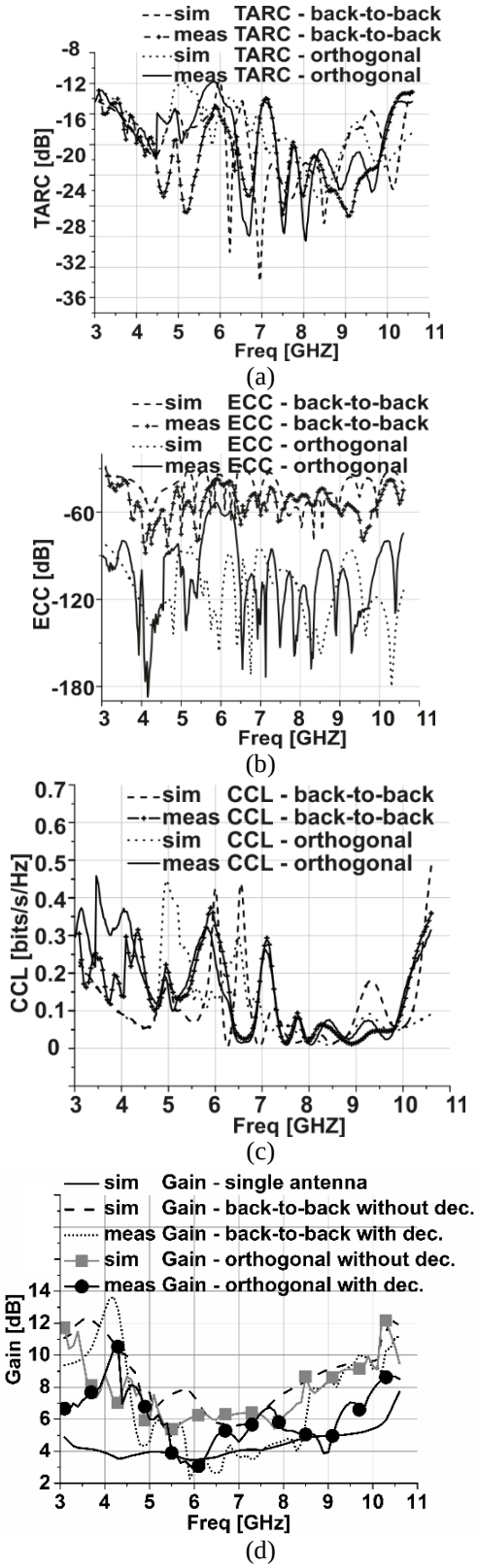

Fig. 6. MIMO performance criteria: (a) TARC, (b) ECC, (c) CCL, and (d) Gain.

E. Radiation patterns

The simulated E-plane radiation patterns at 3 GHz and 10 GHz, for both orthogonal and back-to-back configurations, are shown in Fig. 7. The results indicate some degree of pattern distortion which is not uncommon for non-planar antenna configurations, as also reported in the existing literature [4, 10].

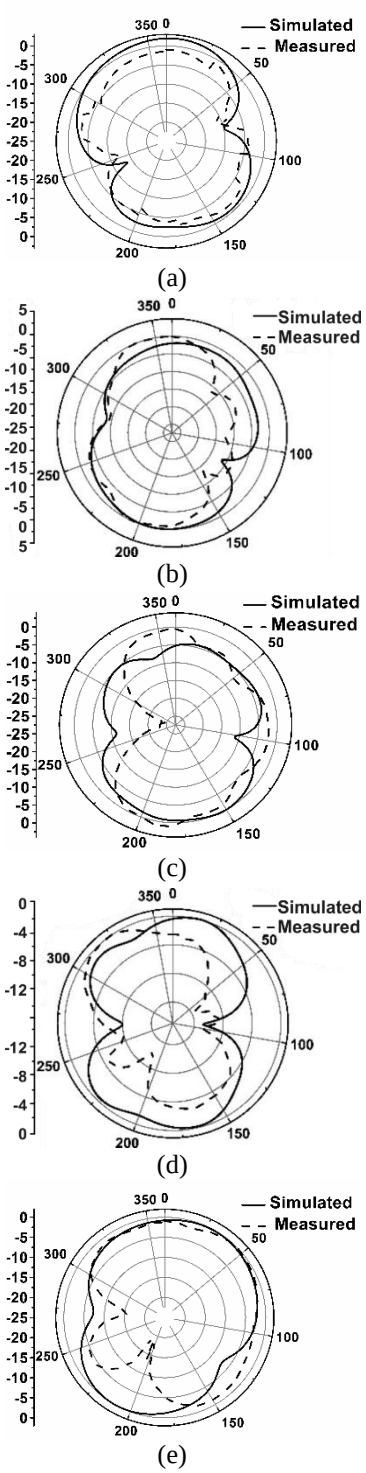

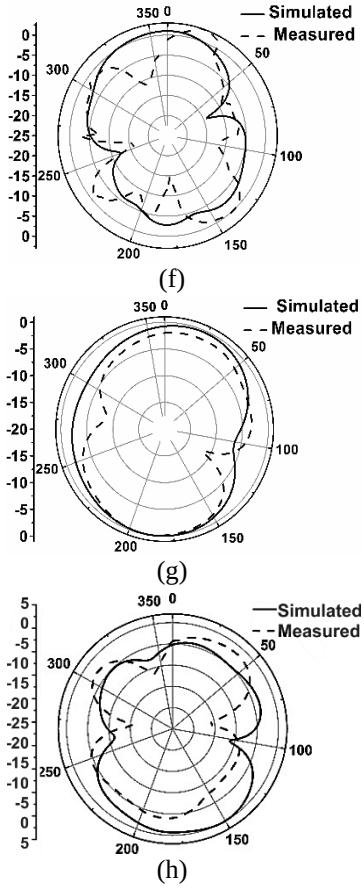

Fig. 7. Radiation patterns: (a) E-field at 3 GHz back-to-back, (b) H-field at 3 GHz back-to-back, (c) E-field at 3 GHz orthogonal, (d) H-field at 3 GHz orthogonal, (e) E-field at 10 GHz back-to-back, (f) H-field at 10 GHz back-to-back, (g) E-field at 10 GHz orthogonal, and (h) H-field at 10 GHz orthogonal.

IV. CONCLUSION

In this paper, a dual element MIMO antenna array is proposed for UWB communication. Two diff erent configurations, i.e., back-to-back and orthogonal provide employability in 3-D system-in-package application. The proposed design achieves significant isolation among MIMO ports while also maintaining ECC, TARC, channel capacity loss and gain within the acceptable limits. For the proposed design, simulated and measured results are in good agreement. More importantly, miniaturized dimensions, performance parameters and ease of integration suggest suitability of the proposed array for 3-D system-in-package UWB-MIMO applications.

REFERENCES

[1] R. Saleem, M. Bilal, K. B. Bajwa, and M. F. Shafique, "Eight-element UWB-MIMO array with three distinct isolation mechanisms," *Electronics Lett.*, vol. 51, no. 4, pp. 311-313, 2015.

[2] Y. L. Q. Chu, J. F. Li, and Y. T. Wu, "A planar H-shaped directive antenna and its application in compact MIMO antenna," *IEEE Trans. Antennas Propagat*., vol. 61, no. 9, pp. 4810-4814, 2013.

[3] H. Peng, R. Tao, W. Y. Yin, and J. F. Mao, "A novel compact dual-band antenna array with high isolations realized using the neutralization technique," *IEEE Trans. Antennas Propagat.*, vol. 61, no. 4, pp. 1956-1962, 2013.

[4] M. T. Islam and M. S. Alam, "Compact EBG structure for alleviating mutual coupling between patch antenna array elements," *Progress In Electromagnetics Research*, vol. 137, pp. 425-438, 2013.

[5] B. K. Lau and J. B. Andersen, "Simple and efficient decoupling of compact arrays with parasitic scatterers," *IEEE Trans. Antennas Propagat.*, vol. 60, no. 2, pp. 464-472, 2012.

[6] W. Xie, T. Yang, X. Zhu, F. Yang, and Q. Bi, "Measurement-based evaluation of vertical separation MIMO antennas for base station," *IEEE Antennas and Wireless Propagat. Lett.*, vol. 11, pp. 415-418, 2012.

[7] M. S. Sharawi, M. U. Khan, A. B. Numan, and D. N. Aloi, "A CSRR loaded MIMO antenna system for ISM band operation," *IEEE Trans. Antennas Propagat.*, vol. 61, no. 8, pp. 4265-4274, 2013.

[8] A. Elsherbini and K. Sarabandi, "Dual-polarized coupled sectorial loop antennas for UWB applications," *IEEE Antennas and Wireless Propagat. Lett.*, vol. 10, pp. 75-78, 2011.

[9] G. Adamiuk, T. Zwick, and W. Wiesbeck, "Compact, dual-polarized UWB-antenna, embedded in a dielectric," *IEEE Trans. Antennas Propagat.*, vol. 58, no. 2, pp. 279-286, 2010.

[10] M. Bilal, R. Saleem, H. H. Abbasi, M. F. Shafique, and A. K. Brown, "An FSS based non-planar quad element UWB-MIMO antenna system," *IEEE Antennas and Wireless Propagat. Lett.*, vol. PP, no. 99, pp. 1-1, 2016.

Muhammad Bilal received his B.S degree in Telecommunication Engineering in 2011 from Baluchistan University of Information Technology, Engineering and Management Sciences, Quetta, Balochistan, Pakistan and Masters in Telecommunication Engineering in 2014 from University of Engineering and Technology (UET) Taxila, Pakistan. In, 2014, he was awarded a funded Ph.D. studentship by UET Taxila. His main research interests are in UWB-MIMO systems, Frequency Selective Surfaces and reflectarrays.

Kashif Khalil received his B.Sc. degree in Electronics Engineering in 2012 and Masters in Telecommunication Engineering in 2014 from University of Engineering and Technology (UET) Taxila, Pakistan. He worked as Research Assistant at UET Taxila from 2012-2014. His main research interests are in UWB Antennas, UWB-MIMO systems, RF and Microwave Engineering.

Rashid Saleem received B.S. Electronic Engineering from Ghulam Ishaq Khan Institute of Engineering Sciences and Technology, Pakistan, in 1999. He pursued a career in the telecommunication industry for several years while continuing education. He received M.S. from UET Taxila through Center for Advanced Studies in Engineering, Pakistan, in 2006 and Ph.D. from The University of Manchester, United Kingdom in 2011. He worked on antennas, channel modeling and interference aspects of Ultra Wideband systems during his Ph.D. and was also member of a team designing and testing arrays for the Square Kilometer Array project. Currently, he is working as Assistant Professor at University of Engineering and Technology (UET), Taxila, Pakistan where he is heading the MAP (Microwaves, Antennas and Propagation) research group. His research interests include antennas, angle-of-arrival based channel modeling, microwave periodic structures and metamaterials

Farooq Ahmad Tahir received his Bachelor's degree in Electrical Engineering from University of Engineering and Technology Lahore, Pakistan in 2005. In 2008, he was awarded Master's degree in Radio Frequency Telecommunications and Microelectronics (TRFM) from the University of Nice, Sophia Antipolis, France. Since Sept. 2008 to Sept. 2011, he was working towards his Ph.D. degree in a leading French Research Lab, LAAS-CNRS (National Scientific Research Center) Toulouse, France under the Research Group "Micro and Nano Systems for Wireless Communications". He received Doctorate degree in September 2011 from National Polytechnic Institute of Toulouse (INPT), University of Toulouse, France. Currently he is working as Assistant Professor at National University of Sciences and Technology (NUST), Islamabad.

Muhammad Farhan Shafique received B.Eng. degree from Hamdard University, Karachi, Pakistan, in 2003, M.S. degree from the University of Paris East (Marne-La-Vall´ee, Paris), France, in 2005 and Ph.D. in Electronic and Communications Engineering from The University of Leeds, Leeds, U.K in 2010. In 2005, he was an Intern at Conservatoire National des Arts et M´etiers, Paris, France, where he was involved in the study of blind frequency and phase estimation in short radio burst. From 2007 to 2010 he was involved in establishing the LTCC fabrication facility at Institute of Microwave and Photonics, The University of Leeds, UK. He is working as an Assistant Professor at COMSATS Institute of Information Technology, Islamabad, Pakistan where he has established the Microwave Components and Devices (MCAD) research group, Associate Director of Center for Advanced Studies in Telecommunications (CAST). His research interests involve multilayered-microwave device fabrication on LTCC and thick-film technology, RF antenna and antenna arrays, ultra wideband diversity antennas and MEMS packaging.

Design of Planar Differential-Fed Antenna with Dual Band-Notched Characteristics for UWB Applications

Wei Hu [1,2], Zhaoyang Tang [1], Lixue Zhou [1], and Yingzeng Yin [1]

[1] National Laboratory of Science and Technology on Antennas and Microwaves
Xidian University, Xi'an 710071, China
mwhuwei@163.com, zhaoyangt@126.com, vesslan_zhou@163.com, yzyin@mail.xidian.edu.cn

[2] Collaborative Innovation Center of Information Sensing and Understanding
Xidian University, Xi'an 710071, China

Abstract ─ A planar differential-fed antenna with dual band-notched characteristics is presented for ultra-wideband (UWB) applications. The proposed antenna mainly consists of two V-shaped radiating patches placed face to face and an octagonal slot ground plane. To avoid the potential electromagnetic interference from narrowband services, V-shaped slots embedded in the radiating patches are adopted to reject 5.5 GHz WLAN band, while T-shaped stubs connected with the radiating patches are introduced to filter 8 GHz ITU band. A prototype of the proposed antenna is fabricated and tested. Measured results demonstrate that the obtained impedance bandwidth is from 2.82 to more than 11 GHz, along with two notched bands of 4.83-6.12 GHz and 7.86-8.57 GHz. In addition, the proposed antenna exhibits good radiation patterns and stable gain.

Index Terms ─ Differential-fed, notched band, T-shaped stub, UWB antenna, V-shaped slot.

I. TRODUCTION

With the allocation of 3.1-10.6 GHz band for ultra-wideband (UWB) applications by the Federal Communications Commission (FCC), ultra-wideband wireless communication technology has attracted increasing attention due to the inherent features such as high data rate, wide bandwidth, low power consumption and low cost. As an important component of the UWB wireless communication systems, various UWB antennas with good performances have been developed [1-9]. In practical applications, existing narrowband services like 5.15-5.825 GHz WLAN and 8.025-8.4 GHz ITU may cause electromagnetic interference with the UWB band. To reduce interference, bandstop filters are often utilized to realize the desired notched band. However, it is inevitable to increase the complexity and the size of communication systems. Therefore, UWB antennas with band-notched characteristics are desirable [10-18]. In the design of UWB antenna [19], by applying an electromagnetic band-gap (EBG) structure, a notched band around 5.5 GHz is obtained to filter the 5.5 GHz WLAN band. In [20], a Koch fractal slot is used to yield a notched band covering from 4.65 to 6.40 GHz to reject the 5.5 GHz WLAN.

Recently, with the widespread application of differential signal operation in the radio frequency systems, the conventional single-ended antenna is not suitable for the differential circuits because it cannot be integrated with the differential circuit. Generally, baluns are needed to transform differential signals into single-ended signals between the differential circuits and the conventional antennas, which would cause additional losses and decrease the impedance matching bandwidth. Hence, differential-fed antennas excited by two signals with out of phase but equal amplitude are particularly significant, due to the fact that they can be directly integrated with differential circuits and no baluns are needed. In the design of [21], a differential-fed microstrip antenna is presented for UWB applications. Nevertheless, the proposed antenna does not have band-notched characteristics. In [22], a differential-fed magneto-electric dipole antenna is reported, but the antenna is not a planar structure. A differential UWB patch antenna with band-notched characteristics is developed in [23]. However, the rejected band only covers 5.2-6.0 GHz, and it cannot cover the 8 GHz ITU band.

In this paper, a planar differential-fed antenna with dual band-notched characteristics is proposed for UWB applications. This antenna, with a simple structure, is composed of two V-shaped radiating patches placed face to face and an octagonal slot ground plane. To diminish potential electromagnetic interference, V-shaped slots and T-shaped stubs are employed to achieve dual notched bands to filter 5.5 GHz WLAN and 8 GHz ITU, respectively. Details of the antenna design and the measured results are presented and discussed.

Submitted On: July 17, 2016
Accepted On: January 28, 2017

II. ANTENNA DESIGN

As is generally known, standard two-port s-parameter matrix is shown in (1):

$$S^{std} = \begin{bmatrix} S_{11} & S_{12} \\ S_{21} & S_{22} \end{bmatrix}. \quad (1)$$

For the convenience in analyzing differential signals, a form of mixed-mode s-parameter matrix S^{mm} is developed in [24], which apply to describe the transmission characteristic of four-port differential microwave circuits.

Usually, a differential-fed antenna can be regarded as a differential two-port network. And the mixed-mode s-parameter matrix can be simplified as (2):

$$S^{mm} = \begin{bmatrix} S_{dd} & S_{dc} \\ S_{cd} & S_{cc} \end{bmatrix}. \quad (2)$$

Each of the mixed-mode s-parameter terms is as follows:

$$S_{dd} = \frac{1}{2}\left(S_{11} - S_{12} - S_{21} + S_{22}\right), \quad (3)$$

$$S_{dc} = \frac{1}{2}\left(S_{11} + S_{12} - S_{21} - S_{22}\right), \quad (4)$$

$$S_{cd} = \frac{1}{2}\left(S_{11} - S_{12} + S_{21} - S_{22}\right), \quad (5)$$

$$S_{cc} = \frac{1}{2}\left(S_{11} + S_{12} + S_{21} + S_{22}\right), \quad (6)$$

S_{dd}: Differential-mode s-parameters;
S_{dc}: Common-mode to differential-mode;
S_{cd}: Differential-mode to common-mode;
S_{cc}: Common-mode s-parameters.

Thus, the differential reflection coefficient of the proposed antenna can be calculated as below:

$$\Gamma_{odd} = S_{dd} = \frac{\left(S_{11} - S_{12} - S_{21} + S_{22}\right)}{2}. \quad (7)$$

Figure 1 shows various planar antenna structures involved in the design evolution process, and the corresponding simulated reflection coefficients for each antenna are depicted in Fig. 2. Note that, antennas involved in Fig. 1 are all designed on 1 mm-thick FR-4 epoxy substrates with a relative permittivity of 4.4 and loss tangent of 0.02. Each antenna is a double-layer metallic structure. The V-shaped radiating patches are printed on the top layer of the substrate, compared with the ground plane with an octagonal slot etched on the bottom layer. In the beginning, the antenna (Ant. 1) is two UWB V-shaped monopoles placed face to face. This simple design can obtain a wide frequency band ranging from 2.97 to more than 11 GHz. The feeding lines are tapered from 1.9 to 0.7 mm to reach good impedance matching. For the purpose of minimizing the electromagnetic interference from narrowband communication systems of WLAN (5.15-5.825 GHz) and ITU (8.025-8.4 GHz), two different approaches are applied to realize filtering behavior. In Ant. 2, V-shaped slot structures are etched on the radiating patches of Ant. 1 to achieve a notched band for rejecting 5.5 GHz WLAN. And the corresponding reflection coefficient of Ant. 2 is plotted in Fig. 2. This notched band can be controlled by adjusting the dimension of the V-shaped slots because the length of each slot is approximately equal to half of one guided wavelength λ_g at 5.6 GHz. The guided wavelength λ_g is defined as:

$$\lambda_g = \frac{c}{f\sqrt{\varepsilon_{eff}}}, \quad (8)$$

where c is the free-space speed of light, f is the center frequency of notched band, and ε_{eff} is the effective relative permittivity of the substrate. Based on the Ant. 2, two T-shaped stubs are introduced to obtain the other notched band around 8.25 GHz to filter 8 GHz ITU. Notably, the length of the T-shaped stub determines the center frequency of the notched band. The final antenna (Ant. 3) proposed in this design is obtained as shown in Fig. 1.

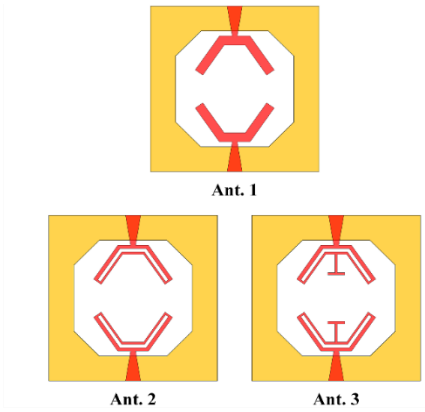

Fig. 1. Geometry of various antennas involved in the design evolution process.

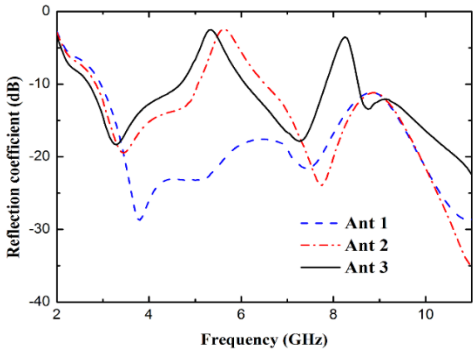

Fig. 2. Simulated reflection coefficients of various antennas involved.

To further investigate the dual band-notched working mechanism of the proposed antenna, the surface

current distributions of the whole antenna at frequencies of 5.6 and 8.25 GHz are presented in Fig. 3. It is clear that the surface current distributions mainly concentrate along the edges of the V-shaped slots at 5.6 GHz in Fig. 3 (a), whereas a large surface current density is observed along the T-shaped stubs at 8.25 GHz in Fig. 3 (b). The results from figures indicate that the V-shaped slots and T-shaped stubs work as resonators at rejected frequencies. This leads to serious impedance mismatching of the proposed antenna at 5.6 and 8.25 GHz. Thereby, the antenna cannot radiate electromagnetic energy outside in the notched bands.

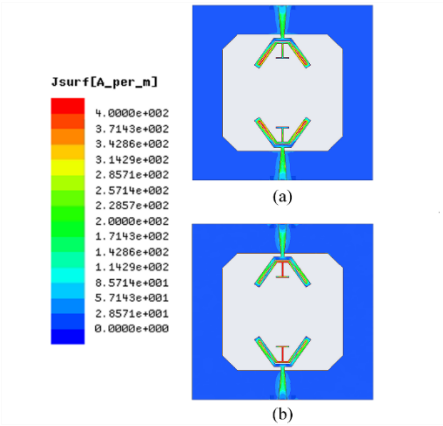

Fig. 3. Surface current distributions of proposed antenna at (a) 5.6 GHz and (b) 8.25 GHz.

The geometry of the proposed antenna (Ant. 3) with the detailed design parameters is illustrated in Fig. 4. The antenna consists of two parts: two V-shaped monopoles placed face to face and a square ground plane with an octagonal slot. A V-shaped slot and a T-shaped stub are embedded in each monopole. The simulation and analysis for the proposed antenna are performed using the electromagnetic simulator ANSYS HFSS. The optimized dimensions of the antenna are listed in Table 1.

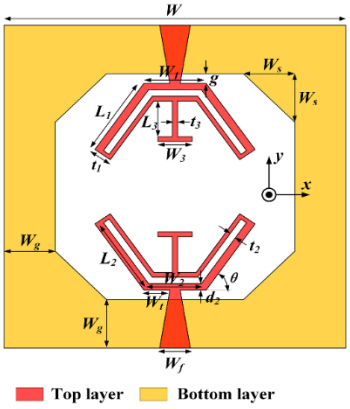

Fig. 4. Geometry of the proposed antenna with the detailed design parameters.

Table 1: Optimized parameters of the proposed antenna

Parameters	W	W_g	W_s
Values (mm)	42.0	7.0	3.5
Parameters	W_f	W_t	g
Values (mm)	1.9	1.4	0.8
Parameters	W_1	L_1	t_1
Values (mm)	4.0	8.0	1.4
Parameters	W_2	L_2	t_2
Values (mm)	3.5	6.7	0.2
Parameters	d_2	W_3	L_3
Values (mm)	0.8	3.0	3.3
Parameters	t_3	θ	
Values (mm)	0.3	55 *deg*	

III. RESULTS AND DISCUSION

Based on the optimized dimensions indicated in Table 1, a prototype of the proposed antenna is fabricated and tested to verify the operation performance. The photograph of the fabricated antenna is given in Fig. 5. The impedance bandwidth is measured by using a WILTRON 37269A vector network analyzer. Figure 6 shows the simulated and measured reflection coefficients of the proposed antenna. It is found that the antenna has a wide bandwidth from 2.82 to more than 11 GHz, along with two notched bands of 4.83-6.12 GHz and 7.86-8.57 GHz. There is a good agreement between the simulated and measured results. The discrepancy at high frequencies may be attributed to the fabrication errors.

Figure 7 exhibits the measured and simulated far-field normalized radiation patterns for frequencies at 4, 7 and 9 GHz, respectively. From the figure, we can conclude that the proposed antenna features good quasi-omnidirectional radiation patterns in the H-plane and dipole-like radiation patterns in the E-plane. Meanwhile, the proposed antenna also achieves relatively low cross polarization. The simulated and measured gains of the antenna are shown in Fig. 8. It can be seen that the measured gain is flat in all operating bands, and it declines rapidly in the notched bands.

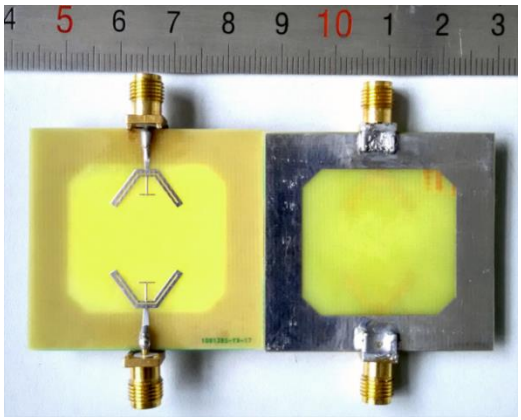

Fig. 5. Photograph of the fabricated antenna.

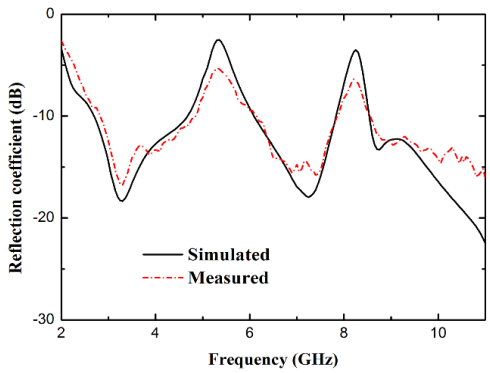

Fig. 6. Simulated and measured reflection coefficients of the proposed antenna.

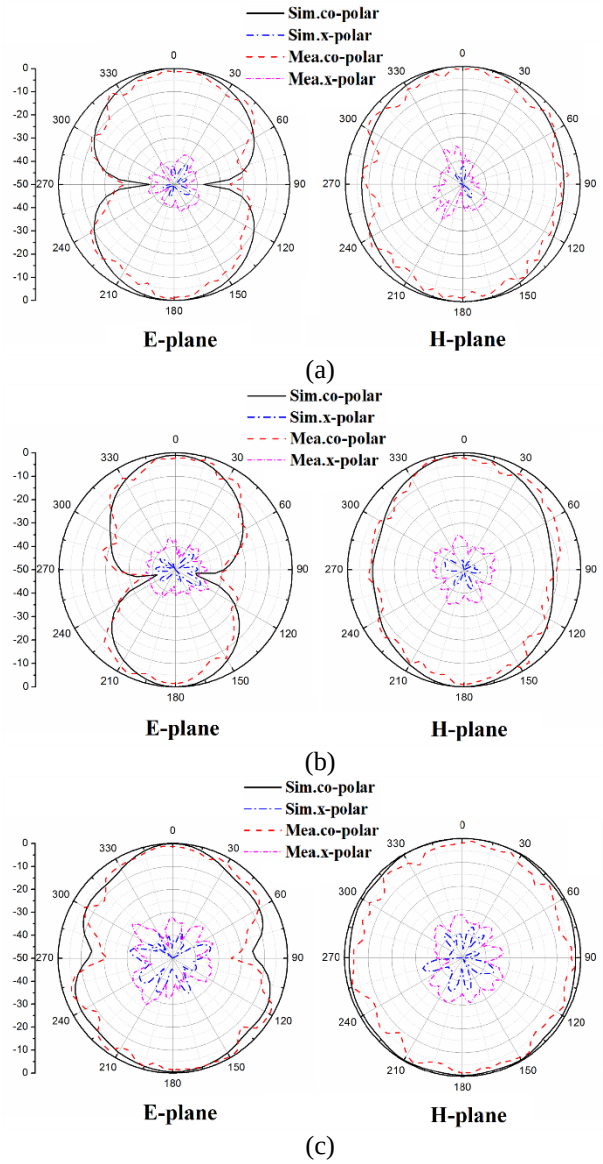

Fig. 7. Simulated and measured radiation patterns of the proposed antenna at (a) 4 GHz, (b) 7 GHz, and (c) 9 GHz.

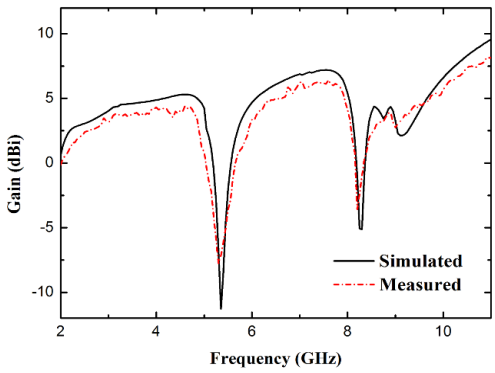

Fig. 8. Simulated and measured gains of the proposed antenna.

IV. CONCLUSION

A planar differential-fed ultra-wideband antenna with dual band-notched characteristics is proposed in this paper. To generate filtering behavior, the V-shaped slots and the T-shaped stubs are introduced in the antenna design. The obtained two notched bands of 4.83-6.12 GHz and 7.86-8.57 GHz can cover the 5.5 GHz WLAN and 8 GHz ITU bands. The antenna prototype has been designed, fabricated and tested. Measured results show reasonable agreement with simulated results, validating our design concept. Moreover, the proposed antenna features good radiation patterns, relatively low cross polarization and stable gain, which indicates it can be a good candidate for the UWB communication systems.

ACKNOWLEDGMENT

This work was supported by the National Natural Science Foundation of China (No. 61501340).

REFERENCES

[1] J. J. Liu, S. S. Zhong, and K. P. Esselle, "A printed elliptical monopole antenna with modified feeding structure for bandwidth enhancement," *IEEE Trans. Antennas Propagat.*, vol. 59, no. 2, pp. 667-670, Feb. 2011.

[2] A. K. Gautam, S. Yadav, and B. K. Kanaujia, "A CPW-fed compact UWB microstrip antenna," *IEEE Antennas Wireless Propagat. Lett.*, vol. 12, pp. 151-154, 2013.

[3] K. Song, Y. Z. Yin, B. Chen, and S. T. Fan, "Bandwidth enhancement design of compact UWB step-slot antenna with rotated patch," *Progress In Electromagnetics Research Letters*, vol. 22, pp. 39-45, 2011.

[4] M. N. Shakib, M. Moghavvem, and W. N. L. Mahadi, "Design of a compact planar antenna for ultra-wideband operation," *Applied Computational Electromagnetics Society (ACES) Journal*, vol. 30, no. 2, pp. 222-229, Feb. 2015.

[5] L. Wang, W. Wu, X. W. Shi, F. Wei, and Q. L.

Huang, "Design of a novel monopole UWB antenna with a notched ground," *Progress In Electromagnetics Research C*, vol. 5, pp. 13-20, 2008.

[6] G. P. Gao, B. Hu, and J. S. Zhang, "Design of a miniaturization printed circular-slot UWB antenna by the half-cutting method," *IEEE Antennas Wireless Propagat. Lett.*, vol. 12, pp. 567-570, 2013.

[7] Q. Wu, R. H. Jin, J. P. Geng, and M. Ding, "Printed omni-directional UWB monopole antenna with very compact size," *IEEE Trans. Antennas Propagat.*, vol. 56, no. 3, pp. 896-899, Mar. 2008.

[8] B. S. Yildirim, B. A. Cetiner, G. Roqueta, and L. Jofre, "Integrated bluetooth and UWB antenna," *IEEE Antennas Wireless Propagat. Lett.*, vol. 8, pp. 149-152, 2009.

[9] A. Foudazi, H. R. Hassani, and S. M. A. Nezhad, "Small UWB planar monopole antenna with added GPS/GSM/WLAN bands," *IEEE Trans. Antennas Propagat.*, vol. 60, no. 6, pp. 2987-2992, June 2012.

[10] M. Moosazadeh and Z. Esmati, "Simple and compact dual-notched monopole antenna using U-shaped forms on the conductor-backed plane for UWB applications," *Applied Computational Electromagnetics Society (ACES) Journal*, vol. 28, no. 11, pp. 1074-1079, Nov. 2013.

[11] N. Ojaroudi, M. Ojaroudi, and N. Ghadimi, "Square monopole antenna with band-notched characteristic for UWB communications," *Applied Computational Electromagnetics Society (ACES) Journal*, vol. 28, no. 8, pp. 712-718, Aug. 2013.

[12] K. S. Ryu and A. A. Kishk, "UWB antenna with single or dual band-notches for lower WLAN band and upper WLAN band," *IEEE Trans. Antennas Propagat.*, vol. 57, no. 12, pp. 3942-3950, Dec. 2009.

[13] J. W. Jang and H. Y. Hwang, "An improved band-rejection UWB antenna with resonant patches and a slot," *IEEE Antennas Wireless Propagat. Lett.*, vol. 8, pp. 299-302, 2009.

[14] M. Shokri, Z. Amiri, S. Asiaban, and B. Virdee, "Diamond shaped ring antenna for UWB applications with inherent band-notched functionality," *Applied Computational Electromagnetics Society (ACES) Journal*, vol. 29, no. 11, pp. 911-915, Nov. 2014.

[15] Y. Ojaroudi, N. Ojaroudi, N. Ghadimi, and S. Ojaroudi, "Design of UWB CPW-fed slot antenna with a band-stop notch using a parasitic strip on the substrate backside," *Applied Computational Electromagnetics Society (ACES) Journal*, vol. 29, no. 8, pp. 618-624, Aug. 2014.

[16] J. R. Kelly, P. S. Hall, and P. Gardner, "Band-notched UWB antenna incorporating a microstrip open-loop resonator," *IEEE Trans. Antennas Propagat.*, vol. 59, no. 8, pp. 3045-3048, Aug. 2011.

[17] A. Chen, C. Yang, Z. Chen, K. An, J. Fang, and W. Jiang, "A CPW-fed band-notched UWB antenna with T-shape construct and matching branches," *Applied Computational Electromagnetics Society (ACES) Journal*, vol. 29, no. 2, pp. 134-139, Feb. 2014.

[18] Y. Ojaroudi, S. Ojaroudi, and N. Ojaroudi, "An UWB microstrip-fed slot antenna with enhanced bandwidth and WLAN band-notched characteristics," *Applied Computational Electromagnetics Society (ACES) Journal*, vol. 29, no. 9, pp. 685-691, Sep. 2014.

[19] M. Yazdi and N. Komjani, "Design of a band-notched UWB monopole antenna by means of an EBG structure," *IEEE Antennas Wireless Propagat. Lett.*, vol. 11, pp. 170-173, 2011.

[20] W. J. Lui, C. H. Cheng, and H. B. Zhu, "Compact frequency notched ultra-wideband fractal printed slot antenna," *IEEE Microw. Wireless Compon. Lett.*, vol. 26, no. 7, pp. 481-483, July 2016.

[21] J. H. Wang and Y. Z. Yin, "Ultra-wideband (UWB) differential-fed antenna with improved radiation patterns," *Progress In Electromagnetics Research C*, vol. 53, pp. 1-10, 2014.

[22] M. J. Li and K. M. Luk, "A differential-fed magneto-electric dipole antenna for UWB applications," *IEEE Trans. Antennas Propagat.*, vol. 61, no. 1, pp. 92-99, Jan. 2013.

[23] Z. H. Tu, W. A. Li, and Q. X. Chu, "Single-layer differential CPW-fed notch-band tapered-slot UWB antenna," *IEEE Antennas Wireless Propagat. Lett.*, vol. 13, pp. 1296-1299, 2014.

[24] W. R. Eisenstadt and B. M. Thompson, *Microwave Differential Circuit Design Using Mixed-Mode S-Parameters*. Artech House, 2006.

Wei Hu received the B.S. and Ph.D. degrees in Electromagnetic Fields and Microwave Technology from Xidian University, Xi'an, China, in 2008 and 2013, respectively. He is currently a Lecturer with the National Laboratory of Science and Technology on Antennas and Microwaves, Xidian University, Xi'an, China.

His research interests include multiband antennas, UWB antennas, dual-polarized antennas, reconfigurable antenna and MIMO technologies.

Zhaoyang Tang received the B.S. and M.S. degrees from Xidian University, Xi'an, China, in 2013 and 2016, respectively. He is currently pursuing the Ph.D. degree in Electromagnetic Field and Microwave Technology from the National Laboratory of Science and Technology on Antennas and Microwaves, Xidian University, Xi'an, China.

His research interests include multiband antennas, UWB antennas, and antennas for base stations.

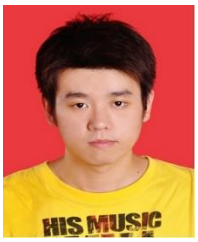

Lixue Zhou received the M.S. degree in Electromagnetic Fields and Microwave Technology from Nanjing University of Science and Technology, Nanjing, China, in 2010. He is now working toward the Ph.D. degree in the Electrical Engineering department of Xidian University, Xi'an, China.

His research interests include microwave and millimeter-wave planar type circuit and multilayered circuit design and planner filter design in microwave and millimeter-wave frequency band.

Yingzeng Yin received the B.S. degree and the M.S. degree and Ph.D. degree in Electromagnetic Wave and Microwave Technology from Xidian University, Xi'an, China, in 1987, 1990 and 2002, respectively. From 1990 to 1992, he was a Research Assistant and an Instructor at The Institute of Antennas and Electromagnetic Scattering, Xidian University. From 1992 to 1996, he was an Associate Professor in the Department of Electromagnetic Engineering, Xidian University. Since 2004, he has been a Professor at Xidian University.

His research interests include design of microstrip antennas, feeds for parabolic reflectors, artificial magnetic conductors, phased array antennas, and computer aided design for antennas.

PSO Algorithm Combined with Parallel Higher-Order MoM to Compensate the Influence of Radome on Antennas

Chang Zhai [1], Xunwang Zhao [1], Yong Wang [1], Yu Zhang [1], and Min Tian [2]

[1] Key Laboratory of Antennas and Microwave Technology
Xidian University, Xi'an 710071, China
xwzhao@mail.xidian.edu.cn

[2] National Supercomputer Center in Jinan
Jinan 250101, China

Abstract ─ For the design and optimization of radome-enclosed antenna arrays, a fast numerical optimization algorithm is proposed to compensate the distortion error of radome-enclosed antenna arrays by correcting amplitude and phase of the excitations. Higher-order method of moments (MoM) is used to extract the eigen solution for each antenna element. In combination with the particle swarm optimization (PSO) algorithm, the antenna radiation characteristics can be quickly obtained by updating feeds, which avoid the repeated solution of the MoM matrix equation in the optimization process. Meanwhile, in the process of the eigen solution extraction, the use of the parallel technique significantly accelerates the solving of matrix equation. Finally, a radome-enclosed antenna array with 247,438 unknowns was optimized as an example, and the numerical results demonstrate effectiveness of the method.

Index Terms ─ Parallel algorithms, particle swarm optimization, radome-enclosed antenna array, the eigen solution.

I. INTRODUCTION

Due to good protectiveness and penetrability of electromagnetic wave, radome-enclosed antennas are widely used in many fields, such as aviation, ship-borne radars and base-station antennas. However, there exists distortion of radiation patterns of antennas when electromagnetic wave gets through the radome, producing error relative to the sighting axis (called as bore sight error (BSE)) [1]. Meanwhile the radiating wave of an antenna can be absorbed and reflected by the radome, which changes the energy distribution of the antenna in free space and destroy its electrical properties. Aiming at BSE and pattern aberrance, a lot of methods have been used to regulate patterns in the design, such as processing antennas, grinding the radome, and adjusting the downtilt. The fundamental method remains making rational optimization and adjustment of the antenna characteristics at the initial stage of the design. The mainly used approach is to optimize and adjust physical properties like materials, sizes and so on, to get the desired results [2, 3]. However, the sizes and materials of most radome-enclosed antennas are relatively fixed due to its practical purposes. Therefore, an alternative optimization method, optimizing amplitude and phase of feeds, gradually becomes popular [4]. With antenna structures and materials becoming more and more complex, it is very difficult for commercial software to compute and analyze antennas. Although fast methods such as fast multipole method (FMM) can be used, the computing time may be extremely long. It is well known that optimization algorithms need plenty of iterations, in which FMM needs repeated solution of matrix equations due to its iterative nature, and thus the use of FMM may take a very long time and is hard to optimize large radome-enclosed antennas.

To solve the problem, this paper adopts the eigen solution extraction technique, utilizing method of moments (MoM) to extract the eigen solution for each antenna array element and computing radiation patterns of the antenna array by using linear combination of the eigen solution. The LU (lower/upper) decomposition based direct solver is used to solve MoM matrix equations. The matrix needs to be factorized only once, and is reused to extract the eigen solution. Through rapid combination of the eigen solution, new radiation patterns of the antenna array is obtained. The proposed method solves the problem that the time is too long for each round of optimization and greatly enhances optimizing efficiency.

MoM is a numerically accurate method for analysis of electromagnetic field [5]. However, given a large dense matrix generated by MoM, electrically large problems can hardly be computed. To reduce the number of unknowns and matrix size, higher-order polynomial basis functions are employed in MoM, and moreover, the parallel computing technique is utilized to further

Submitted On: September 19, 2016
Accepted On: January 28, 2017

improve the method. In the previous works, the method was used to accurately simulate large electromagnetic models [6–8].

Comparing to traditional optimizing methods, the particle swarm optimization (PSO) algorithm is widely used in the antenna design as a new evolutionary algorithm [10]. It's a kind of bionic algorithms and originates from the research of the predation of birds, with characteristics of easy implementation, high precision and fast convergence. Its main idea is to use the sharing of individual information in the population and then make the whole population orderly movement to find the optimal solution. The inertia weight factor ω in this algorithm has the feature of controlling searching ability. The larger ω is, the stronger the global searching ability is. The small ω is, the stronger the local searching ability is [9]. Based on this feature, references [11, 12] propose a self-adaptive PSO algorithm to overcome the defect that the PSO algorithm is easy to fall into local optimum.

This paper presents a method of using the eigen solution extraction technique to accelerate optimization, adopts self-adaption PSO and parallel higher-order MoM to optimize the performance of radome-enclosed antennas. This method realizes efficient optimization by using the eigen solution extraction technique to avoid repeated solution of MoM matrix equations, obtaining accurate results compared with the traditional optimized patterns. The effectiveness of the proposed method is verified by using the Tianhe-2 supercomputer to optimize a radome-enclosed antenna array with 247,438 unknowns.

II. ANALYSIS OF THE OPTIMIZATION METHOD FOR COMPENSATING RADOME

A. Influence of radome on the electrical performance of antennas

The influence of radome on the system of radome-enclosed antennas can be divided into two categories: the first-order influence and the second-order influence. The first-order influence factors include the uneven insert transmission coefficient, the field strength transmission coefficient and the surface wave generated by the incident wave on the surface of radome. These changes mainly affect the variation of antenna pattern, and lead to the reduction of maximum gain, the null depth of difference beam increase, the side lobe level rise, the main beam deformation and so on. The main cause of the second-order influence is the second-reflected wave and the reflection wave generated by the radome wall. This mainly results in the generation of BSE and the change of VSWR.

There are two main factors caused the error of radome-enclosed antenna systems. On the one hand, it is due to the shape of radome, the material (such as dielectric constant, conductivity), and the relative position of radome and antenna. On the other hand, it is caused by the non-uniformity of the feed's phase and amplitude, which is the object of main analysis in the design of radome-enclosed antennas. It is assumed that radome-enclosed antennas have N performance parameters to optimize. The n-th can be expressed as follow:

$$F_n = F_n(S, E, \theta, f) \qquad n = 1, 2, \ldots, N, \tag{1}$$

where S is radome material and structural parameters, in most cases, it has been determined in practical design. E is excitation parameters of array antenna. $\theta \in \Theta$ is antenna pointing and $\Theta=[\theta_{\min}, \theta_{\max}]$. $f \in \Gamma$ is the working frequency.

When θ, f and S are determined, it can be optimized by E that further enhances the performance of radome-enclosed antennas. Such problems can be summarized in the following form:

$$\begin{cases} \min\ Z = \sum_{i=1}^{N} F_i(E)\omega_i \\ \text{Subject to } A_i \le F_i(E) \le B_i \qquad i = 1, 2, \ldots, N, \\ E = [e_1\ e_2\ \ldots\ e_m]^T \end{cases} \tag{2}$$

where A_i, B_i are the upper and lower limits of the range of performance parameter F_i. e_m represents the amplitude and phase characteristics of each feed. ω_i is the weight factor that can eliminate radome affect by selecting appropriate value.

In this paper, a linear decreasing inertia weight PSO algorithm, which is proposed by Eberhart [13], is used to optimize the radome-enclosed antennas. This method not only has the advantages of standard PSO algorithm with easy realization, high accuracy, fast convergence properties and other characteristics, but also overcome the problems of premature convergence and slow convergence rate in the later period of the optimization. Meanwhile it makes good effect on the multidimensional discrete problem such as antenna design.

B. Extracting the eigen solution by MoM

The MoM matrix equation can be written as follows:

$$\begin{bmatrix} Z_{11} & Z_{12} & \cdots & Z_{1n} \\ Z_{21} & Z_{22} & \cdots & Z_{2n} \\ \vdots & \vdots & \ddots & \vdots \\ Z_{n1} & Z_{n2} & \cdots & Z_{nn} \end{bmatrix} \cdot [I] = \begin{bmatrix} V_1 \\ V_2 \\ \vdots \\ V_n \end{bmatrix}. \tag{3}$$

For the antenna radiation problem, the excitation V_i on the right side of the matrix equation is the ith feed. When all the units are fed, radiation characteristics of the antenna can be quickly obtained after solving the current coefficient I in the (3). Since the matrix equation is a linear equation, the excitation vector on the right side of

the equation can be divided into the superposition of n units:

$$\begin{bmatrix} Z_{11} & Z_{12} & \cdots & Z_{1n} \\ Z_{21} & Z_{22} & \cdots & Z_{2n} \\ \vdots & \vdots & \ddots & \vdots \\ Z_{n1} & Z_{n2} & \cdots & Z_{nn} \end{bmatrix} \cdot \left([I_1] + [I_2] + \cdots + [I_n] \right) = \left(\begin{bmatrix} V_1 \\ 0 \\ \vdots \\ 0 \end{bmatrix} + \begin{bmatrix} 0 \\ V_2 \\ \vdots \\ 0 \end{bmatrix} + \cdots + \begin{bmatrix} 0 \\ 0 \\ \vdots \\ V_n \end{bmatrix} \right), \quad (4)$$

where I_i is the current coefficient corresponding to the i-th unit feed in (4). Then it can be written as a matrix equation when an arbitrary unit is excited, the form is as follows:

$$\begin{bmatrix} Z_{11} & Z_{12} & \cdots & Z_{1n} \\ Z_{21} & Z_{22} & \cdots & Z_{2n} \\ \vdots & \vdots & \ddots & \vdots \\ Z_{n1} & Z_{n2} & \cdots & Z_{nn} \end{bmatrix} \cdot [I_i] = \begin{bmatrix} 0 \\ V_i \\ \vdots \\ 0 \end{bmatrix}. \quad (5)$$

In (5), if V_i=1, the eigen solution $\tilde{I}_i$ of the ith unit can be obtained:

$$[\tilde{I}_i] = \begin{bmatrix} Z_{11} & Z_{12} & \cdots & Z_{1n} \\ Z_{21} & Z_{22} & \cdots & Z_{2n} \\ \vdots & \vdots & \ddots & \vdots \\ Z_{n1} & Z_{n2} & \cdots & Z_{nn} \end{bmatrix}^{-1} \cdot \begin{bmatrix} 0 \\ 1 \\ \vdots \\ 0 \end{bmatrix}. \quad (6)$$

Since the matrix equation is linear, the solution of MoM with any excitation can be obtained by the linear combination of the eigen solution as long as the eigen solution for each unit is obtained. It can be seen that the impedance matrix is constant when the eigen solution is solved in (6), that is to say, it only needs to solve the inverse matrix at once. Accordingly, the calculation of the eigen solution does not significantly increase the computation. For any combination of feed (V_1, V_2, …, V_n), the corresponding MoM solution is as follow:

$$[I] = \sum_{i=1}^{n} V_i [\tilde{I}_i]. \quad (7)$$

The extraction of the eigen solution brings great convenience for optimizing of the feed. The optimize algorithm only need to update the feed (V_1, V_2, …, V_n) and to quickly combine the response of this feed, and then the radiation characteristics of the antenna with this feed can be calculated.

III. INTRODUCTION OF THE COMPUTING PLATFORM

The computing platform used in this paper is Tianhe-2 supercomputer at the National Super Computer Center in Guangzhou, which was ranked No. 1 among the World's TOP500 Supercomputers with 33.86 PFlop/s Linpack performance. It has 16,000 nodes, each of which contains two 12-core Xeon E5 CPU and 64 GB memory. In the following section, 20 nodes with 480 cores are used.

IV. OPTIMIZATION EXAMPLE AND ANALYSIS

The reliability and accuracy of the higher-order MoM has been verified in the literature [6–8, 14], and the literature [2, 3] has verified the feasibility of the PSO algorithm to optimize the two-dimensional radome-enclosed antennas.

To illustrate the validity of the proposed method, a radome-enclosed antenna array is optimized, as shown in Fig. 1. The height of the radome is 1500 mm, the bottom radius is 450 mm, and the thickness is 32.275 mm. The dielectric constant of the radome is 2.4, and the loss tangent is 0.015. The microstrip antenna array has 10×10 elements and works at 3.0 GHz. The distance between neighboring elements along x direction and y direction are 0.46 λ and 0.65 λ, respectively, as shown in Fig. 1 (b). Each microstrip element consists of a pair of patches with the sizes of 0.33 λ×0.14 λ×0.02 λ, as shown in Fig. 1 (c). Parallel higher-order MoM running on 480 CPU cores is used to simulate the model, which generates 247,438 unknowns.

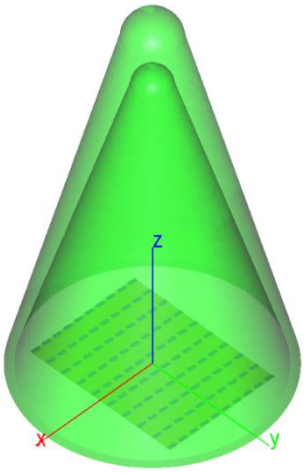

(a)

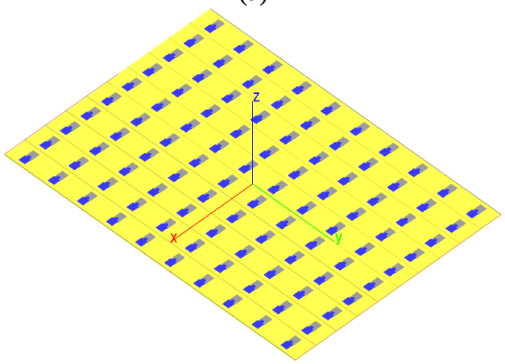

(b)

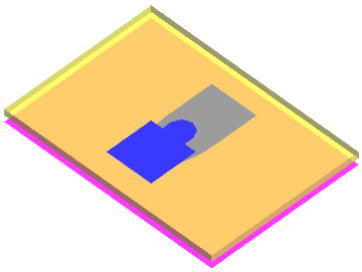

(c)

Fig. 1. Radome-enclosed microstrip antenna array: (a) the whole model, (b) the 10×10 microstrip antenna array, and (c) the microstrip element.

The excitation of the antenna array is in the form of –30 dB Taylor distribution with a phase shift that makes the mainlobe point to the direction of $\phi = 0^\circ$ and $\theta = 20^\circ$, as listed in Table 1. Figure 2 (a) shows the three-dimensional (3D) difference-beam patterns of the radome-enclosed antenna array before optimization and Fig. 3 shows the patterns in the mainlobe cut plane. It can be seen that, the maximum gain of the radome-enclosed antenna array before optimization is 16.63 dB and the null depth of difference beam is 15.205 dB, which deteriorates compared with the pattern of the original antenna array without the radome.

Then the influence of the radome on the pattern is compensated through optimizing the excitation amplitude and phase. The optimized design specifications are as follows: the maximum gain is greater than 17 dB, and the null depth of difference beam is larger than 20 dB. Set the particle number to 5, the iterations number to 1000, c_1 and c_2 to 2.0, and the weight factor range to [0.4, 0.8]. The optimized excitation is also listed in Table 1. The pattern after optimization is shown in Fig. 2 (b) and Fig. 3. It is obvious that, the maximum gain of the radome-enclosed antenna array after optimization is 17.66 dB and the null depth of difference beam is 21.76 dB, which meet the design requirements. The computation time is given in Table 2, and the matrix equation solving procedure involves the matrix factorization and the extraction of the eigen solution. During extracting the eigen solution for each array element, the factored matrix is reused and thus the method significantly saves time compared with iterative based methods, such as FMM. When the eigen solution is obtained, the PSO algorithm is carried out on an ordinary desktop computer, because it needs much fewer computational resources than the matrix equation solving procedure.

Besides null depth of difference beam, electromagnetic parameters of antennas, such as front-to-back ratio and the average sidelobe level, can also be optimized by using the proposed method.

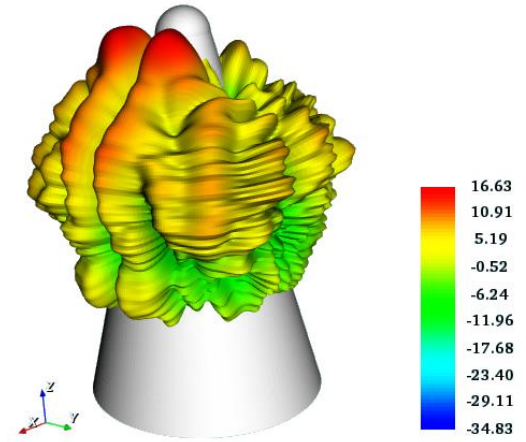

(a)

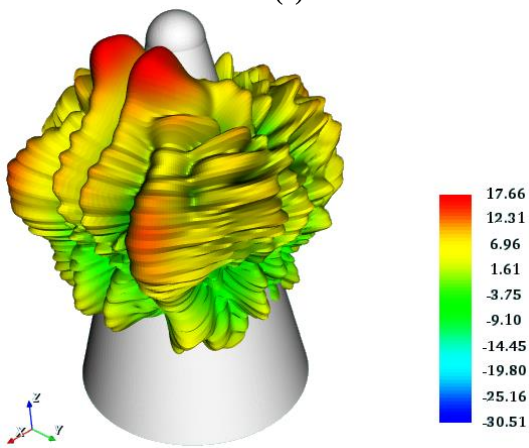

(b)

Fig. 2. 3D difference-beam patterns of the radome-enclosed antenna array: (a) before and (b) after optimization.

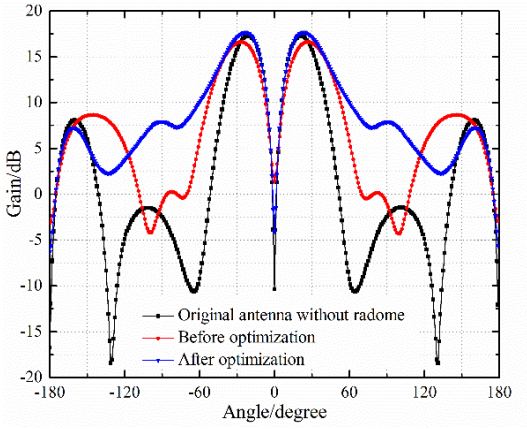

(a)

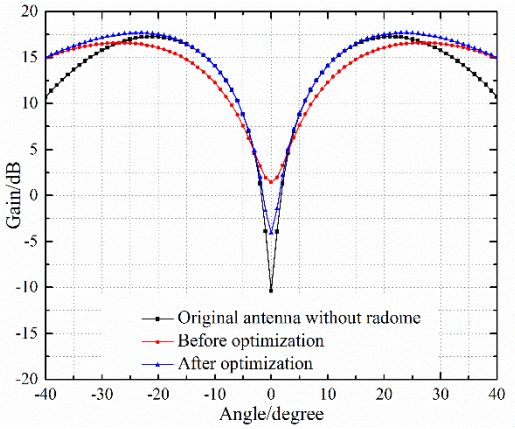

(b)

Fig. 3. Difference-beam patterns in the mainlobe cut plane before and after optimization: (a) angle range [–180°, 180°] and (b) angle range [–40°, 40°].

Table 1: Excitations of the radome-enclosed antenna array before and after optimization

No.	Initial Amplitude (V)	Initial Phase (°)	Optimized Amplitude (V)	Optimized Phase (°)
1	0.08936	0	0.06507	-79.97183
2	0.13349	0	0.26866	5.31126
3	0.20333	0	0.22841	3.54343
4	0.26381	0	0.04087	18.5360
5	0.29892	180	0.38811	-8.33680
6	0.29892	180	0.38811	171.66319
7	0.26381	180	0.04087	-161.46396
8	0.20333	180	0.22841	-176.45657
…	…	…	…	…
94	0.26381	-161.68642	0.34793	179.92870
95	0.29892	-161.68642	0.37986	-146.17421
96	0.29892	18.31366	0.37986	33.82578
97	0.26381	18.31369	0.34793	-0.07131
98	0.20333	18.31369	0.21166	24.92824
99	0.13349	18.31369	0.33065	7.35495
100	0.08936	18.31369	0.07010	11.13298

Table 2: Time for optimization of the radome-enclosed antenna array

Matrix Filling (s)	Matrix Equation Solving (s)	Optimization Iteration (s)	Total (s)
756.8	7619.2	4988.0	13,363.9

V. CONCLUSION

In this paper, a new method, which is based on the eigen solution extraction technique and combined with the adaptive PSO and the parallel higher-order MoM, is proposed to solve the optimization problem of large-scale radome-enclosed antennas. Compared with the traditional radome-enclosed antenna optimization method, the proposed method gives a new way to optimize radome-enclosed antennas. By using the eigen solution extraction technique, a large number of repeated computations are avoided in the process of optimization, which greatly accelerates the optimization. Moreover, the parallel higher-order MoM ensures that this method is capable of accurately solving electrically large problems and the adaptive PSO algorithm eliminates the problem of premature convergence in the optimization process. Numerical results demonstrate that the method is suitable for large-scale radome-enclosed antenna optimization problems and it provides a new research idea for the optimization of airborne antennas.

ACKNOWLEDGMENT

This work is supported by the program of International S&T Cooperation (2016YFE0121600), the NSFC (61301069), the program for New Century Excellent Talents in University of China (NCET-13-0949), the Fundamental Research Funds for the Central Universities (JB160218), and the National High Technology Research and Development Program of China (863 Program) (2012AA01A308), and by the Special Program for Applied Research on Super Computation of the NSFC-Guangdong Joint Fund (the second phase).

REFERENCES

[1] W. Xu, B. Y. Duan, P. Li, N. Hu, and Y. Qiu, "Multiobjective particle swarm optimization of boresight error and transmission loss for airborne radomes," *IEEE Trans. Antennas Propagat.*, vol. 62, no. 11, pp. 5880-5885, Nov. 2014.

[2] H. Chiba, Y. Inasawa, H. Miyashita, and Y. Konishi, "Optimal radome design with particle swarm optimization," *Proc. IEEE Int. Symp. Antennas Propag.*, San Diego, CA, pp. 1-4, July 2008.

[3] H. Meng, W. Dou, and K. Yin, "Optimization of radome boresight error using genetic algorithm," *China-Japan Joint Microwave Conference*, Shanghai, pp. 27-30, Sept. 2008.

[4] W. Wang, G. Wan, L. Wang, and J. Shen, "Fast optimization of radome boresight error based on array elements phase regulation," *Chinese Journal of Radio Science*, vol. 30, no. 3, pp. 470-475, 2015.

[5] R. F. Harrington, *Field Computation by Moment Method*. IEEE Press, New York, 1993.

[6] Y. Zhang, Z. Lin, X. Zhao, and T. K. Sarkar, "Performance of a massively parallel higher-order method of moments code using thousands of CPUs and its applications," *IEEE Trans. Antennas Propag.*, vol. 62, no. 12, pp. 6317-6324, Dec. 2014.

[7] W.-H. Ge, Z.-F. LV, X.-W. Zhao, Y. Yan, Y. Zhang, and H. Qu, "Simulation of a microstrip array antenna using parallel higher-order MoM,"

IET International Radar Conference, Xi'an, pp. 1-4, Apr. 2013.

[8] Y. Zhang, Z.-C. Lin, Z.-N. Yang, W.-H. Ge, X.-W. Zhao, and H. Zhao, "Simulations of airborne phased array using parallel MoM," *IET International Radar Conference*, Xi'an, pp. 1-4, Apr.2013.

[9] J. Jiang, M. Tian, X. Wang, X. Long, and J. Li, "Adaptive particle swarm optimization via disturbing acceleration coefficients," *Journal of Xidian University*, vol. 39, no. 4, pp. 93-101, Aug. 2012.

[10] J. Robinson and Y. Rahmat-Samii, "Particle swarm optimization in electromagnetics," *IEEE Trans. Antennas Propag*., vol. 52, no. 2, pp. 397-407, Feb. 2004.

[11] C.-H. Hsu, C.-H. Chen, W.-J. Shyr, K.-H. Kuo, Y.-N. Chung, and T.-C. Lin, "Optimizing beam pattern of linear adaptive phase array antenna based on particle swarm optimization," *International Conference on Genetic and Evolutionary Computing*, Shenzhen, pp. 586-589, Dec. 2010.

[12] J.-W. Li, Y.-M. Cheng, and K.-Z. Chen, "Chaotic particle swarm optimization algorithm based on adaptive inertia weight," *Chinese Control and Decision Conference*, Changsha, pp. 1310-1315, June 2014.

[13] R. C. Eberhart and Y. Shi, "Comparing inertia weights and constriction factors in particle swarm optimization," *Proceedings of the 2000 Congress on Evolutionary Computation*, La Jolla, CA, vol. 1, pp. 84-88, July 2000.

[14] Z. Lin, Y. Chen, Y. Zhang, S. Jiang, X. Zhao, and Z. LV, "Study of parallel higher-order MoM on a domestically-made CPU platform," *Journal of Xidian University*, vol. 42, no. 3, pp. 43-47, June 2015.

Two Dimensional Frequency-Angle Domain Adaptive Combined Interpolation Method for Electromagnetic Scattering Analysis of Precipitation Particles

Jiaqi Chen [1,2,3], Jianan Lin [1], Zhiwei Liu [4], Ning Li [3], Ping Ping [1], and Xuewei Ping [1]

[1] College of Computer and Information Engineering
Hohai University, Nanjing, 210098, China
cjq19840130@163.com, linjianannuli@163.com, pingpingnjust@163.com, xwping@hhu.edu.cn

[2] State Key Laboratory of Millimeter Wave
Southeast University, Nanjing, 210096, China

[3] Department of Space Microwave Remote Sensing System, Institute of Electronics
Chinese Academy of Sciences, Beijing, 100190, China
lining_nuaa@163.com

[4] School of Information Engineering
East China Jiaotong University, Nanchang, 330013, China
zwliu1982@hotmail.com

Abstract ─ A combined 2-D interpolation method is proposed for the efficient electromagnetic scattering analysis of precipitation particles over a broad frequency and angular band. This method combines the cubic spline interpolation method and the Steor-Bulirsch model. The cubic spline interpolation method is applied to model the induced current over wide angular band. The Steor-Bulirsch model is applied to accelerate calculation over wide frequency band. In order to efficiently compute electromagnetic scattering, sparse-matrix/canonical grid method (SM/CG) is applied to accelerate the matrix vector multiplication in EFIE. Therefore, the calculation time of frequency and angular sweeps become shorter. Numerical results demonstrate that this combined method is efficient for wide-band scattering calculation of precipitation particles with high accuracy.

Index Terms ─ Electromagnetic scattering, frequency-angle domain interpolation, precipitation particles, sparse-matrix/canonical grid method.

I. INTRODUCTION

In recent years, for environmental applications in remote sensing, the research on characterization of the electromagnetic wave interaction with complex rainfall particles has become more and more important [1-4]. Several analytical methods based on wave theory, such as quasi-crystalline approximation, are frequently used [5]. However, these approaches are not able to capture the essential physics of many real world problems [6]. Alternatively numerical technologies can be used to deal with scattering of complex rainfall particles, for instance, the method of moment (MoM) [7]. While the MoM can provide accurate solution of complex media scattering [8-9], the main disadvantages of MoM are significant calculation time and large memory requirements for the storage of impedance matrix. In order to alleviate these bottlenecks, a series of accelerate methods are proposed, such as fast multiple method (FMM) [10], as well as sparse-matrix/canonical grid (SM/CG) [11] method, which is proposed as an efficient method for calculating the scattering from three-dimensional dense media [12-13].

The radar cross section (RCS) contains both frequency and angle information simultaneously. In many practical applications, it is desirable to predict the monostatic RCS of a target in both the frequency domain and spatial domain simultaneously. Although the computational complexity and memory requirement can be reduced by the SM/CG method, we still have to repeat the calculations at each frequency or angle of interest to obtain the RCS over a wide frequency-angle band. In order to alleviate this difficulty, many interpolation methods have been proposed and applied for acceleration, such as the asymptotic waveform evaluation (AWE) [14] method and the model-based parameter estimation (MBPE) [15] method. However,

Submitted On: May 21, 2016
Accepted On: January 28, 2017

there are difficulties in implementing these methods. For the widely used AWE [16], sometimes it is difficult to obtain the derivatives of the impedance matrix and the induced current vector. Singularity problem is the main weakness of the MBPE method [15] as it needs matrix inversion to get the coefficients of the substitute model.

In this paper, we investigate a novel adaptive frequency-angle domain interpolation method based on Stoer-Bulirsch model [17-19] and cubic spline algorithm [20], combined with SM/CG method for fast analysis of precipitation particles scattering over broad frequency-angle band. In frequency domain, two approximate rational function models are required in Stoer-Bulirsch algorithm for each iterative step. Both models could be constructed by using functions with the same set of samples. With the increase of samples, the difference between the two models will decrease. Therefore, when the termination criterion is achieved, both of approximate models could be used as the interpolation model for final results. In angle domain, cubic Hermite interpolation formulation is the basic model of cubic spline (CS) method, which utilizes the information of C1-continuous to evaluate the first derivative of the incident current vector instead of solving the large linear equations. Compared to traditional extrapolation or interpolation methods, such as AWE and MBPE, this novel method needs no matrix inversion and avoids calculating derivatives. This advantage and SM/CG combined together virtually yield an extremely efficient technique that seems something of a novelty compared to both AWE and MBPE method.

This paper is structured as follows. In Section II we describe the EFIE formulation and the SM/CG method. Section III describes the basic theory of the novel combined 2-D adaptive interpolation method based on cubic spline interpolation method in angle domain and Stoer-Bulirsch model in frequency domain with coarse-to-fine hierarchy. Numerical results which demonstrate the accuracy and efficiency of the proposed method are given in Section IV. Conclusions and comments are provided in Section V.

II. EFIE FORMULATION AND SM/CG METHOD

When a finite body of arbitrary shape, with permittivity $\varepsilon(\mathbf{r})$ and conductivity $\sigma(\mathbf{r})$, is exposed in free space to a plane electromagnetic wave, the induced current could be accounted for by replacing the body with an equivalent free-space current density $\boldsymbol{J}_{\mathrm{eq}}$, which can be written as:

$$\boldsymbol{J}_{eq} = \left[\sigma(\mathbf{r}) + j\omega\left(\varepsilon(\mathbf{r}) - \varepsilon_0\right)\right]\boldsymbol{E}(\mathbf{r}) = \tau(\mathbf{r})\boldsymbol{E}(\mathbf{r}). \quad (1)$$

The conduction current is the first term of (1), whereas the second term represents the polarization current. ε_0 is the free-space permittivity and $\boldsymbol{E}(\mathbf{r})$ is the total electric field inside the body. According to reference [9], the scattered field $\boldsymbol{E}^{\mathrm{s}}$ at an arbitrary point inside the body can be expressed as:

$$\boldsymbol{E}^s(\mathbf{r}) = pv\int_V \boldsymbol{J}_{eq}(\mathbf{r}')\cdot\overline{\overline{\boldsymbol{G}}}(\mathbf{r},\mathbf{r}')dV' - \frac{\boldsymbol{J}_{eq}(\mathbf{r})}{3j\omega\varepsilon_0}, \quad (2)$$

where $\mathbf{r}'$ denotes a source point, and $\mathbf{r}$ denotes a field point:

$$\overline{\overline{\boldsymbol{G}}}(\mathbf{r},\mathbf{r}') = -j\omega\mu_0\left[\overline{\overline{I}} + \frac{\nabla\nabla}{k_0^2}\right]\psi(\mathbf{r},\mathbf{r}'), \quad (3)$$

$$\psi(\mathbf{r},\mathbf{r}') = \frac{\exp(-jk_0|\mathbf{r}-\mathbf{r}'|)}{4\pi|\mathbf{r}-\mathbf{r}'|}. \quad (4)$$

In (4), $k_0=\omega(\mu_0\varepsilon_0)^{1/2}$and μ_0 is the permeability of free space. The symbol *pv* in (2) represents the principal value of the integral. The sum of the incident electric field $\boldsymbol{E}^{\mathrm{i}}$ and the scattering field $\boldsymbol{E}^{\mathrm{s}}$ can be written as:

$$\boldsymbol{E}(\mathbf{r}) = \boldsymbol{E}^i(\mathbf{r}) + \boldsymbol{E}^s(\mathbf{r}). \quad (5)$$

By substituting (2) into (5), the integral equation for $\boldsymbol{E}(\mathbf{r})$ can be demonstrated as:

$$\left[1 + \frac{\tau(\mathbf{r})}{3j\omega\varepsilon_0}\right]\boldsymbol{E}(\mathbf{r}) - pv\int_V \tau(\mathbf{r}')\boldsymbol{E}(\mathbf{r}')\cdot\overline{\overline{\boldsymbol{G}}}(\mathbf{r},\mathbf{r}')dV' = \boldsymbol{E}^i(\mathbf{r}), \quad (6)$$

where $\boldsymbol{E}^{\mathrm{i}}(\mathbf{r})$ is the known incident electric field, and $\boldsymbol{E}(\mathbf{r})$ is the unknown total electric field in (6). By using moment methods, (6) could be transformed into a matrix equation [9]:

$$\begin{bmatrix} [\boldsymbol{G}_{xx}] & [\boldsymbol{G}_{xy}] & [\boldsymbol{G}_{xz}] \\ [\boldsymbol{G}_{yx}] & [\boldsymbol{G}_{yy}] & [\boldsymbol{G}_{yz}] \\ [\boldsymbol{G}_{zx}] & [\boldsymbol{G}_{zy}] & [\boldsymbol{G}_{zz}] \end{bmatrix} \bullet \begin{bmatrix} [\boldsymbol{E}_x] \\ [\boldsymbol{E}_y] \\ [\boldsymbol{E}_z] \end{bmatrix} = -\begin{bmatrix} [\boldsymbol{E}_x^i] \\ [\boldsymbol{E}_y^i] \\ [\boldsymbol{E}_z^i] \end{bmatrix}. \quad (7)$$

In the following, we rewrite (7), let $\boldsymbol{G}$ denote the coefficient matrix in Equation (7), $\boldsymbol{E}=\{E_{\mathrm{n}}\}$, and $\boldsymbol{b}=\{E^{\mathrm{i}}_{\mathrm{m}}\}$ for simplicity. Then, the matrix Equation (7) can be symbolically rewritten as:

$$\boldsymbol{GE} = \boldsymbol{b}. \quad (8)$$

To employ sparse-matrix/canonical grid method (SM/CG) to accelerate the matrix vector multiplication, the whole structure is enclosed in a rectangular region at first and then we recursively subdivides it into small rectangular grids. The impedance matrix $\boldsymbol{G}$ is decomposed into the sum of a sparse matrix $\boldsymbol{G}^{\mathrm{s}}$ denoting the strong neighborhood interactions, which can be computed directly by MoM and a dense matrix $\boldsymbol{G}^{\mathrm{w}}$, denoting the weak far interactions:

$$\boldsymbol{G} = \boldsymbol{G}^{\mathrm{s}} + \boldsymbol{G}^{\mathrm{w}}. \quad (9)$$

The majority of computation of an iterative method is to perform the matrix-vector multiplication between $\boldsymbol{G}^{\mathrm{w}}$ and $\boldsymbol{E}$. We translate the original basis functions on the triangular elements to the rectangular grids in SM/CG. After we put Taylor expansion of the Green's functions [9] in here that the matrix $\boldsymbol{G}^{\mathrm{w}}$ is further written as:

$$\left[\boldsymbol{G}^{w}\right]=\sum_{i=0}^{K}\left[\boldsymbol{G}_{i}^{w}\right], \tag{10}$$

where K is the total number of terms of the expansion. Each term in the series corresponds to a Taylor series expansion term [11-12]. If the expansion order of Taylor series is selected too small, the uncertainty of calculation accuracy will be caused. However, when the expansion order is chosen too large, it will lead to a large consumption of computing resources, as well as calculation time. Through numerical experiments, the Taylor expansion order is chosen to be 2 in our experiment, as this choice is a tradeoff between accuracy and efficiency. Finally, the matrix-vector in SM/CG will be efficiently done using O(Nlog$N$) FFT-based methods, could be represented:

$$\left[\boldsymbol{G}^{w}\right]\boldsymbol{E}=\sum_{i}\left[\boldsymbol{T}_{ti}\right]\left[\boldsymbol{G}_{i}\right]\left[\boldsymbol{T}_{si}\right]\boldsymbol{E}. \tag{11}$$

Each term in the summation consists of a pre-multiplication of the current vector with a block-diagonal matrix [$\boldsymbol{T}_{si}$] followed by a multiplication with a block-Toeplitz matrix [$\boldsymbol{G}_i$] and a post-multiplication with another block-diagonal matrix [$\boldsymbol{T}_{ti}$].

III. TWO DIMENSIONAL ADAPTIVE COMBINED INTERPOLATION TECHNIQUE IN FREQUENCY-ANGLE DOMAIN

In wide frequency-angle band scattering analysis of precipitation particles, repeated solution of (8) is required at each incident direction and frequency. In order to improve efficiency, in this section, a novel combined 2-D adaptive interpolation technique is proposed to accelerate precipitation particles electromagnetic properties calculation. This adaptive strategy with the idea of coarse-to-fine hierarchy which considered as an iterative process is proposed to generate a set of nonuniform sampling nodes. There are two basic problems that need to be emphasized in the approach. One is how to keep the iterative process going on and the other is when to stop the process.

Both of problems are controlled by error. Correspondingly, there are two types of error that need to be defined. The error for judging whether or not more samples are required is called convergence error (CE), and the error used to locate the next possible sample is called maximum error (ME), which ensures a successively adaptive process. A good definition of CE leads to high precision and a good definition of ME leads to few samples.

A. Cubic spline method in angle domain

In angular domain, two interpolation models are applied, while one is linear interpolation model and the other is cubic spline interpolation model. The number of sampling nodes will be enough when linear model and cubic spline model obtain almost the same result. As a result, CE is defined as a tolerance between the two different models. The whole sampling process will end off until the error between the two models is smaller than CE.

Assuming that the sampling nodes in angular domain are $\varphi_0, \varphi_1, \ldots, \varphi_n$ which divide the whole range into several intervals. Within each interval such as $[\varphi_{i-1}, \varphi_i]$, $I(\varphi)$ could be expanded as a third-order polynomial on φ. According to Hermite interpolation theory [20], the interpolation formula of $I(\varphi)$ can be described as:

$$\begin{aligned} I(\varphi)=&\frac{(\varphi-\varphi_{i})^{2}\left[h_i+2(\varphi-\varphi_{i-1})\right]}{h_i^{3}}I(\varphi_{i-1})\\ &+\frac{(\varphi-\varphi_{i-1})^{2}\left[h_i+2(\varphi_i-\varphi)\right]}{h_i^{3}}I(\varphi_i)\\ &+\frac{(\varphi-\varphi_i)^{2}(\varphi-\varphi_{i-1})}{h_i^{2}}I'(\varphi_{i-1})+\frac{(\varphi-\varphi_{i-1})^{2}(\varphi-\varphi_i)}{h_i^{2}}I'(\varphi_i), \end{aligned} \tag{12}$$

where φ_i is the sampling point and $h_i=\varphi_i-\varphi_{i-1}$. Obviously, $I(\varphi_i)$ and $I'(\varphi_i)$ are needed in order to estimate the value of $I(\varphi)$ in the angle range $[\varphi_{i-1}, \varphi_i]$. Suppose the number of sampling points to be n, then n times of solution is needed to obtain the value of $I(\varphi_i)$ ($i=1,2,\ldots,n$), when another n times of solution is also required to get corresponding derivative value $I'(\varphi_i)$ ($i=1,2,\ldots,n$). Therefore, the times of solution of Equation (8) is $2n$ [20]. It is thus a waste of time to compute the first derivative of induced current vector of each sampling node.

Cubic-spline interpolation method applies another way to obtain the first derivative of each sampling node instead of solving the linear Equation (8) repeatedly [20]. This method just needs to compute the first derivative of φ_0 and φ_n by (1), which has been proved to be unnecessary. We can put them into zero under the natural boundary condition [20]. The first derivative of other sampling points are then given by:

$$\begin{bmatrix} 2 & \lambda_1 & & & \\ \mu_2 & 2 & \lambda_2 & & \\ & \ddots & \ddots & \ddots & \\ & & \mu_{n-1} & 2 & \lambda_{n-1} \\ & & & \mu_{n-1} & 2 \end{bmatrix}\begin{bmatrix} I'(\varphi_1) \\ I'(\varphi_2) \\ \vdots \\ I'(\varphi_{n-2}) \\ I'(\varphi_{n-1}) \end{bmatrix}=\begin{bmatrix} g_1-\lambda_1 I'(\varphi_0) \\ g_2 \\ \vdots \\ g_{n-2} \\ g_{n-1}-\mu_{n-1}I'(\varphi_n) \end{bmatrix}, \tag{13}$$

where

$$\lambda_i=\frac{h_{i+1}}{h_i+h_{i+1}},\quad \mu_i=\frac{h_i}{h_i+h_{i+1}},$$

and

$$g_i=3\left[\mu_i\frac{I(\varphi_{i+1})-I(\varphi_i)}{h_{i+1}}+\lambda_i\frac{I(\varphi_i)-I(\varphi_{i-1})}{h_i}\right].$$

Due to the large time consumed in calculating the derivative, the cubic-spline interpolation approach is able to reduce a great deal of cost in angular domain.

B. Store-Bulirsch algorithm in frequency domain

In frequency domain, the interpolation function is described in the form of a fractional polynomial function with numerator of order N and denominator of order D for the frequency f by:

$$S(f)=\frac{a_0+a_1 f+a_2 f^2+\ldots}{1+b_1 f+b_2 f^2+\ldots}=\frac{a_0+\sum_{n=1}^{N} a_n f^n}{1+\sum_{d=1}^{D} b_d f^d} S. \quad (14)$$

For given orders of N and D, the coefficients a_n and b_d can be determined from $k=N+D+1$ samples of $S(f)$ by solving a set of linear systems. The Store-Bulirsch algorithm does not require the inversion of matrix to get the coefficients of the rational function. The main idea of the algorithm is given as follows:

Suppose that there are a group of samples $(f_i, S(f_i))$, $i=1,\ldots,k$ available for obtaining a rational function interpolation of function value $S(f)$ at any $f \in (f_1,f_2)$, whereas the explicit expression of rational function is unknown. The recursive process of Store-Bulirsch algorithm starts with the initial condition:

$$R_{i,1}=S(f_i), i=1,\ldots,k, \quad (15)$$

which constructs the first column of the triangle table. Starting from the second column, all elements are obtained using a recursive formula associated with two or three elements in the preceding columns.

Store-Bulirsch algorithm provides two 'triangle rules':

$$R_{j,k}=\frac{(f-f_j)R_{j+1,k-1}+(f_{j+k}-f)R_{j,k-1}}{f_{j+k}-f_j}, \quad (16)$$

and

$$R_{j,k}=\frac{f_{j+k}-f_j}{\frac{f-f_j}{R_{j+1,k-1}}+\frac{f_{j+k}-f}{R_{j,k-1}}}, \quad (17)$$

and one 'rhombus rule':

$$R_{j,k}=R_{j+1,k-2}+\frac{f_{j+k}-f_j}{\frac{f-f_j}{R_{j+1,k-1}-R_{j+1,k-2}}+\frac{f_{j+k}-f}{R_{j,k-1}-R_{j+1,k-2}}}. \quad (18)$$

Based on these recursive rules, SB algorithm is organized as follow.

Let the whole frequency band to be defined from f_1 to f_2. The results recursively calculated by formula (16), (17), (18) are $S_1(f)$, $S_2(f)$, and $S_3(f)$ respectively. A testing point within the frequency band of interest is f_t and a sample is f_s. The true value from electromagnetic simulation or from experiment is denoted as $EM(f_s)$. In the interpolation process, a rational interpolation is implemented by using a distinct combination of the above three recursive rules. Pair one ((16) and (17)) and pair two ((16) and (18)) are alternately utilized to find the point at which the maximum sampling error occur, then add this sample into the sample group, until three recursive formulas, i.e., (16), (17) and (18), are sufficiently close to each other. In this paper, Equation (16) is used for interpolating frequency response at any given frequency f for final results. Specific algorithm steps are as follows.

Step 1: Set $f_{s1}=f_1$ and $f_{s2}=f_2$, and compute $EM(f_{s1})$ and $EM(f_{s2})$.

Step 2: Choose Equations (16) and (17) as the recursive formula and find the point at which the maximum sampling error occur, say at point f_{s3}, such that,

$$|S_1(f_{s3})-S_2(f_{s3})|=\max_i |S_1(f_{ti})-S_2(f_{ti})|. \quad (19)$$

Step 3: Compute $EM(f_{s3})$. If a given convergence error (CE) is larger than the sampling error in step 2, that is $|S_1(f_{s3})-S_2(f_{s3})|<CE$, then the process switches to step 6 for termination. Otherwise, add the sample $\{f_{s3}, EM(f_{s3})\}$ into the sample group and goes to next step for finding next samples.

Step 4: Change the recursive formula into (16) and (18), compare the sampling value at all testing points and find the point at which the maximum sampling error occurs, say at point f_{s4}, such that,

$$|S_1(f_{s4})-S_3(f_{s4})|=\max_i |S_1(f_{ti})-S_3(f_{ti})|. \quad (20)$$

Step 5: Compute $EM(f_{s4})$, if $|S_1(f_{s4})-S_3(f_{s4})|<CE$, it means that the samples obtained are enough for the sampling for rule (16). Then the process goes to step 6. Otherwise, add the point $\{f_{s4}, EM(f_{s4})\}$ into the sample group and go back to step 2 to find next samples.

Step 6: Suppose sufficient samples have been obtained for sampling. Saving the sample group $\{(f_{si}, EM(f_{si})), i=1,\ldots,N\}$, which is the only required knowledge for rational function interpolation, and N is the number of samples in the last step.

C. Two-dimensional combined adaptive interpolation technique

For a desired frequency domain and angular domain, Fig. 1 shows the adaptive process for 2-D combined interpolation technique in details. The coarse-to-fine hierarchy strategy is applied to carry out 2-D adaptive sampling. Compared to 1-D adaptive strategy which is applied to decide the sampling node, 2-D adaptive strategy is used to select the "sampling line". The dashed in Fig. 1 is the "sampling line" in adaptive sampling process, which divides the whole surface into many lattices. Specifically speaking, ME which defined by the difference between linear model and cubic spline model is applied to decide the location of "good sampling line" in angular domain, while Store-Bulirsch algorithm is utilized to obtain the location of "good sampling line" in frequency domain. As same as 1-D method, the process will end when there is no "sampling line" needed. When the value of CE is set appropriately, the meshing lines could avoid losing performance and

accuracy.

It is assumed that the whole surface is defined by $[f_1, f_m] \times [\varphi_1, \varphi_m]$. A testing point within the range of interest is (f_{t1}, φ_{t2}) and a sampling point is (f_{s1}, φ_{s2}). The incident current vector for (f, φ) is $I(f, \varphi)$ and the electromagnetic properties from EM simulation is denoted as rcs(f, φ).

Step 1: Initialize four sampling points, (f_1, φ_1), (f_1, φ_n), (f_m, φ_1) and (f_m, φ_n). Then acquire $I(f_1, \varphi_1)$, $I(f_1, \varphi_n)$, $I(f_m, \varphi_1)$ and $I(f_m, \varphi_n)$.

Step 2: Assume there are $m \times n$ samples on the whole surface, and the number of rows is m and the number of columns is n. Applying linear interpolation method to obtain the approximate surface rcs_a1(f, φ) and applying cubic spline interpolation method to obtain the approximate surface rcs_a2(f, φ).

Step 3: For each interval $[\varphi_{sj}, \varphi_{sj+1}]$ $(j=1,2,\ldots,n)$, find the "sampling line" at which the ME occurs, say, at φ_{tj}, such that,

$$\max \sum_{si} \left| \text{rcs\_a1}(f_{si}, \varphi_{tj}) - \text{rcs\_a2}(f_{si}, \varphi_{tj}) \right|, \varphi_{sj} \le \varphi_{tj} \le \varphi_{sj+1}.$$

Step 4: If a given error tolerance, denoted as CE(φ), is larger than the ME in step 3, that means the samples obtained are enough; otherwise, adding the "sample line" of $I(f, \varphi_{sj})$ into the sample collection.

Step 5: For each interval $[f_{si}, f_{si+1}]$ $(i=1,2,\ldots,m)$, Applying Store-Bulirsch algorithm to obtain the "sampling line" at which the ME occurs.

Step 6: If a given error tolerance, denoted as CE(f), is larger than the ME in step 5, that means the samples obtained are enough; otherwise, adding the "sample line" of $I(f_{si}, \varphi)$ into the sample collection.

Step 7: If each interval $[\varphi_{sj}, \varphi_{sj+1}]$ satisfies the condition mentioned in step 4 and each interval $[f_{si}, f_{si+1}]$ satisfies the condition mentioned in step 6, the whole process terminates.

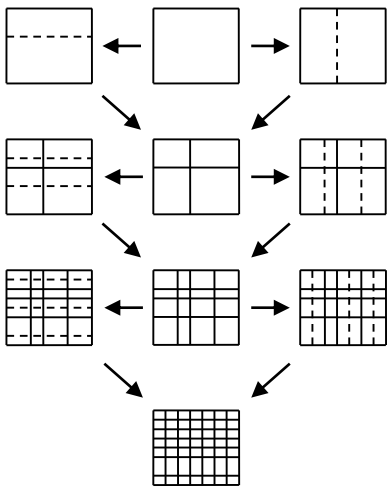

Fig. 1. Process of two dimensional frequency-angle adaptive combined sampling.

IV. NUMERICAL RESULTS

In this section, two numerical results are presented to demonstrate the efficiency of the proposed two-dimensional combined adaptive interpolation technique (SB-CS) method for fast calculation of wideband electromagnetic scattering of precipitation particles. In the implementation of the SB-CS method, we use GPBi-CG [21] algorithm to solve linear systems arising from electromagnetic wave scattering problems. In the simulation, θ and φ mean pitch angle and azimuth angle, respectively. Both experiments are conducted on an Intel Core i7 with 8 GB local memory and run at 3.6 GHz in single precision. The iteration process is terminated when the 2-norm residual error is reduced to 10^{-5}, and the limit of the maximum number of iterations is set as 10000. Two examples are applied to illustrate the performance of SB-CS method as follows.

Case I. 1000 spherical particles of arbitrary radius with random position

In the first simulation, scattering properties of 1000 spherical particles under random distribution in the space of $0.3*0.3*0.3m^3$ are researched. Particle parameter for simulation in this part is set as follows: the rain group is constituted by 1000 homogeneous spheres with random diameters range from 0.1 to 4*mm*, with 35308 unknowns.

The complex refractive index m varies from $4+0.04i$ to $3.5245+0.08755i$, when testing frequency band is from 1 GHz to 20 GHz. The direction of incident wave is fixed at $\theta = 0^\circ$, while φ is from 0° to 180°.

Case II. 500 precipitation particles with random position under certain axis ratio distribution [22]

In actual rainfall, the shape of precipitation particles is closely related to the size of water drops. In general, raindrop can be seen as sphere when volume is small. With increasing of raindrop size, the profile of precipitation particle is more close to the ellipsoid shape. This relationship has been studied by several researchers, and results of relevant research could be found in [22-24]. In this section, 500 precipitation particles under Keenan model [22] in the space of $0.5*0.5*0.5m^3$ are investigated. Particle parameter for simulation in this part is set as follows: minor axis of the ellipsoidal particles is varied from 0.1 to 4*mm*. The number of unknowns is 27498 and the complex refractive index m varies from $4+0.04i$ to $3.3495+0.105i$. The testing frequency band is from 8 GHz to 12 GHz. The direction of incident wave is fixed at at $\theta = 0^\circ$, while φ is from 0° to 180°.

Both the directly calculated and the interpolated results are presented in Figs. 2-3, while the relative error of SB-CS method for two examples has also been quantitative evaluated, shown in Fig. 4. These examples demonstrate that the SB-CS method is able to

approximate the 3-D RCS precisely. As shown in Fig. 2, the real curve is obtained by using original SM/CG method with the interval of 100 MHz, which needs 34571 exact calculated sampling points. With the SB-CS technique, the sampling nodes reduce to 2267. For the second example depicted in Fig. 3, the standard sampling interval changes to 20 MHz. The total number of exact calculated nodes is 36381, when the proposed method also needs only 2070 sampling points to obtain the approximate simulation curve.

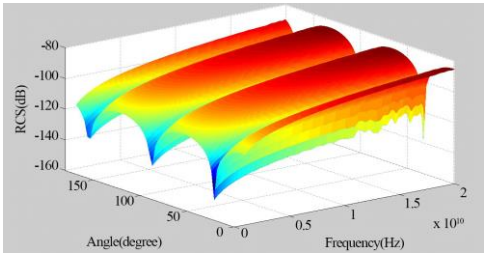

(a)

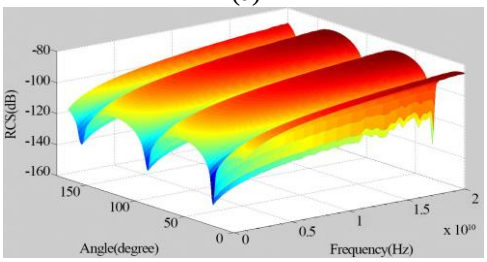

(b)

Fig. 2. 3-D RCS of 1000 spherical precipitation particles simultaneous versus frequency and angle. (a) SM/CG repeated solution, and (b) SB-CS method.

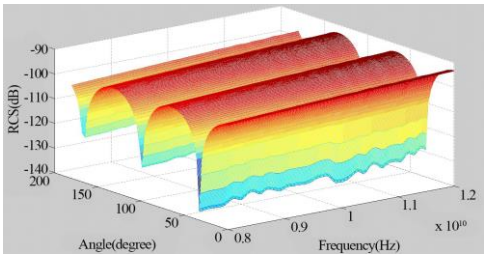

(a)

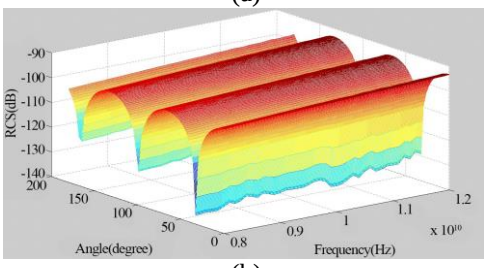

(b)

Fig. 3. 3-D RCS of 500 precipitation particles under Keenan model simultaneous versus frequency and angle. (a) SM/CG repeated solution, and (b) SB-CS method.

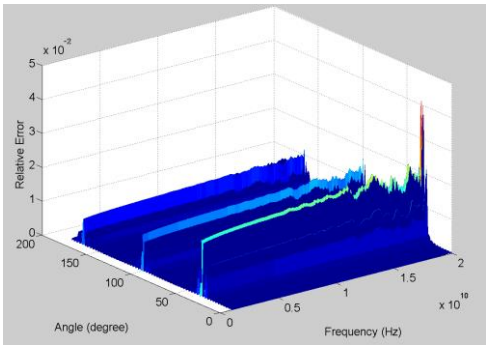

(a)

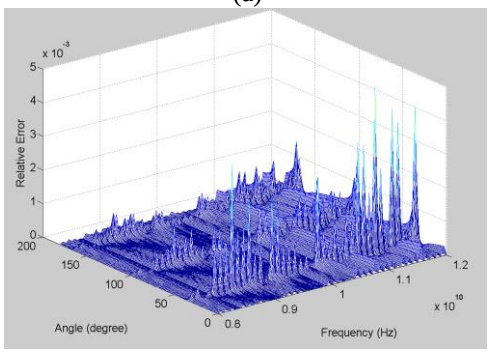

(b)

Fig. 4. The relative error of SB-CS method for two examples. (a) 1000 spherical precipitation particles, and (b) 500 precipitation particles under Keenan model.

Since a good interpolation method depends not only on its agreement performance, but also on its computational cost, Table 1 compares the number of calculated nodes, number of iterations and solution time between the traditional SM/CG method and the SB-CS method. Compared with the direct SM/CG method, it could be seen that the SB-CS method decreases the number of calculated nodes by a factor of 15.25 and 17.58 on both examples. Similar improvements could also be found in number of iterations, while solution time compression ratio is 14.68 and 17.06 for these two examples. AWE method is also applied on these two cases, corresponding solution time compression ratio is 11.25 and 13.93. In this paper, the order of AWE is 6 and 4, which means numerator is a sixth-order polynomial and denominator is a fourth-order polynomial. As the sampling points are selected adaptively across the broad frequency and angular band of interest, efficiency of SB-CS is better than AWE in some extent. Since the proposed method can determine the number and the location of sampling points automatically, more sampling nodes are required when the real curve is complex, as the simple curve needs less number of samples. These results demonstrate the effectiveness and flexibility of SB-CS method applying for wideband electromagnetic scattering calculation of precipitation particles in frequency-angle domain.

Table 1: Comparison of the cost and performance between direct SM/CG and SB-CS method

Object		Case I	Case II
Number of Unknowns		35308	27498
Calculated nodes	SM/CG	34571	36381
	AWE	3015	2558
	SB-CS	2267	2070
Number of iterations	SM/CG	187715	217284
	AWE	16224	15099
	SB-CS	12167	12262
Solution time (min)	SM/CG	30187	38873
	AWE	2683	2791
	SB-CS	2056	2278

V. CONCLUSIONS AND COMMENTS

In this paper, a novel two dimensional adaptive combined interpolation algorithm based on cubic spline technique and the Stoer-Bulirsch model is proposed for fast wideband electromagnetic computation of precipitation particles in frequency-angle domain. Using the proposed method, the frequency-angle domain response could be modeled by the adaptive sampling strategy to generate new sampling points automatically in both frequency and angle domain with quite less number of sampling points than traditional direct solvers. Compared to traditional AWE technique, this novel method needs no matrix inversion and avoids calculating derivatives, thus the derived fitting model could be applicable in an almost unlimited frequency and angle band. Numerical results indicate that this combined interpolation strategy performs well in terms of both simulation time and computation accuracy.

ACKNOWLEDGMENT

The authors would like to thank the assistance and support by National Natural Science Foundation of China (No: 61301025, 61261005), Jiangsu Provincial Natural Science Foundation of China (No: BK20130853, BK20130852), the Fundamental Research Funds for the Central Universities (No: 2016B07114), China Postdoctoral Science Foundation (No: 2013M541035), Open Project of State Key Laboratory of Millimeter Wave (No: K201404), Priority Academic Program Development of Jiangsu Higher Education Institutions (PAPD).

REFERENCES

[1] G. J. Huffman, et al., "The TRMM multisatellite precipitation analysis (TMPA): Quasi-global, multiyear, combined-sensor precipitation estimates at fine scales," *Journal of Hydrometeorology*, vol. 8, pp. 38-55, 2007.

[2] R. F. Adler, et al., "Tropical rainfall distributions determined using TRMM combined with other satellite and rain gauge information," *Journal of Applied Meteorology*, vol. 39, no. 12, pp. 2007-2023, 2000.

[3] B. Yong, B. Chen, J. J. Gourley, L. Ren, Y. Hong, X. Chen, W. Wang, S. Chen, and L. Gong, "Intercomparison of the version-6 and version-7 TMPA precipitation products over high and low latitudes basins with independent gauge networks: Is the newer version better in both real-time and post-real-time analysis for water resources and hydrologic extremes?," *J. Hydrol.*, vol. 508, pp. 77-87, 2014.

[4] Z. Li, D. Yang, B. Gao, Y. Jiao, Y. Hong, and T. Xu, "Multiscale hydrologic applications of the latest satellite precipitation products in the Yangtze River Basin using a distributed hydrologic model," *Journal of Hydrometeorology*, vol. 16, pp. 407-426, 2015.

[5] M. I. Mishchenko, L. D. Travis, and A. A. Lacis, *Scattering, Absorption, and Emission of Light by Small Particles*. Cambridge University Press, 2002.

[6] D. W. Mackowski and M. I. Mishchenko, "Calculation of the T matrix and the scattering matrix for ensembles of spheres," *J. Opt. Soc. Am. A*, vol. 13, pp. 2266-2278, 1996.

[7] R. F. Harrington, *Field Computation by Moment Methods*. R. E. Krieger, Malabar, Fla., 1968.

[8] J. J. H. Wang, *Generalized Moment of Methods in Electromagnetics: Formulation and Computer Solution of Integral Equation*. John Wiley & Sons, New York, 1990.

[9] E. K. Miller, L. M. Mitschang, and E. H. Newman, *Computational Electromagnetics: Frequency-Domain Method of Moments*. IEEE Press, New York, 1992.

[10] J. M. Song, C. C. Lu, and W. C. Chew, "Multilevel fast multipole algorithm for electromagnetic scattering by large complex objects," *IEEE Trans. Antennas Propagat.*, vol. 45, no. 10, pp. 1488-1493, 1997.

[11] M. Y. Xia, et al., "An efficient algorithm for electromagnetic scattering from rough surfaces using a single integral equation and multilevel sparse-matrix canonical-grid method," *IEEE Trans. Antennas Propagat.*, vol. 51, no. 6, pp. 1142-1149, 2003.

[12] P. Xu and L. Tsang, "Scattering by rough surface using a hybrid technique combining the multilevel UV method with the sparse matrix canonical grid method," *Radio Science*, vol. 40, no. 4, pp. 2227-2252, 2005.

[13] Q. Li, L. Tsang, K. S. Pak, and C. H. Chan, "Bistatic scattering and emissivities of random rough dielectric lossy surfaces with the physics-based two-grid method in conjunction with the sparse-matrix canonical grid method," *IEEE*

Trans. Antennas Propagat., vol. 48, no. 1, pp. 1-11, 2000.

[14] J. Ling, S. X. Gong, X. Wang, B. Lu, and W. T. Wang, "A novel two-dimensional extrapolation technique for fast and accurate radar cross section computation," *IEEE Antennas & Wireless Propagation Letters*, vol. 9, no. 1, pp. 244-247, 2010.

[15] E. K. Miller, "Model-based parameter estimation in electromagnetics. III. Applications to EM integral equations," *IEEE Antennas and Propagation Magazine*, vol. 40, no. 3, pp. 49-66, 1998.

[16] B. Y. Wu and X. Q. Sheng, "Application of asymptotic waveform evaluation to hybrid FE-BI-MLFMA for fast RCS computation over a frequency band," *IEEE Trans. Antennas Propagat*., vol. 61, no. 5, pp. 2597-2604, 2013.

[17] J. Stoer and R. Bulirsch, *Introduction to Numerical Analysis*. Spring-Verlag, Berlin, 1980.

[18] Y. Ding, K.-L. Wu, and D. G. Fang, "A broad-band adaptive frequency sampling approach for microwave-circuit EM simulation exploiting Stoer-Bulirsch algorithm," *IEEE Transactions on Microwave Theory and Techniques*, vol. 51, no. 3, pp. 928-934, 2003.

[19] J. Chen, Z. Liu, P. Shen, D. Ding, and H. Peng, "Adaptive frequency-sampling method for wideband electromagnetic scattering of precipitation particles," *IEEE Antennas and Wireless Propagation Letters*, vol. 10, pp. 835-838, 2011.

[20] Z. W. Liu, R. S. Chen, and J. Q. Chen, "Adaptive sampling cubic-spline interpolation method for efficient calculation of monostatic RCS," *Microwave & Optical Technology Letters*, vol. 50, pp. 751-755, 2008.

[21] S. L. Zhang, "GPBi-CG: Generalized product-type methods based on Bi-CG for solving nonsymmetric linear systems," *SIAM J. Sci. Comput.*, vol. 18, no. 2, pp. 856-869, 1997.

[22] V. N. Bringi and V. Chandrasekar, *Polarimetric Doppler Weather Radar: Principles and Application*. Cambridge University Press, 2004.

[23] H. R. Pruppacher and R. L. Pitter, "A semi-empirical determination of the shape of cloud and rain drops," *Journal of the Atmospheric Sciences*, vol. 28, pp. 86-94, 1970.

[24] A. W. Green, "An approximation for the shapes of large raindrops," *Journal of Applied Meterology*, vol. 14, pp. 1578-1583, 1975.

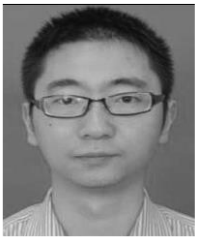

Jiaqi Chen was born in Gansu, China. He received the Ph.D. degree in Communication Engineering from Nanjing University of Science and Technology (NUST), Nanjing, China, in 2012. He was with the Center for Sensor Systems (ZESS), University of Siegen, Siegen, Germany, as a Visiting Scholar in 2009. He is currently working at the College of Computer and Information Engineering, Hohai University. His research interests include computational electromagnetics, SAR imaging and precipitation radar.

Design of All-Dielectric Half-wave and Quarter-wave Plates Microwave Metasurfaces Based on Elliptic Dielectric Resonators

Ali Yahyaoui [1,2], Hatem Rmili [1,3], Muntasir Sheikh [3], Abdullah Dobaie [3], Lotfi Laadhar [3], and Taoufik Aguili [1]

[1] Communications Systems Laboratory (SysCom), National Engineering School of Tunis (ENIT)
University of Tunis El Manar (UTM), BP 37, Belvédère 1002 Tunis, Tunisia
ali.yahyaoui@enit.utm.tn, taoufik.aguili@enit.rnu.tn

[2] Electrical and Computer Engineering Department
University of Jeddah, P.O. Box 80327, 21589 Jeddah, Saudi Arabia
amalyahyaoui@uj.edu.sa

[3] Electrical and Computer Engineering Department
King Abdulaziz University, P.O. Box 80204, Jeddah 21589, Saudi Arabia
hmrmili@kau.edu.sa, mshaikh@kau.edu.sa, adobaie@kau.edu.sa, llaadhar@kau.edu.sa

Abstract ─ In this paper, we propose a numerical study for the design of Quarter-Wave Plate (QWP) and Half-Wave Plate (HWP) all-dielectric metasurfaces of relative permittivity 10.2, loss tangent 0.003 and thickness 5.12 mm. The devices based on Elliptic Dielectric Resonators (EDRs) may operate in the microwave band 20-30 GHz. First, we have studied the variation of the metasurface transmission, under x- and y-polarizations of the incident electric fields, when we vary the resonator ellipticity τ in the range 1:1.94. Next, we have optimized the resonator orientation (the rotation angle θ is situated in the range 0:45°) to improve further the moduli of transmission coefficients. Finally, from these previous parametric studies, we have designed QWP and HWP metasurfaces with the selected ellipticities τ_1=1.4 and τ_2=1.6. For example, we have obtained for ellipticity τ_1 that the metasurface may acts as HWP device at frequencies 26.08 GHz and 28.03 GHz with bandwidths 175 MHz and 75 MHz, respectively and as QWP device at 29.02 GHz with a bandwidth of 150 MHz. In addition, the transmission bandwidths of HWP metasurface was increased from 75 to 225 MHz when we vary the rotation angle of the EDR from θ=0° to 10°.

Index Terms ─ All-dielectric, dielectric resonator, half-wave plat, metasurface, quarter-wave plate, transmission coefficient.

I. INTRODUCTION

Control of the propagation of electromagnetic waves is an exciting topic in applied electromagnetics, and the complete control is still a challenge. Recently, metasurfaces have emerged as effective means for controlling the amplitude, phase and polarization of electromagnetic waves, see e.g. [1].

Metasurfaces [2-3], which are the 2-D version of metamaterials [4-7], are artificial structures designed by arranging a set of scattering elements in a regular pattern throughout a two-dimensional surface. These scattering elements can alter the propagation properties of incident electromagnetic waves, equipping metasurfaces with desirable functionalities and permitting the realization of innovative microwave devices such as cloaks, lens, absorbers, and polarizers [1].

Contrary to metasurfaces designed with conducting elements, characterized by high metallic losses especially in optical range, all-dielectric metasurfaces have emerged as a potential alternative for designing new microwave and optical devices with novel performances, due to their inherent advantages notably low-losses, high-refractive-index material, high overall efficiency and especially the possibility of realizing new functionalities by controlling both electric and magnetic resonances through optimization of the dielectric resonators' shape and spacing [8]-[12].

The majority of designed all-dielectric metasurfaces use dielectric resonators due to their particularity to excite both electric and magnetic resonant modes and to obtain miniaturized structures by using high dielectric constant materials. In addition to the possibility of using various canonical shapes such as spheres, cubes, cylindrical/elliptical disks and rods offering more flexibility in the design process.

In this paper, employing the Ansys-HFSS software package, we have investigated numerically the design of

Submitted On: August 9, 2016
Accepted On: January 21, 2017

QWP and HWP all-dielectric metasurfaces based on Elliptic Dielectric Resonators (EDRs), operating in the microwave band 20-30 GHz. We have first studied the effects of the EDR ellipticity and orientation on the transmission through the determination of both x- and y-polarized transmission coefficients (moduli and phases). Then, selecting proper frequency sub-bands, with the moduli being equal, and the phase shift between x- and y-transmission coefficients being close to ±90° and ±180°, we have designed Quarter-Wave Plate (QWP) and Half-Wave Plate (HWP) metasurfaces. Next, we have presented examples of metasurfaces having particular values of the EDR ellipticity and orientation. Finally, we have analyzed the resonances of the proposed QWP and HWP metasurfaces based on the electric field distribution at their resonating frequencies.

II. METASURFACE DESIGN

Employing the ANSYS-HFSS software package we have designed the proposed all-dielectric metasurface for operation in the frequency range 20-30 GHz. The structure is composed of an infinite 2D-array of connected dielectric resonators (Rogers RO3210) of relative permittivity 10.2, loss tangent 0.003 and thickness 5.12 mm (Fig. 1 (a)).

The used resonator is characterized by an elliptic shape of minor axis "a" along the x-direction, major axis "b" along the y-direction, and an ellipticity factor $\tau = b/a$. The unit cell (Fig. 1 (b)) considered in the simulations is a box of longitudinal dimension Lz = 160 mm along the z-direction (Lz > λ), and transverse dimensions Lx and Ly along the x- and y-directions, respectively (Lx < λ and Ly < λ), with λ being the free-space wavelength associated with the upper frequency of the band 20-30 GHz (λ=10 mm). The connection (along the x-direction) between resonators were ensured with dielectric strips of thickness 5.12 mm, length Lc=(Lx/2)-a and width W_c=0.5 mm.

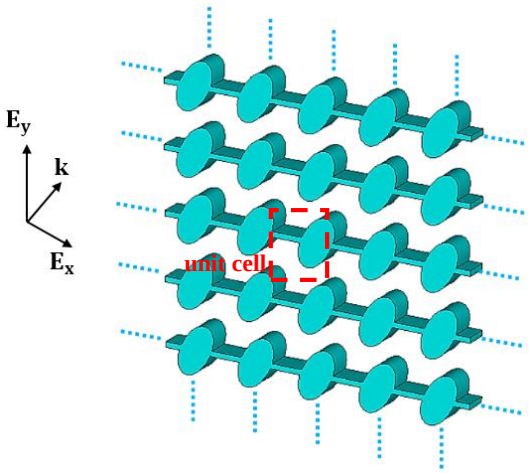

(a)

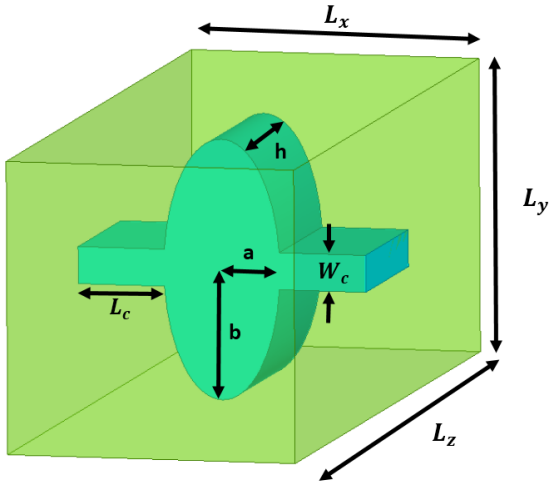

(b)

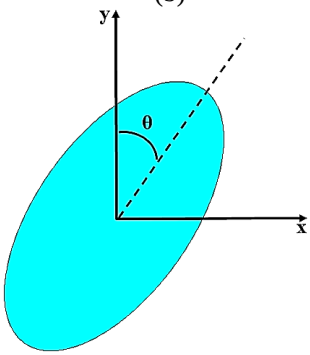

(c)

Fig. 1. Sketch of the proposed all-dielectric metasurface: (a) 2D connected EDR array with x- and z-polarizations of the electric field, (b) HFSS-model for the unit cell, and (c) definition of the rotation angle θ.

The influence of the ellipticity of the resonator was studied by varying only the major radius b, without changing the cell size; to this end τ is assumed to be in the range 1:1.94. The minor radius was kept constant (a = 2.5 mm (λ/4)). The orientation of the resonator was studied by modifying the angle θ ($0 \le \theta \le 45°$) between the EDR major axis and y-direction (see Fig. 1 (c)).

III. RESULTS AND DISCUSSIONS

In order to design QWP and HWP all-dielectric metasurfaces, we have analyzed their transmission properties when excited under normal incidence waves having orthogonal polarizations parallel to the x- and y-axis. From moduli and phases of incident and transmitted electric fields, we have defined $T_{xx} = \frac{|E_x^t|}{|E_x^i|}$ and $T_{yy} = \frac{|E_y^t|}{|E_y^i|}$ as the transmission moduli of the x- and y-polarization, respectively, where E_x^i is the x-polarized incident electric field, E_x^t is the x-polarized transmitted electric field, E_y^i is the y-polarized incident electric field, and E_y^t

y-polarized transmitted electric field. $\Delta\phi = \phi_x - \phi_y$ is the phase difference between x- and y-polarizations. Then, the moduli T_{xx} and T_{yy} vary from 0 to 1, and the phase difference from -360° to +360°.

In the design process, we have first fixed the thickness of the resonator to be 5.12 mm, and its minor radius to be 2.5 mm. Then, we have determined the values of resonator ellipticity τ resulting in high transmission moduli and phase shift around ±90° for the QWP and ±180° for the HWP metasurfaces. Next, we have selected two ellipticity values ($\tau_1 = 1.4$ and $\tau_2 = 1.6$), and we have studied the effect of the rotation angle θ on the metasurface transmission in order to improve further the obtained transmission moduli and phases. Finally, we have represented the transmission coefficients and determined the bandwidth obtained with the optimized structures, over the frequency band 20-30 GHz.

For illustration of achieved results, we have selected two configurations; the first shows the possibility to design a unique metasurface with both QWP and HWP effects, and the second illustrates the possibility to improve a QWP or HWP metasurface transmission by adjusting the orientation of the resonators.

A. Effect of the EDR ellipticity

In this section, we have investigated the effect of the resonator ellipticity on the metasurface transmission. We have first simulated the variation of the transmission coefficients T_{xx} and T_{yy} (moduli and phases) when the ellipticity τ is varied from 1 to 1.94. Then, we have deduced the moduli ratio in logarithm scale and the phase shift $\Delta\phi$. Finally, we have filtered these values to keep only high and equal transmission moduli ($0.7 \leq T_{xx} \leq 1$ and $0.7 \leq T_{yy} \leq 1$) and phase shifts $\Delta\phi$ close to ±90° and ±180° for both QWP and HWP behaviors, respectively.

In Fig. 2, we have presented the effect of the resonator ellipticity on the metasurface transmission in colored maps. From these values, we have deduced (see Fig. 2 (b)), the logarithm of ratio between the moduli ($\log(T_{xx}/T_{yy})$) and the phase difference $\Delta\phi$, then filtered values of the moduli corresponding to $0.7 \leq T_{xx} \leq 1$ and $0.7 \leq T_{yy} \leq 1$, and phases corresponding to $\Delta\phi = \pm 90° \pm 5°$ and $\Delta\phi = \pm 180 \pm 5°$. In fact, the QWP and HWP metasurfaces are obtained when the moduli are equal ($T_{xx} = T_{yy}$) and the phase shift is $\Delta\phi = \pm 90°$ for QWP and $\Delta\phi = \pm 180°$ for HWP.

The highest values of the moduli T_{xx} and T_{yy} are given with red color in Fig. 2 (a), and the equality between them ($T_{xx} = T_{yy}$) is represented with green color ($\log(T_{xx}/T_{yy})$ close to 0) in Fig. 2 (b) (left graph), while high and equal moduli are given in the right graph of Fig. 2 (b).

For the phase, Fig. 2 (a) gives all phases ϕ_x and ϕ_y, the left graph of Fig. 2 (b) gives all values of the phase difference $\Delta\phi$, whereas right graph of Fig. 2 (b) gives the filtered values close to ±90° and ±180°.

In the two graphs of Fig. 2 (b) related to filtered moduli and phases, each couple (f, τ) which has a color in both figures is a possible solution for the design of QWP or HWP metasurface.

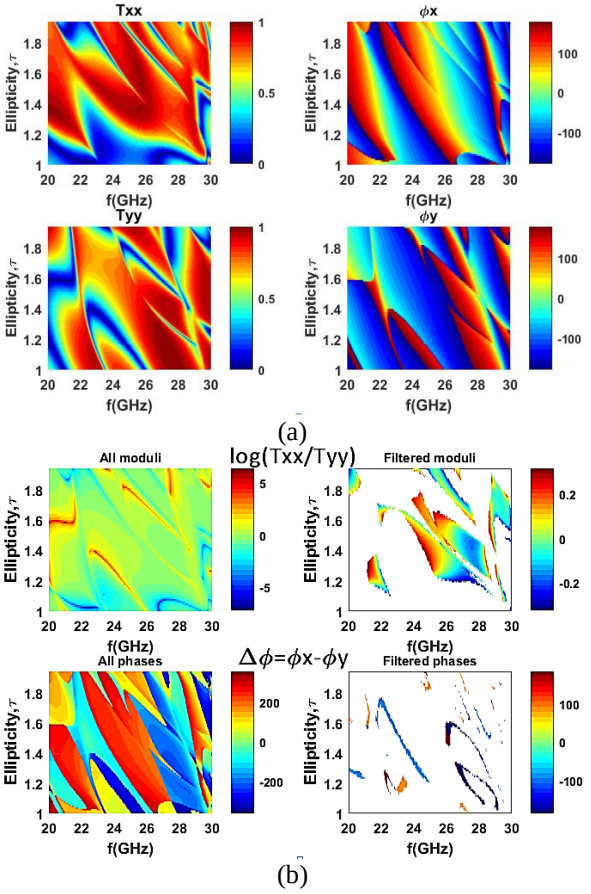

Fig. 2. Effect of the resonator ellipticity on the all-dielectric metasurface transmission: (a) moduli and phases of the x- and the y-polarized transmission coefficients; (b) all and filtered values of both moduli ratio and phase difference.

B. Effect of the EDR orientation

After establishing the color map (Fig. 2) illustrating the best ellipticity values giving high transmission, we have investigated the possibility to improve further the metasurface transmission by optimizing the resonator orientation, and rotating it in the x-y plane around z-axis. To conduct this parametric study, we have selected from the previous study (Fig. 2) two resonators of ellipticities τ_1=1.4 and τ_2=1.6 showing high transmission levels.

Again, for each resonator, we have first simulated the variation of the transmission coefficients T_{xx} and T_{yy} (moduli and phases) when its rotation angle θ is varied from 0° to 45° with a step of 5°. Then, we have deduced the moduli ratio in logarithm scale and the phase shift

$\Delta\phi$. Finally, we have filtered these values to keep only high and equal transmission moduli ($0.7 \leq T_{xx} \leq 1$ and $0.7 \leq T_{yy} \leq 1$) and phase shifts $\Delta\phi$ close to ±90° and ±180° for both QWP and HWP behaviors, respectively.

In Figs. 3 (a) and 4 (a), we have presented moduli and phases of the x- and the y-polarized transmission coefficients, in the frequency range 20-30 GHz, for different rotation angles θ. The equality between the moduli T_{xx} and T_{yy}, and the phase shift $\Delta\phi$ variation with the EDR orientation are given in Fig. 3 (b) and Fig. 4 (b), as well as the filtered values corresponding to high and equal moduli, and particular values of the phase shift corresponding to $\Delta\phi = \pm 180°$ or $\Delta\phi = \pm 90°$.

The right graphs of Fig. 3 (b) and Fig. 4 (b) give the useful parameters for the design of QWP and HWP metasurfaces with EDRs. Each couple (f, θ) represented with a color in both right graphs of Fig. 3 (b) or Fig. 4 (b), is a possible solution for the design of QWP or HWP metasurface with resonators of ellipticity 1.4 or 1.6, respectively.

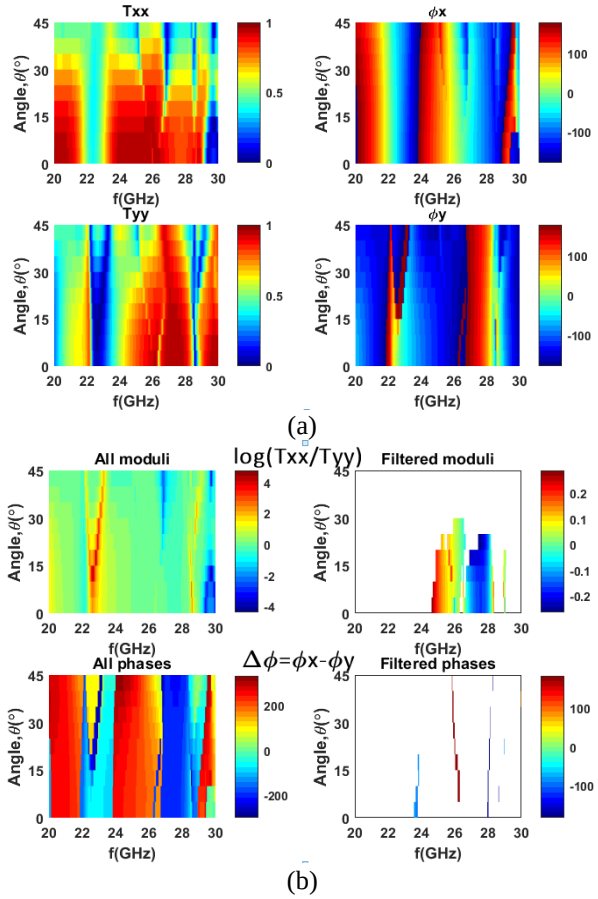

Fig. 3. Effect of the rotation angle of a resonator of ellipticity τ_1=1.4 on the all-dielectric metasurface transmission: (a) the moduli and phases of the x- and the y-polarized transmission coefficients; (b) all and filtered values of both moduli ratio and phase difference.

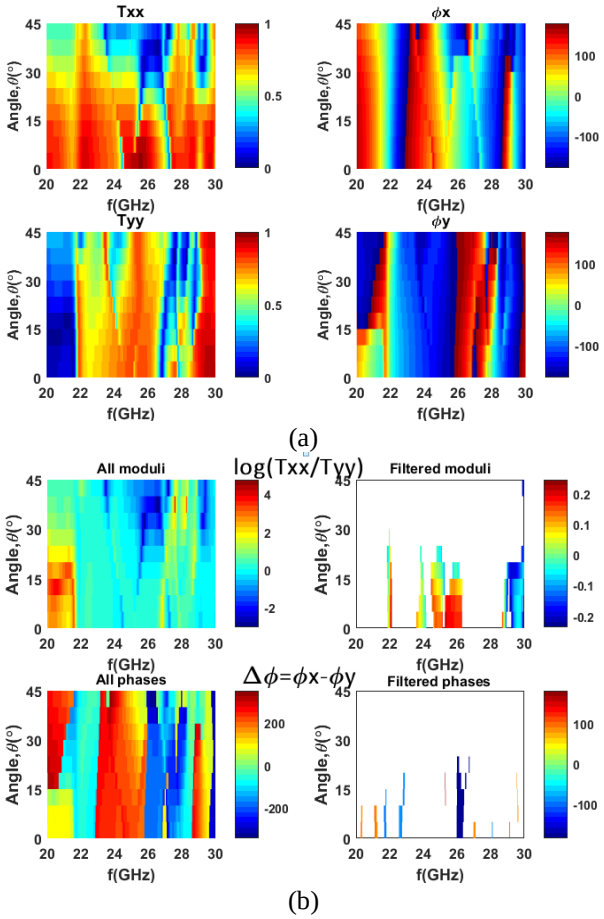

Fig. 4. Effect of the rotation angle of a resonator of ellipticity τ_1=1.6 on the all-dielectric metasurface transmission: (a) the moduli and phases of the x- and the y-polarized transmission coefficients; (b) all and filtered values of both moduli ratio and phase difference.

We conclude from the color distribution in Fig. 3 (b) and Fig. 4 (b), that we have more possibility to design QWP or HWP metasurface with EDR ellipticity 1.6 than 1.4 since we have more superposition between filtered values of moduli and phases in Fig. 4 (b) (τ_2=1.6) than in Fig. 3 (b) (τ_1=1.4). In fact, each superposition between filtered values of moduli and phases means that we have the possibility to design QWP or HWP metasurfaces with high transmission ($0.7 \leq T_{xx} \leq 1$ and $0.7 \leq T_{yy} \leq 1$) and phase shifts $\Delta\phi$ close to ±90° or ±180°.

C. Application: QWP and HWP metasurfaces

Table 1 summarizes the main obtained results in sections A and B, for the design of all-dielectric QWP and HWP metasurfaces based on EDRs. For each resonator of ellipticity τ (τ_1=1.4 or τ_2=1.6), we have presented different orientations (angles θ) (in column 2) giving QWP or/and HWP behaviors. In columns 3 and 4, we have indicated respectively, the central frequency f_0

and the bandwidth BW of the frequency sub-band in which the designed metasurfaces may operate.

Table 1: Main QWP and HWP metasurfaces properties deduced from Figs. 3 (b) and 4 (b)

Ellipticity, τ	Rotation Angle, θ(°)	Central Frequency, F_0 (GHz)	Bandwidth, BW (MHz)	QWP	HWP
τ_1=1.4	0	27.98	75		√
	5	26.25	150		√
		27.98	75		√
	10	26.16	225		√
		28.01	75		√
	15	26.08	175		√
		28.03	75		√
		29.02	150	√	
	20	26.05	150		√
		28.06	75		√
	25	25.93	125		√
	30	25.91	75		√
τ_2=1.6	0	26.13	325		√
		29.60	-	√	
	5	26.13	325		√
		29.12	-		√
		29.60	50	√	
	10	26.15	350		√
		27.87	-		√
		29.12	-		√
		29.58	75	√	
	15	25.22	50		√
		26.06	175		√
		29.10	-		√
		29.51	75	√	
	20	25.07	-		√

The main conclusion from Table 1 is that, for a fixed ellipticity, the metasurface behavior depends on the resonator orientation. For example, the bandwidth may be improved by varying the rotation angle θ, in addition to the possibility of realizing both QWP and HWP with a unique metasurface for certain orientations.

We remark also that ellipticity τ_1 is more adequate for the realization of HWP metasurfaces (θ=0, 5, 10, 15, 20, 25 and 30°), whereas ellipticity τ_2 is more adequate for realization of both QWP and HWP metasurfaces (θ=0, 5, 10 and 15°).

In Fig. 5, we have illustrated the dual-effect (QWP and HWP) by giving the variation, over the range 20-30 GHz, of moduli ratio (in log scale) and phase shift $\Delta\phi$ for two metasurfaces based on EDRs of fixed orientation (θ=15°) and ellipticity's τ_1 and τ_2, respectively.

In Fig. 5 and Fig. 6, the yellow and blue strips correspond to sub-bands with QWP and HWP behaviors, respectively. Therefore, we can note that the metasurface based on EDRs of ellipticity τ_1 may acts as HWP device at frequencies 26.08 GHz and 28.03 GHz with bandwidths 175 MHz and 75 MHz, respectively and as QWP device at 29.02 GHz with a bandwidth of 150 MHz. Whereas for ellipticity τ_2, we have obtained the HWP behavior at frequencies 25.22 GHz and 26.06 GHz with bandwidths 50 MHz and 175 MHz, respectively and the QWP behavior at 29.51 GHz with a bandwidth of 75 MHz.

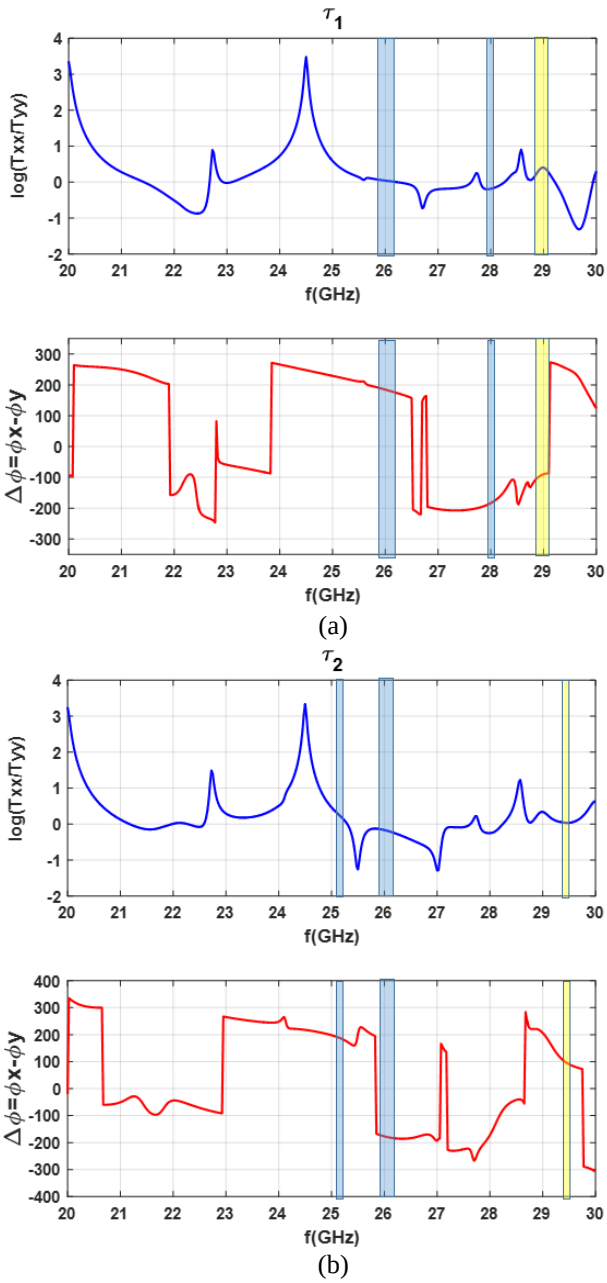

Fig. 5. Variation, over the frequency band 20-30 GHz, of the x- and y-polarized moduli ratio and phase shift for an all-dielectric metasurface based on EDRs of rotation angle θ=15° and ellipticity: (a) τ_1=1.4; (b) τ_2=1.6.

The effect of EDR orientation on the metasurface transmission is shown in Fig. 6. We note from Fig. 6 (a) that the transmission bandwidths are 75, 150 and 225 MHz for rotation angles θ=0°, 5° and 10°, respectively, which means that the bandwidth of the HWP metasurface designed with ellipticity τ_1 was ameliorated by simple optimization of the angle θ. Similarly, for the QWP metasurface designed with ellipticity τ_2 (Fig. 6 (b)), the transmission bandwidth was increased by varying the resonator orientation.

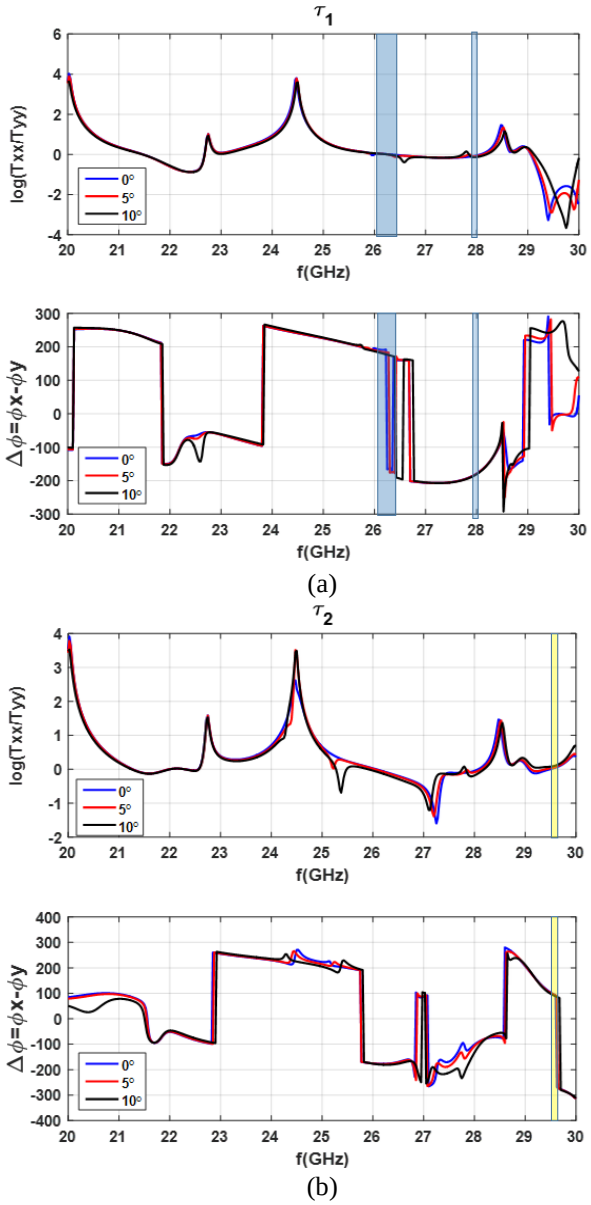

Fig. 6. Variation, over the frequency band 20-30 GHz, of the x- and y-polarized moduli ratio and phase shift for an all-dielectric metasurfaces based on EDRs of rotation angles θ=0°, 5° and 10°, and ellipticity: (a) τ_1=1.4; (b) τ_2=1.6.

The electric field distributions in the yz-plane at the middle of the resonator (cut plane (x=0) of both QWP and HWP all-dielectric metasurfaces (excided with the y-polarization) based on EDRs of ellipticity τ_1=1.4 and for different orientations are given in Figs. 7 and 8, respectively. For each device (QWP or HWP), the structure was selected to resonate at the same frequency with two different rotation angles θ; permitting the analysis of the effect of the EDR orientation on the electric field distribution.

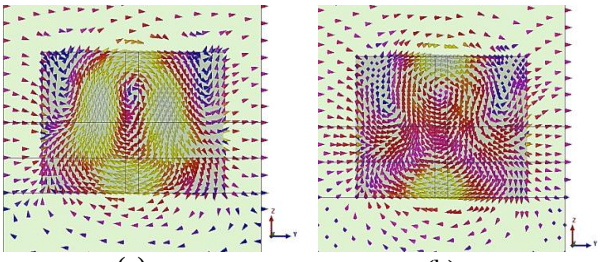

Fig. 7. Electric-field distribution on the yz-plane at the middle (cut plane x=0) of the unit cell for a QWP-metasurface based on EDRs of ellipticity τ_1=1.4 and rotation angle θ, resonating around the frequency f=29 GHz: (a) θ = 0°; (b) θ = 15°.

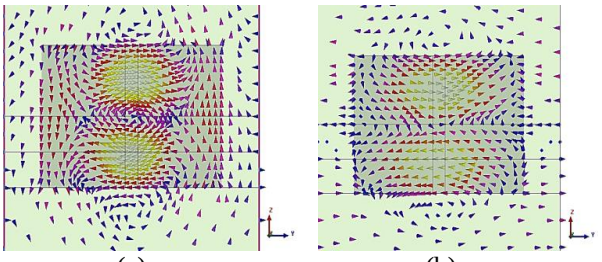

Fig. 8. Electric-field distribution on the yz-plane at the middle (cut plane x=0) of the unit cell for a HWP-Metasurface based on EDRs of ellipticity τ_1=1.4 and rotation angle θ, resonating around the frequency f=26.15 GHz: (a) θ = 0°; (b) θ = 10°.

Analysis of Figs. 7 and 8 reveals that rotation of the resonator about the z-axis within it, which in turns may reduce the resonance strength of the structure excited with-y-polarization. This result may be explained by the decrease of the exciting the y-electric field component with the rotation of the resonator. However, we note a slight improvement of the useful bandwidth for both QWP and HWP devices.

IV. CONCLUSION

In this work, we have investigated numerically the design of QWP and HWP all-dielectric metasurfaces

based on EDRs operating in the microwave frequency band 20-30 GHz. We have investigated first the effect of the EDR ellipticity on the metasurfaces transmission; then we aimed at improving the resulting transmission by rotation of the resonator about its z-axis. It is found that by optimizing the rotation angle we can improve the bandwidth of both QWP and HWP metasurfaces in addition to the possibility of realizing a unique device with both QWP and HWP behaviors at some selected frequencies.

ACKNOWLEDGMENT

This project was funded by the Deanship of Scientific Research (DSR), King Abdulaziz University, under Grant No. (25-135-35-HiCi). The authors therefore, acknowledge technical and financial support of KAU.

REFERENCES

[1] H. T. Chen, A. J. Taylor, and N. Yu, "A review of metasurfaces: Physics and applications," *Reports on Progress in Physics*, vol. 79, no. 7, June 2016.

[2] C. Holloway, M. Mohamed, E. F. Kuester, and A. Dienstfrey, "Reflection and transmission properties of a metafilm: With an application to a controllable surface composed of resonant particles," *IEEE Trans. Electromagn. Compat.*, vol. 47, pp. 853-865, 2005.

[3] C. Holloway, E. F. Kuester, J. Gordon, J. O'Hara, J. Booth, and D. Smith, "An overview of the theory and applications of metasurfaces: The two-dimensional equivalents of metamaterials," *IEEE Antennas. Propag. Mag*., vol. 54, pp. 10-35, 2012.

[4] F. Capolino, ed., *Theory and Phenomena of Metamaterials*. CRC, 2009.

[5] J. B. Pendry, "Negative refraction makes a perfect lens," *Phys. Rev. Lett.*, vol. 85, pp. 3966-3969, 2000.

[6] J. B. Pendry, D. Schurig, and D. R. Smith, "Controlling electromagnetic fields," *Science*, vol. 312, pp. 1780-1782, 2006.

[7] A. Silva, F. Monticone, G. Castaldi, V. Galdi, A. Alú, and N. Engheta, "Performing mathematical operations with metamaterials," *Science*, vol. 343, pp. 160-163, 2014.

[8] A. Arbabi, Y. Horie, M. Bagheri, and A. Faraon, "Dielectric metasurfaces for complete control of phase and polarization with subwavelength spatial resolution and high transmission," *Nature Nanotechnology*, vol. 10, pp. 937-943, 2015.

[9] K. Achouri, G. Lavigne, A. S. Mohamed, and C. Caloz, "Metasurface spatial processor for electromagnetic remote control," *IEEE Trans Ant. and Prop.*, vol. 64, no. 5, 2016.

[10] I. Staude, A. E. Miroshnichenko, M. Decker, N. T. Fofang, S. Liu, E. Gonzales, J. Dominguez, T. S. Luk, D. N. Neshev, I. Brener, and Y. Kivshar, "Tailoring directional scattering through magnetic and electric resonances in subwavelength silicon nanodisks," *ACS Nano*, vol. 7, pp. 7824-7832, 2013.

[11] Y. M. Dai, W. Z. Ren, H. B. Cai, H. Y. Ding, N. Pan, and X. P. Wang, "Realizing full visible spectrum metamaterial half-wave plates with patterned metal nanoarray/insulator/metal film structure," *Optics Express*, vol. 22, pp. 746-7472, 2014.

[12] J. Cheng, D. Ansari-Oghol-Beig, and H. Mosallaei, "Wave manipulation with designer dielectric metasurfaces," *Optics Letters*, vol. 39, pp. 6285-6288, 2014.

Ali Yahyaoui received the Master degree in Electrical and Electronics from the University of Tunis El Manar, Faculty of Sciences, in 2012. He is currently working toward the Ph.D. degree in Communication Systems at the National Engineering School of Tunis (ENIT), University of Tunis El Manar.

His areas of interests are antenna designs, metamaterials and metasurfaces.

Hatem Rmili received the B.S. degree in General Physics from the Science Faculty of Monastir, Tunisia in 1995, and the DEA diploma from the Science Faculty of Tunis, Tunisia, in Quantum Mechanics, in 1999. He received the Ph.D. degree in Physics (Electronics) from both the University of Tunis, Tunisia, and the University of Bordeaux 1, France, in 2004. From December 2004 to March, 2005, he was a Research Assistant in the PIOM Laboratory at the University of Bordeaux 1. During March 2005 to March 2007, he was a Postdoctoral Fellow at the Rennes Institute of Electronics and Telecommunications, France. From March to September 2007, he was a Postdoctoral Fellow at the ESEO Engineering School, Angers, France. From September 2007 to August 2012, he was an Associate Professor with the Mahdia Institute of Applied Science and Technology (ISSAT), department of Electronics and Telecommunications, Tunisia. Actually, he is Associate Professor with the Electrical and Computer Engineering Department, Faculty of Engineering, King Abdulaziz University, Jeddah, Saudi Arabia. His main research activities concern antennas, metamaterials and metasurfaces.

Muntasir Sheikh received his B.Sc. from King Abdulaziz University, Saudi Arabia, in Electronics and Communications Engineering, M.Sc. in RF Communications Engineering from the University of Bradford, U.K., and Ph.D. from the University of Arizona, U.S.A.

Since then he has been teaching in the Electrical and Computer Engineering Dept. in KAU. His research interests are Antenna Theory and Design, Radar applications, and electromagnetic metamaterials.

Abdullah Dobaie received the Ph.D. degree in Electrical Engineering from the University of Colorado, USA, in 1995. Actually, he is Associate Professor with the Electrical and Computer Engineering Department, Faculty of Engineering, King Abdulaziz University, Jeddah, Saudi Arabia.

His main research activities concern wireless communication, digital image signal processing, and antennas design.

Lotfi Ladhar received his Engineering degree and his Ph.D. degrees in Telecommunications from High Institute of Communications of Moscow (RUSSIA) in 1985. From 1990 to 2001, he was Assistant Professor at the Air force Academy in Tunis – Tunisia.

His research activities include patch antennas and propagation.

Taoufik Aguili received his Engineering degree in Electrical Engineering and his Ph.D. degree in Telecommunications from INSA, France. He is working as Professor at the National Engineering School of Tunis (ENIT).

His research activities include electromagnetic microwave circuits modelling and analysis of scattering and propagation phenomena in free space.

Compact Differential Parallel Coupled Line Band-pass Filter with Open Stub

Dong-Sheng La [1,2], Shou-Qing Jia [1], Long Cheng [1], and Xue-Lian Ma [1]

[1] School of Computer Science and Engineering
Northeastern University, Shenyang, 110819, P. R. China
ladongsheng@163.com, jiashouqing@163.com, chenglong8501@gmail.com, xuelianma2011@163.com

[2] State Key Laboratory of Millimeter Waves
Southeast University, Nanjing, 210096, P. R. China.

Abstract ─ A novel differential narrow-band band-pass filter design method is presented based on the parallel coupled line and the open stub. Based on the transmission line model, the proposed differential band-pass filter is analyzed by using even- and odd-mode analytical method. The central resonant frequency of the proposed differential filter is given. The relations between the filtering performance and the impedance parameters are discussed. A compact differential band-pass filter is designed based on the resonant conditions. The common mode signal is well suppressed. The differential band-pass filter is simulated, fabricated and measured. The measured results and the simulated results are basically consistent.

Index Terms ─ Differential band-pass filter, even- and odd-mode analysis, microwave components, open stub, parallel coupled line.

I. INTRODUCTION

Due to its insensitivity to fabrication tolerance and simple synthesis procedures, the parallel coupled line structure is finding wide use in many band-pass filters [1, 2]. The differential filters can suppress the crosstalk, environmental noise, and interference between different elements, so they are widely used in microwave systems. Wang proposed an ultra-wideband differential band-pass filter based on a self-coupled ring resonator. The differential-mode circuit is composed of the meandered fully coupled parallel microstrip lines and short end fully coupled parallel microstrip lines in shunt [3]. Wang proposed a differential broadband filter, which is composed of four quarter-wavelength coupled lines and four quarter-wavelength microstrip lines [4]. By adding the quarter-wavelength microstrip lines, the filtering response has been improved. A differential narrow-band band-pass filter with the input and output capacitive feedings is presented. It is composed of the open end fully coupling parallel microstrip lines and short end fully coupling parallel microstrip lines in shunt [5]. Li presented a differential wide-band band-pass filter composed of a coupled fully wavelength loop [6].

The differential parallel coupled line filters which are the simple structures suffer from spurious responses at the multiples of operating frequency. To eliminate the spurious responses, especially for the second spurious responses, some methods have been proposed. Zhou proposed a novel differential band-pass filter based on the cascaded parallel coupled lines [7]. The spurious response at $2f_0$ moves to higher frequency. Based on the modified coupled feed lines and the coupled line stubs/the coupled line stub loaded resonators, the wideband balanced filters with high selectivity and common mode (CM) suppression are proposed and designed [8].The spurious response at $2f_0$ is suppressed.

In this paper, a differential narrow-band band-pass filter is proposed. The proposed differential band-pass filter is composed of the parallel coupled line and the open stub. Based on odd-even mode analytical method, the differential mode (DM) equivalent circuit is analyzed and discussed. The relations between the filtering response and the filter's parameters are discussed. The harmonic frequencies at the multiples of operating frequency are suppressed. At the same time, the common mode interference is well restrained. Comparing the simulation result with experimental result, it is found that they are basically consistent.

II. DIFFERENTIAL FILTER DESIGN

The schematic of the proposed differential parallel coupled line band-pass filter is shown in Fig. 1 (a). The proposed differential band-pass filter is composed of the parallel coupled line and the open stub. The filter's DM and CM equivalent circuits are derived in Figs. 1 (b) and (e), respectively. The filter's DM equivalent circuit is symmetric, so it can be studied through even- and odd-mode analytical method. Figures 1 (c) and (d) are the even mode half equivalent circuit and the odd mode half equivalent circuit of the filter's DM equivalent circuit.

Submitted On: May 27, 2016
Accepted On: December 26, 2016

The electric lengths of the proposed differential band-pass filter are a_1, a_2 and a_3. The characteristic impedance of the open stub is Z_1. The odd mode impedance and the even mode impedance of the parallel coupled lines are Z_o and Z_e, respectively.

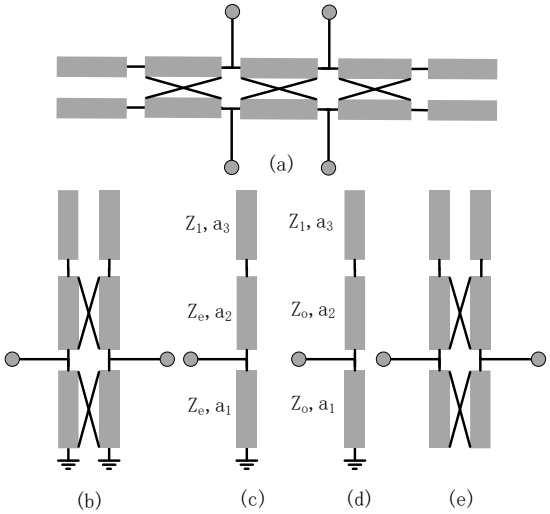

Fig. 1. Proposed differential band-pass filter. (a) Circuit, (b) DM circuit, (c) the even mode half equivalent circuit, (d) the odd mode half equivalent circuit, and (e) CM circuit.

A. Filter design equation

For simplicity, it is assumed that the even mode propagation is equal to the odd mode propagation ($\theta_e = \theta_o = \theta_0$). It is also assumed that the electric lengths are $a_1 = \theta$, $a_2 = 2\theta$, $a_3 = 2\theta$. The form of the even mode half equivalent circuit is the same as the odd mode half equivalent circuit, so the even mode input impedance expression is the same as the odd mode input impedance expression. The even (or odd) mode input impedance can be calculated by the formula (1). By enforcing $Z_{ine(o)} = \infty$, the solutions of $\tan\theta$ for the corresponding resonant frequencies can be obtained by using formula (2). The corresponding resonant frequencies include the central resonant frequency (θ_0), the even mode resonant frequency (θ_e) and the odd mode resonant frequency (θ_o). In order to realize the miniaturization of the filter, the smaller solution of $tan\theta$ can be calculated by using formula (3):

$$Z_{ine(o)} = \frac{jZ_e \tan\theta[Z_1 \tan^4\theta - (4Z_e + 2Z_1)\tan^2\theta + Z_1]}{(2Z_e + 3Z_1)\tan^4\theta - (6Z_e + 4Z_1)\tan^2\theta + Z_1}, \quad (1)$$

$$(2Z_e + 3Z_1)\tan^4\theta - (6Z_e + 4Z_1)\tan^2\theta + Z_1 = 0, \quad (2)$$

$$\tan\theta = \sqrt{\frac{3Z_e + 2Z_1 - \sqrt{9Z_e^2 + 10Z_eZ_1 + Z_1^2}}{2Z_e + 3Z_1}}. \quad (3)$$

Based on the impedance characteristics of the microstrip line, it is assumed that the range of the normalized Z_1 is from 1.6 to 1.8. It is also assumed that the range of θ is from 13.5° to 22.5°. Figure 2 shows the variation of the normalized $Z_{e(o)}$ against different normalized Z_1 and θ_0. When Z_1 is fixed, $Z_{e(o)}$ will decrease with the increase of θ. When θ is fixed, $Z_{e(o)}$ will increase with the increase of Z_1. Since Z_e is more than Z_o, $\theta_e < \theta_0 < \theta_o$ is obtained. If θ_e, θ_0 and θ_o are chosen, the impedance parameters can be obtained in Fig. 2. It is possible to realize the proposed band-pass filter based on the angle parameters and the impedance parameters.

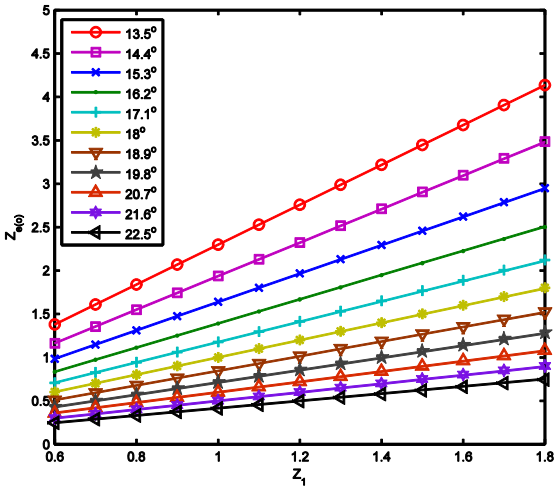

Fig. 2. Variation of the normalized Z_e (or Z_o) against different normalized Z_1 and θ.

B. Performance of the proposed differential filter

In order to study the DM filtering response of the proposed differential band-pass filter, the following three conditions are analyzed and discussed. The proposed differential band-pass filter against different Z_1 is analyzed when $\theta_0 = 18^o$, $\theta_e = 17.1^o$ and $\theta_o = 18.9^o$ are fixed. Table 1 gives three groups of the proposed differential band-pass filter's normalized impedance parameters when $\theta_0 = 18^o$, $\theta_e = 17.1^o$ and $\theta_o = 18.9^o$ are assumed. Based on the parameters in Table 1, the DM S-parameters of the proposed differential band-pass filter can be calculated by using formula (4) and (5) [9]:

$$S_{11dd} = S_{22dd} = \frac{Z_{ine}Z_{ino} - 1}{(Z_{ine} + 1)(Z_{ino} + 1)}, \quad (4)$$

$$S_{21dd} = S_{12dd} = \frac{Z_{ine} - Z_{ino}}{(Z_{ine} + 1)(Z_{ino} + 1)}. \quad (5)$$

The calculated DM S-parameters of the proposed differential band-pass filter with different Z_1 are shown in Fig. 3. With the decrease of Z_1, the DM filtering response has been improved in the pass-band. The DM

performance will become worse in the pass-band when Z_1 decreases to a certain value.

Table 1: The differential band-pass filters' normalized impedance parameters ($\theta_0 = 18^o$, $\theta_e = 17.1^o$, $\theta_o = 18.9^o$)

	Z_1	Z_e	Z_o
Filter 1	1.1	1.30	0.93
Filter 2	1.3	1.53	1.10
Filter 3	1.5	1.77	1.27

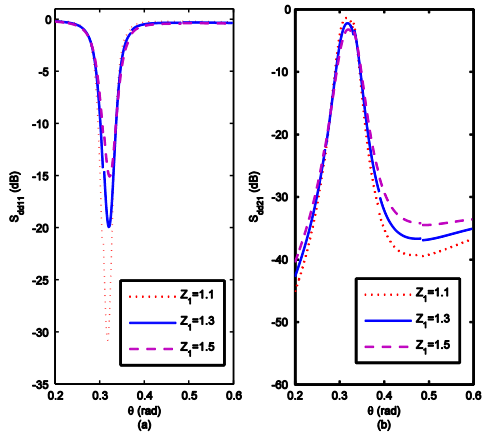

Fig. 3. Variation of (a) S_{dd11} and (b) S_{dd21} against different Z_1.

At the same time, the proposed differential band-pass filter against different $\theta_e - \theta_o$ is analyzed when Z_1 and θ_0 are fixed. Table 2 gives the angle parameters and the normalized impedance parameters of the proposed differential band-pass filter. Figure 4 shows the calculated DM S-parameters of the proposed differential band-pass filter with different $\theta_o - \theta_e$, 0.9º, 1.8º and 3.6º, respectively. When Z_1 and θ_0 are fixed, the DM performance of the proposed differential band-pass filter is improved with the increase of $\theta_o - \theta_e$. Similarly, the DM performance will be worse when $\theta_o - \theta_e$ increases to a certain value. When Z_1 and θ_0 are fixed, the location of the transmission zero remains the same.

When $(\theta_e - \theta_o)/\theta_0$ (fractional bandwidth) and Z_1 are fixed, the DM performance of the proposed differential band-pass filter against different θ_0 is discussed. Table 3 gives the angle parameters and the normalized impedance parameters. Figure 5 shows the calculated DM S-parameters of the proposed differential band-pass filter against different θ_0 . The calculated DM S-parameters of the proposed differential band-pass filter with different θ_0 are shown in Fig. 5. The DM performance of the proposed differential band-pass filter is improved with the increase of θ_0 . As before, the DM performance of the proposed differential band-pass filter becomes worse when θ_0 reaches to a certain value. The location of the transmission zero moves to low frequency with the increase of θ_0 .

Table 2: The differential band-pass filters' angle parameters and normalized impedance parameters ($Z_1 = 1.3$, $\theta_0 = 18^o$)

	θ_e (deg)	θ_o (deg)	Z_e	Z_o
Filter 4	17.55	18.45	1.41	1.20
Filter 2	17.1	18.9	1.53	1.10
Filter 5	16.2	19.8	1.81	0.93

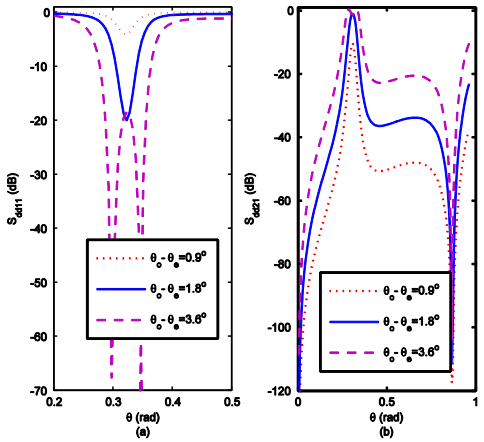

Fig. 4. Variation of (a) S_{dd11} and (b) S_{dd21} against different $\theta_e - \theta_o$.

When $(\theta_e - \theta_o)/\theta_0$ (fractional bandwidth) and Z_1 are fixed, the DM performance of the proposed differential band-pass filter against different θ_0 is discussed. Table 3 gives the angle parameters and the normalized impedance parameters. Figure 5 shows the calculated DM S-parameters of the proposed differential band-pass filter against different θ_0 . The calculated DM S-parameters of the proposed differential band-pass filter with different θ_0 are shown in Fig. 5. The DM performance of the proposed differential band-pass filter is improved with the increase of θ_0 . As before, the DM performance of the proposed differential band-pass filter becomes worse when θ_0 reaches to a certain value. The location of the transmission zero moves to low frequency with the increase of θ_0 .

Table 3: The differential band-pass filters' normalized impedance parameters and angle parameters ($Z_1 = 1.3$, $(\theta_e - \theta_o)/\theta_0 = 0.1$)

	θ_0 (deg)	θ_e (deg)	θ_o (deg)	Z_e	Z_o
Filter 6	16	15.2	16.8	2.17	1.62
Filter 2	18	17.1	18.9	1.53	1.10
Filter 7	20	19	21	1.08	0.74

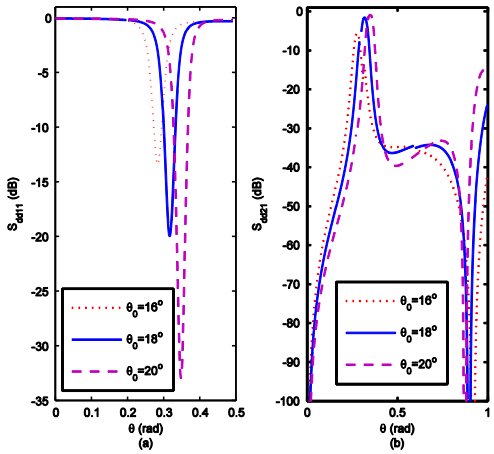

Fig. 5. Variation of (a) S_{dd11} and (b) S_{dd21} against different θ_0.

III. SIMULATION AND MEASUREMENT

To verify the design theory, a differential band-pass filter is designed based on the angle parameters and the normalized impedance parameters of Filter 2 in Table 1. Figure 6 (a) shows the proposed differential band-pass filter's configuration. The open stubs are bent for filter's size reduction. The substrate with a relative dielectric constant of 2.2, thickness of 0.508 mm and loss tangent of 0.0009 is used. Based on the parameters in Table 1, the initial physical sizes of the proposed differential band-pass filters are obtained by ADS LineCalc tool. Considering the bends and open ends, the final physical sizes of Filter 2 are a=t=1 mm, b=10 mm, c=2 mm, d=8 mm, g=0.4 mm, w=1.55 mm. A differential band-pass filter is fabricated based on Rogers RT/duroid 5880 (tm) and shown in Fig. 6 (b).

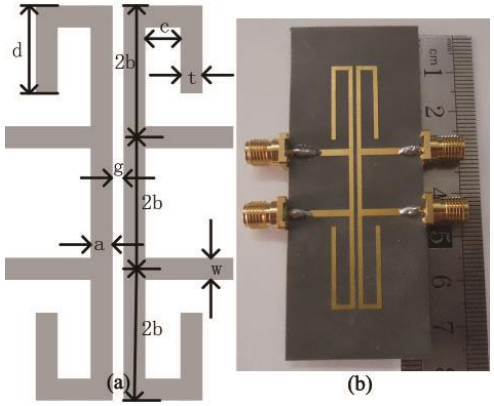

Fig. 6. (a) Configuration and (b) photograph of the proposed differential band-pass filter.

DM and CM S-parameters are simulated by HFSS 14.0 and measured by Agilent Technologies' 5230 A vector network analyzer, which are shown in Fig. 7. The measured results of Filter 2 in Fig. 7 show that the differential mode filtering performance is good. 3 dB bandwidth is 0.25 GHz which is from 1.04 GHz to 1.29 GHz. There are five transmission zeros, which are located at 0, 1.72 GHz, 3.45 GHz, 4.35 GHz and 6.25 GHz. A wide stop-band and good selectivity are obtained through the transmission zeros. The common mode suppression is good out of band. The simulated and measured results show a good agreement and validate the proposed theory. The tiny difference between the simulated results and the test results is due to the unexpected tolerance of fabrication, the substrate dielectric loss, and SMA connectors. The frequency differences between the calculated results and the measured results are derived from the effect of the open ends and the bends. The central frequency of the differential band-pass filter can be adjusted by the electric length θ. 3 dB bandwidth can be adjusted through the gap width g.

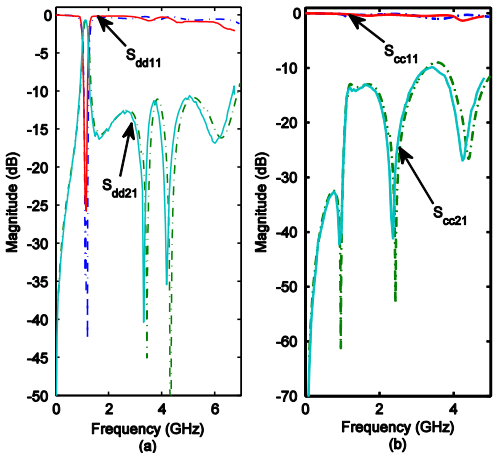

Fig. 7. Simulated and measured results of Filter 2: (a) DM response and (b) CM response (the solid line is the measured results, and the dotted line is the simulated results).

Table 4 shows the comparisons with the proposed differential parallel coupled line band-pass filter. As can be seen in Table 4, the size of the filter in Ref. [3] is small, but the harmonic suppression needs to be improved. In Ref. [4] and Ref. [5], the sizes of the filters are larger and the harmonic suppression also needs to be improved. The harmonic suppression of the filter in Ref. [7] is better, but the size of the filter is larger. In this paper, the proposed differential parallel coupled line filter has both good harmonic suppression and small size, which can realize the miniaturized wide-stop-band differential band-pass filter design. In addition, the structure of the proposed differential parallel coupled line band-pass filter is simple, so it is convenient for theoretical calculation and filter design.

Table 4: Comparisons with the proposed differential parallel coupled line band-pass filter

	The First Spurious Response (GHz)	Transmission Zeros	Out-band Rejection (dB)	Size (λ_g^2)
[3]	$2.5f_0$	2	>10	0.0300
[4]	$2.3f_0$	2	>10	0.4998
Filter 1 in [5]	$2.1f_0$	3	>18	0.1681
[7]	$> 2.7f_0$	5	>20	0.2000
This work	$> 6f_0$	5	>11	0.0139

IV. CONCLUSION

A differential band-pass filter based on the parallel coupled lines and the open stubs is proposed. The transmission line model of the differential band-pass filter is given. The design equations are obtained through even and odd analytical method. The relations between the parameters of the proposed differential filter and the filtering response are analyzed and discussed. The differential band-pass filter is designed, simulated, fabricated and measured. Comparing the simulation result with experimental result, it was found that they were basically consistent, which verifies the design theory. The proposed differential band-pass filter exhibits good DM performance and good CM suppression. Both the structure and the design process of the proposed differential filter are simple, so it can be widely used in microwave circuits.

ACKNOWLEDGMENT

This work was supported by National Natural Science Foundation of China under Grant 61501100, 61403068, 61601105, Research Fund for Higher School Science and Technology in Hebei Province under Grant QN20132014, the Fundamental Research Funds for the Central Universities under Grant N142303003, N110323006 and the Open Project of the State Key Laboratory of Millimeter Waves under Grant K201705.

REFERENCES

[1] Y. Li, H. C. Yang, Y. W. Wang, and S. Q. Xiao, "Ultra-wideband band-pass filter based on parallel-coupled microstrip lines and defected ground structure," *ACES Journal*, vol. 28, no. 1, pp. 21-26, Jan. 2013.

[2] W. J. Feng, M. L. Hong, and W. Q. Che, "Narrow-band band-pass filters with improved upper stop-band using open/shorted coupled lines," *ACES Journal*, vol. 31, no. 2, pp. 152-158, Feb. 2016.

[3] H. Wang, Y. Q. Yang, W. Kang, W. Wu, K. W. Tam, and S. K. Ho, "Compact ultra-wideband differential band-pass filter using self-coupled ring resonator," *Electronics Letters*, vol. 49, no. 18, pp. 1156-1157, Aug. 2013.

[4] X. H. Wang, S. Hu, and Q. Y. Cao, "Differential broadband filter based on microstrip coupled line structures," *Electronics Letters*, vol. 50, no. 15, pp. 1069-1070, July 2014.

[5] H. Wang, K. W. Tam, W. W. Choi, W. Y. Zhuang, S. K. Ho, W. Kang, and W. Wu, "Analysis of coupled cross-shaped resonator and its application to differential band-pass filters design," *IEEE Transactions on Microwave Theory and Techniques*, vol. 62, no. 12, pp. 2942-2953, Dec. 2014.

[6] L. Li, J. Bao, J. J. Du, and Y. M. Wang, "Compact differential wideband band-pass filters with wide common-mode suppression," *IEEE Microwave and Wireless Components Letters*, vol. 24, no. 3, pp. 164-166, Mar. 2014.

[7] J. G. Zhou, Y. C. Chiang, and W. Q. Che, "Compact wideband balanced band-pass filter with high common-mode suppression based on cascade parallel coupled lines," *IET Microwaves, Antennas and Propagation*, vol. 8, no. 8, pp. 564-570, Aug. 2014.

[8] Q. X. Chu and L. L. Qiu, "Wideband balanced filters with high selectivity and common-mode suppression," *IEEE Transactions on Microwave Theory and Techniques*, vol. 63, no. 10, pp. 3462-3468, Oct. 2015.

[9] J. S. Hong and M. J. Lancaster, *Microstrip Filters for RF/Microwave Applications*. New York: Wiley, 2001.

Dong-Sheng LA was born in Hebei, P. R. China. He has received his Masters degrees from Xinjiang Astronomical Observatory, Chinese Academy of Sciences in 2008, and his Ph.D. degrees from Beijing University of Posts and Telecommunications in 2011. He is currently a Lecturer in the School of Computer Science and Engineering, Northeastern University in P. R. China. His recent research interests include passive RF components, patch antennas and electromagnetic compatibility. He has authored or coauthored over 20 journal and conference papers.

Shou-Qing JIA was born in Henan, China, in 1981. He received his M.Sc. degree and Ph.D. in Electromagnetic Field and Microwave Technology both from Peking University, respectively in 2007 and 2013. He is currently working at the School of Computer Science and

Engineering, Northeastern University in P. R. China. His research interests include computational electromagnetic and Radar signal processing.

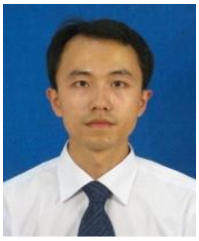

Long CHENG received his B.S. degree in Automatic Control from Qingdao University of Science and Technology, Qingdao, China, in 2008, the M.S. degree in Pattern Recognition and Intelligent System from Northeastern University, Shenyang, China, in 2010. He received Ph.D. degree in Pattern Recognition and Intelligent System from Northeastern University, Shenyang, China, in 2013. Now, he is an Assistant Professor in Northeastern University. His research interests include wireless sensor networks and distributed system.

Xue-Lian MA was born in Liaoning, China, in 1981. She received her Ph.D. in Radio Physics at Peking University. She is currently a Lecturer in the School of Computer Science and Engineering, Northeastern University in China. Her recent research interests include fiber communication, wireless optical communication and atmospheric optics.

A Compact Dual-band Planar 4-Way Power Divider

Ahmad Mahan [1], Seyed Hassan Sedighy [2*], and Mohammad Khalaj-Amirhosseini [1]

[1] Department of Electrical Engineering
Iran University of Science and Technology, Tehran, Iran
ahmad_mahan@elec.iust.ac.ir, khalaja@iust.ac.ir

[2] School of New Technologies
Iran University of Science and Technology, Tehran, Iran
sedighy@iust.ac.ir

Abstract ─ In this paper, an optimized approach based on T-shaped step impedance transmission line is proposed to design a compact dual band 4-way planar power divider. In the proposed structure, the 100 Ω quarter wavelength transmission lines are equaled by the T-shaped step impedance transmission lines (SITLs) which achieve the design equations with two freedom degrees. Then, the invasive weed optimization is used to find the optimized design parameters. Three power dividers with different operation frequencies ratio are designed and simulated to show the method ability. Finally, one 4-way planar power divider is fabricated and measured to verify the ability and power of the proposed approach which shows 53% compactness and proper specifications in both the operation frequencies.

Index Terms ─ Compact, dual band, planar, power divider.

I. INTRODUCTION

Power dividers are key passive components in microwave and millimeter-wave systems. The Wilkinson power divider, branch line and rate race are some examples of these passive devices [1]. These power dividers have narrow bandwidth and occupy large sizes, which limit their application and flexibility in the microwave circuits. Due to the dual band requirement in wireless communication systems, some techniques have been used to achieve the dual band attribute in these power dividers scheme such as non-uniform transmission lines, using non-uniform transmission lines, stubs and reactive components [2-5]. The 4-way power divider which is a useful component in RF applications have been considered in the literature. A 4-way Wilkinson power divider with band passes filtering response has been proposed in [6]. Very recently, a compact four-way dual-band microstrip power divider has been proposed in [7] by using RLC lumped elements which can limit the fabrication process and increase the cost. In this paper, a planar compact dual band 4-way power divider is proposed. This divider is based on the planar single band divider scheme proposed in [8] composed of four 100 Ω quarter wavelength transmission lines where its output ports are connected by 70.711 Ω resistors to enhance the output isolations. To achieve the compact and dual band specifications in this divider, the quarter wavelength transmission line segments are replaced by T-shaped step impedance transmission lines (SITLs). Using step impedance transmission line technique is a well-known approach to compact the microwave circuits as discussed in [9-11]. The proposed T-shaped SITL is composed of a stepped transmission line with an open stub in the middle which increases the freedom degrees in the design process. The T-shaped SITLs have been used previously to achieve dual band applications in some RF devices such as [12-13]. Here, a symmetric simple T-shaped SITL is used to achieve dual band and compact specifications in a planar divider. For this purpose, the equality between 100 Ω quarter wavelength transmission lines and T-shaped SITLs achieves the complex design equations. Then, a stochastic invasive weed optimization algorithm (IWO) [14-18] is used to find the best answer of the design equations, which is the desired dual band and compact planar 4-way divider. This optimization has been applied previously to compact the microwave devices such as filters [19-20], also. Three different planar compact power dividers are designed with different arbitrary operation frequencies to verify the proposed design approach. Finally, one of these cases is fabricated and measured which works at f_1=450 MHz and f_2=2.835 GHz with 56 mm×56 mm dimensions ($0.51\lambda_{g0} \times 0.51\lambda_{g0}$, where λ_{g0} is the guided wavelength at the center frequency between f_1 and f_2) which shows 53% compactness compared with one composed of two sections transmission line topology in [21]. The mean value of the insertion losses and isolation at both operation frequencies are better than 6.5 dB and 15 dB, respectively. These good specifications are comparable

Submitted On: May 8, 2016
Accepted On: October 31, 2016

with the proposed divider in [7] but without lumped element usage limitations. The simplicity, arbitrary ratio of two operation frequencies, high enough port isolation and low insertion loss verify the ability of the proposed divider compared with the references.

II. THEORY AND DESIGN

A. Design equation

A planar 4-way power divider has been introduced in [1] which is composed of four equal 100 Ω transmission lines. The output ports are connected by 70.711 Ω resistors to enhance the output isolations. The main part of this structure is the quarter wavelength transmission lines which limit the device operation bandwidth and occupies a large area.

To achieve a compact and dual band structure, T-shaped step impedance transmission lines (SITL) are used instead of these quarter wavelength transmission lines as shown in Fig. 1. The T-shaped SITL is composed of three different transmission line segments with Z_1, Z_2 and Z_3 characteristic impedances and θ_1, θ_2 and θ_3 electrical lengths, respectively as shown in Fig. 1. These T-shaped SITLs and quarter wavelength 100 Ω transmission line should have equal properties at two different frequencies, f_1 and f_2. For this purpose, the ABCD matrices of these structures should be equaled at these two frequencies as:

$$\begin{bmatrix} 0 & j100 \\ j\frac{1}{100} & 0 \end{bmatrix} = \begin{bmatrix} \cos(\theta_1^{f_i}) & jZ_1\sin(\theta_1^{f_i}) \\ j\frac{1}{Z_1}\sin(\theta_1^{f_i}) & \cos(\theta_1^{f_i}) \end{bmatrix} \times \begin{bmatrix} \cos(\theta_2^{f_i}) & jZ_2\sin(\theta_2^{f_i}) \\ j\frac{1}{Z_2}\sin(\theta_2^{f_i}) & \cos(\theta_2^{f_i}) \end{bmatrix} \times \begin{bmatrix} 1 & 0 \\ j\frac{1}{Z_3}\tan(\theta_3^{f_i}) & 1 \end{bmatrix} \times \begin{bmatrix} \cos(\theta_2^{f_i}) & jZ_2\sin(\theta_2^{f_i}) \\ j\frac{1}{Z_2}\sin(\theta_2^{f_i}) & \cos(\theta_2^{f_i}) \end{bmatrix} \times \begin{bmatrix} \cos(\theta_1^{f_i}) & jZ_1\sin(\theta_1^{f_i}) \\ j\frac{1}{Z_1}\sin(\theta_1^{f_i}) & \cos(\theta_1^{f_i}) \end{bmatrix}, \quad (1)$$

where f_i denotes f_1 and f_2. The middle stub (Z_3, θ_3) is considered as loaded shunt impedance which is located between two transmission line segments.

Notice that the effect of discontinuities has been ignored in this relation for simplicity. Since the T-shaped SITL is considered as symmetric, reciprocal and lossless circuit, only two independent equations are achieved at each frequency from (1). The electrical lengths of T-shaped SITL segments are related to their physical length by:

$$\theta_{1,2,3}^{f_i} = \frac{2\pi}{\lambda_g^{f_i}} l_{1,2,3}, \quad (2)$$

where $\lambda_g^{f_i}$ is the guided wavelength at f_i. If the ratio of two operation frequencies are considered as K, then,

$$f_2 = Kf_1 \qquad \lambda_g^{f_2} = \frac{1}{K}\lambda_g^{f_1} \qquad \theta_{1,2,3}^{f_2} = K\theta_{1,2,3}^{f_1}. \quad (3)$$

In other words, to design a dual band divider, we have four independent equations with six unknown variables, Z_1, Z_2, Z_3, θ_1, θ_2 and θ_3. After some complex algebraic calculations, these equations can be expressed as:

$$\begin{aligned} &\left(\cos^2(\theta_1^{f_i}) - \sin^2(\theta_1^{f_i})\right)\left(\cos^2(\theta_2^{f_i}) - \sin^2(\theta_2^{f_i})\right) \\ &-\left(\frac{1}{2}\sin(2\theta_1^{f_i})\sin(2\theta_2^{f_i})\right)\left(\frac{Z_2^2 + Z_1^2}{Z_1 Z_2}\right) \\ &+\left(\frac{\tan(\theta_3^{f_i})}{2Z_3}\right)\left(Z_2(2\sin^2(\theta_1^{f_i}) - 1)\sin(2\theta_2^{f_i})\right) \\ &+\sin(2\theta_1^{f_i})\left(\frac{Z_2^2}{Z_1}\sin^2(\theta_2^{f_i}) - Z_1\cos^2(\theta_2^{f_i})\right) = 0, \end{aligned} \quad (4)$$

$$\begin{aligned} &\sin(2\theta_2^{f_i})\left(Z_2\cos^2(\theta_1^{f_i}) - (\frac{Z_1^2}{Z_2})\sin^2(\theta_1^{f_i})\right) + \\ &Z_1\sin(2\theta_1^{f_i})\left(2\cos^2(\theta_2^{f_i}) - 1\right) - \left(\frac{\tan(\theta_3^{f_i})}{Z_3}\right) \\ &\times\left(\begin{aligned} &Z_1^2\sin^2(\theta_1^{f_i})\cos^2(\theta_2^{f_i}) + Z_2^2\sin^2(\theta_2^{f_i})\cos^2(\theta_1^{f_i}) \\ &+\frac{Z_1 Z_2}{2}\sin(2\theta_1^{f_i})\sin(2\theta_2^{f_i}) \end{aligned}\right) = 100. \end{aligned} \quad (5)$$

It can be seen that there are two freedom degrees in these equation systems. An optimization algorithm is used to solve this nonlinear equation system in the next section.

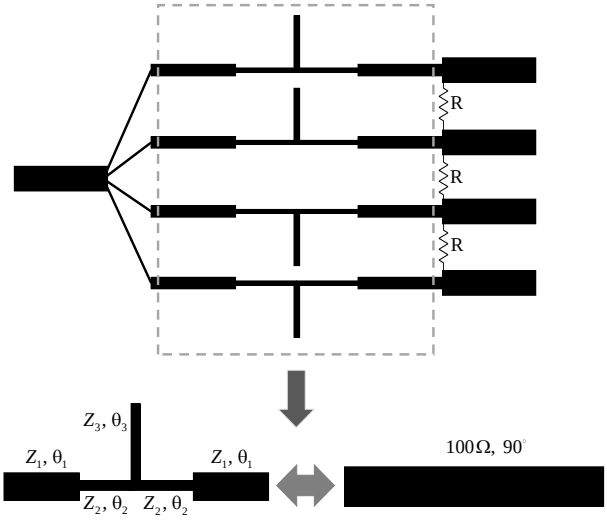

Fig. 1. (a) Structure of proposed planar dual band 4-way power divider, and (b) equivalent circuit of quarter wavelength transmission line with T-shaped SITL.

B. Optimization

The invasive weed optimization (IWO) algorithm is composed of the natural inspired behaviours of invasive weeds such as seeding, growth, and competitive exclusion

to reach the rich soil area. This optimization process is initialized by random spatial dispersion of the seed population, P_{max}. After seeds growth to weeds, their fitness are calculated based on the predefined cost function. Then each weed reproduces some new seeds between S_{min} and S_{max} corresponding to its relative fitness in the weed population. This distribution is performed by a normal distribution with variable variance versus the iterations around the corresponding weed as:

$$\sigma_{iter} = \frac{(iter_{max} - iter)^n}{(iter_{max})^n}(\sigma_{initial} - \sigma_{final}) + \sigma_{final}, \qquad (6)$$

where *iter* and $iter_{max}$ are the current and maximum iteration numbers, respectively. Therefore, the dispersion variance is decreased from $\sigma_{initial}$ value to σ_{final} which leads the seeds to focus around the optimum answer. All of the new grown seeds and old weeds compete with each other to eliminate the week members when the population is reached to the maximum allowable members, P_{max}. This process continues through the iterations to achieve the best cost function value and the global optimum problem response, consequently. This optimization method has been verified to be effective in converging to an optimal solution by employing basic properties such as seeding, growth, and competition in a weed colony. The main advantage of the IWO algorithm is its independency from the initial conditions [14].

In this problem, the optimal goal is solving (4) and (5) as well as decreasing the total circuit length to achieve a compact dual band 4-way divider which can be formulated as:

$$e_t = \sqrt{e_{A_1}^2 + e_{A_2}^2 + 0.01\times e_{B_1}^2 + 0.01\times e_{B_2}^2 + W\theta_{Total}}, \qquad (7)$$

where $\theta_{Total} = 2(\theta_1 + \theta_2)$ is the total electrical length of the T-shaped SITL, and e_{A1} and e_{A2} are the differences between two sides of (4) at f_1 and f_2, respectively. In a same way, e_{B1} and e_{B2} are the differences between two sides of (5) at f_1 and f_2, respectively. This cost function should be minimized to achieve the best solution for (4) and (5) as well as compactness. Notice these errors are multiplied by 0.01 to achieve balanced values compared with e_{A1} and e_{A2}. Since there is a trade-off between the equations satisfactions (e_{Ai} and e_{Bi}) and compactness (θ_{Total}), *W* is considered as a weighting factor in (7) for their importance balancing. In other words, *W* should be chosen as high as that (4) and (5) are satisfied at both frequencies, properly. The simulation results shown that 0.25 is a good value for this coefficient.

The optimization algorithm tries to minimize this error function by proper choosing of design variables, Z_1, Z_2, Z_3, θ_1, θ_2 and θ_3. The optimization parameters are tabulated in Table 1.

Table 1: IWO optimization parameters

Parameters	Description	Range
$Z_{1,2,3}$ (Ω)	Impedance	10Ω~170Ω
$\theta_{1,2,3}$ (deg)	Electrical length	1°~30°
N	Initial population	200
P_{max}	Maximum population	200
S_{min}	Minimum seed	2
S_{max}	Maximum seed	10
$\sigma_{initial}^{Z}$	Initial impedance variance	75
$\sigma_{initial}^{\theta}$	Initial electrical lengths variance	30
$\sigma_{final}^{Z,\theta}$	Final variance	0.5
Iteration	Repeat operations	1000

III. SIMULATION AND MEASUREMENT RESULTS

A. Different cases

To validate the proposed design process, three power dividers with different *K* are designed as tabulated in Table 2. Also, the design parameters are reported in this table. As it can be seen, the T-shaped SITs in these three cases are compact rather than the uniform quarter wavelength transmission lines. The compactness reported in the table is achieved by comparison of each case with two sections transmission line topology, one works at the first operation frequency, f_1=450 MHz and the other one works at the second one, f_2. Notice that this technique can be used to achieve dual band operation in Wilkinson power dividers as reported in [21]. All electrical lengths reported in the table are computed respect to f_1=450 MHz, also. Figure 2 depicts the error functions versus the iterations for Case A, B and C which prove the convergence of the algorithm in different cases. Notice that the stepwise behavior depicted in Fig. 2 is due to go out of the algorithm from the local minimums and converge to the global minimum response.

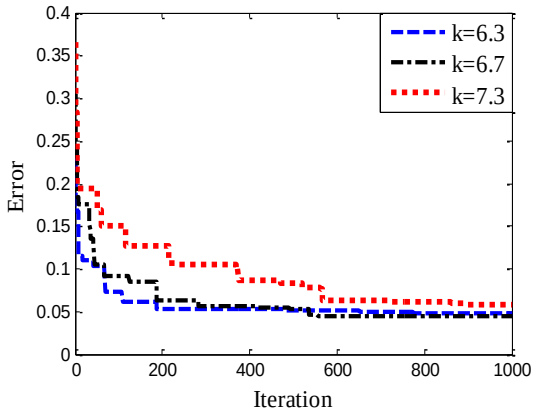

Fig. 2. The error function versus iterations in Case A.

Table 2. Characteristic impedances and electrical length of three T-shaped SITLs cases

Case	*A* *K=6.3*	*B* *K=6.7*	*C* *K=7.3*
$Z_1(\Omega)$	169.6	169.6	87.7
$Z_2(\Omega)$	148.3	162.0	169.9
$Z_3(\Omega)$	132.7	101.9	157.8
$\theta_1^{f_1}$ (deg)	13.5	11.1	7.2
$\theta_2^{f_1}$ (deg)	19.2	20.2	24.4
$\theta_3^{f_1}$ (deg)	29.37	32.4	44.8
θ_{Total} (deg)	65.4	62.6	63.2
Compactness	52.97%	54.75%	54.55%
Error	0.048	0.045	0.058

Figure 3 shows the simulation results of three 4-way power dividers. Theses dividers are implemented on RO4003 substrate with $\varepsilon_r = 3.55$ and 0.762 mm thickness. As it can be seen, all of these three cases are works at f_1=450 MHz, properly as it expected from the design process. The simulation results depict a very small deviation in the second operation frequencies, f_2 and small change in K, consequently. Notice that all simulations are performed by using Advance Design System Software, ADS 2011. These results verify that ignoring the step discontinuities which was not considered in the design equations, are not affected the design process, significantly.

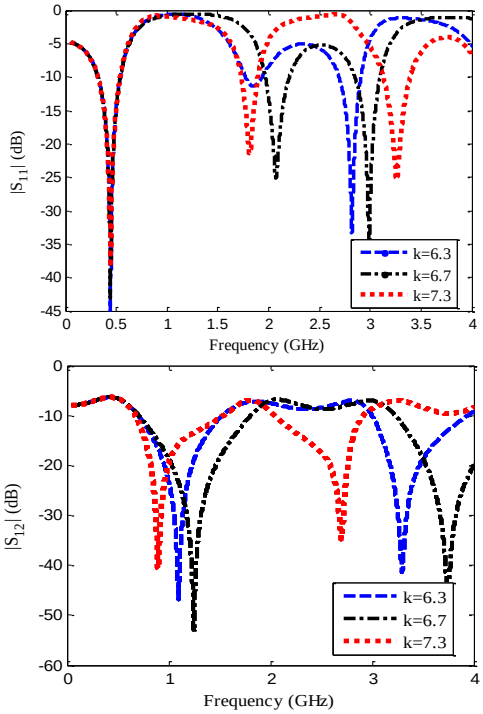

Fig. 3. The simulation results of $|S_{11}|$ and $|S_{12}|$ in three design cases.

B. Fabrication and measurement

To validate the design process, one of the proposed cases, the Case A is fabricated on RO4003 substrate with 0.762 mm thickness as shown in Fig. 4. The meander line technique is used in this 4-way power divider to achieve more compactness. Also, the 402 surface mounted resistors are used to achieve the designed isolation between the output ports. The total length of this fabricated divider is 56 mm×56 mm dimensions ($0.51\lambda_{g0} \times 0.51\lambda_{g0}$, λ_{g0} = the guided wavelength at the center frequency between f_1 and f_2) which shows 53% compactness compared with the one proposed in [21]. Notice that the meander line contribution in the power divider length reduction is about 5%.

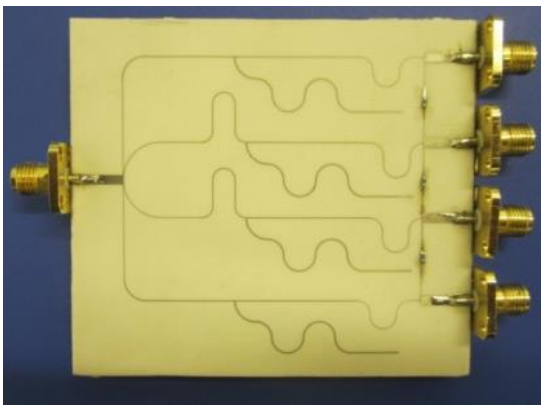

Fig. 4. The fabricated 4-way compact dual-band planar power divider (case A with *K*=6.3).

The simulation and measurement results of the proposed divider are depicted in Fig. 5. Notice that the small differences between simulation and measurement results are due to the fabrication process limitation. The mean value of the insertion losses and isolation at both operation frequencies are better than 6.3 dB and 15 dB, respectively. Therefore, this compact dual band power divider has a small insertion loss, good matching, and isolation performances at the desired dual bands. These good specifications verify the capability and ability of the proposed method.

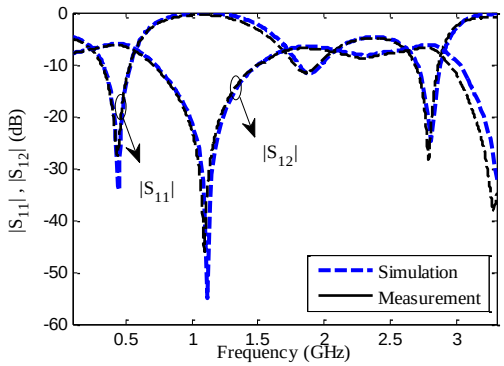

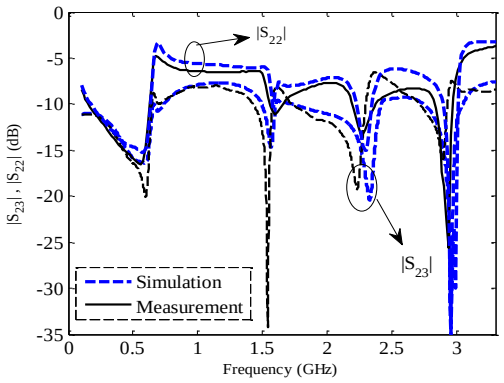

Fig. 5. Simulation and measurement results of $|S_{11}|$, $|S_{12}|$, $|S_{22}|$ and $|S_{23}|$.

IV. CONCLUSION

An optimized approach has been proposed to design a 4-way planar compact dual band power divider. In this approach, the 100 Ω quarter wavelength transmission lines have been replaced by the T-shaped SITLs. The invasive weed optimization has been used to find the optimized design parameters of the divider. Three power dividers with different frequencies ratio were designed and simulated to verify the idea. Finally, one of these dividers has been fabricated and measured which showed 53% compactness and proper specifications in both the operation frequencies.

REFERENCES

[1] D. M. Pozar, *Microwave Engineering*. 3rd ed., New York: J. Wiley & Sons, 2005.

[2] D. Hawatmeh, K. Al Shamaileh, and N. Dib, "Design and analysis of multi-frequency unequal-split Wilkinson power divider using non-uniform transmission lines," *ACES*, vol. 27, no. 3, 2012.

[3] K.-K. M. Cheng and F.-L. Wong, "A new Wilkinson power divider design for dual band application," *IEEE Microw. and Wireless Components Letters*, vol. 17, no. 9, pp. 664-666, September 2007.

[4] Y. Wu, Y. Liu, Y. Zhang, J. Gao, and H. Zhou, "Dual band unequal Wilkinson power divider without reactive components," *IEEE Trans. Microwave Theory Tech. MTT*, vol. 57, no. 1, January 2009.

[5] X. Wang, I. Sakagami, K. Takahashi, and S. Okamura, "Generalized dual-band Wilkinson power divider with parallel L, C, and R components," *IEEE Trans. Microwave Theory and Tech. MTT*, vol. 60, no. 4, April 2012.

[6] F.-J. Chen, et al., "A four-way microstrip filtering power divider with frequency-dependent couplings," *Microwave Theory and Techniques, IEEE Transactions on*, vol. 63, no. 10, pp. 3494-3504, 2015.

[7] T. Zhang, et al., "A compact four-way dual-band power divider using lumped elements," *Microwave and Wireless Components Letters, IEEE*, vol. 25, no. 2, pp. 94-96, 2015.

[8] A. A. M. Saleh, "Planar electrically symmetric n-way hybrid power dividers/combiners," *IEE Transactions on Microwave Theory and Techniques MTT*, vol. 28, pp. 555-563, 1980.

[9] S. H. Sedighy and M. Khalaj-Amirhosseini, "Compact Wilkinson power divider using stepped impedance transmission lines," *Journal of Electromagnetic Waves and Applications*, vol. 25, iss. 13, pp. 1773-1782, 2011.

[10] S. Sun and L. Zhu, "Compact dual-band microstrip bandpass filter without external feeds," *Microwave and Wireless Components Letters, IEEE*, vol. 15, no. 10, pp. 644-646, 2005.

[11] Q.-X. Chu and F.-C. Chen, "A compact dual-band bandpass filter using meandering stepped impedance resonators," *Microwave and Wireless Components Letters, IEEE*, vol. 18, no. 5, pp. 320-322, 2008.

[12] C. Quendo, E. Rius, and C. Person, "Narrow bandpass filters using dual-behavior resonators based on stepped-impedance stubs and different-length stubs," *Microwave Theory and Techniques, IEEE Transactions on*, vol. 52, no. 3, pp. 1034-1044, 2004.

[13] M. D. C. Velazquez-Ahumada, et al., "Application of stub loaded folded stepped impedance resonators to dual band filters," *Progress in Electromagnetics Research*, vol. 102, pp. 107-124, 2010.

[14] A. R. Mehrabian and C. Lucas, "A novel numerical optimization algorithm inspired from weed colonization," *Ecological Informatics*, vol. 1, iss. 4, pp. 355-366, December 2006.

[15] Y. Li, et al., "Synthesis of conical conformal array antenna using invasive weed optimization method," *Applied Computational Electromagnetics Society Journal*, vol. 28, no. 11, 2013.

[16] B. Bahreini, A. Mallahzadeh, and M. Soleimani, "Design of a meander-shaped MIMO antenna using IWO algorithm for wireless applications," *Applied Computational Electromagnetics Society Journal*, vol. 25, no. 7, pp. 631-638, 2010.

[17] A. R. Mallahzadeh and P. Taghikhani, "Cosecant squared pattern synthesis for reflector antenna using a stochastic method," *Applied Computational Electromagnetics Society Journal*, vol. 26, no. 10, 2011.

[18] S. H. Sedighy, et al., "Optimization of printed Yagi antenna using invasive weed optimization (IWO)," *IEEE Antennas and Wireless Propagation Letters*, vol. 9, pp. 1275-1278, 2010.

[19] M. Hayati, M. Amiri, and S. H. Sedighy, "Design of compact and wideband suppression low pass elliptic filter by n-segment step impedance transmission line," *Applied Computational Electromagnetics Society Journal*, vol. 30, iss. 5, pp. 510-518, May 2015.

[20] H. Khakzad and S. H. Sedighy, "Design of compact SITLs low pass filter by using invasive weed optimization (IWO) technique," *Applied Computational Electromagnetics Society Journal*, vol. 25, no. 3, March 2013.

[21] N. Gao, G. Wu, and Q. Tang, "Design of a novel compact dual-band Wilkinson power divider with wide frequency ratio," *IEEE Microwave and Wireless Components Letters*, vol. 24, no. 2, pp. 81-83, 2014.

Ahmad Mahan was born in Qom, Iran, 1993. He received his B.Sc. in Electrical Engineering from Iran University of Science and Technology (IUST), in 2015. He is working toward the M.Sc. degree in Electrical Engineering at IUST. His research interests is broadband power amplifiers.

Seyed Hassan Sedighy was born in Qaen, South Khorasan, Iran, in 1983. He received his B.Sc., M.Sc. and Ph.D. degrees all in Electrical Engineering from Iran University of Science and Technology (IUST), in 2006, 2008 and 2013, respectively. From December 2011 to July 2012, he was with the University of California, Irvine as a Visiting Scholar. He joined the School of New Technologies at IUST, as an Assistant Professor in 2013.

Mohammad Khalaj Amirhosseini was born in Tehran, Iran in 1969. He received his B.Sc, M.Sc. and Ph.D. degrees from Iran University of Science and Technology (IUST) in 1992, 1994 and 1998 respectively, all in Electrical Engineering. He is currently an Associate Professor at College of Electrical Engineering of IUST. His scientific fields of interest are electromagnetic direct and inverse problems including microwaves, antennas and electromagnetic compatibility.

Compact Bandpass Filter with Sharp Out-of-band Rejection and its Application

Lixue Zhou [1,2], YingZeng Yin [1], Wei Hu [1], and Xi Yang [1]

[1] National Key Laboratory of Science and Technology on Antennas and Microwaves
Xidian University, Xi'an 710071, P. R. China

[2] Microwave Engineering of Department
Xi'an Electronic Engineering Research Institute, Xi'an 710100, P. R. China
Vesslan_zhou@163.com, yyzeng@mail.xidian.edu.cn, mwhuwei@163.com, yangxi@mail.xidian.edu.cn

Abstract ─ A novel compact bandpass filter considered as the harmonic suppression circuit is designed in this paper. Because of the application of a T-shaped structure, the filter is improved in performance and reduced in size. Two transmission zeros at passband edge can be conveniently adjusted by changing the length of the open stubs located at the center of the T-shaped structure. Two filters with different open-stub structures are designed. Good agreement between the simulation and the measurement is acquired, which verifies the theoretical predictions. Benefiting from this feature, an active frequency multiplier with the proposed filter as the output matching network is designed. When input signal is set to be 6 dBm, output power of the second harmonic varies from 6 to 8 dBm with 20 dBc suppression for the first, third and fourth harmonics.

Index Terms ─ Harmonic suppression, multiplier, output power, passband, T-shaped structure, transmission zero.

I. INTRODUCTION

As one of the most important microwave component, filters with high performance and compact size are highly desirable in wideband microwave circuit. Structures of ring resonators, short/open stubs, multiple-mode resonators and so on [1-9] have been utilized to design the wideband bandpass filter in the past few years. In [1-3], traditional coupled lines are considered as the key substitute for the wideband filter of compact size and simple structure. However, due to the limit of process technique, it is difficult to realize small size of gap and line width. To tackle the problem of process, low-pass and high-pass filters are connected serially to achieve the wideband system [4-5]. Unfortunately, this kind of structure will lead to the increase of volume. In [6-7], kinds of patterns are etched on the ground plane of substrate to reach the wideband performance. Unfortunately, disadvantages of package, integration and electromagnetic leakage are inevitable. In [8-9], a novel concept of signal interaction is adopted to design the wideband filters by introducing two parallel transmission paths. In order to realize sharp-rejection bandpass filters, it is the most effective to create two transmission zeros at either side of the passband. In [10-12], quarter/half wavelength open stubs connected to the center of the resonator are proposed to realize transmission zeros located at lower or upper stopband. In summary, the performance of bandpass filter has been improved. However, the application of the proposed filter in microwave circuit is rarely involved.

In this paper, a novel structure with its series quarter-wavelength line replaced with an equivalent T-shaped structure is presented, as shown in Fig. 1. The new transmission zero can be controlled exactly by adjusting the length of the open-circuited stub. Two different wideband filters are designed and fabricated for demonstration. In addition, the filter size is reduced for use of the T-shaped structure. Two transmission zeros located at each side of the passband can be observed in simulation and measurement results. Besides, to demonstrate its advantage in engineering application, an active frequency multiplier based on the proposed filter is designed. And tunable transmission zeros produced by the filter can be employed to suppress the first, third and fourth harmonics

II. ANALYSIS OF THE WIDEBAND BANDPASS FILTER

Figure 1 (a) shows the conventional bandstop filter with two open stubs (Z_0) connected by the quarter-wavelength (Z) line. A passband can be realized between f_0 (the central frequency of the bandstop filter) and $3f_0$. But, the filter has spurious passband at $4f_0$ and several cascaded open stubs are needed to realize good impendence match. By replacing the quarter-wave length line with a T-structure, a novel bandpass filter is proposed

Submitted On: May 16, 2016
Accepted On: January 28, 2017

in this paper, as shown in Fig. 1 (b).

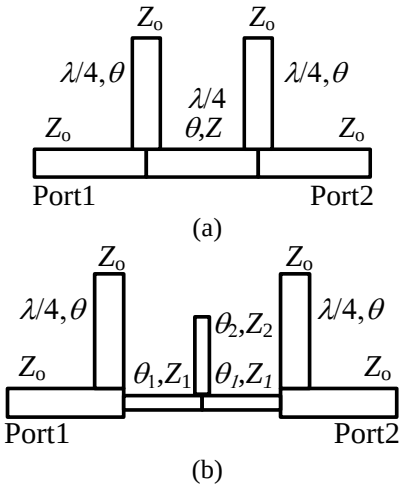

Fig. 1. (a) Conventional filter circuit and (b) novel bandpass filter circuit.

As shown in Fig. 1 (b), one open stub of Z_0, θ and another stub of Z_2, θ_2 are adopted to produce two transmission zeros which can be utilized not only to suppress unwanted harmonics, but also to adjust the bandwidth of the filter. And the filter is much more compact due to the small size of T-shaped structure over the quarter-wavelength line. In Fig. 1 (b), Z_1, Z_2, θ_1 and θ_2 represent the characteristic impedances, the electrical lengths of the series and shunt sections of the T-shaped structure respectively. ABCD matrix is used to obtain design equations and prove equivalence between T-shaped structure and a quarter-wavelength line. The ABCD matrix of a microstrip line with electrical length θ_0 is:

$$\begin{bmatrix} A & B \\ C & D \end{bmatrix} = \begin{bmatrix} \cos\theta_0 & \mathrm{j}Z\sin\theta_0 \\ jY\sin\theta_0 & \cos\theta_0 \end{bmatrix}. \quad (1)$$

The ABCD matrix of the T-shaped structure can be written as $M_1 \times M_2 \times M_1$:

$$M_1 = \begin{bmatrix} \cos\theta_1/2 & jZ_1\sin\theta_1/2 \\ jY_1\sin\theta_1/2 & \cos\theta_1/2 \end{bmatrix}, \quad (2)$$

$$M_2 = \begin{bmatrix} 1 & 0 \\ jY_2\tan\theta_2 & 1 \end{bmatrix}. \quad (3)$$

In the work here, the T-shaped model is equivalent to the quarter-wavelength line (θ_0=90°at f_0,), and we thus have:

$$\begin{bmatrix} A_T & B_T \\ C_T & D_T \end{bmatrix} = \begin{bmatrix} A & B \\ C & D \end{bmatrix} = \begin{bmatrix} 0 & \mathrm{j}Z \\ jY & 0 \end{bmatrix}. \quad (4)$$

From (1)-(3), Z_1, Z_2 can be found based on Eqs. (5) and (6):

$$Z_1 = Z/\tan\theta_1, \quad (5)$$

$$Z_2 = \frac{Z\times\tan\theta_2}{1-\tan^2\theta_1}. \quad (6)$$

When θ_2=90°, the open stub looks like an impedance inverter, and if it is terminated in an impedance Z_U on one port, the impedance Z_L seen at the other port can be calculated by Eq. (7). As is known, Z_U here is infinite, so its impedance at another port is zero which makes the symmetrical part of the filter shorted. In this case, the transmission zero $f_{\theta 2}$ that makes θ_2=90° appears and can be acquired by Eq. (8):

$$Z_L = K^2/Z_U, \quad (7)$$

$$f_{\theta 2}/f_0 = 90^o/\theta_2. \quad (8)$$

In order to achieve a compact equivalent T-shape model, θ_1 should be less than 45°. And, the transmission zero $f_{\theta 2}$ created by the stub θ_2 can be adjusted easily, with Z_1, Z_2, f_0 and θ_1 fixed. Relation curve of $f_{\theta 2}/f_0$ and θ_2 (0° < θ_2 < 360°) is shown in Fig. 2. With the increase of θ_2, $f_{\theta 2}/f_0$ becomes less and less. When θ_2=90°, the novel created transmission zero of $f_{\theta 2}$ and f_0 are coincident.

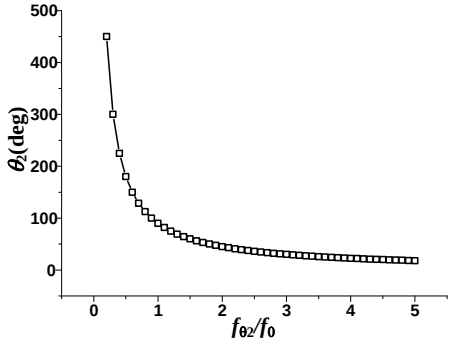

Fig. 2. Relationship between transmission zero $f_{\theta 2}$ and θ_2.

In order to validate above design ideas, a bandpass circuit with $Z_0 = Z = 50\Omega$, f_0 = 3 GHz and θ_0 = 90° are simulated with Advanced Design System (ADS). Here we choose θ_1 = 26.5°, two different θ_2, saying, 23° and 35° are chosen to indicate the transmission zero produced by open-ended stub can be adjusted. From (4), it is easy to get $Z_1 = 100\Omega$. From (5), the corresponding Z_2 in two cases of θ_2 are found to be 28Ω and 46.6Ω, respectively. In addition, transmission zeros for two different θ_2 can be calculated by (8). $f_{\theta 2}$ = 11.7 GHz and 7.7 GHz respectively. Figure 3 shows the simulated results for two cases with different impedance values. Comparing the simulated and the calculated results, we may see that when θ_2 < 30°, a wideband bandpass filter can be implemented between f_0 and $3f_0$, while the created transmission zero $f_{\theta 2}$ can be used to suppress the fourth harmonic, thus resulting in wider upper stopband for the bandpass filter; when 30° < θ_2 < 90°, a narrowband bandpass filter between f_0 and $f_{\theta 2}$ is achieved, and the transmission zero $f_{\theta 2}$ can be used to improve the rejection

performance. It is true that a transmission $f_{\theta 2}$ zero can be also located below f_0, when $\theta_2 > 90°$. However, the passband performance is dissatisfactory. In this way, two different bandpass filters with an adjustable bandwidth can be realized by controlling the location of the transmission zero $f_{\theta 2}$ created by the open stub (θ_2). In addition, the filter size is much reduced by the introduced T-shaped lines.

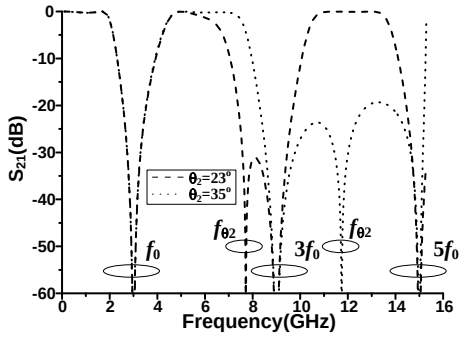

Fig. 3. Simulated results for two different $f_{\theta 2}$, $Z_0 = 50$ ohm, $f_0 = 3$ GHz, $\theta_0 = 90°$, $\theta_1 = 26.5°$, $Z_1 = 100\Omega$.

III. TWO WIDEBAND BANDPASS FILTERS

In this work, the quarter-wavelength line of the conventional bandstop filter is replaced with proposed T-shaped structure. For demonstrating the design strategies discussed in Section 2, two different wideband bandpass filters are designed. Here we choose $\theta_2 < 30°$ for filter A and $\theta_2 > 30°$ for filter B to realize wide passband. The two filters are all simulated with Ansoft HFSS and constructed into the Rogers4350B substrate with $\varepsilon_r = 3.66$ and $h = 0.508$ mm. Figure 4 illustrates the simulation model of bandpass filters. For filter A, $Z_0 = 50\Omega$, $f_0 = 3.2$ GHz, $\theta_0 = 90°$, $Z = 50\Omega$, $\theta_1 = 27°$, $\theta_2 = 24°$, $Z_1 = 80\Omega$, and $f_{\theta 2} = 4f_0 = 12.8$ GHz. To obtain better passband characteristics, the optimized impedance $Z_2 = 80\Omega$. For filter B, $Z_0 = 50\Omega$, $f_0 = 3.2$ GHz, $\theta_0 = 90°$, $Z = 50\Omega$, $\theta_1 = 15°$, $\theta_2 = 40°$, $Z_1 = 100\Omega$, $f_{\theta 2} = 7.9$ GHz, and $Z_2 = 120\Omega$.

The simulated and measurement performances of the two filters are shown in Fig. 5, good agreement can be observed between the results. For filter A, the central frequency is 6.07 GHz with two transmission zeros at f_0 and $3f_0$ at either side of the passband. The transmission zero $f_{\theta 2}$ created by the open stub (θ_2) is located at around 12.8 GHz to suppress the fourth harmonic $4f_0$ and a wider upper stopband is thus realized by this simple and effective method. In addition, in the whole passband there are two poles with return loss below 20 dB, as can be seen in Fig. 5 (a). From Fig. 5 (b), the bandpass filter B covers the band of 4.6-7.1 GHz, the transmission zero $f_{\theta 2}$ is located at around 7.9 GHz, three transmission poles are observed with return loss below 20 dB in the whole passband. The comparisons of measured results for several wideband filters [16, 17] are shown in Table 1.

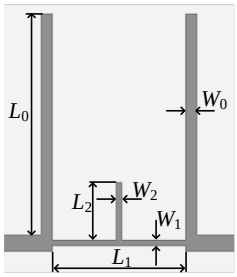

Fig. 4. The configuration of proposed filters: filter A ($L_0 = 14.8$ mm, $L_1 = 9.0$ mm, $L_2 = 3.88$ mm, $W_0 = 0.77$ mm, $W_1 = 0.37$ mm, $W_2 = 0.36$ mm), and filters B ($L_0 = 14.8$ mm, $L_1 = 4.99$ mm, $L_2 = 6.08$ mm, $W_0 = 1.94$ mm, $W_1 = 0.26$ mm, $W_2 = 0.11$ mm).

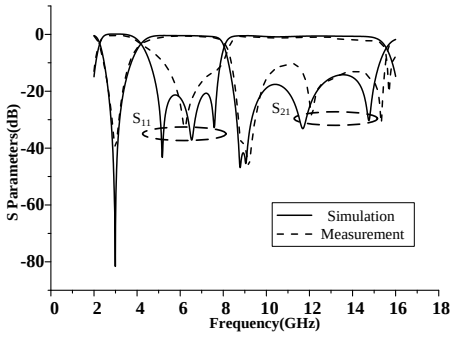

(a)

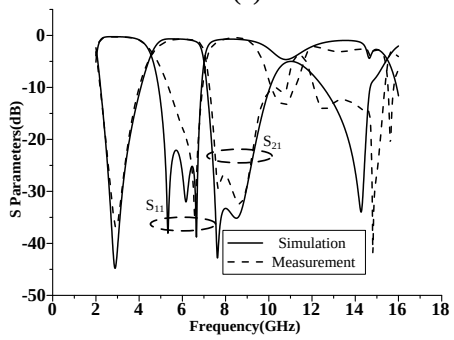

(b)

Fig. 5. (a) The simulated and measured results of filters A, and (b) The simulated and measured results of filters B.

Table 1: Comparisons with wideband filters

Different Structures	Filter A in This Paper	Ref. [16]	Ref. [17]
f_0	6.07 GHz	1.54 GHz	6.8 GHz
Circuit size (λ_o)	0.54×0.37	0.05×0.21	0.17×0.32
$(f_{40dB}-f_{3dB}) / f_{3dB}$	9%	23%	13%
Transmission poles	3	3	3
Second harmony suppression	20 dB	30 dB	20 dB

IV. THE APPLICATION OF THE NOVEL FILTER

As analyzed in the Section 3, the novel filter can be used to suppress the undesired harmonics of f_0, $3f_0$ and $4f_0$, but keeping the harmonic of $2f_0$. And according to the given center frequency f_0, one is able to calculate the physical size of the filter based on (4) and (5). Besides, to make the filter more compact, a T-shaped structure with an open-circuited stub is employed to replace the conventional quarter-wavelength line. Thus, due to the advantages presented above, it is extremely useful in RF circuit design [13-15]. In this paper, an active frequency doubler is designed by incorporating the proposed filter in the output matching network, as shown in Fig. 6. A quarter-wavelength line at the center frequency f_0 is adopted to bias the gate of FET, while a quarter-wavelength line at the second harmonic $2f_0$ is employed to bias the drain of FET. Properly adjusting the location of three transmission zeros at f_0, $3f_0$ and $4f_0$ as shown in Fig. 5, the output harmonics except $2f_0$ will be suppressed greatly. And, it behaves as a 50Ω line at the second harmonic $2f_0$ and also plays an important role in matching output circuit of the multiplier. So, when determining the size of the filter, harmonic suppression and port reflection coefficient should be considered simultaneously.

In fact, the designed filter can be considered as a 50Ω transmission line at the second harmonic $2f_0$ for its excellent matching that has been proved in Section 3. Thus, as shown in Fig. 6, a novel output matching network in which the proposed filter is introduced is designed. And, due to the compact feature of the filter, the size of multiplier is reduced further.

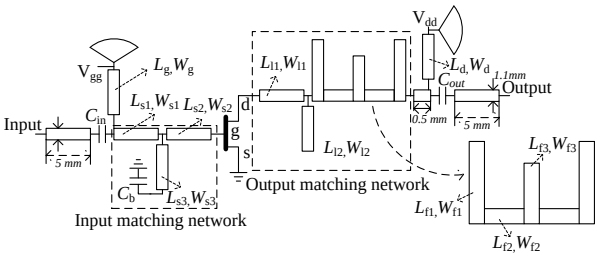

Fig. 6. The circuit of the frequency doubler (L_g = 6.9 mm; W_g = 0.2 mm; L_d = 3.3 mm; W_d = 0.2 mm; L_{s1} = 15.6 mm; L_{s2} = 1.69 mm; L_{s3} = 9.9 mm; W_{s1} = 2.0 mm; W_{s2} = 0.2 mm; W_{s3} = 0.2 mm; L_{11} = 9.0 mm; L_{12} = 1.5 mm; W_{11} = 0.2 mm; W_{12} = 0.25 mm; L_{f1} = 9.25 mm; L_{f2} = 1.81 mm; L_{f3} = 2.85 mm; W_{f1} = 0.83 mm; W_{f2} = 0.15 mm; W_{f3} = 0.46 mm).

A Hetero-Junction FET NE3210S01 whose model can be found on official website is adopted for the design of the multiplier simulated by the Agilent's Advanced Design System (ADS). The gate voltage is set to -0.25 V to reach the nonlinear field of the FET and drain voltage is fixed to be 2 V. The PCB with 14 internal ports inserted is optimized in ADS software, and then the external power, DC blocking capacitor, FET and so on is connected to be ports. Finally, a 14 ports block diagram based on S parameters of PCB is simulated to test the performance of multiplier.

For demonstrating the introduced technique and validating the simulation result, an active multiplier of 4.5~5.5 GHz implemented on Rogers 4350B substrate with ε_r =3.66 and h = 0.508 mm is designed. It can be seen in Fig. 7 that input return loss is below 20 dB for simulation and 10 dB for measurement, while the output return loss below 10 dB both for simulation and measurement in the whole band. Figure 8 tells that under 6 dBm input power, the output power of second harmonic variates from 6 to 8 dBm, and the elimination for first harmonic, third harmonic and forth harmonic is lower than 20 dBc. To indicate the relationship between the input power and output power of second harmonic more clearly, Fig. 9 is introduced. Besides, the total length of output matching network is 15 mm, while the circuit without novel filter reaches 21 mm. And, nearly no suppression for the harmonic is produced. Finally, picture of the fabrication circuit is shown in Fig. 10.

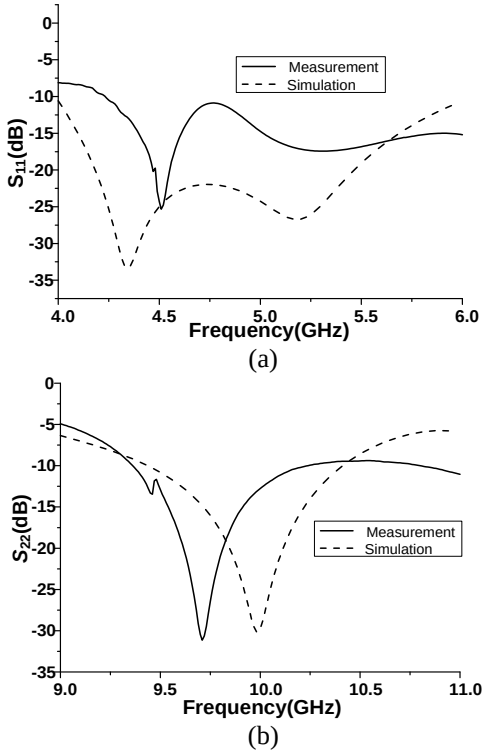

Fig. 7. (a) The simulated and measured results of S_{11}, and (b) the simulated and measured results of S_{22}.

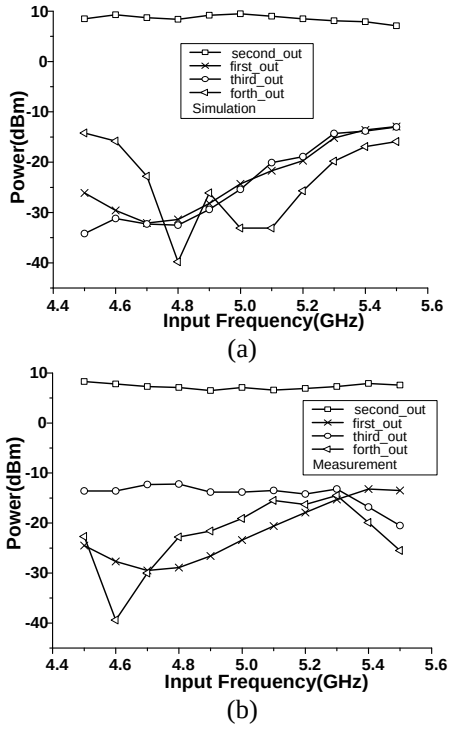

Fig. 8. (a) The output power of different harmonics for simulation, and (b) the output power of different harmonics for measurement.

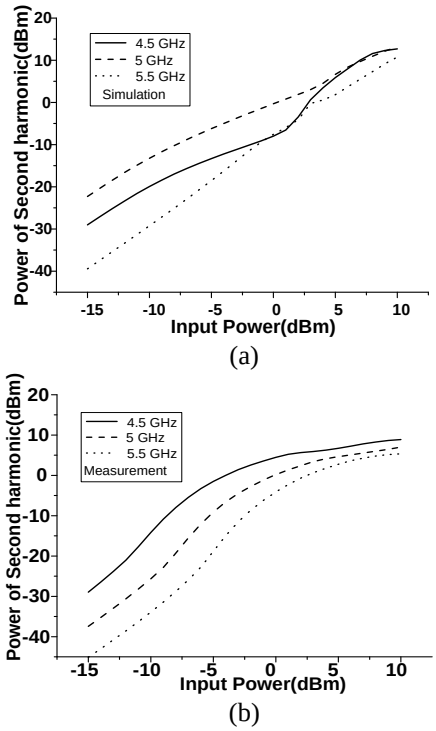

Fig. 9. (a) The output power of second harmonic for simulation, and (b) the power of output second harmonic for measurement.

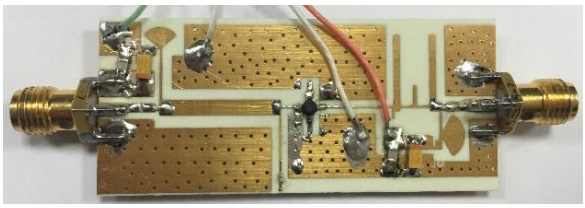

Fig. 10. The photograph of the designed multiplier.

V. CONCLUSION

In this work, two kinds of novel bandpass filters are proposed and demonstrated. What's more, the designed filter is applied to form an active multiplier. The highlight of the design is to replace the quarter-wavelength line of bandstop filter with a T-shaped open stub structure. One advantage is the size reduction of the structure; another is the flexible adjustability of transmission zero created by the open stub and thus easy bandwidth control of the passband. In addition, the transmission zero created by the central open stub of the T-shaped lines can be used to suppress the harmonic or improve the roll-off skirt selectivity; high out-of-band rejection can thus be realized. Two novel compact wideband bandpass filters are modeled and simulated for demonstration, good agreement can be observed between the simulation and theoretical analysis, indicating the validity of the proposed design strategies. With those good performances, a kind of active frequency doubler is designed based on the novel filter. In on hand, the size of output matching network is reduced; on the other hand, the output undesired harmonics is suppressed greatly.

ACKNOWLEDGMENT

This work was supported by the National Natural Science Foundation of China (No. 61501340).

REFERENCES

[1] P. K. Singh, S. Basu, and Y.-H. Wang, "Planar ultra-wideband bandpass filter using edge coupled microstrip lines and stepped impedance open stub," *IEEE Microw. Wireless Compon. Lett.*, vol. 17, no. 9, pp. 649-652, Sep. 2008.

[2] L. Zhu, H. Shi, and W. Menzel, "Coupling behaviors of quarter wavelength impedance transformers for wideband CPW bandpass filters," *IEEE Microw. Wireless Compon. Lett.*, vol. 15, no. 1, pp. 13-15, Jan. 2005.

[3] C.-Y. Hung, M.-H. Weng, Y.-K. Su, and R.-Y. Yang, "Design of parallel coupled-line microstrip wideband bandpass filter using stepped-impedance resonators," *Microw. Opt. Technol. Lett.*, vol. 49, no. 4, pp. 795-798, Feb. 2007.

[4] C. L. Hsu, F. C. Hsu, and J. T. Kuo, "Microstrip bandpass filters for ultra-wideband (UWB) wireless communications," *IEEE MTT-S Int. Microw. Symp.*

Dig., pp. 679-682, June 2005.

[5] J. Garcia-Garcia, J. Bonache, and F. Martin, "Application of electromagnetic bandgaps to the design of ultra-wide bandpass filters with good out-of-band performance," *IEEE Trans. Microw. Theory Tech*., vol. 54, no. 12, pp. 4136-4140, Dec. 2006.

[6] A. Boutejdar, A. Batmanov, M. H. Awida, E. P. Burte, and A. Omar, "Design of a new bandpass fitler with sharp transmission band using multilayer-technique and U-defected ground structure," *IET Microwaves, Antennas and Propagation*, vol. 4, no. 9, pp. 1415-1420, Apr. 2010.

[7] J.-S. Lim, C.-S. Kim, D. Shn, Y.-C. Jeong, and S. Nam, "Design of low-pass filters using defected ground structure," *IEEE Trans. Microw. Theory Tech*., vol. 53, no. 8, pp. 2539-2545, Aug. 2005.

[8] R. Gómez-García and J. I. Alonso, "Design of sharp-rejection and low-loss wide-band planar filters using signal-interference techniques," *IEEE Microw. Wireless Compon. Lett*., vol. 15, no. 8, pp. 530-532, Aug. 2005.

[9] R. Gómez-Garciá, "High-rejection wideband signal-interference microstrip filters using rat-race couplers," *Electron. Lett*., vol. 42, no. 20, pp. 1162-1163, Sep. 2005.

[10] J. R. Lee, J. H. Cho, and S. W. Yun, "New compact bandpass filter using microstrip λ/4 resonators with open stub inverter," *IEEE Microw. Microw. Guide Wave Lett*., vol. 10, no. 12, pp. 526-527, Dec. 2000.

[11] J. T. Kuo, W. H. Hsieh, and M. Jiang. "Design of two-stage UIR and SIR bandpass filters with an elliptic function-like response," *IEEE MTT-S Int. Microw. Symp. Dig*., pp. 1609-1612, June 2004.

[12] H. Gan, D. W. Lou, and D. X. Yang. "Compact microstrip bandpass filter with sharp transition bands," *IEEE Microw. Wireless Compon. Lett*., vol. 16, no. 3, pp. 107-109, Mar. 2006.

[13] Y. Park, "Class-F technique as applied to active frequency multiplier designs," *IEEE Trans. Microw. Theory Tech*., vol. 57, no. 12, pp. 3212-3218, Dec. 2009.

[14] D. G. Thomas and G. R. Branner, "Optimization of active microwave frequency multiplier performance utilizing harmonic terminating impedances," *IEEE Trans. Microw. Theory Tech*., vol. 44, no. 12, pp. 2617-2624, Dec. 1996.

[15] S. Maas, *Nonlinear Microwave Circuits*. Norwood, MA: Artech House, pp. 59-80, 1988.

[16] J. Xu, "Compact dual-wideband BPF based on quarter-wavelength open stub loaded half-wavelength coupled-line," *Applied Computational Electromagnetics Society Journal*, vol. 30, no. 9, pp. 1024-1028, 2015.

[17] L. X. Zhou, Y. Z. Yin, W. Hu, and X. Yang, "Design and realization of a wideband microstrip filter using signal-interaction techniques," *Applied Computational Electromagnetics Society Journal*, vol. 31, no. 5, pp. 562-567, 2016.

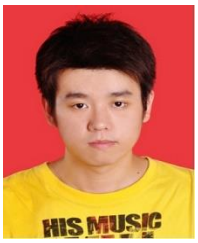

Lixue Zhou received the M.S. degree in Electromagnetic Fields and Microwave Technology from Nanjing University of Science and Technology, Nanjing, China, in 2010. He is now working toward the Ph.D. degree in Electrical Engineering Department of Xidian University, Xi'an, China. Since 2010, he has been an Electronic Engineer in Xi'an Electronic Engineering Institute, where he developed the microwave and millimeter-wave circuit and RF component.

His research interests include microwave and millimeter-wave planar type circuit and multilayered circuit design and planner filter design in microwave and millimeter-wave frequency band.

Yingzeng Yin Received the B.S. degree, M.S. degree and Ph.D. degree in Electromagnetic Wave and Microwave Technology from Xidian University, Xi'an, P. R. China, in 1987, 1990 and 2002, respectively.

From March 1990 to June 1992, he was a Research Assistant and an Instructor at the Institute of Antennas and Electromagnetic Scattering, Xidian University. From July 1992 to June 1996, he was an Associate Professor in the Department of Electromagnetic Engineering, Xidian University. Since June 2004, he has been a Professor at the University. His research interest includes the areas of design of antennas, feeds for parabolic reflectors, microstrip antennas, artificial magnetic conductors, phased array antennas, and computer aided design for antennas. He has published over 180 refereed journal articles.

Wei Hu received the B.S. and Ph.D. degrees in Electromagnetic Fields and Microwave Technology from Xidian University, Xi'an, China, in 2008 and 2013, respectively. He is a Lecturer with the National Laboratory of Science and Technology on Antennas and Microwaves, Xidian University, Xi'an, China.

His research interests include multiband antennas, dual-polarized antennas, waveguide slot antenna arrays and feeding networks. He has published more than 20

research papers in refereed international journals and conferences, such as IEEE Transaction on Antennas and Propagation, IEEE Antennas and Wireless Propagation Letters, IET Electronics Letters and so on.

Xi Yang received the Ph.D. degrees in Electromagnetic Fields and Microwave Technology from Xidian University, Xi'an, China, 2011. He is now a Lecturer with the National Laboratory of Science and Technology on Antennas and Microwaves, Xidian University, Xi'an, China.

His research interests include phased array antenna, compact antennas, reconfigurable antenna and MIMO technologies. He has published more than 20 research papers in refereed international journals and conferences, such as IEEE Transaction on Antennas and Propagation, IEEE Antennas and Wireless Propagation Letters, IET Electronics Letters.

A Robust Scheme for TD-MoM Analysis of Planar PEC Objects

A. Soltani [1], Z. H. Firouzeh [1], and H. R. Karami [2]

[1] Department of Electrical and Computer Engineering
Isfahan University of Technology, Isfahan, 8415683111, Iran
afsun.soltani@ec.iut.ac.ir, zhfirouzeh@gmail.com

[2] Department of Electrical Engineering
Bu-Ali Sina University, Hamedan, 65178, Iran
hamidr.karami@basu.ac.ir

Abstract ─ A robust, fast and simple scheme for calculation of potential integrals that encountered singular terms in time domain integral equation (TDIE) for planar PEC scatterers in free space is presented. In this method singular terms of the potential integrals, like other terms, calculated numerically by selecting some points in the source and observation patches in TD-MoM solver. In fact this method cancelled dealing with the singularity of self-terms.

The numerical integration of the potential integrals is almost two times faster than other methods that extracted or cancelled singularity of self-terms. Numerical results illustrate the accuracy and simulation time of the proposed technique.

Index Terms ─ Potential integral, singularity, time domain and numerical integration.

I. INTRODUCTION

Perfect electric conductor (PEC) surfaces in electromagnetic structures are used in many applications such as electromagnetic interference (EMI), electronic packaging, radar cross section, and antenna design [1, 2]. Numerical techniques for the prediction of electromagnetic fields scattered by complex objects, directly operating in time domain (TD), have recently received considerable attention [3].

Time domain analysis of PEC surfaces is required due to using narrow band exciting pulse to obtain the transient response in initial moments in some cases. Numerically solutions for this analysis are usually based on surface integral equation (IE) formulations [4]. To solve the time-domain integral equations, method of moments (MoM) [5] is selected as the most common numerical method. In the MoM solution, the induced electric and magnetic currents are unknowns, and the surface of the scatterers or targets is usually subdivided into small planar patches of a simple shape [6]. These unknown currents approximated by the basis functions. Depending on the shape of patches, the suitable basis function is selected.

In the process of MoM, we deal with evaluation of double integrals with singular kernels of surface integral equation (IEs) [6]. These singular kernels related to the potential integrals in the IEs of electromagnetics need to be evaluated analytically or numerically. Singularities occur when testing and source subdomains coincide in the kernels of self-terms in the MoM procedure [7].

Several singularity subtraction or cancellation methods have been proposed. For example, analytic and numerical integration are proposed by Gibson [1], a new singularity subtraction integral formula [6], Duffy's transformation [8], Khayat-Wilton method [7], analytical evaluation method [9], analytical computation of singular part [10], an accurate method for the calculation of singular integrals [11] and a proposed method in [12] for the evaluation of singular integrals arising in method of moments. Almost all the methods suffer from a few disadvantages; for instance, Duffy's transformation is derived for functions having a point singularity of order 1/R so singularities of order $\nabla(1/R)$ appeared in integral equations cannot be easily evaluated [13]. Also, Duffy's transformation does not work well for nearly singular integrals occurring when an observation point is near a source point [3]. For the method presented in [6], a new subtraction method is introduced that covers both triangular and rectangular basis functions but the singularity subtraction is based on Taylor's series at R=0 in which R is the distance between testing and source subdomains. Therefore, it is valid only for sufficiently small values of R and the accuracy of the computation is deteriorated for large values of R [6]. In another research [12], the kernels of integrals arising in method of moments are categorized to regular, nearly singular, weakly singular and strongly singular. For each of these different types of integrals, a particular method is presented leading to complicated calculation procedure. Other mentioned methods also suffer from complexity

Submitted On: October 28, 2016
Accepted On: January 28, 2017

analytical computation of singular terms in regard to the other terms.

In this paper, we analyse the time-domain mixed potential integral equation (TD-MPIE) of PEC surfaces in free space with calculation of the potential integrals by a simple method that does not deal with extracting or cancelling the singularity of self-terms. In fact, a few points are used for source and observation patches resulting in the calculation of the potential integrals numerically. The proposed method based on Makarov's work [14] is extended for multi-points in source and observation patches in time domain. This method is compared with analytic and numerical integration proposed by Gibson [1] since the Gibson method has used analytical singularity calculation regarding to the other introduced methods. The Gibson method can be applied to N-sided planar polygons of an arbitrary shape. Also, its singularity computation is independent on the type of integral equation formulation. Also the Gibson method is accurate enough to compare with the other methods.

II. FORMULATION

Let *S* denote the surface of a finite PEC in free space illuminated by a transient electromagnetic pulse as shown in Fig. 1. This pulse induces a surface current, $\boldsymbol{J}(\boldsymbol{r}, t)$, on *S* which then reradiates a scattered field.

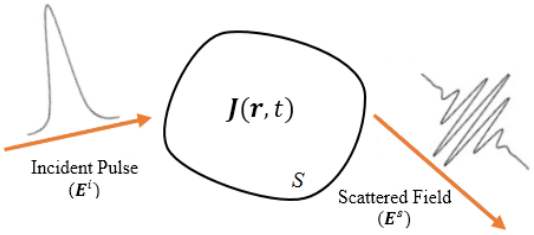

Fig. 1. A PEC excited by incident electromagnetic field.

The boundary conditions require that the total tangential electric field on PEC be zero or,

$$\{\boldsymbol{E}^s + \boldsymbol{E}^i\}_{tan} = 0. \quad (1)$$

The scattered fields radiated by the current $\boldsymbol{J}(\boldsymbol{r}, t)$, may be written in terms of the magnetic vector $\boldsymbol{A}(\boldsymbol{r}, t)$ and electric scalar potentials $\Phi(\boldsymbol{r}, t)$ as [15]:

$$\boldsymbol{E}^s = -\frac{\partial \boldsymbol{A}}{\partial t} - \nabla\Phi, \quad (2)$$

where

$$\boldsymbol{A}(\boldsymbol{r}, t) = \mu \int \frac{\boldsymbol{J}(\boldsymbol{r}', t - R/c)}{4\pi R} ds', \quad (3)$$

and

$$\Phi(\boldsymbol{r}, t) = \frac{1}{\epsilon} \int \frac{q_s(\boldsymbol{r}', t - R/c)}{4\pi R} ds', \quad (4)$$

and $R = |\boldsymbol{r} - \boldsymbol{r}'|$. In Equations (1)-(4), μ and ϵ are the permeability and permittivity of the surrounding medium, *c* is the velocity of propagation of the electromagnetic wave, and $\boldsymbol{r}$ and $\boldsymbol{r}'$ are the arbitrarily located observation point and source point on the scatterer, respectively.

Surface charge density q_s in Equation (4) is related to the surface divergence of $\boldsymbol{J}$ through the continuity equation, so the scalar potential term can be given as:

$$\Phi(\boldsymbol{r}, t) = -\frac{1}{4\pi\epsilon} \int \int_0^{t - R/c} \frac{\nabla_s \cdot \boldsymbol{J}(\boldsymbol{r}', \tau)}{R} d\tau ds'. \quad (5)$$

Using Equation (1) and Equation (2), the time domain electric field integral equation (TD-EFIE) can be obtained as follows:

$$\left\{\frac{\partial \boldsymbol{A}(\boldsymbol{r}, t)}{\partial t} + \nabla\Phi(\boldsymbol{r}, t)\right\}_{tan} = \boldsymbol{E}^i_{tan}(\boldsymbol{r}, t). \quad (6)$$

For the numerical solution of Equation (6), we now approximate the conducting surface by triangular patches and employ the triangular current expansion on *S* by:

$$\boldsymbol{J}(\boldsymbol{r}, t) = \sum_{k=1}^{N} I_k(t) \boldsymbol{f}_k(\boldsymbol{r}). \quad (7)$$

N is the number of non-boundary edges. Note that a boundary edge is an edge which is associated with only one triangular patch. $I_k(t)$ represents a temporal basis function and $\boldsymbol{f}_k(\boldsymbol{r})$ is the vector basis function associated with the *k*th edge. As in [16], the vector basis function is defined as:

$$\boldsymbol{f}_k(\boldsymbol{r}) = \begin{cases} \frac{l_k}{2A_k^{\pm}} \boldsymbol{\rho}_k^{\pm} & \boldsymbol{r} \in T_k^{\pm} \\ 0 & otherwise \end{cases}, \quad (8)$$

where l_k and $A_k^{\pm}$ are the length of the edge and the area of the triangle $T_k^{\pm}$, respectively and $\rho_k^{\pm}$ are the position vectors referenced at the free vertex of $T_k^{\pm}$, as shown in Fig. 2. The surface divergence is then given by:

$$\nabla . \boldsymbol{f}_k(\boldsymbol{r}) = \begin{cases} \frac{l_k}{A_k^+} & \boldsymbol{r} \in T_k^+ \\ -\frac{l_k}{A_k^-} & \boldsymbol{r} \in T_k^- \\ 0 & otherwise \end{cases}. \quad (9)$$

Using time domain MoM (TD-MoM) solver for the TD-MPIE and Galerkin method, the spatial test functions are the same as the expansion function $\boldsymbol{f}_k(\boldsymbol{r})$. The inner product is chosen as:

$$\langle \boldsymbol{a}, \boldsymbol{b} \rangle = \int \boldsymbol{a} . \boldsymbol{b}\, ds. \quad (10)$$

We divide the times axis into equal intervals of segment Δt, and define $t_j = j\Delta t$. By applying the testing procedure to Equation (6), and approximating the time derivative by the forward-difference approximation, we can rewrite Equation (6) as:

$$\begin{aligned} &\langle \boldsymbol{f}_k, \boldsymbol{A}(\boldsymbol{r}, t_j) \rangle + \langle \boldsymbol{f}_k, (\Delta t)\nabla_s \Phi(\boldsymbol{r}, t_j) \rangle = \\ &\langle \boldsymbol{f}_k, (\Delta t)\boldsymbol{E}^i(\boldsymbol{r}, t_j) \rangle + \langle \boldsymbol{f}_k, \boldsymbol{A}(\boldsymbol{r}, t_{j-1}) \rangle . \end{aligned} \quad (11)$$

Next, using the vector identity $\nabla_s . (\Phi \boldsymbol{A}) = \boldsymbol{A} . \nabla_s \Phi + \Phi \nabla_s . \boldsymbol{A}$, and using the properties of the basis function [16], we rewrite Equation (11) as:

$$\begin{aligned} &\langle \boldsymbol{f}_k, \boldsymbol{A}(\boldsymbol{r}, t_j) \rangle - \langle \nabla_s . \boldsymbol{f}_k, (\Delta t)\Phi(\boldsymbol{r}, t_j) \rangle = \\ &\langle \boldsymbol{f}_k, (\Delta t)\boldsymbol{E}^i(\boldsymbol{r}, t_j) \rangle + \langle \boldsymbol{f}_k, \boldsymbol{A}(\boldsymbol{r}, t_{j-1}) \rangle . \end{aligned} \quad (12)$$

Thus, substituting Equation (3) and Equation (4) into Equation (12) yields, after a few steps of algebra, the following set of Equations [15], given by:

$$\sum_{k=1}^{N} Z_{mk}^{a}(t_j) + \Delta t \sum_{k=1}^{N} Z_{mk}^{b}(t_j) = F_m(t_j) + \sum_{k=1}^{N} Z_{mk}^{a}(t_{j-1}) \quad m = 1,2,\dots N, \tag{13}$$

where

$$Z_{mk}^{a}(t_j) = O_{mk}^{++} + O_{mk}^{\pm} + O_{mk}^{\mp} + O_{mk}^{--}, \tag{14}$$

$$Z_{mk}^{b}(t_j) = Q_{mk}^{++} - Q_{mk}^{\pm} - Q_{mk}^{\mp} + Q_{mk}^{--}, \tag{15}$$

$$O_{mk}^{\pm\pm} = \{I_k(t_R^{\pm\pm})\}\{\frac{\mu l_m l_k}{2A_k^{\pm}}\rho_m^{\pm}.\int_{T_k^{\pm}} \frac{\rho_k^{\pm}}{4\pi R_{mk}^{\pm\pm}} ds'\}, \tag{16}$$

$$Q_{mk}^{\pm\pm} = \left\{\int_0^{t_R^{\pm\pm}} I_k(\tau)d\tau\right\}\left\{\frac{l_m l_k}{\epsilon A_k^{\pm}}\int_{T_k^{\pm}} \frac{ds'}{4\pi R_{mk}^{\pm\pm}}\right\}, \tag{17}$$

and

$$F_m(t_j) = \frac{l_m \Delta t}{2}\{\rho_m^{c+}.\boldsymbol{E}^i(\boldsymbol{r}_m^{c+}, t_j) + \rho_m^{c-}.\boldsymbol{E}^i(\boldsymbol{r}_m^{c-}, t_j)\}. \tag{18}$$

In Equation (16) and Equation (17), $A_k^{\pm}$ represents the area of the triangle $T_k^{\pm}$, $t_R^{\pm\pm} = t_j - R_{mk}^{\pm\pm}/c$, and $R_{mk}^{\pm\pm}$ is the distance between the source and observation patches.

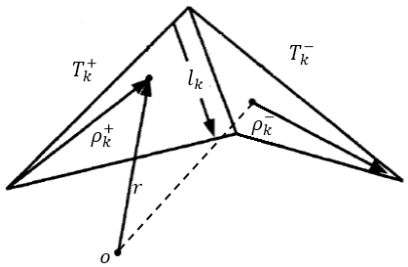

Fig. 2. The spatial vector basis function.

To calculate the distance between the source and observation patches, we consider special points in triangle patches corresponding to the source and observation as shown in Fig. 3 and Fig. 4, respectively. Actually, the distance between source and observation patches is the difference between two matrixes that the elements of each one contain the position of selected points. To clear the matter, if we select n points from p_1 to p_n in the source patch and m points from q_1 to q_m in the observation patch, the distance define as:

$$\boldsymbol{R} = \begin{bmatrix} x_{p1} & x_{p2} & \cdots & x_{pn} \\ y_{p1} & y_{p2} & \dots & y_{pn} \\ z_{p1} & z_{p2} & \dots & z_{pn} \end{bmatrix} - \begin{bmatrix} x_{q1} & x_{q2} & \cdots & x_{qm} \\ y_{q1} & y_{q2} & \dots & y_{qm} \\ z_{q1} & z_{q2} & \dots & z_{qm} \end{bmatrix}. \tag{19}$$

So we obtain:

$$\int_{T_m} \frac{1}{\boldsymbol{R}} = \frac{A_m}{F}\sum_{k=1}^{F} \frac{1}{|\boldsymbol{r}_s(k) - \boldsymbol{r}_o(k)|}. \tag{20}$$

A_m is the area of the triangle, F is the lowest common multiple of the number of source and observation points, and $\boldsymbol{r}_s$ and $\boldsymbol{r}_o$ are the position of source and observation points, respectively.

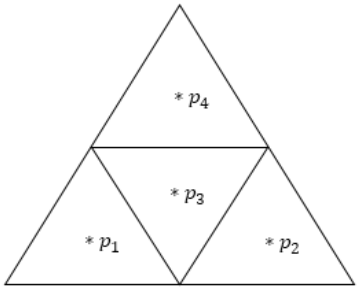

Fig. 3. Source patch barycenteric subdivision.

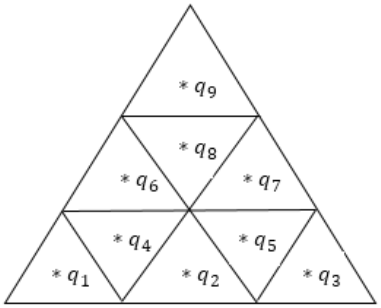

Fig. 4. Observation patch barycenteric subdivision.

III. NUMERICAL RESULTS

In this section, we present the numerical results of applying the presented method on various structures. Also, the results compared within the analytic and numerical method presented by Gibson [1] that calculates potential integrals with singular kernel of $1/R$. All the objects are illuminated by a Gaussian plane wave, given by:

$$\boldsymbol{E^i}(\boldsymbol{r}, t) = E_0 \frac{4}{\sqrt{\pi}T} e^{-\gamma^2}, \tag{21}$$

where

$$\gamma = \frac{4}{T}\{ct - ct_0 - \boldsymbol{r}\cdot\boldsymbol{a_k}\}, \tag{22}$$

with $E_0 = 120\pi \boldsymbol{a_x}, \boldsymbol{a_k} = -\boldsymbol{a_z}, T = 13.34\, ns,$ and $ct_0 = 20\, ns$.

First, to choose optimum number of points in source and observation patches, we consider a 1m × 1m square plate, located in the *xy* plane and centered about the origin. By changing the number of points, some that cause stable response have been listed in Table 1. For each case, the relative error, the exact value presented by Gibson [1] is used, and the computation time have been computed. We select 9 and 16 points for source and observation patches, respectively.

As shown in Table 1, as the number of selection points is greater, the relative error reduces but the

computation time increases. So, this choice of numbers is optimum. The following consideration has been done based on 9 and 16 points for source and observation patches, respectively.

The mentioned unit square PEC plate has been subdivided into 44 triangular patches with 58 unknowns. Figure 5 shows the space-time distribution of *x*-directed current induced at center of the square using the proposed solution and the results are compared with the Gibson method [1]. The curves show the good agreement between two methods. Also, the currents induced at the corners of the square are depicted in Fig. 6.

Table 1: Computation time and relative error for different source and observation points

No. of Source Points	No. of Observation Points	Computation Time (S)	Relative Error (%)
4	9	8.464983	0.0093
9	16	8.860424	0.0063
49	36	14.08472	0.0057

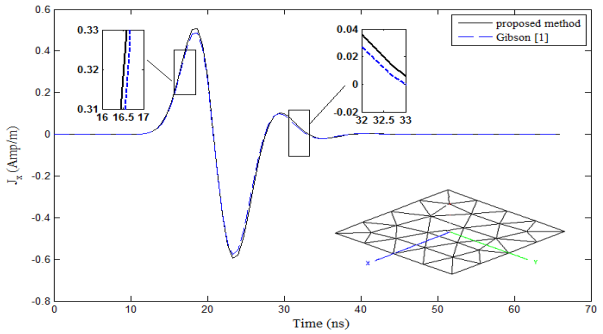

Fig. 5. The *x*-directed induced surface current density at the center of the 1m × 1m square PEC plate.

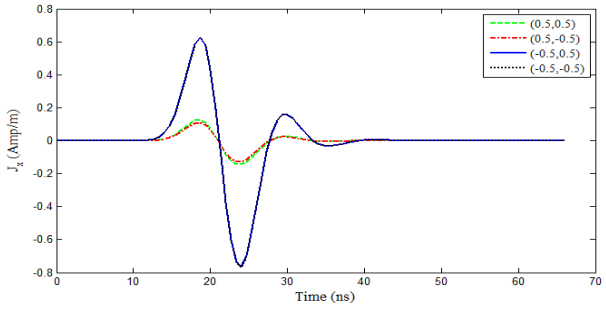

Fig. 6. The *x*-directed induced surface current density at the corners of the 1m × 1m square PEC plate.

As a second example, the *x*-directed current density at the center of an equilateral triangle by means of two methods is shown in Fig. 7. The triangle is subdivided to 29 triangular patches with 35 unknowns. Figure 8 shows the current density at two *x*-axis symmetric points A and B in corners of the triangle.

In the third example, a unit circle that subdivided to 94 triangular patches with 129 unknowns has been considered. Figure 9 shows the *x*-component of the induced current density at the center of this circle by means of two methods. In Fig. 10, the *x*-directed induced current density at two symmetry points on central cross section of the circle is shown.

As the last consideration, we obtain the *x*-directed induced surface current density at point (0,0,0) of a pie shaped plate. The geometry consists of an equilateral triangular plate 1 m on a side joined to a semicircular disk with a 1 m diameter. The plate lies in the *xy* plane with the "center" of the disk located at the origin. The triangular portion is divided into 23 triangles. Also, the disk portion is divided into 16 triangular patches resulting in a total of 39 patches with 74 unknowns. Figure 11 shows the *x*-component of the induced current density for both the proposed method and the Gibson method [1].

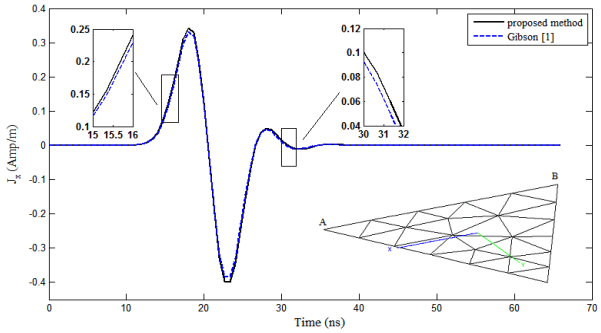

Fig. 7. The *x*-directed induced surface current density at the center of a unique equilateral triangle.

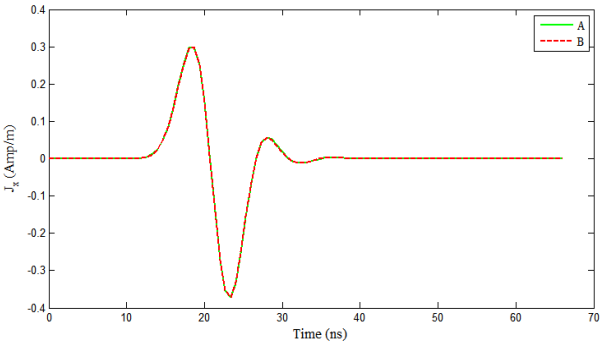

Fig. 8. The current density at two *x*-axis symmetric points A and B in the corners of the triangle.

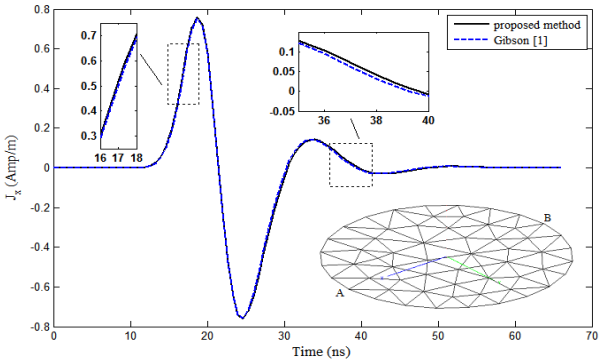

Fig. 9. The x-directed induced surface current density at the center of a unit circle.

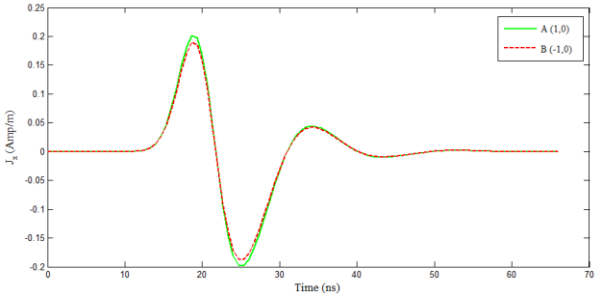

Fig.10. The *x*-directed induced surface current density at two symmetry points on central cross section of the circle.

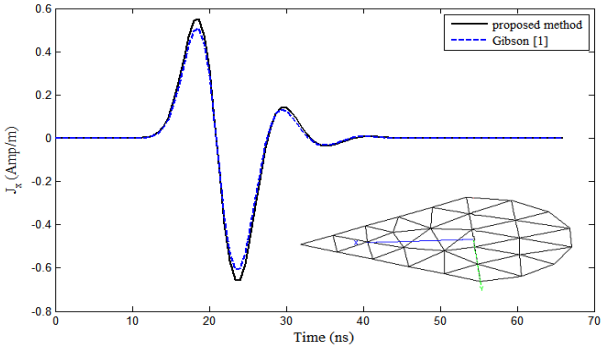

Fig. 11. The *x*-directed induced surface current density at the center of a pie shape.

Relative error between two implemented methods is calculated and shown in Table 2. It is observed that the relative error is smaller than 0.1 percent for all the cases, that means the proposed method is sufficiently accurate. To approve the outstanding property of the presented method, the computation time is reported in Table 3. Note that, the proposed method is about three times faster than the other. The computer used in this comparison has an Intel Core 2 CPU 2.13 GHz processor and 2 GB of RAM.

Table 2: Relative error between the Gibson Method [1] and the proposed method (in percent)

Object	Relative Error
Unit square	0.0063
Triangle	0.0021
Unit circle	0.0047
Pie shape	0.0263

Table 3: Comparison of the computation time between two methods (time in seconds)

Object	Proposed Method	The Gibson Method [1]
Unit square	8.67100	33.30909
Triangle	3.92005	12.97828
Unit circle	38.67338	159.68715
Pie shape	6.85649	24.96783

IV. CONCLUSION

In this work, we presented a computationally efficient method to obtain the solution to the potential integrals of time domain integral equations for the PEC surfaces in free space. This method by selecting some points in the source and observation patches in the MoM context, numerically calculate the potential integrals and does not encounter the singularity of self-terms. This method can be applied for the integral equation formulation of scattering problems dealing with singularity of 1/R. We used the proposed method for triangular basis functions while this method can be used for each arbitrary shapes of basis functions.

In addition, the proposed method can be used to analyze planar PEC structures in multilayered media for both frequency and time domains. It is expected that results of these studies will be reported in the near future.

REFERENCES

[1] W. C. Gibson, *The Method of Moments in Electromagnetics*. CRC Press, 2014.

[2] G. Carvajal, D. Duque, and A. Zozaya, "RCS estimation of 3D metallic targets using the moment method and Rao-Wilton-Glisson basis functions," *ACES Journal-Applied Computational Electromagnetics Society*, vol. 24, pp. 487, 2009.

[3] G. Manara, A. Monorchio, and R. Reggiannini, "A space-time discretization criterion for a stable time-marching solution of the electric field integral equation," *IEEE Transactions on Antennas and Propagation*, vol. 45, pp. 527-532, 1997.

[4] Q.-Q. Wang, C. Yan, Y.-F. Shi, D.-Z. Ding, and R.-S. Chen, "Transient analysis of electromagnetic scattering using marching-on-in-order time-domain integral equation method with curvilinear RWG basis functions," *ACES Journal-Applied Computational Electromagnetics Society*, vol. 26, pp. 429-436, 2011.

[5] R. F. Harrington and J. L. Harrington, *Field Computation by Moment Methods*. Oxford University Press, 1996.

[6] I. Hanninen, M. Taskinen, and J. Sarvas, "Singularity subtraction integral formulae for surface integral equations with RWG, rooftop and hybrid basis functions," *Progress In Electromagnetics Research*, vol. 63, pp. 243-278, 2006.

[7] M. A. Khayat and D. R. Wilton, "Numerical evaluation of singular and near-singular potential Integrals," *IEEE Transactions on Antennas and Propagation*, vol. 53, pp. 3180-3190, 2005.

[8] M. G. Duffy, "Quadrature over a pyramid or cube of integrands with a singularity at a vertex," *SIAM Journal on Numerical Analysis*, vol. 19, pp. 1260-1262, 1982.

[9] A. Azari, Z. H. Firouzeh, and A. Zeidaabadi-Nezhad, "A new efficient technique for transient scattering of conducting cylinders illuminated by a TM-polarized plane wave," *IEEE Antennas and Wireless Propagation Letters*, vol. 13, pp. 1421-1424, 2014.

[10] Z.-J. Qiu, J.-D. Xu, G. Wei, and X.-Y. Hou, "An improved time domain finite element-boundary integral scheme for electromagnetic scattering from 3-D objects," *Progress In Electromagnetics Research*, vol. 75, pp. 119-135, 2007.

[11] M. J. Bluck, M. D. Pocock, and S. P. Walker, "An accurate method for the calculation of singular integrals arising in time-domain integral equation analysis of electromagnetic scattering," *IEEE Transactions on Antennas and Propagation*, vol. 45, pp. 1793-1798, 1997.

[12] A. Herschlein, J. V. Hagen, and W. Wiesbeck, "Methods for the evaluation of regular, weakly singular and strongly singular surface reaction integrals arising in method of moments," *DTIC Document*, 2002.

[13] A. Tzoulis and T. F. Eibert, "Review of singular potential integrals for method of moments solutions of surface integral equations," *Advances in Radio Science*, vol. 2, pp. 93-99, 2005.

[14] S. N. Makarov, *Antenna and EM Modeling with Matlab*. New York, Wiley-Interscience, 2002.

[15] S. M. Rao, *Time Domain Electromagnetics*. Academic Press, 1999.

[16] S. Rao, D. Wilton, and A. Glisson, "Electromagnetic scattering by surfaces of arbitrary shape," *IEEE Transactions on Antennas and Propagation*, vol. 30, pp. 409-418, 1982.

Sensorless Speed Control for Dual Stator Induction Motor Drive Using IFOC Strategy with Magnetic Saturation

Marwa Ben Slimene, Mohamed Arbi Khlifi, and Mouldi Ben Fredj

Department of Electrical Engineering
ENSIT, University of Tunis, Taha Hussein, BP 56, 1008 Tunis, Tunisia
Mohamedarbi.khlifi@issatm.rnu.tn, benslimene.marwa@gmail.com

Abstract ─ A method of a sensorless indirect rotor-field-oriented control of a dual stator induction motor with magnetic saturation is proposed in this paper. Magnetic characteristics of the dual stator induction motor indicate a nonlinear behavior. The computational electromagnetic d-q model when the dual stator are fed by an independently current-controlled pulse width modulation (PWM) two identical three-phase voltage source inverters. By controlling the machine's phase currents, harmonic elimination and torque ripple reduction techniques could be observed. The unbalanced current sharing between the dual stator winding sets is eliminated. High accuracy and performance is obviously demonstrated by comparing experimental and simulation results both in electromagnetic and dynamic features.

Index Terms ─ Dual Stator Induction Machine (DSIM), Field Oriented Control (F.O.C), magnetic saturation, magnetizing inductance.

I. INTRODUCTION

Actually, electromagnetic simulators are essential tools in the analysis and the design of large and complex systems especially the industrial electrical drives. Cost, reliability, robustness and maintenance free operation are among the reasons these machines are replacing DC drive systems. The last two decades have witnessed dramatic improvements in both algorithms for computational electromagnetics and computing hardware [1-3]. However, when an ac machine is supplied from an inverter, the need for a predefined number of phases on stator, such as three, disappears and other phase numbers can be chosen. The early interest in multiphase machines was caused by the possibility of reducing the torque pulsations, minimizing the magnetic flux harmonic, improved reliability and reduction on the power ratings for the static converter [4-5]. In particular, with loss of one or more of stator winding excitation sets, a multi-phase induction machine can continue to be operated with an asymmetrical winding structure and unbalanced excitation [6-7]. By dividing the required power between multiple phases, higher power levels can be obtained and the limits of number of machine phases have been removed when employing voltage source inverter [8-9]. The use of multi-phase machines permits to take advantage of additional degrees of freedom but is likely limited to specialized applications such as electric/ hybrid vehicles, aerospace applications, ship propulsion, and high power application [10-11]. Such a machine, addition to the power segmentation and redundancy it carries, has the advantage of reducing the torque pulsations, rotor losses and the reduction of harmonic current [12-13]. However, the introduction of magnetic nonlinearities in the electrical equations operating has always been a topical issue for polyphase machines. Indeed, taking into account the saturation is not simply dictated by the desire to improve the results, but it can sometimes be a necessity.

One of the most important parts in the modeling of DSIM with closed magnetic circuit is magnetic characteristics of motor. They are directly in correlation with electrical and mechanical subsystems. Moreover, nonlinear behavior of magnetic characteristics makes the nonlinear model and more complex [14-15].

In order to achieve a mathematical model the leakage mutual inductance effect is investigated. In this paper, a nonlinear model including experimental characteristic is proposed to attain transient magnetic characteristics. The specific issue of current control is the problem of unbalanced current sharing between the two three-phase winding sets, due to the small system asymmetries that cannot be eliminated, [16]. In this paper, a d-q model of the dual stator induction machine (DSIM) is developed in a general reference frame and the effect of mutual leakage inductance and magnetic saturation are included. Subsequently, an indirect rotor-field-oriented control for the DSIM is presented and detailed with 0 and 30 electrical degrees shift between the two three phase winding sets. Simulation results are provided to demonstrate the validity of proposed control.

II. COMPUTATIONAL ELECTROMAGNETIC D-Q MODEL OF DSIM

A. Transient model

A common type of multiphase machine is the dual stator induction machine (DSIM), where two sets of three-phase windings, spatially phase shifted by 30 electrical degrees, share a common stator magnetic core as shown in

Submitted On: January 31, 2016
Accepted On: January 31, 2017

Fig. 1.

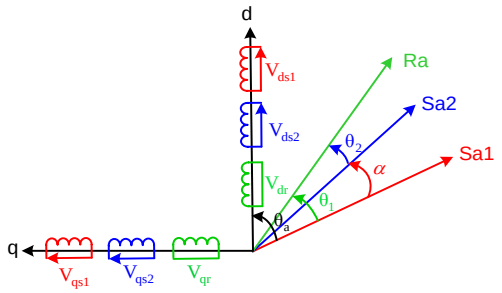

Fig. 1. DSIM windings.

The voltage equations of the dual stator induction machine using decomposition vector space are as follow. For the stator circuit we can write:

$$\begin{cases} V_{ds1} = R_s.i_{ds1} + \dfrac{d\lambda_{ds1}}{dt} - w_a\lambda_{qs1} \\ V_{qs1} = R_s.i_{qs1} + \dfrac{d\lambda_{qs1}}{dt} + w_a\lambda_{ds1} \\ V_{ds2} = R_s.i_{ds2} + \dfrac{d\lambda_{ds2}}{dt} - w_a\lambda_{qs2} \\ V_{qs2} = R_s.i_{qs2} + \dfrac{d\lambda_{qs2}}{dt} + w_a\lambda_{ds2} \end{cases}. \quad (1)$$

And for the rotor circuit we have:

$$\begin{cases} 0 = R_r.i_{dr} + \dfrac{d\lambda_{dr}}{dt} - (w_a - w)\lambda_{qr} \\ 0 = R_r.i_{qr} + \dfrac{d\lambda_{qr}}{dt} + (w_a - w)\lambda_{dr} \end{cases}, \quad (2)$$

where w_a is the speed of the reference frame.

Such as l_{sm} is the common mutual leakage inductance between the two sets of stators windings, L_m is the mutual inductance between stator and rotor, l_s, l_r are the stator and rotor leakage inductance respectively, where

$$\begin{cases} L_s = l_s + l_{sm} + L_m \\ L_r = l_r + L_m \\ L_{ps} = l_{sm} + L_m \\ M = L_m \end{cases}. \quad (3)$$

The writing matrix of flux is characterized by the following relationship:

$$\begin{bmatrix} \lambda_{ds1} \\ \lambda_{qs1} \\ \lambda_{ds2} \\ \lambda_{qs2} \\ \lambda_{dr} \\ \lambda_{qr} \end{bmatrix} = \begin{bmatrix} L_s & 0 & L_{ps} & 0 & M & 0 \\ 0 & L_s & 0 & L_{ps} & 0 & M \\ L_{ps} & 0 & L_s & 0 & M & 0 \\ 0 & L_{ps} & 0 & L_s & 0 & M \\ M & 0 & M & 0 & L_r & 0 \\ 0 & M & 0 & M & 0 & L_r \end{bmatrix} \begin{bmatrix} i_{ds1} \\ i_{qs1} \\ i_{ds2} \\ i_{qs2} \\ i_{dr} \\ i_{qr} \end{bmatrix}. \quad (4)$$

B. Flux linkage determination

The magnetic characteristic data of the linear actuators is obtained from experimental measurements. In order to complete the actuator modeling, data should be employed properly. The method consists to use the data of flux M is to approximate *M-x-*i_m characteristics employing polynomial functions. The main advantage of this method is significant decrease in the calculations complexity. Nevertheless, the relatively much increase of the error in the extrapolation is the fundamental disadvantage. The current increase results in decrease in the flux linkage increase rate, whereas in the polynomial approximation, the estimated value of the flux linkage out of the relevant range might get large values. Since for the large values of ac current, there is restriction in the characteristic measurement, this issue is regarded as a significant disadvantage. By contrast, the actuator can easily operate in high DC currents. On the other hand, in the short-term over currents and transient situations, the amount of winding current could be increased in comparison with the nominal current. However, a proper model must predict the behavior of the system with the minimum error in different situations.

The magnetization curve shown in Fig. 2 was approximated by a polynomial of order 7:

$$M = L_m = k_1 i_m^7 + k_2 i_m^6 + k_3 i_m^5 + k_4 i_m^4 + k_5 i_m^3 + k_6 i_m^2 + k_7 i_m + k_8;$$

$$k_1 = 0.19303; \quad k_2 = -1.4276;$$
$$k_3 = 4.3069; \quad k_4 = -6.8637;$$
$$k_5 = 6.4026; \quad k_6 = -3.8101;$$
$$k_7 = 1.2896; \quad k_8 = 0.51665;$$

Thus, the saturation effect is taken into account by the expression of the static and dynamic magnetizing inductances with respect to the magnetizing current. They are evaluated from the open circuit d-axis magnetizing curve $\lambda_m = f(i_m)$:

$$L_m = \frac{\lambda_m}{i_m} \qquad L_{mdy} = \frac{d\lambda_m}{di_m}. \quad (5)$$

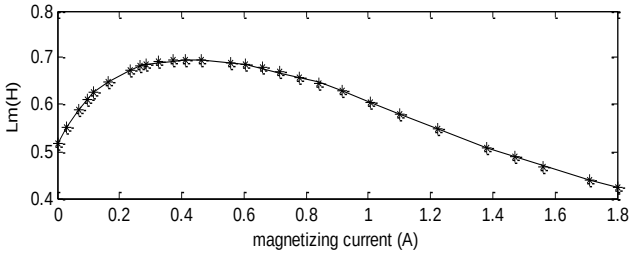

Fig. 2. Approximation of magnetizing curve.

III. PROPOSED CONTROL STRATEGY

A. Derivation of indirect rotor-field oriented control of DSIM

We can determine the reference torque to impose on

the motor and the speed reference from the electromagnetic torque equation expressed in terms of Park's components, as shown in Fig. 3. If we impose the current we should preserve the torque proportional to the quadrature current. The resultant rotor flux λ_r, also known as the rotor-flux linkages phasor, is assumed to be on the direct axis, which corresponds with the reality, that the rotor flux linkages are a single variable. Hence, aligning the d axis with the rotor flux phasor yields such as:

$$\begin{cases} \lambda_{dr} = \lambda_r^* \\ \lambda_{qr} = 0 \end{cases}. \tag{6}$$

The rotor currents in terms of the stator currents are derived from (3) as:

$$\begin{cases} i_{dr} = \dfrac{\lambda_r^* - M(i_{ds1} + i_{ds2})}{L_r} \\ i_{qr} = \dfrac{-M}{L_r}(i_{qs1} + i_{qs2}) \end{cases}. \tag{7}$$

Substituting for direct and quadrature rotor currents from (9) into (2), the following are obtained:

$$\begin{cases} i_{ds1}^* + i_{ds2}^* = \dfrac{1}{M}\lambda_r^* + \dfrac{T_r}{M}\dfrac{d\lambda_r^*}{dt} \\ i_{qs1}^* + i_{qs2}^* = \dfrac{L_r}{n_p M} C_{em}^* \dfrac{1}{\lambda_r^*} \\ w_g^* = \dfrac{M}{T_r}\dfrac{1}{\lambda_r^*}(i_{qs1}^* + i_{qs2}^*) \end{cases}, \tag{8}$$

where

$$T_r = \frac{L_r}{R_r}, \tag{9}$$

T_r denotes the rotor time constant. Equation (9) resembles the field equation in a separately excited DC machine, whose time constant is usually on the order of seconds.

Similarly, the same substitution of the rotor currents from (8) into the electromagnetic torque and stator flux expressions such as:

$$C_{em}^* = n_p \frac{M}{L_r}\lambda_r^*(i_{qs1}^* + i_{qs2}^*), \tag{10}$$

$$\begin{cases} \lambda_{ds1} = \sigma_1 L_s i_{ds1} + \sigma_2 L_{ps} i_{ds2} + \dfrac{M}{L_r}\lambda_{dr} \\ \lambda_{qs1} = \sigma_1 L_s i_{qs1} + \sigma_2 L_{ps} i_{qs2} \\ \lambda_{ds2} = \sigma_2 L_{ps} i_{ds1} + \sigma_1 L_s i_{ds2} + \dfrac{M}{L_r}\lambda_{dr} \\ \lambda_{qs2} = \sigma_2 L_{ps} i_{qs1} + \sigma_1 L_s i_{qs2} \end{cases}, \tag{11}$$

where

$$\sigma_1 = 1 - \frac{M^2}{L_s L_r};\ \sigma_2 = 1 - \frac{M^2}{L_{ps} L_r}.$$

By introducing stator flux expressions into voltage expressions of the DSIM (1), the following are obtained:

$$\begin{cases} V_{ds1}^* = R_s i_{ds1} + (\sigma_1 L_s - \sigma_2 L_{ps})\dfrac{di_{ds1}}{dt} - w_s^*\left((\sigma_1 L_s - \sigma_2 L_{ps}) i_{qs1} + \dfrac{\sigma_2 L_{ps} T_r}{M} w_g^* \lambda_r^*\right) \\ V_{qs1}^* = R_s i_{qs1} + (\sigma_1 L_s - \sigma_2 L_{ps})\dfrac{di_{qs1}}{dt} + w_s^*\left((\sigma_1 L_s - \sigma_2 L_{ps}) i_{ds1} + \left(\dfrac{M}{L_r} + \dfrac{\sigma_2 L_{ps}}{M}\right)\lambda_r^*\right) \\ V_{ds2}^* = R_s i_{ds2} + (\sigma_1 L_s - \sigma_2 L_{ps})\dfrac{di_{ds2}}{dt} - w_s^*\left((\sigma_1 L_s - \sigma_2 L_{ps}) i_{qs2} + \dfrac{\sigma_2 L_{ps} T_r}{M} w_g^* \lambda_r^*\right) \\ V_{qs2}^* = R_s i_{qs2} + (\sigma_1 L_s - \sigma_2 L_{ps})\dfrac{di_{qs2}}{dt} + w_s^*\left((\sigma_1 L_s - \sigma_2 L_{ps}) i_{ds2} + \left(\dfrac{M}{L_r} + \dfrac{\sigma_2 L_{ps}}{M}\right)\lambda_r^*\right) \end{cases}.$$

Considering that the first parts of voltages expressions are the linear parts and adding PI currents regulations to achieve perfect decoupling:

$$\begin{cases} V_{ds1l} = R_s i_{ds1} + L\dfrac{di_{ds1}}{dt} \\ V_{qs1l} = R_s i_{qs1} + L\dfrac{di_{qs1}}{dt} \\ V_{ds2l} = R_s i_{ds2} + L\dfrac{di_{ds2}}{dt} \\ V_{qs2l} = R_s i_{qs2} + L\dfrac{di_{qs2}}{dt} \end{cases}, \tag{12}$$

where

$$L = \sigma_1 L_s - \sigma_2 L_{ps}. \tag{13}$$

The first reason for introducing the current control is the elimination of stator dynamics. Adding compensation terms to make d-q axes completely independent. So we pose the following system which compensates the errors producing during the operations of decoupling:

$$\begin{cases} V_{ds1}^* = V_{ds1l} - V_{ds1c} \\ V_{qs1}^* = V_{qs1l} + V_{qs1c} \\ V_{ds2}^* = V_{ds2l} - V_{ds2c} \\ V_{qs2}^* = V_{qs2l} - V_{qs2c} \end{cases}, \tag{14}$$

$$\begin{cases} V_{ds1c} = w_s^*\left(L i_{qs1} + \dfrac{\sigma_2 L_{ps} T_r}{M} w_g^* \lambda_r^*\right) \\ V_{qs1c} = w_s^*\left(L i_{ds1} + \left(\dfrac{M}{L_r} + \dfrac{\sigma_2 L_{ps}}{M}\right)\lambda_r^*\right) \\ V_{ds2c} = w_s^*\left(L i_{qs2} + \dfrac{\sigma_2 L_{ps} T_r}{M} w_g^* \lambda_r^*\right) \\ V_{qs2c} = w_s^*\left(L i_{ds2} + \left(\dfrac{M}{L_r} + \dfrac{\sigma_2 L_{ps}}{M}\right)\lambda_r^*\right) \end{cases}. \tag{15}$$

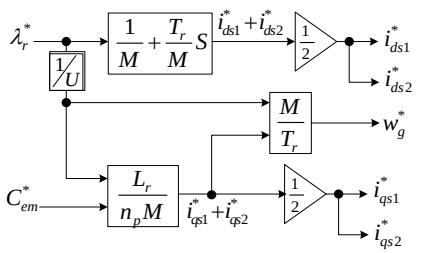

Fig. 3. Bloc of indirect rotor field-oriented.

B. Synthesis of regulators

The control of the stator current is ensured by a PI regulator and the reference rotor flux is given by a weakening-bloc which allows the working of the machine beyond the nominal speed. The PI controller parameters K_p and K_i are determined by pole placement method developed for the linear systems. The closed loop is given in Fig. 4. The closed loop transfer function is given by:

$$\frac{i_{ds1}}{i_{ds1}^*} = \frac{K_i S + K_p}{S^2 + \left(\frac{R_s + K_{pi}}{L}\right) S + \frac{K_{ii}}{L}}. \quad (16)$$

To get a well damped behavior, we use the poles placement approach.

Let $S = \rho_i \pm j\rho_i$, by identification, we obtain the parameters values of PI corrector based on p:

$$\begin{cases} K_p = 2\rho_i L - R_s \\ K_i = 2\rho_i^2 L \end{cases}. \quad (17)$$

Same calculation procedure for the other currents i_{qs1}, i_{ds2} and i_{qs2}. The speed control is simplified by the following diagram closed loop speed control is given in Fig. 5.

By applying the same procedure for calculating PI controller parameters stated above, we will have the following parameters:

$$\begin{cases} K_{pw} = 2\rho_w J - K_f \\ K_{iw} = 2\rho_w^2 J \end{cases}. \quad (18)$$

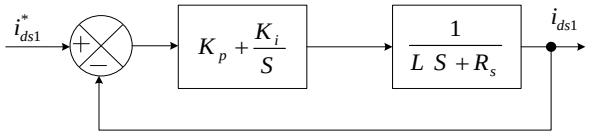

Fig. 4. Closed loop stator current.

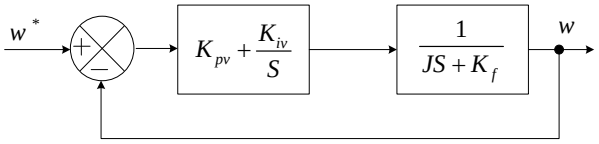

Fig. 5. Closed loop speed control.

C. Implementation of indirect vector control scheme for DSIM (IFOC)

Using the proposed control strategy, the IFOC of a double stator induction motor drive supplied by two CRPWM is shown in Fig. 6. This allows a simple extension of the IFOC principle in that the rotor flux linkage is maintained entirely in the d-axis, resulting in the q-axis component of rotor flux being maintained at zero. This reduces the electromagnetic torque equation to the same form as that of a dc machine or a rotor flux oriented three-phase machine. Thus, the electromagnetic torque and the rotor flux can be controlled independently, by controlling the d and q components of stator current. For this purpose, a vector control receives the speed and rotor flux requests and generates the commanded values of torque and flux producing components of stator current i_{ds1}^*, i_{ds2}^* and i_{qs1}^*, i_{qs2}^* respectively, which is processed through a proportional integral (PI) controller. The outputs of the four currents regulators, after an inverse Park transformation, are the stator voltage reference components in stationary reference frame to be applied to the PWM technique. For this purpose, the two sets of double stator currents are independently controlled and kept balanced for all possible operational conditions.

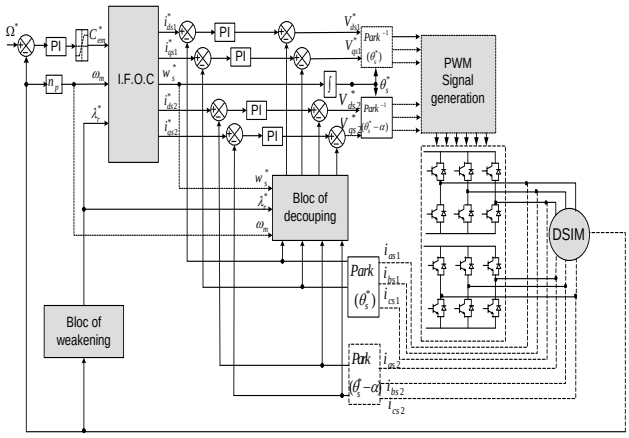

Fig. 6. Indirect rotor field-oriented control scheme for DSIM drive.

IV. ELECTROMAGNETIC SIMULATION AND EXPERIMENTAL RESULTS

A. Effect of flux linkage in DSIM

Though, the theory of main flux saturation is well recognized, a short application on DSIM is added to verify the validity impact of cross saturation in DSIM. Also, the objective of this application is to initially show comparison between models with cross magnetizing and without cross saturation on the machine operating. For that purpose this application treats the build-up of voltage and current during the dual stator induction motor (DSIM). The stator of each machine is rewound specifically for the task with two sets of three phase windings (two stars), Spatial shifting $\theta = 0^o$ between the two stars. The machine is star connected for all tests. The saturation curve was measured with the machine driven at synchronous speed. Figures 7, 8 and 9 simulates at no load the process of build-up of torque, current and air speed respectively, under rated speed.

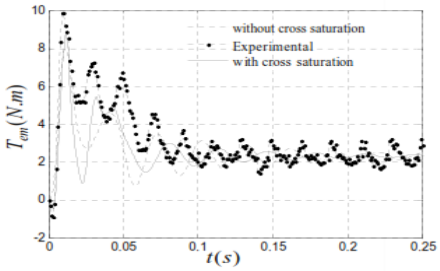

Fig. 7. Comparison between measured transient torque and simulated torque characteristics.

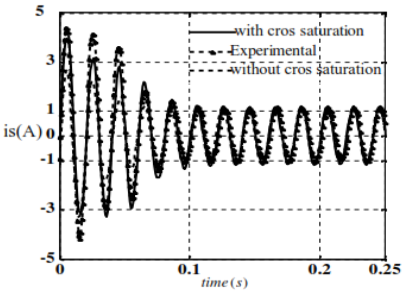

Fig. 8. Stator current of DSIM at load.

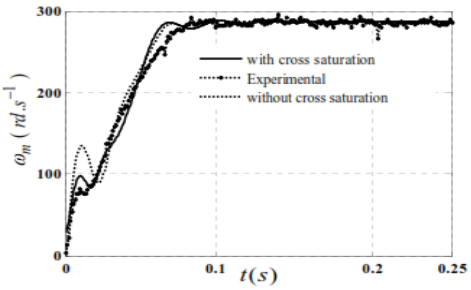

Fig. 9. Comparison between measured and simulated rotor transient rotor speed characteristics.

It is found that the time taken to reach the steady state for accurate model is about to the same for experimental results. Based on these results, we can conclude then, that the starting torque developed by the machine where we take into account main flux saturation is closer to the measurement result that the linear regime.

We also note that at start-up, the rotor speed of the DSIM, if taking into account the saturation with and without cross saturation is closer to the rotor speed measured than if ignored. We can confirm that the impact of the saturation model is clearer in transient regime and especially at start-up.

B. IRFOC control strategy of saturated DSIM

The IFOC control algorithm and precision of is verified using the simulation. It was proven that it is possible to achieve robust and reliable speed sensorless control, with satisfactory performance characteristics. Furthermore, a novel modulation technique allowed for the improvement of control efficiency.

The proposed theoretical consideration of applying known sensorless control principles to a DSIM are verified using computational software. The simulation results show the successful implementation of sensorless speed estimation and decoupled vector control for DSIM. Separate stages, with different sampling times, for current and speed control are set in the simulation.

Speed estimation technique is verified using speed closed control loop for the DSIM with IFOC principles implemented. The flux was set to the nominal value, and the machine was first accelerated to the reference speed of 300 rad/s, while the load torque was kept at zero.

In Fig. 10, DSIM actual and estimated speed is presented, where the obvious transitions of torque and speed can be noted. In addition, the estimated and actual speed match almost perfectly providing the strong ground for practical speed sensorless drive implementation. High precision of speed estimation will ensure decoupled control for IFOC strategy, aligning the synchronous rotating reference frame to the desired position.

As shown in Fig. 10 (b), there seems to be no speed change when a step load change is effected as the large speed range selected for y-axes speed. When y-axis is zoomed, there is a speed variation of 0.7 rad/s, as observed in the extended view of speed.

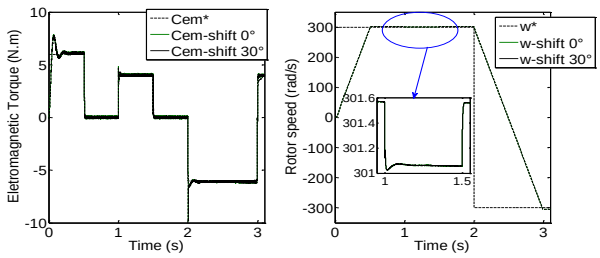

Fig. 10. (a) Electromagnetic torque and (b) rotor speed.

On the results shown in Fig. 11, one can see a high performance stator current response obtained despite the disturbance, and zoom to show the difference between the shift0 and shift30. From these waveforms, it is obvious that the ideal IRFOC is achieved in all working conditions.

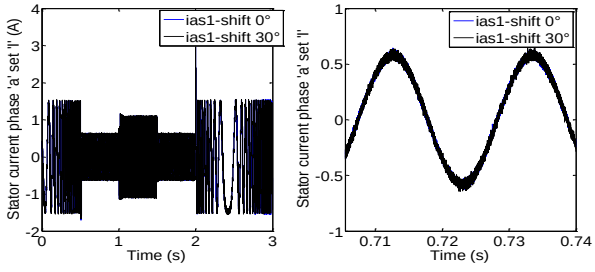

Fig. 11. Stator current per phase ‘a’ set ‘I’ for 0° and 30° shift.

The simulations were also carried out in order to verify the performance of the proposed indirect FOC scheme. The conventional method of field weakening (i.e., to vary the rotor flux reference in proportional to inverse of the rotor speed) was employed, and a step change of load torque 4 N.m at 1.0s was effected.

It is evident from the all pervious simulations results, that there is a very close correlation between the reference and simulated value of torque, current, speed and flux. It can also be clearly adjudged that there is no current unbalance between the two sets of stator windings. It is worth mentioning here that, in all the simulation work, the effect of mutual coupling l_{sm} has been included.

VI. CONCLUSION

In this paper, the vector control is introduced in order to control the dual stator induction motor with maximum power. It is based on a transient model with electromagnetic saturation. It allows precise adjustment of the electromagnetic torque of the machine and can ensure torque at zero speed. In this paper, we have presented the principle of the dual stator induction motor field oriented control, fed by a voltage inverter in the presence of a speed loop with a PI corrector. We can conclude that the field oriented control has a good dynamic and static electromagnetic torque, currents and flux results. We have proposed a simple approach for indirect rotor-field-oriented-control for DSIM drive fed by PWM two identical VSI and verified it by simulations when the acquired waveforms show good results. The effect of mutual leakage inductance between the two stator winding sets has been included in the model. For 30° shift, we concluded a reduction in torque ripples and the rotor heating is also reduced due to reduction in rotor currents. The comparison in experimental and simulation fields demonstrates a proper accuracy for the proposed dynamic modeling.

REFERENCES

[1] T. Yuvaraja and K. Ramya, "Vector control of PMSM take over by photovoltaic source," *ACES Express Journal*, vol. 1, no. 6, June 2016.

[2] M. R. Barzegaran, A. Sarikhani, and O. A. Mohammed, "An optimized equivalent source modeling for the evaluation of time harmonic radiated fields from electrical machines and drives," *Applied Computational Electromagnetics Society (ACES) Journal*, vol. 28, no. 4, pp. 273-283, Apr. 2013.

[3] B. S. Marwa, A. K. Mohamed, B. F. Mouldi, and R. Habib, "Analysis of saturated self-excited dual stator induction generator for wind energy generation," *Journal of Circuits, Systems, and Computers*, vol. 24, no. 9, pp. 196-203, 2015.

[4] B. S. Marwa, A. K. Mohamed, B. F. Mouldi, and R. Habib, "Modeling of dual stator induction generator with and without cross saturation," *Journal of Magnetics*, vol. 20, no. 3, pp. 165-171, 2015.

[5] E. Aycicek, N. Bekiroglu, I. Senol, and Y. Oner, "Rotor configuration for cogging torque minimization of the open slot structured axial flux permanent magnet synchronous motors," *ACES Journal*, vol. 30, no. 4, Apr. 2015.

[6] R. Sadouni and A. Meroufel, "Indirect rotor field-oriented control (IRFOC) of a dual star induction machine (DSIM) using a fuzzy controller," *Acta Polytechnica Hungarica*., vol. 9, no. 4, pp. 177-192, 2012.

[7] A. S. Abdel-Khalik, M. I. Masoud, and B. W. Williams, "Vector controlled multiphase induction machine: Harmonic injection using optimized constant gains," *Electric Power Systems Research*, vol. 89, no. 15, pp. 116-128, 2012.

[8] B. S. Marwa, A. K. Mohamed, B. F. Mouldi, and R. Habib, "Effect of the stator mutual leakage reactance of dual stator induction generator," *International Journal of Electrical Energy*, vol. 2, no. 3, pp. 1810-1818, 2014.

[9] M. B. Slimene and M. A. Khlifi, "Performance limits of three-phase self-excited induction generator (SEIG) as a stand alone DER," *Journal of Electrical Engineering and Technology (JEET)*, vol. 12, no. 1, 2017.

[10] A. S. Abdel-Khalik and S. M. Gadoue, "Improved flux pattern by third harmonic injection for multiphase induction machines using neural network," *Alexandria Engineering Journal*, vol. 50, no. 12, pp. 163-169, 2011.

[11] A. K. Mohamed, B. S. Marwa, B. F. Mouldi, and R. Habib, "Performance evaluation of self-excited DSIG as a stand-alone distributed energy resource," *Electrical Engineering, Springer*, vol. 97, no. 4, pp. 261-345, 2016.

[12] J. H. Alwash and L. J. Qaseer, "Three-dimension finite element analysis of a helical motion induction motor," *ACES Journal*, vol. 25, no. 8, pp. 703-712, Aug. 2010.

[13] A. Shiri and A. Shoulaie, "Investigation of frequency effects on the performance of single sided linear induction motor," *ACES Journal*, vol. 27, no. 6, pp. 497-504, June 2012.

[14] B. S. Marwa, A. K. Mohamed, B. F. Mouldi, and R. Habib, "Modeling and analysis of double stator induction machine supplied by multi-level inverter," *16th IEEE Mediterranean Electrotechnical Conference (MELECON), IEEE*, 2012.

[15] M. Hassani and A. Shoulaie, "Dynamic modeling of linear actuator using fuzzy system to approximate magnetic characteristics," *ACES Journal*, vol. 30, no. 8, Aug. 2015.

[16] A. K. Mohamed and R. Habib R, "General modeling of saturated AC machines for industrial drives," *COMPEL: The International Journal for Computation and Mathematics in Electrical and Electronic Engineering*, vol. 35, no. 1, pp. 44-63, 2016.

3-D Defect Profile Reconstruction from Magnetic Flux Leakage Signals in Pipeline Inspection Using a Hybrid Inversion Method

Junjie Chen

Electric Power Planning & Engineering Institute, Beijing, 100120, China
jjchen@eppei.com

Abstract ─ In this paper, we propose a hybrid inversion approach to reconstruct the profile of arbitrary three-dimensional (3-D) defect from magnetic flux leakage (MFL) signals in pipeline inspection. The region of pipe wall immediately around the defect is represented by an array of partial cylinder cells, and a reduced forward FE model is developed to predict MFL signals for any given defect. The neural network (NN) method is used at first to give a coarse prediction of the defect profile, and the prediction is then utilized as one original solution of the genetic algorithm (GA) to search for the global optimum estimate of the defect profile. To demonstrate the accuracy and efficiency of the proposed inversion technique, we reconstruct defects from both simulated and experimental MFL signals. In both cases, reconstruction results indicate that the hybrid inversion method is rather effective in view of both efficiency and accuracy.

Index Terms ─ Defect reconstruction, genetic algorithm, magnetic flux leakage, neural network, pipeline inspection.

I. INTRODUCTION

Magnetic flux leakage (MFL) inspection is widely used for detecting corrosion defects in pipelines for oil and gas [1]. The inspection devices, referred as in-line-inspection (ILI) tools, are designed for autonomous operation in the pipeline. Once defects have been identified, an equally important problem is the assessment of the size or severity of the defect [2].

In the past, inverse MFL problems were solved based on neural networks [3-5], gradient-based optimization methods [6, 7], GA-based optimization methods [8] and other methods [9, 10]. Neural networks are advantageous in cases where rapid inversions are required. However, their main drawback is that they require a large database for training. The performance of neural networks depends on the data used in training and testing. When the test signal is no longer similar to the training data, performance degrades. In contrast, methods embedding the physical model into the MFL signal inversion process do not require a large database. The physical model and the optimization procedure are crucial for these inversion methods. On the issue of convergence, gradient-based optimization often fails to converge to the global optimum in the presence of multiple local optima, since the optimization problem for defect reconstruction from MFL signals is not a unique solution one. The GA-based approach, on the other hand, begins with a large set of initial search points using well-defined probabilistic tools to guide a search towards regions in the search space that are more likely to contain the global optimum. The GA usually begins with a randomly generated set of original solutions, which may take a long time to converge to the global optimum. Therefore, a suitable selection of the initial search points is rather important for the GA-based approach to improve the efficiency.

In this paper, we propose a hybrid method for 3-D defect reconstruction from MFL signals in pipeline inspection. We develop a reduced forward model of pipe in MFL inspection, and combine NN to GA in inversion process by applying the prediction result of NN as one initial solution of GA. Results of defect reconstruction show that the proposed method has outstanding performance for both simulated and real experimental MFL signals.

The organization of this paper is as follows. In Section II, we introduce the reduced forward FE models of pipe and characterization of defect in MFL inspection. In Section III, we summarize the application of NN and GA to 3-D defect inversion. Section IV gives experimental results based on simulated and realistic experimental MFL data, and Section V gives the conclusions.

II. FORWARD MODEL OF MFL INSPECTION

Figure 1 depicts the corresponding magnetic circuit for an ILI tool for pipe inspection. Permanent magnets magnetize the pipe wall to saturation or near saturation flux density, typically in the axial direction. As shown, the magnetic leakage fields from the pipe wall are detected using uniformly-spaced Hall or coil sensors.

Submitted On: January 14, 2016
Accepted On: February 14, 2017

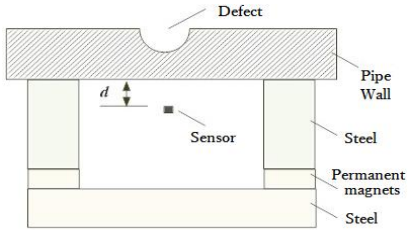

Fig. 1. Simplified magnetic circuit of an ILI tool.

A. Reduced forward model

Based on the magnetic circuit of the ILI tool, we create a 90-degree forward FE model of MFL inspection as shown in Fig. 2 (a), including pipe wall, steel, permanent magnets, air and defect [11, 12]. Compared with the complete 360-degree model, this model could reduce much computation work. Then, a further reduced forward model is proposed as shown in Fig. 2 (b). The reduced forward model only consists of air, nonlinear pipe material and permanent magnets embedded in the pipe wall. The size and distance of permanent magnets could be adjusted so that the simulated MFL signals agree with the real signals.

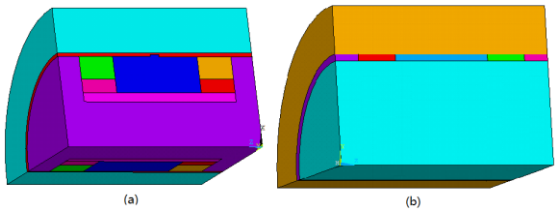

Fig. 2. (a) Basic 90-degree forward model. (b) Reduced forward model.

For the basic forward model and the reduced forward model, the related parameters together with detailed explanations are presented in Table 1, and the Characteristic curves of nonlinear magnetic materials used in the forward model are presented in Fig. 3.

The results of simulation show that, the reduced model only brings less than 5% error while taking one fifth time as the basic model does. Figure 4 shows two samples of MFL images of metal loss defects using the reduced model.

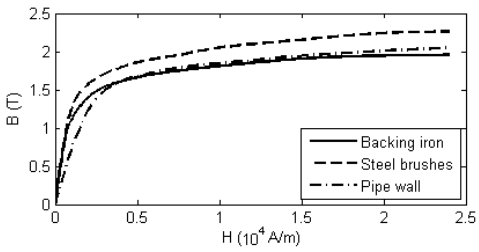

Fig. 3. Characteristic curves of nonlinear magnetic materials used in the forward model.

Table 1: Related parameters for the forward model

Parameter	Value	Unit
Pipe diameter	457	mm
Pipe thickness	14.3	mm
Permanent magnet width	80	mm
Permanent magnet height	30	mm
Brush width	80	mm
Brush height	50	mm
Back height	20	mm
Magnetic pole spacing	1000	mm
Relative permeability	1.26	-
Coercive force	836	KA/m
Lift off value	3	mm

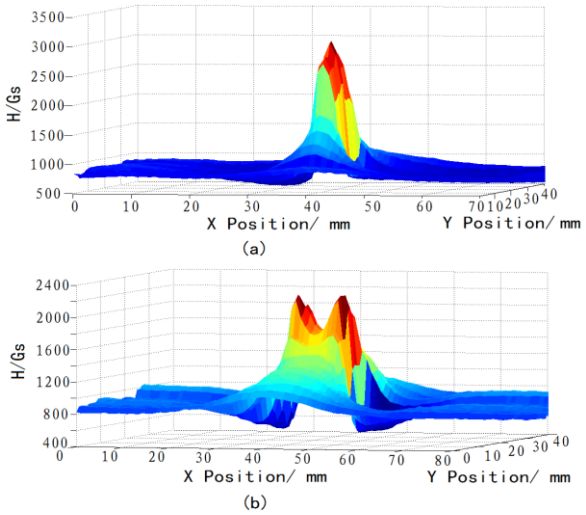

Fig. 4. Simulated MFL images for metal-loss defects using the reduced forward model: (a) internal defect, 100.1 mm×14.3 mm×5.7 mm; (b) external defect, 42.9 mm×42.9 mm×8.6 mm.

B. Defect characterization

The forward computational problem consists of using the reduced FE model to efficiently obtain the magnetic flux field profile for any defect in the pipe. The region of pipe wall immediately around the defect constitutes the 'region of interest' (ROI). To characterize different defect shapes, the radial depth, the tangential width and the axial length of ROI are divided into 7, 10 and 10 parts respectively. Consequently, the ROI could be represented by an array of 7×10×10 partial cylinder cells as illustrated in Fig. 5.

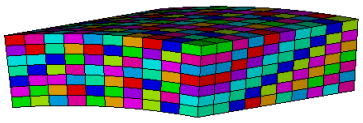

Fig. 5. Defect characterization with 7×10×10 basic model for inversion.

The magnetic conductivity of each cell could be made equal to that of air or iron, resulting in different geometries of the defect. By doing this, any particular defect in the whole defect area could be characterized by a set of 100 depths: $d_1, d_2, ..., d_{100}$, where $\mathrm{di} \in \{0,1,\ldots,7\}$. Thus, the value of a particular depth is encoded as a 3 bit binary string, and the parameter set for the whole defect area can be represented by a 300 bit binary string.

III. INVERSION PROCEDURE USING NN AND GA

In order to take full use of the advantages of both the NN and the GA method, we propose a hybrid method for the defect reconstruction from MFL signals, i.e., to use the results of NN inversion as one initial solution for the GA method.

A. NN prediction

As shown in Fig. 6, a feed-forward NN with a single hidden layer is used to predict the defect profile for the initial solution of GA. The input of the NN consists of feature parameters of MFL signals scanned over the test-pipe, and the output are the parameters of defects corresponding to the MFL signals. The databases of both MFL signals and corresponding defect parameters are separated into training, validation and verification sets.

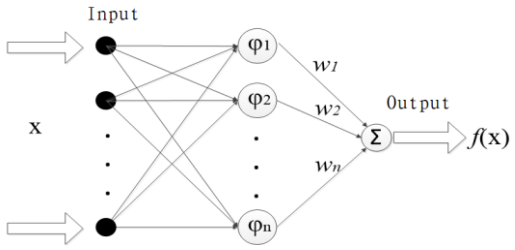

Fig. 6. The feed-forward NN used for prediction.

The training process starts with only one hidden node, and for each training epoch a new node is created. The new input-hidden connections receive random weights and the rest of the weights are obtained by solving (1) with the least square minimization based on the singular value decomposition:

$$A \cdot W_{io} + f_1(A \cdot W_{ih}) \cdot W_{ho} = f_2^{-1}(B), \qquad (1)$$

where A and B represent the input and output training data sets, f_1 and f_2 are nonlinear activation functions for hidden and output nodes, $[W_{ih}]$ the "randomly-fixed" input-hidden weights, and $[W_{io}]$, $[W_{ho}]$ the matrices containing unknown weights, are the input-output and the hidden-output inter-connection weights, respectively.

To generate the training data sets, the reduced forward model shown in Fig. 2 (b) and the defect characterization shown in Fig. 5 were used to get simulated MFL signals. Considering the object for NN inversion result in this paper, only cuboid defects are simulated. Therefore, the trained NN could only provide a cuboid prediction for any arbitrary defect profile as one initial solution.

B. GA inversion process

The flowchart of iterative inversion process using GA for 3-D defect reconstruction is shown in Fig. 7. The inverse problem is solved by minimizing an objective function, representing the difference between the forward model predicted and the realistic measured MFL signal. When the difference is below a pre-set threshold, the defect profile represents the desired solution. The various issues related with the formulation of the inversion process are described below.

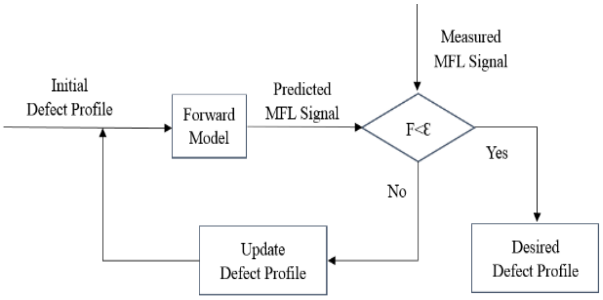

Fig. 7. Iterative inversion flowchart for 3-D defect reconstruction.

As all the three components (radial, tangential and axial) of magnetic flux density carry the information of defect profile, they are all chosen as input signals for the inverse optimization procedure when simulated MFL signals are used. However, only the axial component is used when the inversion is conducted based on realistic measured MFL data, because only the axial component is detected by the ILI tool.

The minimization of an error between measured and predicted MFL signals can be recast as maximizing of the following fitness function:

$$F = \frac{1}{1 + C\sum_{i=1}^{N} \| B_i^m - B_i^{FEM} \|}, \qquad (2)$$

where N is the number of points taken on the signal and C is constant. The global maximum value of F is 1, corresponding to the case the predicted and measured MFL signals are exactly the same. It should also be noted that in case of the error reaching a local minimum other than the global minimum of zero, the relative ratio between the corresponding local and global maximums of F is determined by the constant C.

As shown before, the results of NN inversion is taken as one initial solution for the GA inversion process. This will bring significant help in increasing

both efficiency and possibility for the GA to reach the global optimum solution, which will be presented in Section IV. At the same time, 7 randomly generated original solutions are also used. Furthermore, 2 special 300-bit binary strings, composed of only '0' and only '1' respectively, are added to the initial population for GA in order to keep the diversity of population.

When the original solutions have been selected, a fitness function is used as a measure of closeness of each member in the population to the global optimum solution. Subsequently, a new population is generated by applying genetic operators including reproduction, crossover and mutation on the previous population. The selection mechanism for reproduction favors the highly fit members, so that the members more close to the global optimum are assigned higher probabilities for producing children. Crossover operations ensure that the new population inherits highly fit features, while mutation may add previously unexplored features into the new population. With this, the population drifts to a global or near global solution after a few number of generations in the iterative process.

IV. EXPERIMENTAL RESULTS

In this paper, reconstruction is implemented using biased Roulette-Wheel algorithm with a two-point crossover, and the mutation probability varies between 0.3 and 0.5. The iterative process is terminated when the population of the GA has been updated for 200 times, and at last smoothing is conducted to produce a better defect profile.

Experiments of 3-D defect reconstruction are conducted based on 3-D simulated MFL signals and 1-D measured MFL signals. An internal 100.1 mm× 14.3 mm×5.7 mm cuboid defect (Fig. 8 (a)), an external 42.9 mm×42.9 mm×8.6 mm cuboid defect (Fig. 9 (a)), and an external 42.9 mm×7.15 mm globoid defect (Fig. 10 (a)) are simulated using the reduced forward model. At the same time, the ILI tool is used to measure the axial MFL signals of an 18-inch and 14.3 mm-thick pipe, on which the same defects as the three simulated ones have been artificially made.

The reconstruction is firstly conducted using general GA with initial population composed of 10 randomly generated original solutions. Figure 8 (b), Fig. 9 (b), and Fig. 10 (b) depict the final predicted profiles of the three defects based on 3-D simulated MFL signals. As comparison, Fig. 8 (c), Fig. 9 (c), and Fig. 10 (c) show the predicted defect profiles based on 1-D measured MFL signals. It can be seen that the predicted profiles using 3-D simulated MFL signals match the real defects very well, while at the same time, the inversion results using 1-D measured MFL signals are not so good within a fixed number of iterations. Possible reasons could be lack of enough information carried by the radial and tangential components of magnetic flux density together with error between simulated and realistic MFL signals.

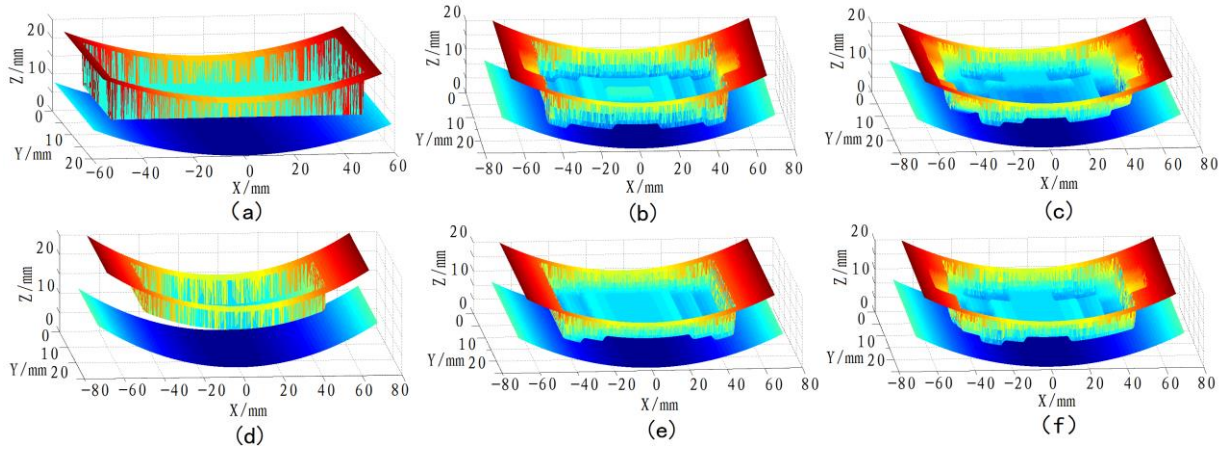

Fig. 8. Reconstruction of internal cuboid defect, 100.1 mm×14.3 mm×5.7 mm: (a) real defect profile; (b), (c) reconstructed defects based on 3-D simulated and 1-D measured signals, using general GA with randomly generated initial population; (d) prediction result of NN inversion; (e), (f) reconstructed defects based on 3-D simulated and 1-D measured signals, using GA with initial solution from NN inversion.

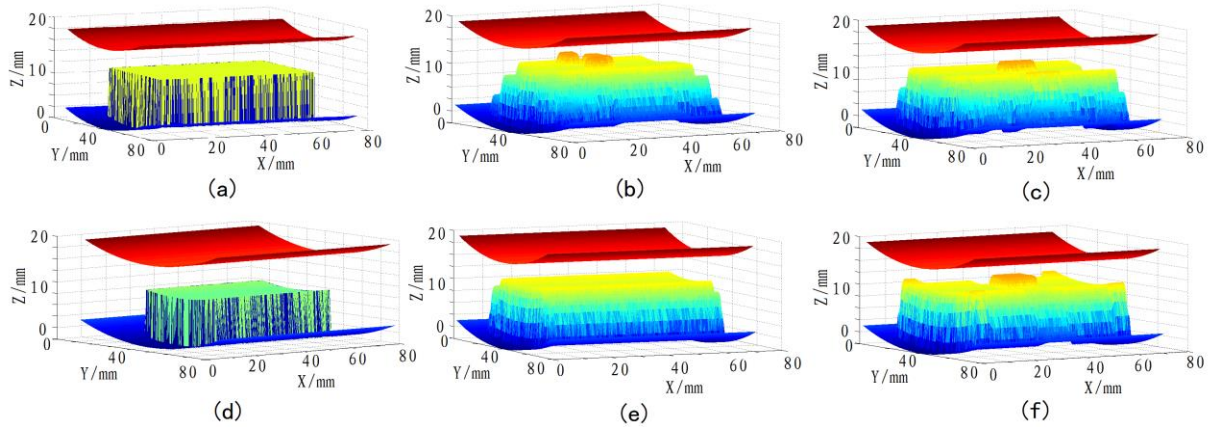

Fig. 9. Reconstruction of external cuboid defect, 42.9 mm×42.9 mm×8.6 mm: (a) real defect profile; (b), (c) reconstructed defects based on 3-D simulated and 1-D measured signals, using general GA with randomly generated initial population; (d) prediction result of NN inversion; (e), (f) reconstructed defects based on 3-D simulated and 1-D measured signals, using GA with initial solution from NN inversion.

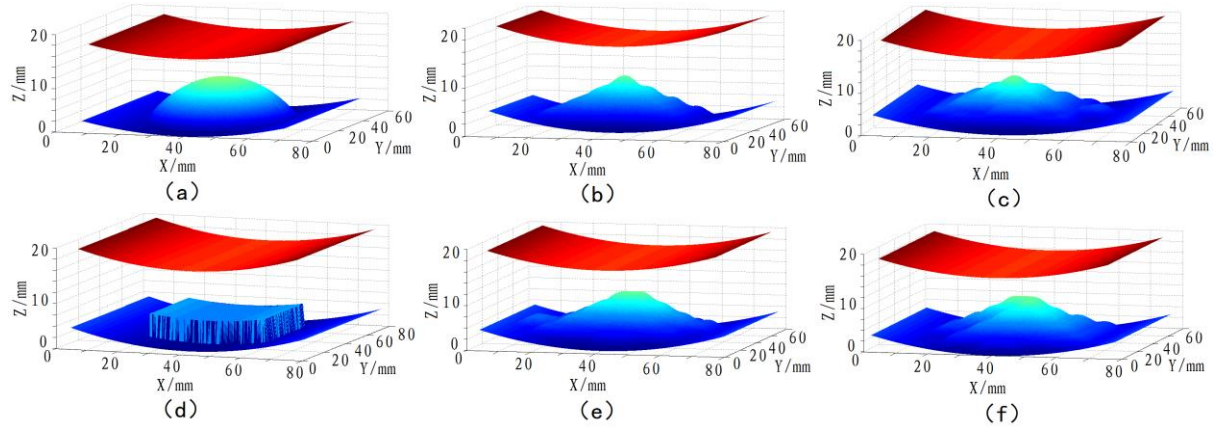

Fig. 10. Reconstruction of external globoid defect, 42.9 mm×7.15 mm: (a) real defect profile; (b), (c) reconstructed defects based on 3-D simulated and 1-D measured signals, using general GA with randomly generated initial population; (d) prediction result of NN inversion; (e), (f) reconstructed defects based on 3-D simulated and 1-D measured signals, using GA with initial solution from NN inversion.

Then the reconstruction is conducted again using the proposed hybrid inversion method, with the prediction of NN as one original solution of the GA inversion. The prediction results for the three defects from NN are shown in Fig. 8 (d), Fig. 9 (d) and Fig. 10 (d). Figure 8 (e), Fig. 9 (e), and Fig. 10 (e) depict the final predicted profiles of the three defects based on 3-D simulated MFL signals. Similarly, Fig. 8 (f), Fig. 9 (f), and Fig. 10 (f) show the predicted defect profiles based on 1-D measured MFL signals. Compared with former inversion results using general GA, reconstructed defects match the real ones better when prediction results of NN are used as the original solutions of the GA in the hybrid inversion procedure. In fact, the efficiency of defect reconstruction has been improved significantly, and the accuracy of reconstruction has increased within same time.

The reconstruction errors in different situations are then calculated and summarized as Table 2. The larger errors of reconstructed results using general GA with randomly generated original solutions demonstrate that the optimization fails to converge to the global minimum solution within fixed number of iterations. When the prediction of NN is used as original solution in the hybrid inversion procedure, the iterative GA could produce obviously better results of defect reconstruction.

To further testify the robustness of the proposed hybrid inversion procedure, a randomly generated internal defect as Fig. 11 (a) is simulated using the reduced forward model to get corresponding 3-D simulated MFL signals. The reconstructed defect profile using the proposed hybrid inversion procedure, based

on the basic 7×10×10 defect model shown in Fig. 5, is shown in Fig. 11 (b). Then the hybrid inversion procedure is conducted again, based on a refined 15×20×20 defect model, to get a new reconstructed defect profile (Fig. 11 (c)). The results of reconstruction show that the proposed hybrid inversion procedure is rather effective and robust even for randomly generated defect profile. Furthermore, the accuracy of reconstruction could get improved using a refined defect model extended from the basic one shown in Fig. 5.

Table 2: Reconstruction errors of different defects

Defect/mm	Simulated Signals		Measured Signals	
	General GA	Hybrid	General GA	Hybrid
Internal cuboid 100.1×14.3×5.7	0.12	0.05	0.21	0.14
External cuboid 42.9×42.9×8.6	0.13	0.05	0.22	0.15
External globoid 42.9×7.15	0.25	0.12	0.41	0.28

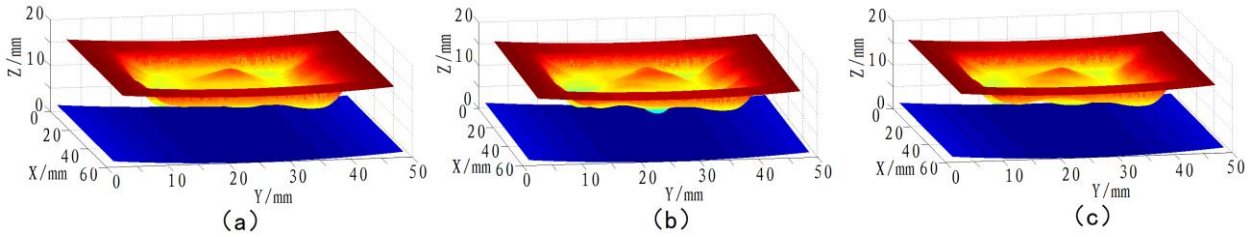

Fig. 11. Reconstruction of randomly generated defect using proposed hybrid inversion method based on 3-D simulated MFL signals: (a) real defect profile; (b) reconstructed defect using basic 7×10×10 defect model; (c) reconstructed defect using refined 15×20×20 defect model.

V. CONCLUSION

In this paper, a hybrid inversion approach is presented to reconstruct the 3-D defect profile from MFL signals in pipeline inspection. The reduced FE forward model of MFL inspection is developed, and the defect area is represented by an array of 7×10×10 partial cylinder cells. The NN is used at first to get a prediction of the defect, which is then utilized as one original solution of the GA to search for the global optimum estimate of the defect profile. Accuracy and efficiency of the proposed hybrid inversion method is demonstrated by the reconstruction results from both simulated and experimental MFL signals. Comparison between results from simulated and measured MFL signals also show that all the three components, instead of only the axial or radial component, of MFL signals in pipeline inspection should be detected for better reconstruction results. Furthermore, the accuracy of reconstruction could get improved using a refined defect model.

Future work will concentrate on optimizing the forward model to reduce time consumption and refining the defect model to increase accuracy of defect prediction. Besides, more kinds of defect shape should be covered in the experiment to test the proposed inversion method.

REFERENCES

[1] A. Khodayari-Rostamabad, J. P. Reilly, N. K. Nikolova, et al., "Machine learning techniques for the analysis of magnetic flux leakage images in pipeline inspection," *IEEE Transactions on Magnetics*, vol. 45, no. 8, pp. 3073-3084, 2009.

[2] M. Ravan, R. K. Amineh, S. Koziel, et al., "Sizing of 3-D arbitrary defects using magnetic flux leakage measurements," *IEEE Transactions on Magnetics*, vol. 46, no. 4, pp. 1024-1033, 2010.

[3] P. Ramuhalli, L. Udpa, and S. S. Udpa, "Electromagnetic NDE signal inversion by function-approximation neural networks," *IEEE Transactions on Magnetics*, vol. 38, no. 6, pp. 3633-3642, 2002.

[4] A. Joshi, "Wavelet transform and neural network based 3D defect characterization using magnetic flux leakage," *International Journal of Applied Electromagnetics and Mechanics*, vol. 28, no. 1, pp. 149-153, 2008.

[5] S. R. H. Hoole, S. Subramaniam, R. Saldanha, et al., "Inverse problem methodology and finite elements in the identification of cracks, sources, materials, and their geometry in inaccessible locations," *IEEE Transactions on Magnetics*, vol. 27, no. 3, pp. 3433-3443, 1991.

[6] R. Priewald, C. Magele, P. Ledger, et al., "Fast magnetic flux leakage signal inversion for the reconstruction of arbitrary defect profiles in steel using finite elements," *IEEE Transactions on Magnetics*, vol. 49, no. 1, pp. 506-516, 2013.

[7] K. C. Hari, M. Nabi, and S. V. Kulkarni, "Improved FEM model for defect-shape

construction from MFL signal by using genetic algorithm," *Science, Measurement & Technology, IET*, vol. 1, no. 4, pp. 196-200, 2007.

[8] M. Yan, S. Udpa, S. Mandayam, et al., "Solution of inverse problems in electromagnetic NDE using finite element methods," *IEEE Transactions on Magnetics*, vol. 34, no. 5, pp. 2924-2927, 1998.

[9] A. A. Adly and S. K. Abd-El-Hafiz, "Utilizing particle swarm optimization in the field computation of non-linear magnetic media," *ACES Journal*, vol. 18, no. 3, pp. 202-209, 2003.

[10] J. Chen, S. Huang, and W. Zhao, "Three-dimensional defect reconstruction from magnetic flux leakage signals in pipeline inspection based on a dynamic taboo search procedure," *Insight-Non-Destructive Testing and Condition Monitoring*, vol. 56, no. 10, pp. 535-540, 2014.

[11] P. S. Kildal and A. Kishk, "EM modeling of surfaces with STOP or GO characteristics-artificial magnetic conductors and soft and hard surfaces," *ACES Journal*, vol. 18, no. 1, pp. 32-40, 2003.

[12] M. M. Bibby and F. P. Andrew, "High accuracy calculation of the magnetic vector potential on surfaces," *ACES Journal*, vol. 18, no. 1, pp. 12-22, 2003.

Junjie Chen was born in 1988. He received his Ph.D. degree from Tsinghua University in 2015. He is currently working on problems in power system.

Investigation on Mechanical and Magnetic Field Behaviors of GIB Plug-in Connector under Different Contact Conditions

Xiangyu Guan [1], Quanyu Shen [1], Minghan Zou [2], Naiqiu Shu [1], and Hui Peng [1]

[1] School of Electrical Engineering
Wuhan University, Wuhan, 430072, China
xiangyuguan1986@163.com

[2] State Grid Nanjing Power Supply Company
Nanjing, 210000, China
773740620@qq.com

Abstract ─ In order to provide an effective detection method for internal contact fault of gas insulated bus (GIB), mechanical and magnetic field behaviors of GIB plug-in connector under different assembly conditions are analyzed by finite element (FEM) method in this paper. Contact forces on individual contact spots are obtained by mechanical field analysis then simulated by imperfect contact bridge models during electromagnetic field analysis. Magnetic field distributions around GIB plug-in connector under the various contact statuses (conductor insert depth and docking angle) are studied through numerical modeling and field testing. Results show that the mechanical contact parameters (contact forces and radiuses) of individual contact fingers vary from each other under the action of holding spring deformation and conductor gravity, and the surrounding magnetic field has strong relationship with the internal mechanical contact status. The magnetic field strength distributes uniformly around the GIB plug-in connector under well assembly condition. However, the magnetic field distorts since mechanical contact status is changed by the contact degradation or contact failure.

Index Terms ─ Contact failure, finite element method, gas insulated bus, magnetic field, plug-in connector.

I. INTRODUCTION

Gas insulate bus (GIB) equipment are of interest in modern power transmission/distribution systems due to their advantages of environmental friendliness, large power transmission capacity, easy-maintenance and high operation reliability [1]. Numerous of slidable plug-in connectors are used as the main electrical loop connections of GIB for absorbing misalignments during manufactory/assembly process and mechanical/thermal stress during operation process [2]. Dynamic contact conditions exist between contact elements for slidable design [3], additional power loss and electromagnetic force will act on plug-in connector due to the current constriction effect, which makes GIB plug-in connector become one of the feeblest components of equipment. If the amount of contact degradation is beyond failure threshold, contact overheating fault may happen and internal flash over could be induced by poor contacts [4-5]. The GIB must be disintegrated since internal fault happens as gas pressure vessel (which is filled with about 0.4Mpa SF6 gas), power supply recovery cycle is considerable and really hard to avoid the greenhouse gas leaking. As a consequence, the contact degradation and overheating fault of the GIB plug-in connector are serious threatening to the safe operation of equipment and power systems.

Due to fearful damages by internal contact fault, several countermeasures such as the electrical loop resistance test [6-7], tank vibration monitoring [8-9], partial discharge [10-11] and temperature monitoring [12] have been investigated and applied to the GIB equipment. Each of mentioned methods has its merits on internal fault/overheating detection, however they are less effective for early stages of contact fault. Lower electrical loop resistance results do not necessarily reply good contacts due to only the total electric loop connection condition evaluated, and contact trouble on single connector may be hidden. It's hard to locate acceleration/temperature sensors inside metal enclosure due to the insulation/sealing design limits of gas insulated equipment, besides, the relationships between inner contact statuses and outer vibration/temperature are not clear. The internal contact has already disabled since detectable partial discharge happens, and there is always not sufficient time for early warning. Magnetic field behaviors can directly reflect early degradation stages of contact failures [13-14], and magnetic field detection method on bolt connections of GIB is studied in [15] by attaching magnetic sensors inside metal tank. However, few previous works has paid attention on the

Submitted On: August 8, 2016
Accepted On: January 28, 2017

relationship between the surrounding magnetic field and contact conditions of GIB plug-in connector.

The fact that assembly conditions of GIB plug-in connector can be changed under cyclic thermal loadings by operation current and environmental temperature has been revealed in our previous study [16]. In order to identify and evaluate the internal contact failure of GIB equipment effectively, relationships between internal contact status and magnetic field are obtained by three-dimensional finite element modeling in this paper. Physical structure of the GIB capsule is shown in Fig. 1. The main electrical bus gets through both ends of disc-type epoxy insulators which is fixed by slidable plug-in connectors. Mechanical and electrical connection between the socket and conductor plug are realized by series of concentric-arranged spring-loaded contact components. Magnetic fields strengths around plug-in connector (C1) are measured by electromagnetic probes. Assumptions about numerical model are as follows.

Electromagnetic field analysis is based on quasi-static approximation with the AC operation current.

Partial tiny component geometry characteristics could not obviously affect distributions of surrounding magnetic field. Based on this concept, several external insulation designing (champers on conductor surface) and supporting/fixing parts (terminal bolts and locating parts) are omitted to minimize computational effort.

Micro-rough features of both contact surfaces are neglected, and the mechanical contact area is assumed equal to electrical contact area with chemical stability of SF_6 insulation gas.

The mechanical contact is rather a stable physical condition comparing with surrounding electromagnetic field, and it can be hypothesized that the weak coupling relation exists between electromagnetic and mechanical fields of GIB plug-in connector.

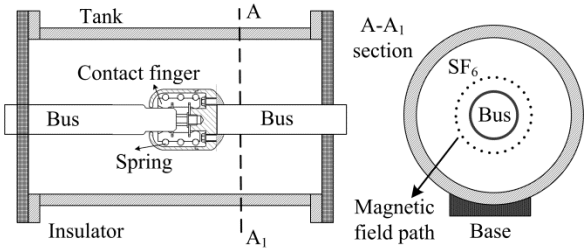

Fig. 1. Schematic structure of GIB capsule.

The research thought of this paper is organized as follows: numerical calculation method is discussed in Section II. Mechanical contact parameters (contact force and radius) of plug-in connector with various assembly conditions are calculated by mechanical FEM analysis in Section III. Electromagnetic field analysis of the GIB equipment using imperfect contact bridge model by the **A-φ** method is introduced in Section IV, and magnetic field results are given in Section V. Finally, relationship between the internal contact status and the surrounding magnetic field are summarized in Section VI.

II. NUMERICAL CALCULATION METHOD

According with the positioning design (deviation of conductor docking angle is limited) and the operation condition (thermal expansion/shrink occurred along bus line) of equipment, the contact status of GIB plug-in connector can be divided into conductor insert depth and docking angle. A sequential coupling method is adopted to analyze the mechanical and electromagnetic field behaviors under various contact conditions.

A. Mechanical contact parameters

Assembly structure of the GIB plug-in connector is described in Fig. 2 and the assembly parameters are listed on the bottom left of the figure. Conductor insert depth on the contact failure point is defined as 18 mm. Positioning design allows only radiation freedom of contact fingers along the direction of contact force, and the deviation of conductor docking angle is limited (less than 2°). Assembly conditions of plug-in connector may be changed by the cyclic thermal loading or short circuit current impact during the service life. Besides, contact forces can be reduced by service temperature, stress relaxation and time [17]. Hence, the mechanical contact statuses of the GIB plug-in connector under various assembly conditions and degradation stages should be accurately modeled for realizing the internal fault identification through magnetic field distributions.

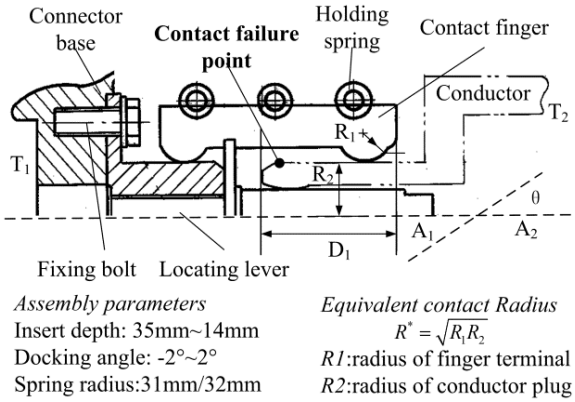

Fig. 2. Assembly structure of GIB plug-in connector.

B. Numerical calculation process

A sequential coupling method is used to analysis the magnetic field distributions around the GIB plug-in connector with various contact status and the numerical calculation flowchart is described in Fig. 3. Firstly, the contact forces of plug-in connector are calculated by mechanical field analysis. Magnetic field distributions around the GIB plug-in connector is then obtained by

electromagnetic field analysis in which the electrical contact between contact elements are simulated by the imperfect bridge model using mechanical contact forces from mechanical analysis as load inputs.

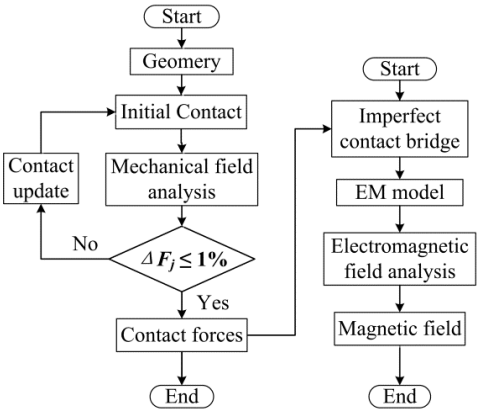

Fig. 3. Flowchart of numerical calculation.

III. MECHANICAL CONTACT ANALYSIS

The mechanical contact of GIB plug-in connector belongs to quasi-static process for the long degradation time, and forces on per contact spots are constrained by holding spring and conductor gravity.

A. Mechanical field modeling

Distribution of contact forces on individual contact fingers under action of holding spring and conductor gravity can be obtained from mechanical finite element analysis by solving displacement equation. Governing equation of static mechanical field is as follows:

$$\left.\begin{aligned}(\lambda+G)\frac{\partial e}{\partial x}+G\nabla^2 u+F_x=0\\(\lambda+G)\frac{\partial e}{\partial y}+G\nabla^2 v+F_y=0\\(\lambda+G)\frac{\partial e}{\partial z}+G\nabla^2 w+F_z=0\end{aligned}\right\}, \tag{1}$$

where λ is lame constant, G is shear modulus and E is Young's modulus, u, v, w are displacement components along space coordinate axis. F_x, F_y, F_z are extern force components along space coordinate axis.

The lame constant and the element displacement can be described as follows:

$$\lambda=\frac{E\mu_e}{(1+\mu_e)(1-2\mu_e)}, \tag{2}$$

$$e=\frac{\partial u}{\partial x}+\frac{\partial v}{\partial y}+\frac{\partial w}{\partial z}, \tag{3}$$

where μ_e means the Poisson's ratio.

Boundary conditions of mechanical field analysis are listed as follows:

$$u=v=w=0\,|_{T_1}. \tag{4}$$

Mechanical contact between contact fingers and conductor plug are analyzed using augmented Lagrange multiplier method [18]:

$$\begin{bmatrix}K+K_P & G^T\\ G & 0\end{bmatrix}\begin{bmatrix}\mathbf{r}\\ \lambda\end{bmatrix}=\begin{bmatrix}F-R\\ -g_0\end{bmatrix}, \tag{5}$$

where K is stiffness matrix of contact elements, K_p is penalty stiffness matrix between contact interfaces, G is contact potential which is defined as the product of λ and g_0, $\mathbf{r}$ is vector matrix of contact gap, λ is Lagrange multiplier, F and R are external force and reactive force (contact force) respectively.

Mechanical contact statuses of plug-in connector are in balance with the elastic deformation of holding springs and conductor gravity. Contact force acting on per contact finger is reactive force of the contact finger and the relationship between contact force and contact radius can be described by the Hertz formula [19]:

$$a=(3F_jR^*/4E^*)^{1/3}, \tag{6}$$

where a is mechanical contact radius, F_j is contact force on contact spot, R^* is equivalent radius (summarized on the bottom right of Fig. 2), E^* is equivalent Young's modulus of different contact materials:

$$\frac{1}{E^*}=\frac{1-\mu_{e1}^2}{E_1}+\frac{1-\mu_{e2}^2}{E_2}. \tag{7}$$

Mechanical stress on different contact spots under well assembly conditions (30 mm conductor insert depth) and partial loosen contact (2 degrees of docking angle deviation) are analyzed by mechanical FEM model and results are illustrated in Fig. 4. The results show that during well assembly condition, maximum mechanical stress concretes on contact spots for the limited contact area, and mechanical stresses on bottom contact fingers are larger than the upper ones under action of conductor gravity. Since the conductor docking angle deviates, the mechanical stress on the bottom contact fingers could increase up to 5.82 times higher than the one in well assembly conditions, meanwhile mechanical stress on the upper contact fingers reduced to zero, which means that mechanical contact is lost on these spots and no operation current could flow through.

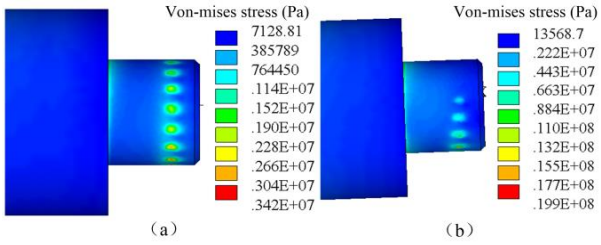

Fig. 4. Mechanical stress distributions of GIB plug-in connector under different contact conditions: (a) well assembly, and (b) conductor docking angle deviation (-2°).

Mechanical contact parameters of the GIB plug-in connector under well assembly and conductor docking angle deviation are presented in Fig. 5. Results show that the contact forces and radiuses increase from upper contact fingers to lower ones with the action of conductor gravity, and mechanical contact distributes nearly uniform among under well assembly condition. However, since the conductor docking angle deviates, mechanical contact varies obviously from each contact finger, and several bottom contact spots even lose mechanical contact (contact force reduce to 0) under seriously distorts of holding springs.

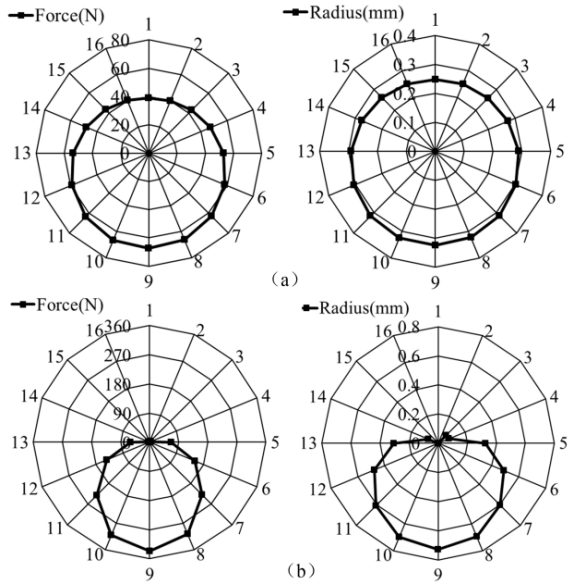

Fig. 5. Mechanical contact forces and radiuses of GIB plug-in connector: (a) well assembly, and (b) conductor docking angle deviation (-2°).

B. Electrical contact parameters

Contact resistance of plug-in connector consists only of the constriction resistance, and the relationship between resistance and contact radius is described by the Holm's contact resistance theory:

$$R_c = \rho_0 / 2a, \tag{8}$$

where ρ_0 is resistivity of contact elements and a is the equivalent radius of individual contact spot.

IV. ELECTROMAGNETIC FIELD ANALYSIS WITH POOR CONTACTS

Based on the results of mechanical contact force and radius analysis of GIB plug-in connector mentioned above, operation current flows among different contact spots can be varied from each other for deviation of the contact resistance, resulting no-uniform surrounding magnetic field distributions. A finite element model which considers the current constriction on contact spots with various mechanical contact statuses is built to obtain current and electromagnetic field behaviors of plug-in connector under different contact conditions.

A. Imperfect contact bridge model

Current conduction on contact interfaces is usually simulated by contact bridge during numerical modeling [20]. However several contact spot of plug-in connector with the poor contact status are hard to geometrically model in the electromagnetic field environment. To overcome this shortage, an imperfect contact bridge model is constructed in this paper by two parameters: the equivalent contact bridge radius and the equivalent resistivity. Mathematical expression of the imperfect contact model is as follows:

$$\begin{cases} a = a_0 & a \geq 0.1mm \\ a = 0.1 & a < 0.1mm \end{cases}, \tag{9}$$

$$\rho = \eta \rho_{\text{silver}}. \tag{10}$$

The ratio η among different contact fingers has an essential contribution to the current and magnetic field distribution of GIB plug-in connector:

$$\begin{cases} \eta = 1 & a \geq 0.1mm \\ \eta = 0.1/a & 0 < a < 0.1mm \\ \eta = \infty & a = 0mm \end{cases}. \tag{11}$$

B. Electromagnetic field analysis

Electromagnetic field analysis of GIB equipment is conducted by magnetic vector potential **A** and electric scalar potential φ in this paper (**A**-φ method). Maxwell's equations of the quasi-static electromagnetic field in source current region (conductor, V_1), Eddy current region (metal tank, V_2) and non-conductor region (SF_6 and air) can be summarized as follows:

$$\begin{cases} \nabla^2 \mathbf{A} = \mu(\mathbf{J_s} + \mathbf{J_e}) & \text{in } V_1 \\ \nabla^2 \mathbf{A} = \mu \mathbf{J_e} & \text{in } V_2 \end{cases}, \tag{12}$$

$$\nabla^2 \mathbf{A} = 0 \quad \text{in } SF_6 \text{ and Air}, \tag{13}$$

where μ is magnetic permeability, the source current **Js** and the Eddy current $\mathbf{J_e}$ can be shown as:

$$\mathbf{J_s} = -\sigma \nabla \varphi, \ \mathbf{J_e} = -\sigma \frac{\partial \mathbf{A}}{\partial t}, \tag{14}$$

where σ is electrical conductivity.

Boundary conditions on the medium interface of conductor and surrounding gas and the total numerical solution region are described as follows:

$$\left.\begin{array}{l} \mathbf{A_1} = \mathbf{A_2} \\ \mu_1 \nabla \times \mathbf{A_1} \cdot n_{12} = \mu_2 \nabla \times \mathbf{A_2} \cdot n_{12} \\ n \cdot (-j\omega\varepsilon \mathbf{A} - \varepsilon \nabla \varphi) = 0 \end{array}\right\} \text{ on S}, \tag{15}$$

$$\mathbf{A}|_{C1} = 0, \tag{16}$$

where C_1 is the boundary of FEM solution region (air boundary), S is the interface of conductor material and

medium gas, ω is the power angular frequency and ε is the dielectric constant.

V. MAGNETIC FIELD RESULTS

Current and magnetic flux density distributions of GIB equipment under two extreme contact conditions (well assembling and partial loosen contact) under 8000A operation current are investigated by numerical model in this paper. Model parameters are presented in Table 1. The calculated and measured magnetic fluxes around the plug-in connector are compared to each other to verify the validity of numerical calculation model.

Table 1: Geometric parameters of GIB model

Tank material	Aluminum alloy 6063-T6
Bus material	Aluminum alloy 6063-T6
Finger material	Copper alloy T2-Y
Spring material	Beryllium bronze
Finger number	16
Insulator material	Epoxy resin
Tank size	Φ248mm/Φ232mm
Bus size	Φ85mm/Φ65mm
Span	672mm
Field path diameter	107mm

A. Current distributions

Operation currents flow through individual contact finger of GIB plug-in connector under well assembly and partial loosen contact (2 degrees conductor docking angle deviation) are described in Fig. 6. It can be seen from results that the current distributes approximately uniformly among different contact spots under well assembly condition, and maximum current deviation is 189A. However, since seriously contact failure happens, operation currents flow through upper contact fingers (loose contact) decrease to 0 A, whereas current on the bottom contact finger increase up to 1271A.

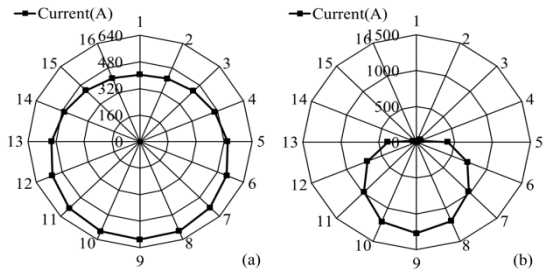

Fig. 6. Current distributions of GIB plug-in connector: (a) well assembly, and (b) conductor docking angle deviation.

B. Magnetic field distributions

The magnetic field distributions of plug-in connector under well assembly (30 mm inserting depth) and partial loosen contact (2 degrees docking deviation) conditions are described in Fig. 7. It can be seen that magnetic flux around each contact finger distributes near uniformly under the well assembly condition. However, when the seriously contact degradation/failure happens, magnetic flux is noticeable distorted and focused around the bottom contact fingers. This is due to the operation current on bottom contact fingers being larger than upper ones with lower contact resistances, exciting larger magnetic field strength round these contact fingers.

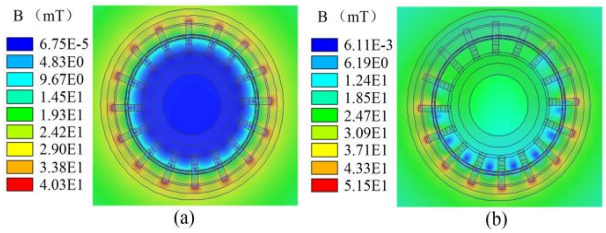

Fig. 7. Magnetic flux density around connector: (a) well assembly, and (b) conductor docking angle deviation.

C. Model verification

Magnetic flux densities around plug-in connector are obtained by both field measurement and numerical modeling. Results are described in Fig. 8. The maximum magnetic flux is averaged for minimize uncontrollable errors during the measuring probes attachment and numerical solution region discretization. Calculated and measured magnetic flux densities around the plug-in connector presents close values since well assembled. Bigger difference can be noticed since contact failure happens with larger field distortions.

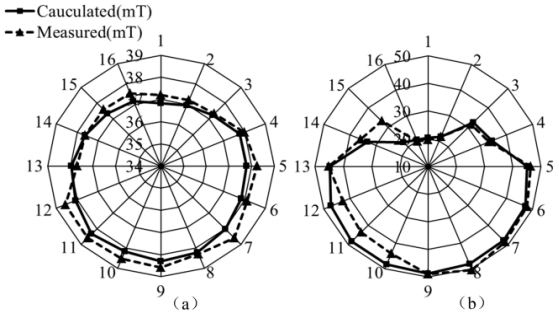

Fig. 8. Magnetic flux around GIB plug-in connector: (a) well assembly, and (b) conductor docking angle deviation.

VI. MAGNETIC FIELD UNDER VARIOUS CONTACT STATUES

The magnetic field distributions around GIB plug-in connector under various contact status are obtained by mechanical-electromagnetic coupling FEM model built in this paper. Operation current is set to 8000A as mentioned before, and the internal contact conditions of GIB plug-connector are constrained by two assembly categories (conductor insert depth and docking angle).

A. Insufficient conductor inserts depth

Figure 9 shows surrounding magnetic field responses under various conductor inserting depths with the same docking angle (0°). Results indicate that the maximum magnetic field strength differs from individual contact fingers of plug-in connector under non-uniform exciting currents. Deviations of magnetic field are not obvious among contact fingers with sufficient conductor insert depth (more than contact failure point). If conductor inserting depth exceeds contact failure point, magnetic field gathers around bottom contact fingers for larger operation currents and lower contact forces. The maximum deviation value of magnetic flux density are increasing with conductor inserting depth decreasing, deviation value is 2mT with the sufficient conductor inserting depth, 5mT at the contact failure point, and 26mT since conductor and connector near separation.

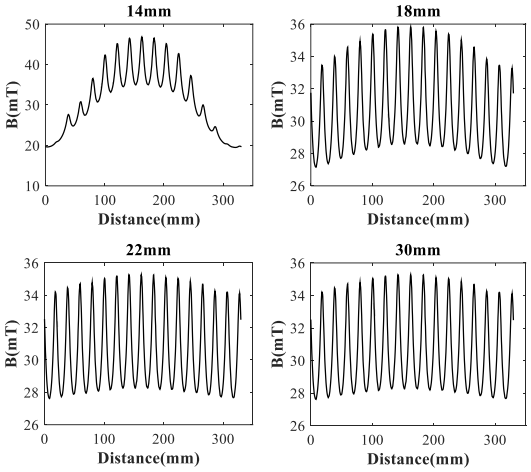

Fig. 9. Magnetic flux strength around plug-in connector under different conductor insert depths.

B. Conductor docking angle deviation (vertical)

Figure 10 shows surrounding magnetic field responses under the various conductor docking angle deviations (vertical direction along the conductor gravity) with the same conductor insert depth (30 mm). Results indicate that the maximum strength of magnetic field differs from vertical contact fingers of plug-in connector under non-uniform exciting currents. Deviations of magnetic field are not obviously among different contact fingers when docking angle less than 2°. If serious conductor docking angular deviation happens, the magnetic field distorts and gathers around contact fingers with lower contact resistances and the larger operation currents. Maximum deviation of magnetic flux density increasing with larger conductor docking angle, and magnetic field deviation value along the conductor gravity (5mT at -0.4° and 30mT at -2°) are larger than those opposite to conductor gravity (1.6mT at +0.4° and 24.5mT at +2°).

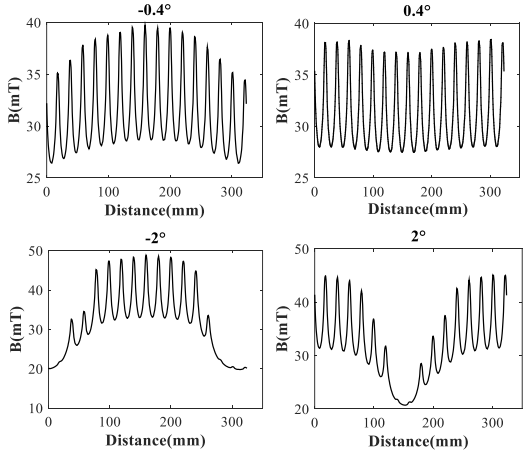

Fig. 10. Magnetic flux around plug-in connector under different vertical conductor docking angles.

C. Conductor docking angle deviation (horizontal)

Figure 11 shows surrounding magnetic field responses under various conductor docking angle deviations (horizontal direction perpendicular to conductor gravity) with the same inserting depth (30 mm). Results indicate that the maximum strength of magnetic field differs from horizontal contact fingers of the plug-in connector under the non-uniform exciting currents. Deviations of magnetic field are not obvious among different contact fingers when docking angle less than 2°. If serious conductor docking angular deviation happens, magnetic field distorts and gathers around left/right side contact fingers with the lower contact resistances and larger currents. Maximum deviation of magnetic flux density increasing with larger conductor docking angles, and the distributions of magnetic field are less influenced by the conductor gravity due to the orthogonal direction. Magnetic field deviation is 5mT at ±0.4°and 30mT at ±2° where conductor is hindered by locating lever.

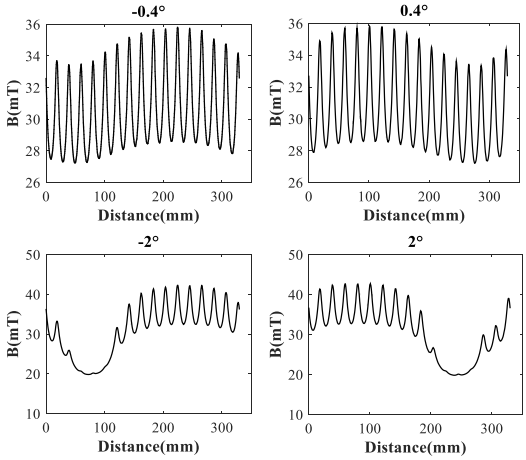

Fig. 11. Magnetic flux around plug-in connector under different horizontal conductor docking angles.

D. Conductor docking angle deviation (arbitrary)

Conductor docking angle deviation θ on arbitrary direction γ can be equivalent by the vector synthesis of horizon direction (x) and vertical direction (y) as follow:

$$\theta\angle\gamma = \theta\cos\gamma + \theta\sin\gamma, \quad (17)$$

where γ is defined by the angle between direction of conductor docking deviation and the horizon axis.

Figure 12 shows surrounding magnetic field responses under the various conductor docking angle deviations (arbitrary direction of 45°) with the same inserting depth (30 mm). Results indicate that the maximum strength of magnetic field around the contact fingers is determined by gravity and the deviation angle of plug-in connector, which could be decomposed into the horizontal and the vertical direction. Deviations of magnetic field are not obvious among different contact fingers when docking angle is less than 2°. If serious conductor docking angular deviation happens, the magnetic field distorts and gathers around the contact fingers with lower contact resistances and larger currents. Maximum deviation of magnetic flux density increasing with larger conductor docking angle, the deviation value is 5mT at ±0.4°docking angle and 25mT at ±2°docking angle where conductor is hindered by locating lever.

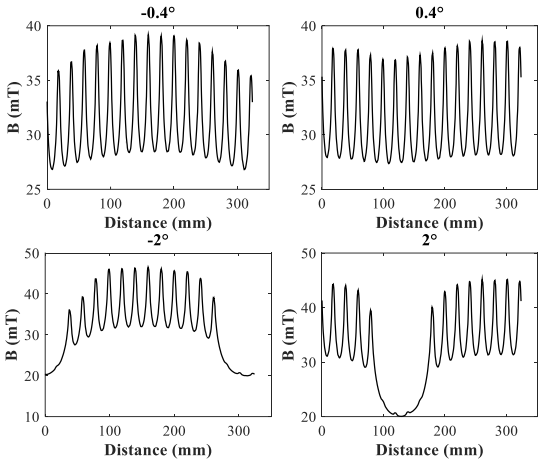

Fig. 12. Magnetic flux around plug-in connector under different 45° conductor docking angles.

VII. CONCLUSION

This work presents a mechanical-electromagnetic coupled FEM model to investigate the magnetic field behaviors of GIB plug-in connector under various assembly conditions and contact failures. The most notable conclusion obtained from this research is that the distribution characteristics of magnetic field around plug-in connector have strong correlation with internal mechanical contact statuses. When assembly conditions between the plug-in connector and conductor change, mechanical contact parameters (forces and radiuses) of different contact fingers deviate, resulting un-uniform distributions of operation current then making magnetic field distorts. The maximum field strength deviation under well assembly condition is about 2mT, and up to 30mT when partial loose contact. According to the analysis results under various contact status, it can be deduced that the surrounding magnetic field can reflect early hidden contact failures of GIB plug-in connector. If significant field deviations occur, equipment is faulty and appropriate action must be undertaken to avoid internal contacts deterioration.

ACKNOWLEDGMENT

This project funded by 60th China Postdoctoral Science Foundation (2016M602352).

REFERENCES

[1] A. Eriksson, K. G. Pettersson, A. Krenicky, et al., "Experience with gas insulated substations in the USA," *IEEE Trans. Power Delivery*, vol. 10, no. 1, pp. 210-218, 1995.

[2] A. E. Emanuel, H. C. Doepken, and P. C. Bolin, "Design and test of a sliding plug-in conductor connector for compressed gas-insulated cables," *IEEE Trans. Power Apparatus and Systems*, vol. 95, no. 2, pp. 570-579, 1976.

[3] Y. Z. Lam, J. W. McBride, C. Maul, J. K Atkinson, "Displacement measurements at a connector contact interface employing a novel thick film sensor," *IEEE Trans. Components and Packaging Technologies*, vol. 31, no. 3, pp. 566-573, 2008.

[4] Y. Mukaiyama, I. Takagi, K. Izumi, T. Sekiguch, A. Kobayashi, et al., "Investigation on abnormal phenomena of contacts using disconnecting switch and detachable bus in 300kV GIS," *IEEE Trans. Power Delivery*, vol. 5, no. 1, pp. 189-195, 1990.

[5] S. Sugiyama, T. Morita, T. Hosokawa, Y. Sekiya, et al., "An investigation of breakdown voltage with small arc current due to poor contact in SF_6 gas," *IEEE Trans. Power Delivery*, vol. 1, no. 7, pp. 332-338, 1992.

[6] M. Runde, O. Lillevik, V. Larsen, et al., "Condition assessment of contacts in gas-insulated substations," *IEEE Trans. Power Delivery*, vol. 19, no. 2, pp. 609-617, 2004.

[7] M. Landry, O. Turcotte, and F. Brikci, "A complete strategy for conducting dynamic contact resistance measurements on HV circuit breakers," *IEEE Trans. Power Delivery*, vol. 23, no. 2, pp. 710-716, 2008.

[8] Y. Ohshita, A. Hashimoto, and Y. Kurosawa, "A diagnostic technique to detect abnormal conditions of contacts measuring vibrations in metal tank of gas insulated switchgear," *IEEE Trans. Power Delivery*, vol. 4, no. 4, pp. 2090-2094, 1989.

[9] N. Okutsu, Y. Takahashi, S. Matsuda, et al., "Pattern recognition of vibrations in metal enclosures of gas insulated equipment and its application," *IEEE*

Trans. Power Apparatus and Systems, vol. PAS-100, no. 6, pp. 2733-2739, 1981.
[10] I. A. Metwally, "Status review on partial discharge measurement techniques in gas-insulated switchgear/lines," *Electric Power Systems Research*, vol. 69, no. 1, pp. 25-36, 2004.
[11] A. J. Reid and M. D. Judd, "Ultra-wide bandwidth measurement of partial discharge current pulses in SF_6," *Journal of Physics D: Applied Physics*, vol. 45, no. 16, pp. 1-10, 2012.
[12] T. M. Lindquist and L. Bertling, "Hazard rate estimation for high-voltage contacts using infrared thermography," 54th *Annual Reliability and Maintainability Symposium*, Las Vegas, USA, pp. 231-237, 2008.
[13] A. Nordstrom and R. Gustafsson, "Magnetic flux density as a probe of the state of electrical contacts," *44th IEEE Holm Conference on Electrical Contacts*, Arlington, USA, pp. 53-56, 1998.
[14] Y. I. Hayashi, "The effect of position of a connector contact failure on electromagnetic near-field around a coaxial cable," *IEICE Trans. Communications*, vol. e92-b, no. 6, pp. 1969-1973, 2009.
[15] H. Fujinami, T. Takuma, and T. Kawamoto, "Development of detection method with a magnetic field sensor for incomplete contact in gas insulated switches and bus connecting parts," *IEEE Trans. Power Delivery*, vol. 10, no. 1, pp. 229-236, 1995.
[16] G. Xiangyu, S. Naiqiu, K. Bing, et al., "Multi-physics calculation and contact degradation mechanism evolution of GIB connector under daily cyclic loading," *IEEE Trans. Magnetics*, vol. 52, no. 3, pp. 1-4, 2016.
[17] R. El Abdi and N. Benjemaa, "Experimental and analytical studies of the connector insertion phase," *IEEE Trans. Components and Packing Technologies*, vol. 31, no. 4, pp. 751-758, 2008.
[18] P. Papadopoulos and R. L. Taylor, "Mixed formulation for the finite element solution of contact problems," *Computer Methods in Applied Mechanics and Engineering*, vol. 94, no. 3, pp. 373-389, 1992.
[19] R Holm, *Electric Contacts, Theory and Applications*. Springer, New York, 1979.
[20] O. Tomohiro, S. Satoshi, and H. Katsuhiro, "Dynamic analysis method of repulsion forces on current-carrying contact using 3-D FEM," *IEEE Trans. Magnetics*, vol. 47, no. 5, pp. 942-945, 2011.

Xiangyu Guan received the B.S. degree of Environmental Science from Xinjiang Normal University, China, in 2010 the M.S and Ph.D. degrees of Power System and Automation from Wuhan University, Hubei, China, in 2015.

He is currently a Lecturer at School of Electrical Engineering Wuhan University. He is Member of ACES and ICS and his research interests mainly focus on electrical contacts, numerical methods of coupling field calculation and condition monitoring of electrical equipment.

Quanyu Shen received the B.S. degree of Electrical Engineering from Hunan University, China, in 2015. He is currently a master candidate in School of Electric Engineering in Wuhan University. His research interests include online monitoring technology and fault diagnosis of electric equipment.

Minghan Zou received the B.S. and M.S. degrees in School of Electrical Engineering Wuhan University, Hubei, China, in 2012 and 2014. He is currently an Engineer in State Grid Nanjing Power Supply Company and his research interest includes electrical equipment monitoring and fault diagnosis technology.

Naiqiu Shu received the M.S. and Ph.D. degrees in Electrical Engineering from Wuhan University. He is currently a Professor in School of Electrical Engineering Wuhan University. His currently research interests mainly focus on sensors technology and its application on condition monitoring of electrical equipment.

Hui Peng received the B.S., M.S. and Ph.D. degrees in Electrical Engineering from Wuhan University. He currently is an Associate Professor in School of Electrical Engineering. His currently research interests mainly focus on condition monitoring of electrical equipment.